The Obscured Universe: Tracing Star Formation and AGN activity across cosmic time

Fergus R. Donnan

Keble College

University of Oxford

A thesis submitted for the degree of

Doctor of Philosophy

Hilary 2025

DECLARATION

I declare that no part of this thesis has been accepted, or is currently being submitted, for any degree or diploma or certificate or any other qualification in this University or elsewhere. Unless it is otherwise stated, the work in this thesis is entirely my own under the supervision of Professor Dimitra Rigopoulou and Dr. Ismael Garcia-Bernete.

Each of the science chapters are based on published works or in prep work. These are:

Chapter 2: F. R. Donnan, D. Rigopoulou, I. García-Bernete, M. Pereira-Santaella, A. Alonso-Herrero, P. F. Roche, S. Aalto, A. Hernán-Caballero, H. W. W. Spoon. *A detailed look at the most obscured galactic nuclei in the mid-infrared.* 2023, A&A, 669, A87

Chapter 3: F. R. Donnan, D. Rigopoulou, I. García-Bernete, M. Pereira-Santaella, A. Alonso-Herrero, P. F. Roche, A. Hernán-Caballero, H. W. W. Spoon. *The obscured nucleus and shocked environment of VV 114E revealed by JWST/MIRI spectroscopy.* 2023, MNRAS, 519, 3691

Chapter 4: F. R. Donnan, D. Rigopoulou, I. García-Bernete, M. Pereira-Santaella, P. F. Roche, A. Alonso-Herrero. *Peeling back the layers of extinction of dusty galaxies in the era of JWST: modelling joint NIRSpec + MIRI spectra at rest-frame 1.5-28 μm.*, 2024, MNRAS, 529, 1386

Chapter 5: F. R. Donnan, et al. in prep.

Fergus R. Donnan — May 16, 2025

Acknowledgements

I first have to thank Dimitra Rigopoulou for her supervision and support throughout my DPhil. From the start you created a welcoming environment full of interesting and stimulating scientific discussion. I also have to thank Ismael Garcia-Bernete for also supervising me and for always being available to provide guidance. I also thank Almudena Alonso-Herrero for hosting me in Madrid for 3 months, a truly fantastic experience. I also have to thank all my other collaborators: Pat Roche, Miguel Pereira-Santaella, Susanne Aalto, Henrik Spoon for providing so much insight.

My experience in Oxford would be nothing without my office mates, Rohan, Phil, Matthew, James, David and Haochuan, who provided constant entertainment and friendship. Also for putting up with me and my nerf gun antics. I am also grateful to Mads, Alex, Casey for the quiz breaks, and always being a source of procrastination. I want to thank the rest of the department for endless banter, friendship and the many pub trips. A big thank you to Ashling Gordon for always being available to provide support and making sure the department functions properly.

I also want to thank Matthew, (also James Matthews for organising) for starting the astro band (Pat and the Roche Lobes) which has truly been a fantastic experience. I have learnt so much from playing live music and writing, instead of just playing guitar in my room. This experience makes me want to pursue music in the future, whether that be playing in a band or writing my own music. A big thank you to Matthew, Phil, Rohan, Emma, Tom, Adriano, Kaustubh, Kevin, Nancy.

Lastly I also have to thank my family for supporting me over these years and for providing train trips back up to Dundee, I am extremely grateful for all they have done.

Abstract

Most galaxies harbour a supermassive black hole at their centre, which are thought to play a key role in the evolution of galaxies, where the extreme energy outputted by accretion onto the SMBH can regulate star-formation in the host galaxy. With a majority of AGN activity heavily obscured by dust, understanding the growth/evolution of SMBHs requires peering behind the dust. The most extreme of these objects can provide a population to explain the hard X-rays in the cosmic X-ray background and may be a critical but hidden phase of galaxy evolution.

In this thesis I present an analysis of mid-infrared spectroscopy to identify and study the most obscured nuclei in the local universe. I begin with archival Spitzer data of a large sample of local ULIRGs, LIRGs and star-forming galaxies, where I demonstrate the effectiveness of the mid-infrared. With the larger samples provided by the mid-infrared selection over sub-mm studies, I better constrain the fraction of local (U)LIRGs hosting deeply obscured nuclei to 36^{+8}_{-7}% of ULIRGs and 17^{+3}_{-3}% of LIRGs.

With early JWST observations of the mid-stage major merger, VV 114, I identify an obscured nucleus consistent with the criteria developed from the Spitzer data. The higher sensitivity afforded by JWST/MIRI results in a lack of any high-IP lines, suggesting the buried AGN within has not cleared any opening which would allow it to ionise the gas. With the increased spatial resolution of MIRI, I study the environment, detecting a large scale shock front, that may have destroyed PAHs behind the shock front in a delayed process.

With the high quality spectra provided by JWST from both NIRSpec and MIRI, modelling the spectra is a challenge. I develop a model that implements differential extinction, where a 2D distribution of dust temperature and extinction defines the model dust continuum. I show that by implementing this model, I detect differential extinction in both star-forming regions and galaxy nuclei where the obscured nuclei show an isolated hot dust component indicative of heating by a buried AGN. By comparing to other tracers of extinction such as H recombination lines and H_2 lines, I find a consistent picture, where the molecular gas is strongly buried alongside the HII regions, while PAHs and the stellar continuum are less obscured.

Finally I model a substantial sample of ULIRGs, LIRGs and Seyfert galaxies with JWST spectra, where I find more evidence of this isolated hot dust component.

I observe a trend in the temperature/extinction of this component, where obscured nuclei appear coldest with a trend towards hotter temperatures as the obscuration decreases. By using libraries of torus models, I show how physical parameters affect the inferred dust distribution, where the trend of the hot component can be explained by an opening tapered disk that must become flared and/or clumpy to match the AGN. However this scenario requires a few face-on counterparts to exist in the local universe.

This thesis provides a detailed analysis of the layers of extinction in local ULIRGs, paving the way for future studies with the abundant and rich data from JWST. With the high sensitivity of JWST, much of this analysis can be performed at higher redshifts, particularly at cosmic noon where ULIRGs dominate the peak of the cosmic star-formation rate density.

Contents

List of Abbreviations

2D . . . . . Two Dimensions

3D . . . . . Three Dimensions

AGB . . . . . Asymptotic Giant Branch Stars

AGN . . . . . Active Galactic Nuclei

ALMA . . . . Atacama Large Millimeter/submillimeter Array

BLR . . . . . Broad Line Region

CON . . . . . Compact Obscured Nuclei

EW . . . . . Equivalent Width

FWHM . . . . Full Width at Half Maximum

Hot-DOG . . . Hot Dust Obscured Galaxy

IRS . . . . . InfraRed Spectrograph onboard Spitzer

IP . . . . . Ionisation Potential

IRAS . . . . . Infrared Astronomical Satellite

ISM . . . . . Interstellar Medium

ISO . . . . . Infrared Space Observatory

JWST . . . . . James Webb Space Telescope

LIRG . . . . . Luminous Infrared Galaxy

LL1, LL2 . . . Long Low channels 1 and 2 of Spitzer spectral mapping observations.

LRD . . . . . Little Red Dots

MCMC . . . . Markov Chain Monte Carlo

MIRI . . . . . Mid-Infrared Instrument onboard JWST

MRS . . . . . Medium Resolution Spectrometer of MIRI

PAH . . . . . Polycyclic Aromatic Hydrocarbon

PSF . . . . . Point Spread Function

SMG . . . . . Sub Millimetre Galaxy

SL1, SL2 . . . Short Low channels 1 and 2 of Spitzer spectral mapping observations.

ULIRG . . . . Ultra Luminous Infrared Galaxy

UV . . . . . Ultraviolet

WISE . . . . . Wide-field Infrared Survey Explorer

1 Introduction

Contents

1.1 Overview

When looking up at the Milky Way, particular towards the galactic centre, William Herschel noticed large dark patches, which he deemed "holes in the heavens" (Herschel, 1785), regions where stars seemed to vanish. It would take until the early 20$^{\text{th}}$ century for astronomers to realise that these regions in fact do contain stars but are simply obscured by some intervening material (Barnard, 1919; Shapley and Curtis, 1921). The first attribution of this obscuration to small dust grains

was suggested by Henyey and Greenstein (1941), who showed that interstellar dust particles can scatter starlight producing the observed diffuse interstellar radiation. Additionally it was noted that the strength of this scattering decreases as wavelength increases (Stebbins et al., 1939), reddening the spectrum of stars.

Soon after the first stars form and they produce supernova, the ISM is enriched with heavy elements (e.g. Kozasa et al., 1989; Ferrara et al., 2016) that can form dust grains of carbon and silicates. Additionally, the winds of AGB stars (e.g. Valiante et al., 2009) can produce dust in the early universe. As dust grains are formed of heavy elements, after galaxies reach a sufficiently high metallicity, dust production escalates rapidly (e.g. Asano et al., 2013), and can grow within the ISM (e.g. Liffman and Clayton, 1989) becoming ubiquitous within key astrophysical processes, namely star-formation and supermassive black hole growth. Understanding the evolution of these galaxies is key to revealing our place in the universe, where the building blocks for life, carbon, oxygen and nitrogen, are locked within dust grains which form disks around young stars out of which planets form.

Observing in the infrared not only limits the effect of dust reddening/obscuration, but provides a view of the emission of the reprocessing of starlight, where the dust itself emits. Therefore infrared observations are key to unlocking the secrets of our obscured universe. However observing at sufficiently long wavelengths (mid-infrared) is challenging using ground based observatories. This is because of water vapour in the atmosphere, which strongly absorbs photons at infrared wavelengths compared to optical wavelengths. Achieving high sensitivities is also a challenge due to contamination by the earth, which glows in the infrared. For these reasons, it would take until the James Webb Space Telescope (JWST) was constructed and launched to produce mid-infrared spectra with a sufficiently high spectral resolution, spatial resolution and sensitivity, comparable to ground based optical data.

Since the launch of the JWST, we have entered a new era of infrared astronomy, which allows us to reveal the crucibles of stars and the hearts of galaxies where supermassive black holes (SMBHs) rapidly accrete material. In this thesis I focus

on the latter and aim to address key questions about the growth of SMBHs through mid-infrared spectroscopy of dusty galaxies in the local universe. In particular,

- How common are the most obscured nuclei ($N_H > 10^{25}$ cm^{-2}) in the local universe?
- What is the nature of the dusty obscuring structure?
- Do ULIRGs host the progenitors of quasars in their nuclei?
- How important is this obscured phase in the evolution of galaxies?

I will address these questions in this thesis by first using archival Spitzer data before moving on to use early data from JWST. The work in this thesis sets a foundation in this new era with JWST, to study the obscured growth of SMBHs. I will start by outlining some key physics in this introduction, and summarising the current state of the field.

1.2 Star Formation

From fragmentation and collapse of giant molecular clouds stars are born. Measuring the rate at which stars form (SFR), provides a measure of how galaxies grow and evolve over cosmic time. In our own Galaxy this is simple, as we are able to observe individual stars in galaxy clusters where one can simply count the relative number of young stars.

In an extragalactic context, resolving individual stars is not possible at high redshift (apart from certain cases using gravitational lensing (e.g. Welch et al., 2022)), and so one sees a population of stars of varying age, metallicity and dust obscuration within a given observation. By modelling the continuum emission of these stars in the rest-frame UV/optical, one can model the population of stars in a galaxy (e.g. Tinsley, 1968). Through this method of Stellar Population Synthesis one can recover the relative population of different stellar ages, inferring not only the current star-formation rate, but the star-formation history of the galaxy (e.g. Cappellari and Emsellem, 2004; Cid Fernandes et al., 2005; Tojeiro et al., 2007; Carnall et al.,

2018). One may also use emission lines, such as hydrogen recombination lines such as H_α, which result from the recombination of free electrons and ionised hydrogen on the edge of HII regions around massive stars (e.g. Glazebrook et al., 1999).

Much of these tracers however become faint and/or inaccurate in the presence of dust, which obscures the UV/optical. Dust absorbs/scatters UV/optical photons from young stars, which is re-radiated thermally in the infrared (e.g. Dole et al., 2006). One can therefore gain an estimate of the obscured star-formation rate by simply measuring the infrared luminosity. By taking a multi-wavelength approach, the total star-formation rate can be measured using both the UV and the infrared/sub-mm (e.g. Boquien et al., 2019).

Measuring how the rate of star-formation per co-moving volume changes as a function of redshift provides a direct measure of the evolution of galaxies by inferring the cosmic star-formation rate density (e.g. Madau and Dickinson, 2014). Fig. 1.1 shows the cosmic star-formation rate density as a function of redshift/lookback time. It is clear that the majority of star-formation is obscured at the peak of cosmic star-formation (e.g. Algera et al., 2023; Zavala et al., 2021; Riguccini et al., 2011). At cosmic noon ($1 < z < 3$), this is dominated by Luminous Infrared Galaxies (LIRGs, $10^{11} < L_{\rm IR} < 10^{12} L_\odot$) and Ultra Luminous Infrared Galaxies (ULIRGs, $10^{12} < L_{\rm IR} < 10^{13} L_\odot$) where this high luminosity results from dust reprocessing of young, newly formed stars.

At redshifts of $z > 2$, so called sub-mm galaxies (SMGs), defined based on their bright emission at sub-mm wavelengths were first detected with SCUBA (Submillimetre Common-User Bolometer Array) on the James Clerk Maxwell Telescope (Blain et al., 1998; Hughes et al., 1998; Holland et al., 1999). These galaxies show extremely high star-formation rates, up to $\sim 1000 M_\odot {\rm yr}^{-1}$ (e.g. Michałowski et al., 2012), however beyond $z \gtrsim 4$ they become a less dominant contributor to the star-formation rate density (e.g. Zavala et al., 2021). Their existence though provides constraints on how quickly dust enrichment occurs in the early universe (e.g. Mancini et al., 2015).

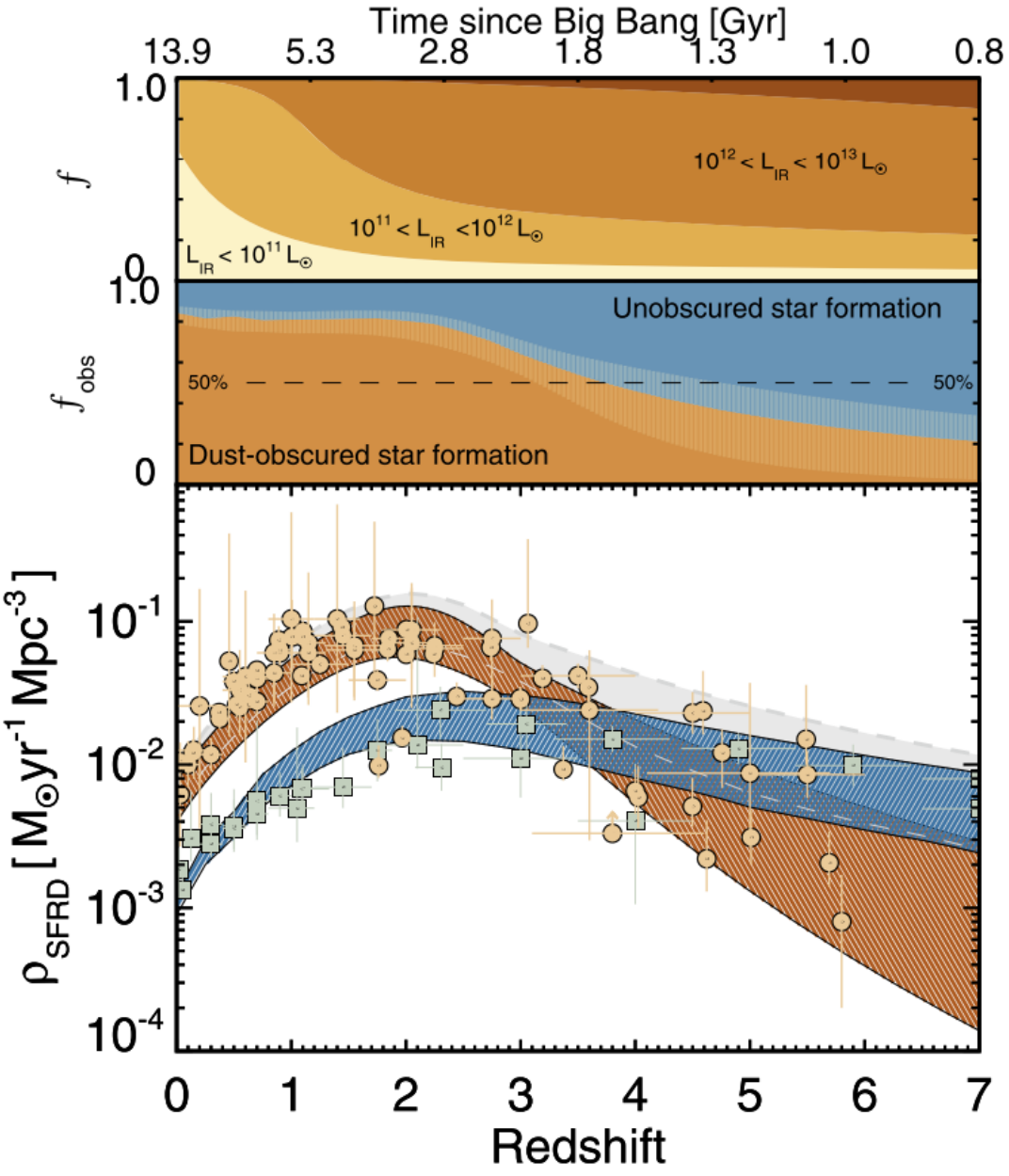

Figure 1.1: The Cosmic Star-Formation Rate Density (SFRD) from Zavala et al. (2021). The blue shaded region shows the average unobscured SFRD while the brown shaded region shows the obscured SFRD. The total is shown by the grey shaded region. The top panel shows the relative contribution from sub-LIRGs ($L_{\rm IR} < 10^{11} L_\odot$), LIRGs ($10^{11} < L_{\rm IR} < 10^{12} L_\odot$), and ULIRGs ($10^{12} < L_{\rm IR} < 10^{13} L_\odot$). The second panel shows the fraction of obscured and unobscured star-formation as a function of redshift. The orange circles are data points taken from IR/sub-mm studies while the green squares are from UV surveys.

1.3 Dust and PAHs

Dust is a key component of the ISM of galaxies and is mainly comprised of carbon and silicates, typically with sizes of $\lesssim 1\mu$m, containing much of the heavy elements in the universe. Dust is an important component in the chemistry of the ISM, where they provide sites for complex chemistry to take place as well as shielding environments from UV rays from young stars. Additionally, they provide the raw material out of which planetesimals can form in protoplanetary disks around young stars, holding the building blocks for life.

It is clear that the role and evolution of dust is critical to understand for a variety of astrophysical phenomena. For the purpose of this work, I will provide an outline the basics to provide context for this thesis, however so much more can be found in textbooks such as Tielens (2005) or Draine (2011).

The main observational characteristic of dust is to redden emission observed in the UV/optical where these photons are scattered or absorbed. This reddening is due to the strength of scattering/absorption by dust grains increasing towards shorter wavelengths. This level of extinction can be described by the optical depth at a given wavelength, and depends on the density of the dust, n_d, the extinction cross-section, $C_{\rm ext}(\lambda)$, and the path length of the photon, L, and has the form

$$\tau(\lambda) = n_d C_{\rm ext}(\lambda) L. \tag{1.1}$$

The extinction cross section describes the probability of a photon absorbing or scattering as a function of wavelength, and depends on intrinsic properties of the dust grains such as composition and size. Typically the wavelength dependence of the interaction cross section consists of a power law with additional features due to silicates at 9.8 μm and 18μm as well as a feature at 0.2175 μm although the origin of the latter is not well understood, but is thought to be either due to graphite grains or Polycyclic Aromatic Hydrocarbons (e.g. Stecher and Donn, 1965; Joblin et al., 1992). There are many extinction curves presented in the literature, which vary in their slopes and the relative strength/inclusion of this

absorption feature (e.g. Calzetti et al., 1994; Draine, 2003; Kemper et al., 2004; Chiar and Tielens, 2006; Gordon et al., 2021).

The simplest model to describe attenuation due to dust is to normalise the extinction curve and simply scale with the optical depth at said wavelength. From the solution to the radiative transfer equation, the first term, which accounts for absorption (Chandrasekhar, 1960) has the form

$$f_{\rm obs} = e^{-\tau_{\lambda_0}\tau_0(\lambda)} f_{\rm Intr} \tag{1.2}$$

where $f_{\rm obs}$ is the observed spectrum and $f_{\rm Intr}$ is the intrinsic spectrum subject to attenuation by the factor $e^{-\tau_{\lambda_0}\tau_0(\lambda)}$. The term $\tau_0(\lambda)$ is known as the extinction curve, and is normalised to 1 at λ_0 such that the total optical depth is given by $\tau(\lambda) = \tau_{\lambda_0}\tau_0(\lambda)$. The level of extinction is therefore controlled by a single parameter, the optical depth, τ_{λ_0}, which scales with the column density along the line of sight.

There are different conventions for this normalisation factor, depending on the wavelength regime. In the optical, extinction is often presented in magnitudes, which due to their logarithmic nature, is a simple conversion from optical depth,

$$\tau(\lambda) = 1.086 A_\lambda, \tag{1.3}$$

where A_λ describes the magnitude difference due to extinction. By normalising the extinction curve in the V band at 5400 Å, the level of extinction can be described by A_V, which is simply the magnitude difference in the V band due to dust. In the mid-infrared, it is typical to normalise at 9.8μm, at the peak of the silicate absorption feature and so the optical depth at 9.8μm, $\tau_{9.8}$, describes the level of extinction. For reference, $\tau_{9.8} \sim 0.1 A_V$ (Draine, 1989), depending on the assumed extinction curve.

Through the absorption of UV photons, dust will reach some temperature and thus will radiate thermally. Due to the wavelength dependence of the absorption efficiency via $C_{\rm ext}(\lambda)$, the dust does not radiate as a perfect blackbody. Instead, the emission can be described by a modified blackbody,

$$I_\nu(\lambda) = \epsilon(\lambda) B_\nu(T_d, \lambda), \tag{1.4}$$

where $B_\nu(T_d, \lambda)$ is a blackbody, described by the Planck function, at a dust temperature T_d, and $\epsilon(\lambda)$ is the emissivity of the dust which depends on wavelength. This term is typically assumed to be a power law in the far-infrared of the form,

$$\epsilon(\lambda) \propto \lambda^{-\gamma}, \tag{1.5}$$

where the exponent γ is a value typically between 1 and 2 (e.g Paradis et al., 2009; Sommovigo et al., 2022; Algera et al., 2024).

In addition to the broad dust continuum, emission from Polycyclic Aromatic Hydrocarbons (PAHs) populates the mid-infrared spectra of star-forming galaxies. PAHs are the smallest particles of dust in the ISM, comprised of numerous carbon rings of 20-1000 carbon atoms. These molecules can come in a variety of sizes and compositions and are extremely abundant in galaxies, both locally (e.g. Brandl et al., 2006; Smith et al., 2007b) and in the early universe (e.g. Spilker et al., 2023), playing an important role in the ISM (e.g. Bakes and Tielens, 1994) and dominating the mid-IR spectra of galaxies.

PAHs are excited by UV photons from young stars (e.g Tielens, 2008), and show broad/complex emission features in the infrared. These features are prominent at 3.3, 6.2, 7.7, 8.6, 11.3, 12.7, and 17 μm, resulting from the bending and stretching of C-H and C-C bonds, (e.g. Tielens, 2008; Li, 2020), where an individual PAH band is made up by multiple emission components (e.g. Rigopoulou et al., 2021; Draine and Li, 2001). Due to their excitation by young stars, they are thought to be excellent tracers of star-formation (e.g. Rigopoulou et al., 1999; Peeters et al., 2004; Shipley et al., 2016), although their emission is known to diminish in low metallicity environments (e.g. Engelbracht et al., 2008; Hunt et al., 2010; Shivaei et al., 2017).

When an AGN is present, the Equivalent Width (EW) of the PAH emission appears much lower (e.g. Netzer et al., 2007). The EW of a feature is defined as

$$\mathrm{EW} = \int \frac{\mathrm{f}_\nu^{\mathrm{PAH}}}{\mathrm{f}_\nu^{\mathrm{cont}}} \mathrm{d}\lambda, \tag{1.6}$$

and is effectively the ratio of the strength of the feature to the continuum. In AGN the high relative strength of the dust continuum or destruction of the PAH grains

in harsh radiation fields (e.g. Rapacioli et al., 2006) results in a low PAH EW. Recent studies have however found that PAHs can survive in the vicinity of AGN (e.g. Jensen et al., 2017; García-Bernete et al., 2022c; García-Bernete et al., 2022a; García-Bernete et al., 2024b; Rigopoulou et al., 2024; Zhang et al., 2024), where the ratios of different PAH bands are altered, reflecting differences in the intrinsic properties of the PAH population in these environments such as the hardness of the radiation field, the charge and the mass (e.g. Peeters et al., 2002; Candian and Sarre, 2015; Shannon and Boersma, 2019). In particular, PAHs appear more neutral in the vicinity of AGN and their outflows, but their size appears unchanged compared to star-forming regions. The exact physical process behind this is unclear, however it is thought that the ionised PAHs are more susceptible to "Coulomb explosions", where upon absorption of ionising photons, the electrons rearrange themselves, creating a repulsive force which breaks apart the molecules (Leach, 1986; Voit, 1992). This behaviour of PAHs around AGN makes them ideal tracers of feedback, particularly in obscured environments where emission lines may not be reliable (García-Bernete et al., 2024b; Zhang et al., 2024).

Accurately measuring the level of extinction is key to obtaining accurate properties of the galaxy one is observing. There are many methods to do this depending on what wavelength regime and/or features are present in one's data.

A simple way to measure the extinction affecting stars within a galaxy is to include a parameter controlling the level of extinction when modelling the stellar population (e.g. Cappellari, 2023). However this requires high quality data (preferably spectra) as there is a degeneracy between stellar age and dust extinction which both can cause a red UV/optical continuum (e.g. Silva et al., 1998; Devriendt et al., 1999). Moreover, the level of extinction may be different for young stars that are embedded within their dusty birth clouds compared to more evolved stars, which are subject to attenuation in the ISM (e.g. Jones et al., 2022).

One can also make the assumption of energy balance, where the level of attenuation in the UV/optical is consistent with the re-radiated infrared /sub-mm emission, leveraging multi-wavelength SEDs (e.g. Boquien et al., 2019; Yang

et al., 2020). Under this assumption, the contribution of AGN heated dust can be estimated by measuring any excess infrared continuum (e.g. Yang et al., 2023; Chien et al., 2024). However the assumption of energy balance relies on the UV/optical and infrared tracing the same intrinsic stellar population, which may not be the case. Observations of dusty SMGs at high-z, show spatial offsets between the UV emission and sub-mm (Bowler et al., 2022; Inami et al., 2022b; Killi et al., 2024), and therefore two separate intrinsic phenomena are contributing to the SED one would observe, breaking down this assumption. Therefore extinction is not as simple as being characterised by a single A_V. This is known as 'differential extinction", where different levels of extinction all contribute to the observed spectrum. Moreover, different methods of measuring extinction are sensitive to different intrinsic phenomena.

A commonly used method is to measure extinction is to use the flux ratio of pairs of hydrogen recombination lines, where the intrinsic ratio is known. Most commonly used is the ratio of Hα and Hβ which appear at restframe optical wavelengths, as is known as the Balmer Decrement. The first use of the Balmer decrement appears in Berman (1936). One can also use many recombination lines simultaneously to effectively derive an extinction curve. Examples pre-JWST, include the Galactic centre (Fritz et al., 2011) or nearby AGN (Osterbrock et al., 1990).

More recently Hernán-Caballero et al. (2020) presented a method to measure extinction using PAHs directly. Much like the hydrogen recombination lines, this relies on assuming an intrinsic flux ratio between two features (although in this case the intrinsic flux ratio is empirically derived), and inferring the level of extinction by comparing the observed ratio to the intrinsic ratio. In Hernán-Caballero et al. (2020), they assumed a constant ratio between the 12.7 μm PAH and the 11.3 μm PAH. Lai et al. (2024) took this a step further, and used all the PAH bands to infer extinction as a function of wavelength, effectively deriving an extinction curve.

In addition to PAHs, many molecules have been observed in the ice-phase such as H_2O, CO, CO_2, and CH (e.g. Gillett and Forrest, 1973; Spoon et al., 2001; Spoon et al., 2002). These ices cause broad absorption features in the infrared

such as H_2O at 3 μm and 6 μm, CO at 4.6 μm, and CH at 7 μm. These features are common in high mass protostars and protoplanetary disks (e.g. Öberg et al., 2011) but also have been detected in an extragalactic context, even at cosmic noon (Sajina et al., 2009). These ices are thought to form on the surface of dust grains (Tielens and Hagen, 1982).

While the 3μm H_2O absorption feature is present in star-forming regions (e.g. Rigopoulou et al., 2024), the 6μm H_2O and CH absorption are typically only found in obscured nuclei (e.g. Spoon et al., 2022). These features are even found in type 2 AGN (see section 1.4 and Fig. 1.2) where their optical depth correlates with the hydrogen column density as inferred from X-ray observations (García-Bernete et al., 2024c).

1.4 Active Galactic Nuclei

Since the fist discovery of quasars by Schmidt (1963) reporting the detection of a compact, luminous extragalactic source, a whole new field of astronomy has opened. These objects are powered by accretion onto Supermassive Black Holes (SMBHs, $M_{\rm BH} > 10^6 M_\odot$) at the centres of galaxies and are able to outshine their entire host galaxy. The high intrinsic luminosity of AGN means they are visible even into the epoch of reionisation ($z \gtrsim 6$) (e.g. Wang et al., 2021). Producing this extreme and sustained luminosity, is enabled by the extremely efficient process of accretion, where the loss of gravitational potential energy as mass moves inwards through an accretion disk, releases an enormous amount of energy. This accretion disk emits thermally as a power law in the UV/optical, as the result of many blackbodies at a variety of temperatures depending on the radius from the black hole (Shakura and Sunyaev, 1973). If one is able to observe and measure the accretion disk spectrum, the accretion rate is easily determined (e.g. Peterson, 1997).

The observed relation between the mass of SMBHs and the velocity dispersion of stars in the host bulge (e.g. Kormendy and Ho, 2013) beyond the sphere of influence of the black hole, led to the suggestion there is a co-evolution between the SMBH and its host galaxy. In particular, this may take the form of feedback, where

through kinetic and radiative processes, the AGN is able to regulate star-formation in the host galaxy (e.g. Fabian, 2012; Morganti, 2017; Harrison and Ramos Almeida, 2024). The evidence is clear that AGN play a key role in the evolution of galaxies, but the mechanisms by which this happens are not fully understood.

Long before the discovery of Schmidt (1963), Seyfert (1943) reported the detection of broad emission lines in the nuclear spectra of six galaxies. It is thought that these lines originate very close to the black hole, where the gas is virialised, and thus the gas is moving at extreme velocities ($v \gtrsim 1000$ kms^{-1}). However broad emission lines are not always present. Type 1 AGN are defined as those with broad lines present while type 2 lack these lines. To explain the presence or lack thereof of broad emission lines in the spectra of AGN, Antonucci and Miller (1985) presented the unified model of AGN, where the differences in spectra were purely attributed to viewing angle, where an optically thick torus of dust obscures the Broad Line Region (BLR) when viewed edge on (Antonucci and Miller, 1985; Antonucci, 1993). A schematic of this model is shown in Fig. 1.2.

In recent times, our understanding of dust around SMBHs has progressed from a simple static torus to an evolving dynamic structure, influenced by the interactions of the AGN and its host galaxy. By leveraging the high angular resolution obtained from interferometry in the infrared, extended dusty structures in the polar direction have been observed on parsec scales (Raban et al., 2009; Hönig et al., 2012; Hönig et al., 2013; López-Gonzaga et al., 2014; Tristram et al., 2014; López-Gonzaga et al., 2016; Leftley et al., 2018), consistent with the narrow-line region. Moreover, the presence of extended polar emission has been observed in both type 1 and type 2 AGN.

More recently with JWST imaging, extended polar emission has been observed in ESO 428-G014, after carefully removing contamination from emission lines (Haidar et al., 2024). It is still unclear however if this extended dust is simply heated by the AGN or if it is launched and radiatively driven as a wind.

Some suggest that the torus itself is the result of a "failed wind", where dusty winds launched by the AGN fail to reach escape velocity and fall back downwards,

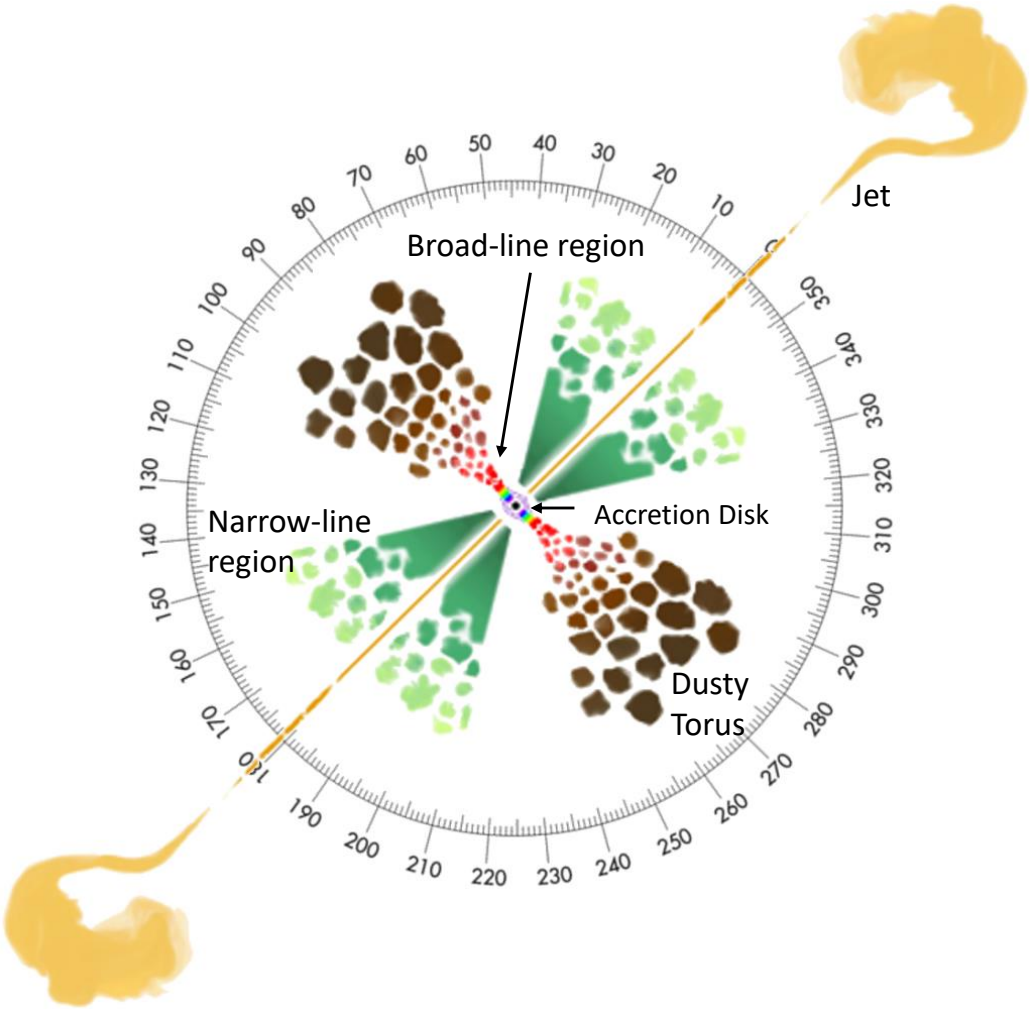

Figure 1.2: Diagram of the unified model of AGN from Marin (2016). The different regions are labelled. In this model of AGN, type 1 AGN viewed at angles of 0° - 60°, and type 2 are at angles of 60° - 90°, where the dusty torus obscured by the Broad Line Region (BLR).

creating a fountain shape (Wada, 2012). It has even been postulated that dust itself can grow in the winds of AGN (Sarangi et al., 2019) although this is hard to prove or disprove.

Whether AGN are viewed either edge-on through a torus or have some other dusty structure, a majority of AGN appear obscured (e.g. Hickox and Alexander, 2018). Even a moderate level of dust is sufficient to obscure the central accretion disk and BLR. This drastically limits what one can learn about the AGN itself, where properties such as the accretion rate and black hole mass largely rely on optical tracers. This is a significant problem, as a majority of AGN are obscured

and moreover, understanding the obscured phases of SMBH growth are critical to understanding the co-evolution between SMBHs and their host galaxies (e.g. Hopkins et al., 2006).

1.5 SMBH Growth

How SMBHs grow across cosmic time is an open question, particularly in the early universe. Recent JWST observations have identified SMBHs at high-z (e.g. Scholtz et al., 2023; Juodžbalis et al., 2023), and attempted to place constraints on their growth by measuring their mass. With our current understanding of how SMBH seeds can form, many of these at least required sustained super-Eddington accretion to generate a rapid growth phase. Of course, the masses measured at high-z require assumptions and scaling relations based on local objects (e.g. Shen and Liu, 2012) and therefore are highly uncertain.

Similar to the cosmic star-formation rate density, the black hole accretion rate density can be measured over cosmic time to map out the growth of SMBHs (e.g. Delvecchio et al., 2014). However, how AGN are selected is crucial to obtaining a complete picture of growth of cosmic time (e.g. Scholtz et al., 2023).

The imprint of the population of AGN can be seen in the cosmic X-ray background (Setti and Woltjer, 1989; Madau et al., 1994). This is the total X-ray spectrum across the whole sky which is dominate by AGN. To produce this spectrum requires populations of AGN with different obscuring column densities, N_H, between $N_H = 10^{20} - 10^{26}$ cm^{-2}. This is a dramatic range of values and suggests a majority of AGN are obscured $N_H > 10^{22}$. Once column densities reach $\sim 10^{24}$ cm^{-2}, the AGN become "Compton Thick", where the optical depth for Compton scattering reaches unity.

The cosmic X-ray background predicts a significant population of objects at $\sim 10^{25}$ cm^{-2} however beyond this limit, high energy X-ray photons become down scattered (e.g. Mushotzky et al., 1993), limiting the sensitivity of X-ray background to $N_H < 10^{26}$ cm^{-2}. Moreover, while detecting X-ray emission from individual Compton Thick sources is possible, at $\sim 10^{25}$ cm^{-2}, current facilities are not

sensitive enough for individual sources (e.g. Ricci et al., 2021). Therefore, infrared emission from the obscuring dust itself has the greatest promise to uncover the most obscured SMBHs.

1.5.1 Role of ULIRGs

As a majority of local ULIRGs are major mergers, they have been suggested as progenitors of Quasars, where the disruption of angular momentum of gas and dust feeds the central SMBH, igniting an AGN (e.g. Sanders et al., 1988; Hopkins et al., 2006). During this phase, the black hole grows while obscured by dust. After reaching a sufficiently high accretion rate relative to the mass of the black hole, the radiation pressure will overcome the gravitational pull of the black hole. This is the Eddington limit (Eddington, 1926), which depends on the opacity of the material receiving the radiation pressure. Typically this is assumed to be the Thompson cross section for scattering elections, as the accretion material is assumed to be ionised hydrogen. However in the presence of dust grains, the opacity will be dominated by the absorption/scattering cross section of the dust which is significantly higher than the Thompson cross section, leading to a higher radiation pressure and thus lower Eddington limit for dusty systems (Fabian et al., 2008). For this reason, dust is likely to be expelled by radiation driven winds earlier than the gas phase.

In Fig. 1.3, I show this evolutionary scenario, where a major interaction/merger triggers star-formation and AGN activity. The peak of this is during stages (d) and (e), however this stage comes with high dust obscuration. Also shown is the timescales for each stage, where the ULIRG phase is short compared to the other stages. Eventually, the AGN clears its dust revealing an unobscured quasar.

1.5.2 Quasars

While a majority of AGN appear obscured when selecting with relatively unbiased indicators such as X-rays, the vast majority ($\gtrsim 75\%$) of so-called quasars, show little to no dust in the UV/optical (e.g. Richards et al., 2003), where their accretion disks show a consistent slope with the thin disk of Shakura and Sunyaev (1973).

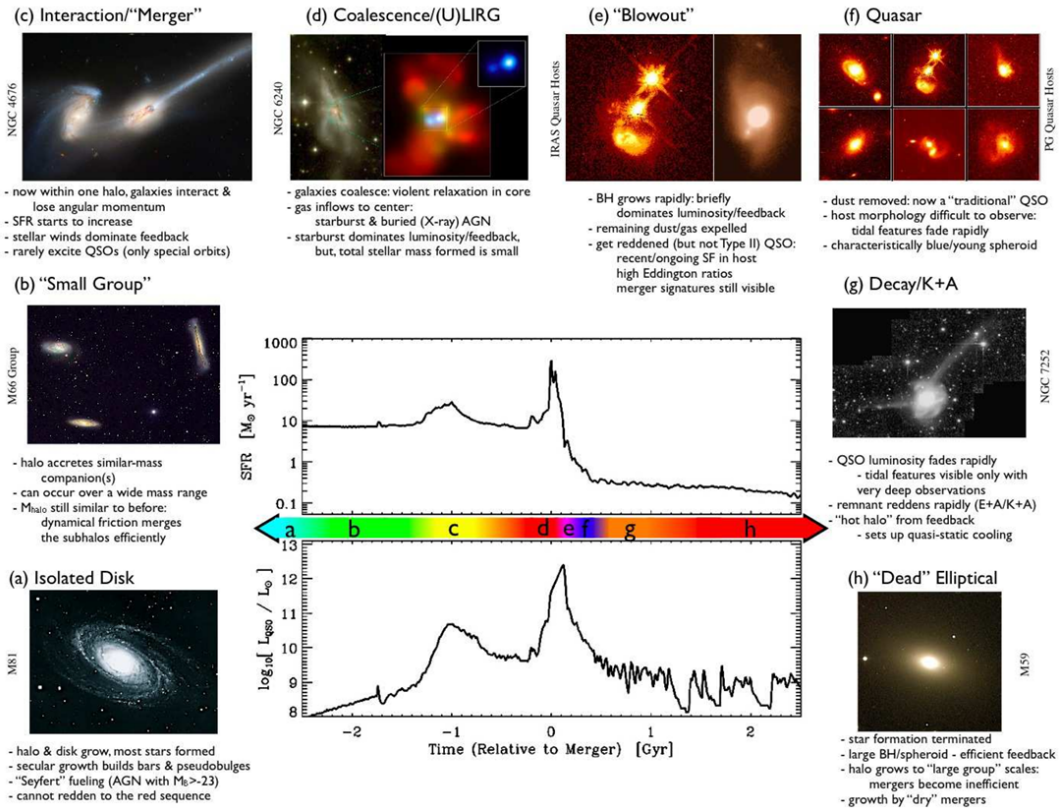

Figure 1.3: Figure from Hopkins et al. (2008) showing a typical evolutionary scenario for a galaxy. The outer panels show different stages of evolution while the middle panels show the star-formation rate (SFR) and AGN luminosity as a function of time.

This suggests that quasars are efficient at destroying dust particles along the line of sight, allowing an unobscured view of the central accretion disk.

A small fraction of quasars do show some dust, the so-called red quasars (e.g. Kim and Im, 2018; Fawcett et al., 2022), which have a reddened UV/optical spectrum. These objects may represent an intermediate population between high obscured sources present in (U)LIRGs and typical unobscured quasars.

1.5.3 Hot-DOGs

At higher redshifts, extreme dusty galaxies have been observed using the Wide-field Infrared Survey Explorer (WISE) telescope, revealing extremely luminous hot Dust Obscured galaxies (hot-DOGs Eisenhardt et al., 2012). Similar to local ULIRGs, these galaxies have been proposed to be an early phase of SMBH growth, triggered by major mergers and characterised by high dust obscuration/infrared luminosity.

Unlike local ULIRGs however, hot-DOGs show a much hotter dust continuum, making their AGN nature more unambiguous. A subsample of these are known as blue hot-DOGs, which show a strong UV continua and a red optical/IR continuum (Assef et al., 2016), and may represent a more evolved system where the AGN has began to clear its obscuring dust.

1.5.4 Little Red Dots

Since the advent of JWST, a new population of objects have been discovered, characterised by their compact size and red colours (e.g. Matthee et al., 2024; Pérez-González et al., 2024; Labbé et al., 2025). The nature of these Little Red Dots (LRDs), is not well understood, with both star-formation and AGN being proposed as potential solutions (e.g. Akins et al., 2024; Ma et al., 2024; Setton et al., 2024; Baggen et al., 2024). Given their compact nature, one would suspect an AGN to be responsible, however their bright UV emission despite red optical colours makes them challenging to fit with contemporary models. Similar to the red quasars, these sources do not require a significant amount of dust and so if they are indeed AGN, they are not extreme like the hot-DOGs or ULIRGs in the local universe and therefore may represent some intermediate evolutionary phase in the growth of SMBHs. Moreover, these objects are faint, lacking sub-mm/radio detections (Labbé et al., 2025; Perger et al., 2025). The exact relevance and role of this population in the growth of SMBHs is uncertain and a current hot topic of extragalactic research.

1.5.5 CONs

At the extreme end of the obscured AGN population, as seen by the cosmic X-ray background, exists objects with column densities in excess of 10^{25} cm^{-2}. At such high column densities, even hard x-rays are attenuated (e.g. Ricci et al., 2021). This makes detecting X-ray photons from individual targets extremely challenging with the sensitivities of our current X-ray facilities and makes it difficult to confirm the presence of an AGN in these targets.

In the local universe, objects with $N_H > 10^{25}$ cm^{-2} have been identified as so-called Compact Obscured Nuclei (CONs) (Aalto et al., 2015b; Aalto et al., 2019; Falstad et al., 2021). These objects exhibit extremely compact sizes ($\lesssim 50$ pc), enclosing a high column density of obscuring gas and dust (Falstad et al., 2021; Pereira-Santaella et al., 2021). As a result, they have extremely high infrared surface brightnesses which likely suggests an AGN power source however one cannot rule out a starburst driven nucleus, although this would require an extremely top-heavy IMF in order to produce enough energy within such a compact region.

Much of the study of CONs has been confined to the sub-mm, for numerous reasons. Firstly, the effects of dust obscuration are lower, however at such high column densities, these objects remain optically thick at long wavelengths (e.g. Falstad et al., 2019). Secondly, with facilities such as ALMA, one can obtain extremely high spatial resolutions (e.g. Gorski et al., 2024), to try and resolve these compact regions. Additionally, the presence of dense molecular gas tracers such as HCN and HCO+, can be used to understand the feeding and outflowing material from these nuclei (Falstad et al., 2018; Falstad et al., 2019; Gorski et al., 2024). In particular the vibrational transitions of HCN have been used to identify CONs (Sakamoto et al., 2010; Falstad et al., 2021). The vibrational states of HCN are populated by a "greenhouse" effect, where the dense gas traps the radiation field from the central source, heating the dust (González-Alfonso and Sakamoto, 2019). An edge-on torus is not sufficient to produce the HCN-vib emission. This effect is thought to require a closed like structure to produce the HCN-vib emission observed in CONs. This specific geometry that is required with the high column densities, has lead to a threshold HCN-vib surface brightness of $\Sigma_{\rm HCN-vib} > 1 L_\odot$ pc^{-2} being used to define an object as a CON (Falstad et al., 2021). Alternatively, the ratio of the HCN-vib luminosity to the total infrared luminosity has been used where $L_{\rm HCN-vib}/L_{\rm IR} > 10^{-8}$ defines a CON.

These extreme objects are not as rare as one might expect. In the CONquest project, Falstad et al. (2021), a search for CONs was carried out in local 46 local galaxies ($z < 0.08$), selected as far-infrared bright. They found that 38^{+18}_{-13}% of

ULIRGs and 21^{+12}_{-6}% of LIRGs hosted CONs while none of their sub-LIRGs appear to host CONs. The prevalence of CONs amongst ULIRGs is significant as the CON phase may be a short but crucial phase of galaxy evolution. Indeed, the increased importance of ULIRGs at higher redshifts (e.g. Zavala et al., 2021), particularly towards cosmic noon where ULIRGs contribute the most towards the peak of the cosmic star-formation rate density, may suggest a large population of CONs. As discussed previously, this can explain the cosmic x-ray background in the hard x-rays, where column densities of $N_H > 10^{25}$ cm^{-2} are required.

Outflows are ubiquitous in CONs (e.g. Falstad et al., 2019; Gorski et al., 2023; Gorski et al., 2024), however they are only detected at extremely small scales ($\sim$ pc) and in the molecular phase (Gorski et al., 2024). Considering the high obscuration prevents one from using traditional measures of the energetics of the power source (e.g. accretion rate), inferring the energetics of these outflows provides a probe into the power source. Early results for high angular resolution ALMA observations suggest momentum fluxes on the order of $\gtrsim 10 L_{\rm total}/c$, which are extremely high if only star-formation were responsible. The role of outflows is key in understanding how these objects evolve.

1.6 Obscuration in the pre-JWST Era

With the majority of star-formation and AGN activity occurring in dust obscured environments (e.g. Hickox and Alexander, 2018; Zavala et al., 2021), observing in the mid-infrared in crucial to understanding these fundamental astrophysical processes. The region of the spectra of galaxies between 3 μm and 30μm is complex, consisting of a complex continuum from dust emission/extinction as well as a stellar continuum at $\lambda \lesssim 3\mu$m and many emission features from PAHs, ionised gas, molecular gas etc. Disentangling these features is challenging and so obtaining spectroscopy rather than photometry is particularly important to understand this emission.

In the early 1980s, infrared observations from ground based observatories (e.g. Roche et al., 1983; Roche et al., 1984; Roche and Aitken, 1985), detected dust emission from the nuclei of numerous Seyfert galaxies between 8-13 μm,

including, then unidentified, PAH emission at 8.6 μm and 11.3 μm and silicate absorption/emission at 9.8 μm. Roche et al. (1986) presented the first spectra of a deeply obscured nucleus, NGC 4418, reporting the deep silicate feature at 9.8 μm. This spectrum is shown in Fig. 1.4, where I compare the spectra of NGC 4418 throughout the years with improving observations. The remarkable agreement of the mid-infrared spectra despite different spatial resolutions of the different telescopes, shows the mid-infrared is dominated by the nucleus. At shorter wavelengths ($<$ 5μm), the host galaxy dominates, where a clear difference can be seen between the low spatial resolution Akari data and the JWST data.

In 1983 the first infrared space telescope, IRAS (Infrared Astronomical Satellite), was launched, which performed the first all sky survey in the infrared (IRAS Working Group, 1983; Lonsdale et al., 1984). IRAS detected $\sim$350000 new sources, of which a substantial portion are extragalactic sources, powered by intense star-formation and AGN activity. The first suggestion of the existence of ULIRGs appeared in Neugebauer et al. (1971) and Rieke and Lebofsky (1979), where galaxies have an infrared luminosity in excess of $10^{12} L_{\odot}$. With IRAS, many of these sources were detected (e.g. Houck et al., 1984).

The Infrared Space Observatory (ISO), launched in 1995 providing a much higher spectral resolution (R$\sim$1200) over previous telescopes. Genzel et al. (1998) presented ISO spectra of 15 local ULIRGs concluding that the majority of ULIRGs are powered by star-formation rather than AGN, based on the strong PAH emission and lack of high-ionisation potential lines. As I will show in Chapter 2, contamination from the host galaxy can cause high PAH EWs and fill up the silicate absorption feature, so it's likely that much of the buried AGN activity was missed in the ISO spectra.

Much work was also done observing the Galactic centre, which shows deep silicates at 9.8 μm in the ISO spectrum (Lutz, 1999). Moreover, with access to multiple hydrogen recombination lines, Fritz et al. (2011) demonstrated how these lines can be used to derive an extinction curve.

The increased sensitivity of the Spitzer space telescope allowed much more extragalactic sources to be studied including PAHs (see Li, 2020, for a recent

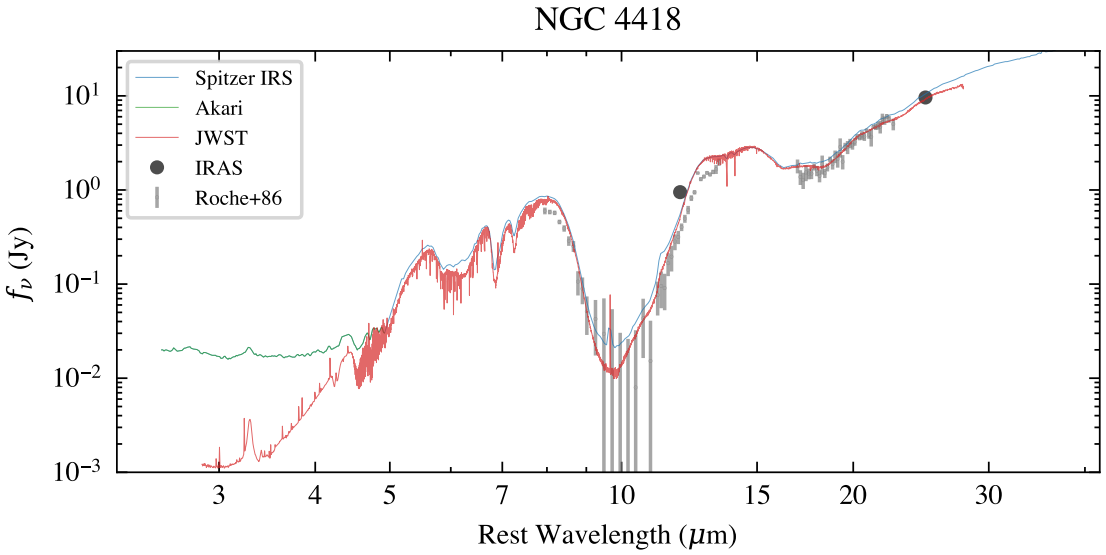

Figure 1.4: Spectra of NGC 4418, hosting a deeply obscured nucleus, as seen by different telescopes over the past 40 years. The remarkable increase in data quality with JWST signifies a truly new era for studying the dust obscured universe. The JWST spectra is from GO 1991 (P.I. George Privon). Note the difference in the Akari plus Spitzer spectrum and JWST, where the greater spatial resolution results in a lower contribution from the host galaxy, which dominates in the near-infrared.

review) and ices up to cosmic noon (e.g. Sajina et al., 2009). In particular I will highlight some key projects with respect to deeply obscured nuclei.

With the large samples of ULIRGs and quasars observed by Spitzer, the Quasar and ULIRG Evolution Study (QUEST) project aimed to test the evolutionary scenario first presented by Sanders et al. (1988) that ULIRGs represent a stage of galaxy evolution where quasars are born (Schweitzer et al., 2006; Netzer et al., 2007; Veilleux et al., 2009). The first key result of this work is that quasars do show PAH emission albeit with a much weaker equivalent width than typical star-forming galaxies, where Schweitzer et al. (2006) suggests that the far-IR emission is dominated by star-formation in quasar hosts. By assuming that the far-IR emission is purely star-formation, Netzer et al. (2007) showed that the intrinsic AGN component was similar across the sample of quasars. This likely reflects what I discussed in section 1.5 that most quasars show no dust reddening along the line of sight (e.g. Richards et al., 2003), suggesting that these objects are largely viewed face-on, resulting in a similar infrared SED.

In Veilleux et al. (2009), Spitzer IRS spectra of many ULIRGs were analysed alongside the quasar sample, and aimed to measure the AGN contribution in ULIRGs. They place the ULIRGs into three categories. Class 1 ULIRGs show low extinction and high PAH EWs, consistent with being dominated by star-formation. Class 2 ULIRGs show a high extinction with weaker PAHs while class 3 are continuum dominated with low PAH EW, consistent with being AGN dominated. Amongst the class 2 sub-sample, the authors note that the contribution of AGN is more difficult to ascertain, however they suggest $\sim 15-35\%$ of "cool" (low 25 μm over 60 μm continuum ratio) ULIRGs have an AGN contribution. These objects are likely CONs, as they tend to show a cooler dust temperatures than typical AGN (Falstad et al., 2021). I will show this in more detail in Chapter 5.

Similarly, Spoon et al. (2007) (and updated in Spoon et al. (2022)) presented a classification of galaxies based on their obscuration from the depth of the 9.8μm silicate feature and the equivalent width of the 6.2 μm PAH feature. The resulting plot of these two quantities showed two distinct branches, earning its name as a "fork" diagram. The PAH equivalent width axis is strongly influenced by how much star-formation vs nuclear continuum is present, where star-formation will produce strong PAH emission while AGN/obscured nuclei will show a strong continuum. As I will demonstrate and discuss in Chapter 2, simply relying on a deep silicate feature is not sufficient for identifying all obscured nuclei as contamination by the host galaxy can weaken the apparent absorption of this feature. For this reason, some CONs such as IC 860, appear alongside star-forming dominated galaxies in the fork diagram (see Fig. 9 of Falstad et al., 2021).

Therefore to more accurately identify deeply obscured nuclei, García-Bernete et al. (2022b) presented a method using the ratio of the EWs of different PAH features. I show in Fig. 1.5 a schematic of a galaxy hosting a deeply obscured nucleus where deep silicate emission is produced by the nucleus while PAH emission results from star-formation in the host galaxy. Therefore the ratio of the EW of the 12.7 μm PAH to the 11.3 μm PAH, and the ratio of the EW of the 6.2 μm to

the 11.3 μm PAH, can be used to successfully identify CONs from the CONquest sample, using the mid-infrared spectra from Spitzer.

This technique works by measuring the ratio of the EW of a PAH feature outside the 9.8 μm silicate absorption (12.7 μm and 6.2 μm) relative to the 11.3 μm PAH that is located within this absorption band. Using the star-forming sample of Hernán-Caballero et al. (2020), García-Bernete et al. (2022b) showed that both of these ratios were constant for the sample although the 6.2/11.3 ratio shows a larger scatter. As the presence of a heavily obscured nucleus results in a suppressed continuum around the 11.3 μm PAH feature due to the silicate absorption (see Fig. 1.5) compared to the 6.2 μm or 12.7 μm PAH, the CON selection region was defined by values of the EW(12.7)/EW(11.3) and EW(6.2)/EW(11.3) ratios below those found for the star-forming sample. These ratios therefore measure the contrast in extinction affecting the PAHs versus the continuum, and therefore are able to select obscured sources even if the PAH EWs are high. There is a limit however as I will show in Chapter 2, where the silicate feature is filled up by the less obscured star-forming dust continuum, making the EW ratio simply trace the circumnuclear emission.

1.7 Thesis Structure

In this thesis, I present how mid-infrared spectroscopy can be used to identify and study the most obscured galaxy nuclei, with a focus on the local universe, where detailed study can be performed.

Fitting the spectra of deeply obscured nuclei presented a considerable challenge throughout this thesis. I therefore developed new fitting tools that are able to fit the spectra in a satisfactory way that can provide inference of the physical nature of the dust in these targets. With each chapter, when confronted with new data and challenges, I progressively develop my fitting tools, building towards Chapter 4, where I present a tool to fit the diverse and complex spectra produced by JWST.

The thesis is structure as follows:

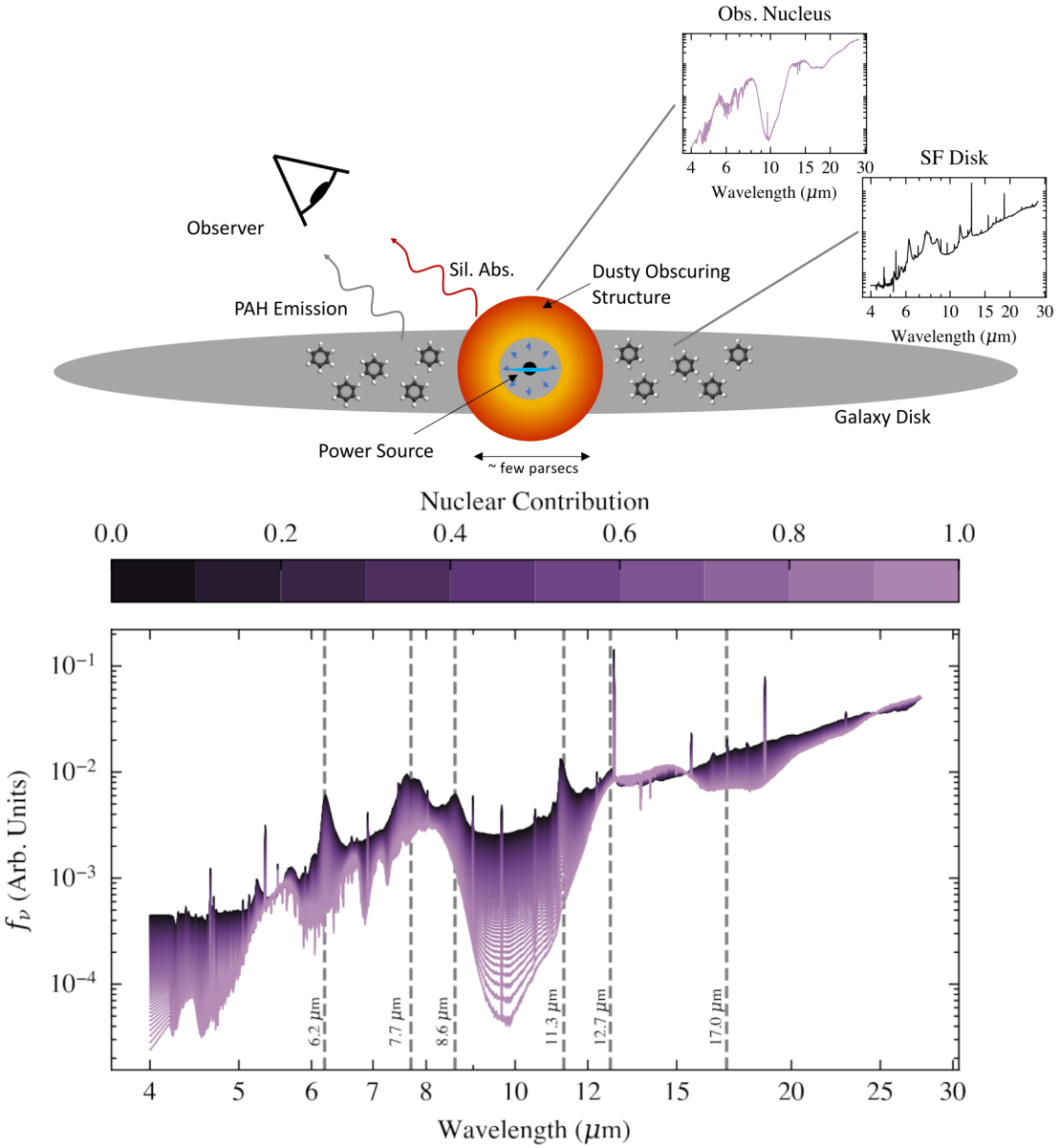

Figure 1.5: Schematic of a galaxy hosting a deeply obscured nucleus (not to scale), where the dust obscuring structure is heated by some power source, generating a dust continuum with deep silicate absorption. The inset panel shows the JWST spectrum of NGC 4418, an example CON. The galaxy disk hosts star-formation producing the PAH emission as demonstrating in the inset panel which is the average spectrum of the SF regions of NGC 3256 and NGC 7469 (see Chapter 4 and Fig. 4.1). The lower panel shows the resulting spectra which consists of the sum of the nuclear and galaxy disk components. The colour indicates the relative contribution of the nucleus compared to the disk of the integrated flux between 4-28 μm.

- Chapter 2. In this chapter I present an analysis of large samples of archival Spitzer IRS data, demonstrating the effectiveness of mid-IR spectroscopy in identifying the most obscured nuclei. With the large samples from Spitzer, I constrain the number of obscured nuclei in ULIRGs and LIRGs.

- Chapter 3. In this chapter I present the first analysis of a deeply obscured nucleus, VV 114, as observed with JWST MIRI MRS data. With the significant increase in spatial resolution over Spitzer, I show that two nuclei are identified with one being highly obscured and compact. Additionally I use the H_2 rotational lines to study the environment, producing maps of the H_2 temperature and column density, identifying a large scale shock passing through the region. This is likely caused by the galaxy-galaxy interaction.

- Chapter 4. Building on the work of the previous two chapters, I present a tool that is able to fit a variety of JWST spectra (NIRSpec + MIRI) and provide physical inference on the nature of the dust geometry. I use a differential extinction model to produce the dust continuum where I demonstrate the tool with 4 LIRGs observed with both NIRSpec IFU and MIRI MRS data which contain different kinds of nuclei. I find differential extinction in all the targets, even star-forming regions. This is consistent with other tracers of extinction, where I find the extinction of H_2 to be the highest followed by the HI recombination lines with the the stellar continuum and PAHs the least obscured.

- Chapter 5. Equipped with the tools to study galaxy nuclei in the era of JWST, I present an analysis of a significant sample of ULIRGs, LIRGs and Seyfert galaxies observed with JWST NIRSpec IFU and MIRI MRS. By inferring the dust distribution using my tool I discover a trend from the most obscured nuclei which appear cold and extinguished to the hotter less obscured Seyferts. I use torus models to reproduce the inferred dust distributions and reproduce the behaviour. From this I conclude that there is an evolutionary link where

deeply obscured nuclei clear their dust, opening up to reveal more typical AGN.

- Chapter 6. I summarise my work in the wider context and provide an outlook for future work.

2

A Mid-Infrared View of the Most Obscured Galaxy Nuclei: Analysis of Archival Spitzer Data.

Contents

This chapter is adapted from: F. R. Donnan, D. Rigopoulou, I. García-Bernete,

M. Pereira-Santaella, A. Alonso-Herrero, P. F. Roche, S. Aalto, A. Hernán-Caballero, H. W. W. Spoon. *A detailed look at the most obscured galactic nuclei in the mid-infrared.* 2023, A&A, 669, A87

2.1 Introduction

To identify Compact Obscured Nuclei in the local universe, rotational-vibrational lines of HCN have been used (e.g. Aalto et al., 2015b; Aalto et al., 2019; Falstad et al., 2021). These lines are a result of a heat-trapping effect (e.g. Kaufman et al., 1998; Rolffs et al., 2011; González-Alfonso and Sakamoto, 2019), where the extreme density of dust and gas traps radiation from a central heating source, increasing its internal temperature and populating the vibrational states of HCN while the external dust remains cool. Falstad et al. (2021) carried out a search for CONs in the local Universe ($z < 0.08$) using a representative sample of 46 galaxies, finding CONs more frequently in ULIRGs than LIRGs. However, this technique relies on a relatively weak emission feature that is extremely challenging to detect at higher redshifts, prompting the need for alternate techniques.

García-Bernete et al. (2022b) showed that polycyclic aromatic hydrocarbon (PAH) features in the mid-infrared can be used to detect highly obscured nuclei via their equivalent width (EW) ratios. The presence of a highly obscured nucleus will cause deep absorption at 9.8 μm from silicates, which will suppress the nuclear continuum around the 11.3 μm PAH feature, increasing its EW relative to the 6.2 μm and 12.7 μm PAH features, which are less affected by extinction. Therefore, highly obscured nuclei can be revealed through lower EW ratios of the 12.7 μm feature relative to the 11.3 μm and the 6.2 μm to the 11.3 μm PAH (García-Bernete et al., 2022b). Pure star-forming galaxies show near-constant PAH EW ratios as the intrinsic flux ratio is approximately constant and the PAHs are subject to the same extinction as the continuum (Hernán-Caballero et al., 2020).

Additional techniques of identifying highly obscured nuclei in the mid-infrared include the 14 μm HCN absorption feature (Lahuis et al., 2007) and the various crystalline absorption bands (e.g. Spoon et al., 2022). However, the former was

difficult to observe with *Spitzer*, as this feature is faint and easily diluted, and the latter relies on absorption at 28 μm and 33 μm, which are outside the observing range of the *James Webb* Space Telescope (JWST), limiting future application.

In this chapter I investigate the properties of deeply obscured nuclei based on mid-infrared spectroscopy and evaluate the efficacy of different methods in identifying such objects. Utilising *Spitzer* InfraRed Spectrograph (IRS; Houck et al., 2004) spectra, I introduce a new spectral decomposition method that separates the continuum into a relatively unobscured star-forming component and a nuclear component, which is subject to higher extinction. I apply the new decomposition method to samples of LIRGs and ULIRGs to determine the properties of their nucleus. I also use spatially resolved spectra to test how dilution from the host galaxy affects the measured PAH EW ratios.

The chapter is structured as follows: In Sect. 2.2 I describe the samples of the IRS staring mode data and the construction of cubes for the spectral mapping data. In Sect. 2.3 I describe my new spectral decomposition method. In Sect. 2.4 I explore the properties derived from the spectral decomposition and analyse the spectral mapping data. Finally, in Sect. 2.5 I estimate the number of CONs in ULIRGs and LIRGs and discuss the effect of galaxy inclination.

2.2 Observations

For this work I used archival spectroscopic data from the Spitzer space telescope. I use both Staring mode data (slit mode spectroscopy) and spectral mapping data (spatially resolved spectra).

2.2.1 Spitzer Staring Mode

The reduced Staring Mode data was downloaded from the IDEOS database (Spoon et al., 2022), comprising four samples of LIRGs and ULIRGs. For a representative sample of ULIRGs, I used the *HERschel* Ultra luminous infrared galaxy Survey (HERUS) sample (Farrah et al., 2013), consisting of the 42 local ULIRGs. For a complete sample of LIRGs I used the Great Observatories All-sky LIRG Survey (GOALS)

(Armus et al., 2009) sample, consisting of 179 LIRGs and 22 ULIRGs. Out of this full sample, I use the 143 LIRGs and 15 ULIRGs that were observed with *Spitzer*.

I also used a reference sample of purely star-forming galaxies (Hernán-Caballero et al., 2020), hereafter known as the HC sample.

Lastly I used the CONquest sample (Falstad et al., 2021), which consists of 44 declination and distance limited objects selected from the IRAS revised bright galaxy sample (Sanders et al., 2003). Of these 44 galaxies, 29 have *Spitzer* spectra with the majority of the objects without spectra being sub-LIRGs. Many of these objects are already part of the GOALS and HERUS samples.

2.2.2 Spitzer Spectral Mapping

I used a sub-sample of LIRGs from the GOALS sample that had *Spitzer* IRS spectral mapping observations with the SL1 and SL2 modules, providing spectra between $\sim 5 - 14$ μm (Alonso-Herrero et al., 2009; Pereira-Santaella et al., 2010; Alonso-Herrero et al., 2012). In order to include more targets that were not observed with the Staring Mode, I selected targets lacking staring mode data. I additionally supplemented the data with NGC 6926, which was selected as a CON candidate (García-Bernete et al., 2022b), providing an additional candidate to investigate. The resulting sample presented in this work is shown in Table 2.1 together with some basic properties.

After downloading the basic calibrated data from the *Spitzer* Heritage Archive[1], data cubes were constructed using CUBISM (Smith et al., 2007a). This process combines the different slit exposures, subtracts the sky background and rejects bad pixels yielding a spectral cube for each module and an associated cube containing the flux errors.

To accurately extract spectra from the two SL modules, I aligned the individual cubes using the DAOStarFinder algorithm (Stetson, 1987) from the PHOTUTILS python package, to obtain positions of sources in the image. The nuclear position was determined using the integrated intensity (moment 0) maps of the 5.4 μm

[1] https://sha.ipac.caltech.edu/applications/Spitzer/SHA/

Table 2.1: Spectral mapping sources.

Name	RA	Dec	z	$\log\left(\frac{L_{\rm IR}}{L_\odot}\right)$	Merger Class
(1)	(2)	(3)	(4)	(5)	(6)
Mrk 938	00h11m06.56s	-12d06m28.2s	0.01962	11.49	d
MCG-02-01-051A	00h18m49.85s	-10d21m34.0s	0.02710	11.48	b
Arp 236 B (VV 114 W)	01h07m46.72s	-17d30m27.9s	0.02007		
Arp 236 A (VV 114 E)	01h07m47.54s	-17d30m25.6s	0.02007	11.71	c
UCG 03410 (UGC03405)	06h13m57.90s	+80d28m34.7s	0.01247	11.10	N
ESO557-G002	06h31m45.71s	-17d38m44.9s	0.02099	11.25	-
NGC 2342 A (NGC2341)	07h09m12.01s	+20d36m11.2s	0.01722	11.31	a
NGC 2369	07h16m37.7s	-62d20m37s	0.01081	11.16	a
NGC 2388 A (NGC2389)	07h29m04.59s	+33d51m38.0s	0.01316	11.28	a
Arp 299 B (NGC 3690)	11h28m30.987s	58d33m40.80s	0.01041		
Arp 299 A (IC 694)	11h28m33.626s	58d33m46.65s	0.01041	11.93	c
ESO320-G030	11h53m11.7s	-39d07m49s	0.01078	11.17	N
NGC 4922	13h01m25.27s	+29d18m49.5s	0.02359	11.38	c
MCG-03-34-063	13h22m19.02s	-16d42m30.0s	0.02133	11.28	d
NGC 5257 A (NGC5258)	13h39m57.72s	+00d49m53.0s	0.02254	11.62	b
NGC 5395	13h58m37.96s	+37d25m28.1s	0.01158	11.08	N
IC 4518 E	14h57m45.33s	-43d07m57.0s	0.01573	11.23	a
ZW 049.057	15h13m13.1s	+07d13m32s	0.01306	11.35	N
IC 4687	18h13m39.80s	-57d43m30.7s	0.01734	11.62	b
NGC 6786 A	19h11m04.37s	+73d25m32.5s	0.02502	11.49	c
NGC 6926	20h33m06.1s	-02d01m39s	0.02001	11.32	d
IC 5179	22h16m09.1s	-36d50m37s	0.01141	11.24	N
NGC 7552	23h16m10.7s	-42d35m05s	0.00536	11.11	N
NGC 7592 B (W)	23h18m21.78s	-04d24m57.0s	0.02444		
NGC 7592 A (E)	23h18m22.60s	-04d24m58.0s	0.02444	11.40	b
NGC 7674	23h27m56.71s	+08d46m44.3s	0.02903	11.56	a
NGC 7752 A (NGC 7753)	23h47m04.84s	+29d29m00.5s	0.01720	11.07	c

Column (1): Source name. Column(2): Source right ascension from GOALS targets (Armus et al., 2009). Column (3): Source declination from GOALS targets. Column (4): Redshift obtained from NED. Column (5): Total infrared luminosity. Many of these contain multiple nuclei; see Armus et al. (2009) for more details. Column (6): Merger Class (Stierwalt et al., 2013) where N = non-merger, a = pre-merger, b = early stage merger, c = mid-stage merger, and d = late stage merger.

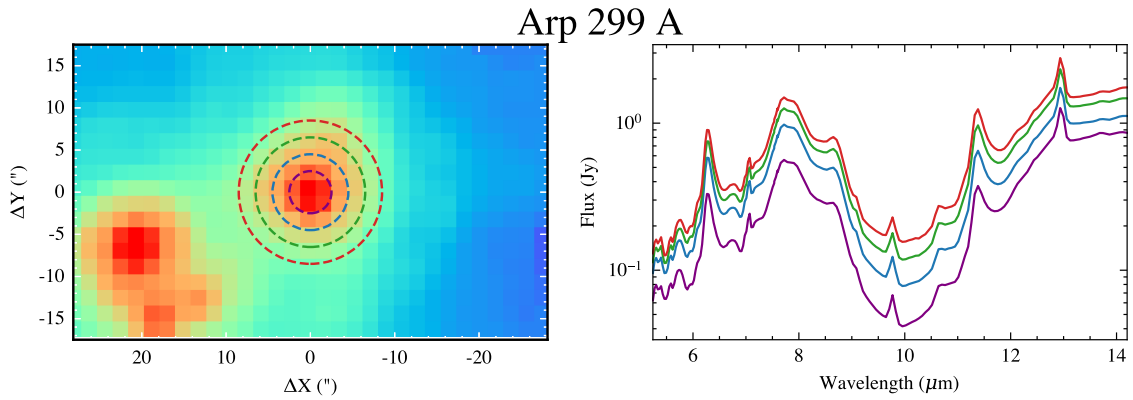

Figure 2.1: Example of the spectral extraction, in this case for Arp 299 A, at different spatial scales. *Left*: Integrated intensity map of the SL1 cube (7.46-14.29 μm) overlaid with circular apertures of radii 2.5, 4.5, 6.5, and 8.5", shown as the dashed lines. *Right*: Extracted spectra from the apertures in the left panel with the corresponding colour. The innermost spectrum (purple) has had an aperture correction applied.

continuum (5.44 - 5.47 μm). I then aligned the cubes using the overlapping channels (7.53 - 7.60 μm). The spatial offset was typically small but non-negligible in some cases (up to $\sim$ 1"). This offset correction was then applied when extracting the spectra from each cube.

Due to the large PSF for these observations (FWHM of $\sim$ 3.8" at 14 μm), I extracted spectra in circular apertures each of which contain different contributions of the galaxy disc with respect to the nuclear region. In particular I used circular apertures of radius 2.5, 4.5, 6.5, and 8.5 arcseconds, which are shown in Fig. 2.1 for Arp 299 A. These apertures were chosen as they provide distinct differences in contribution from the host galaxy with a reasonable signal to noise.

As the smallest aperture excludes flux from the wings of the PSF, to achieve a point-source extraction, I use a standard star to calculate the loss. This produces a wavelength dependant factor, to correct the extracted spectra within the 2.5" aperture. I determine this by calculating the flux ratio between an aperture containing the total flux of the star, (7.5", to encompass the stellar flux without excess noise) and the nuclear aperture (2.5"). A smooth function of the correction factor as a function of wavelength was obtained by fitting a 4^{th} order polynomial to the measured flux ratios.

The majority of spectra analysed in this work consists only of the Short-Low, SL1 & SL2 modules (< 14 μm). This is because the longer wavelength, Long Low, LL1 & LL2 modules ($> 14\mu$m) probe larger spatial scales and so galaxies containing an active galactic nucleus (AGN) or a CON will have different relative contributions of the host at long wavelengths compared to short wavelengths if the full spectral range was used. Therefore, in order to avoid making physical assumptions when applying a correction factor we simply restrict our analysis to the SL modules.

2.3 Spectral Fitting

As mention in Section 1.7, fitting the spectra of deeply obscured nuclei proved a considerable challenge, prompting me to continually develop new tools to fit the spectra. In this work I begin with Spitzer spectra, where I develop PAHDecomp[2] (Donnan, 2022). This tool fits the PAHs and emission lines with a continuum consisting of two components, namely Star-forming and Nuclear.

2.3.1 Star-forming component

To model the star-forming component of the continuum I generated templates by fitting the HC star-forming sample (Hernán-Caballero et al., 2020) with PAHFIT (Smith et al., 2007b). The left panel of Fig. 2.2 shows the resulting continuum templates ordered by their flux ratio between 8 and 13 μm. Rather than selecting an individual template, I linearly interpolate between the templates ordered in this way with a single parameter between 0 and 1 where 0 corresponds to the steepest template. The resulting template, $C_{\rm SF}(\lambda)$, is then subject to extinction (assuming mixed geometry) of the form $\frac{1-e^{-\tau_\lambda}}{\tau_\lambda}$, where I restrict the optical depth, τ_λ, using a half-normal prior based on the resulting fits from the star-forming sample. This is shown in the right panel of Fig. 2.2, where the histogram shows the optical depths at 9.8 μm inferred from the star-forming sample and the red line shows the half-normal prior used for the extinction of the star-forming component for the spectral decomposition.

[2] https://github.com/FergusDonnan/PAHDecomp

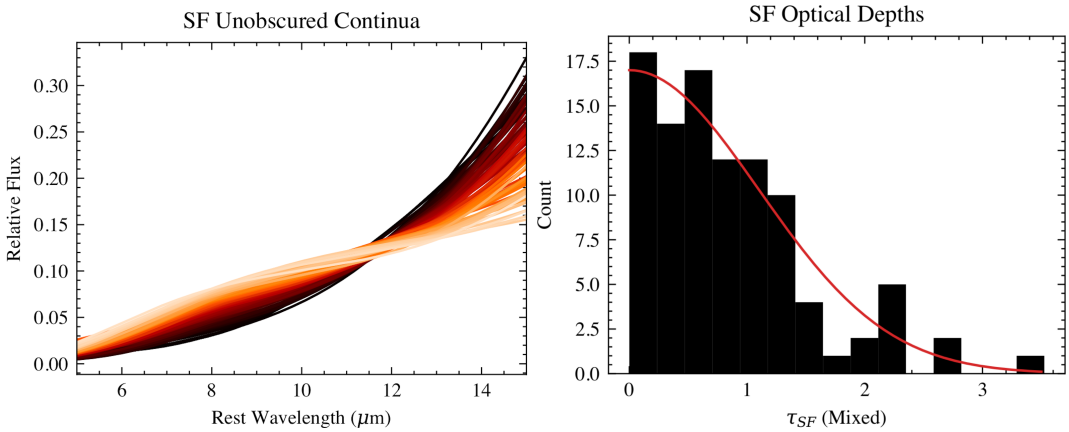

Figure 2.2: Star-forming continuum templates derived from the star-forming sample. *Left:* Unobscured continua, $C_{\rm SF}(\lambda)$, obtained from the fits to the star-forming sample, used as templates for the spectral decomposition. The colour indicates the steepness (8.0 μm to 13 μm): the darker the colour, the steeper the continuum. *Right:* Histogram of the optical depths, assuming mixed geometry, for the star-forming sample. The red line shows the half-normal prior used for the spectral decomposition based on these results.

2.3.2 Nuclear component

The nuclear component in the model consists of a continuum with some extinction applied. The continuum, $C_{\rm Nuc}(\lambda)$, is modelled as a quadratic spline with three evenly spaced anchor points at 5.5 μm, 9.85 μm and 14.2 μm. The y-value of these knots is allowed to vary as a free parameter. As the continuum is normalised by the total flux and scaled by the nuclear fraction, β, the spline has effectively only two free parameters. Extinction is then applied to the continuum as a screen using the ice template and silicate template derived from NGC 4418 and has the form $e^{-(\tau_{\rm Ice}(\lambda)+\tau_N(\lambda))}$. The silicate template is normalised to 1 at 9.8 μm, and therefore the optical depth, τ_N, is that measured at 9.8 μm. By measuring the optical depth using a nuclear component, the aim is to recover the obscuration of the nucleus much more accurately than simply measuring the silicate depth for the observed spectrum.

The ice template (including the CH absorption) is allowed to vary separately to the silicate template, resulting in a total of four free parameters (two for the shape of the spline, $C_{\rm Nuc}(\lambda)$, and two for the extinction, $\tau_{\rm Ice}$ and τ_N) determining the shape of the nuclear component. I show how these templates were created in Section 2.3.3.

For the silicate profile I used a template derived from a highly obscured source,

namely NGC 4418, because the composition of silicates is likely different (resulting in a different profile) compared to extinction laws derived from the Milky Way (Tsuchikawa et al., 2021) or the line of sight is more complex than towards the galactic centre. I describe this in section 2.3.3.

It is also worth noting that the optical depth peak of the silicate profile of NGC 4418 is ~ 4.4 from the *Spitzer* spectroscopy whereas ground based observations with a smaller beam find a higher peak ~ 7 (Roche et al., 2015). This means that the silicate profile used is still contaminated by some amount of star formation continuum and so the nuclear optical depth values inferred should be taken as lower limits for the true optical depth. In Appendix A.1.1 I compared this silicate template (NGC 4418) to another one - that of IRAS 08572+3915. From this testing I find the inferred optical depths to be higher where for all objects, the values are simply higher by a constant number. This results in the same trend as seen in Fig. 2.8, but shifted up by a constant.

For objects where the nuclear optical depth (star-forming dominated galaxies) is minimal, the continuum decomposition is unreliable as there is nothing to differentiate the star-forming component from the nuclear one. However, the total continuum should be reliable. Therefore, the decomposition is particularly sensitive to cases where the optical depth is high (as in the case of a CON) and the contribution of the nuclear component is above a certain threshold. We investigate this further in Sect. 2.3.6.

2.3.3 Extinction Templates

There are absorption features observed between 5.5 - 8 μm in strongly obscured galaxies, commonly attributed to water ice absorption at $\sim 6\mu$m (Spoon et al., 2001) and the deformation mode of aliphatic CH molecules at 6.85 and 7.25μm (Dartois et al., 2007) in addition to the deep silicate absorption at $\sim 9.8\mu$m. A theoretical template remains elusive as the molecular composition responsible for this absorption is very complex; therefore, I follow Spoon et al. (2022) and resort to constructing

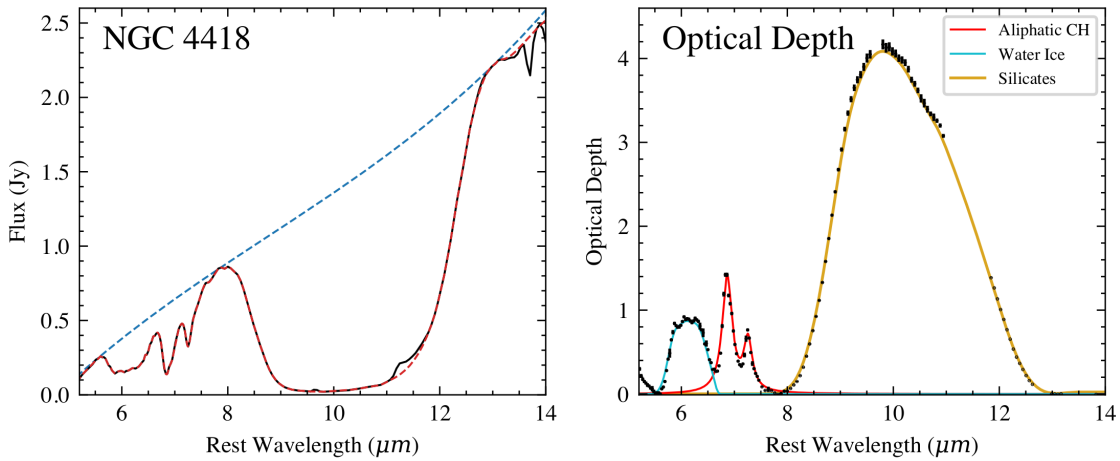

Figure 2.3: Creation of the extinction templates. *Left:* IRS spectrum of NGC 4418 (black) with the spline-interpolated underlying continuum as the dashed blue line. The dashed red line shows the spectrum with emission features removed. *Right:* Optical depth profile using the underlying continuum, overlaid with the inferred template for water ice (cyan), aliphatic CH absorption (red), and silicates (gold).

an empirical template from a heavily obscured source, similar to the silicate feature, that has very little PAH emission contaminating the region, namely NGC 4418.

Using *Spitzer* IRS spectra of NGC 4418, I determine the local underlying continuum using a cubic spline interpolation anchored at 5.5, 7.8, 13.0 and 14.5 μm. This is shown in the left panel of Fig. 2.3 as a blue dashed line. To extract an optical depth, I first mask out any PAH emission or lines before taking the natural log of the ratio of the spline continuum to the masked data. This results in the optical depth in the right panel of Fig. 2.3.

I fitted the optical depth profile with three components, the ice, CH, and silicates. Spoon et al. (2022) used two Gaussian profiles centred at 6.85 and 7.25μm to represent the CH deformation mode. However, I find the fit is poor and required broader wings to fit the optical depth spectrum. Therefore, I fitted two Drude profiles to the optical depth spectrum instead, which is shown in the right panel of Fig. 2.3 (Lorentzian profiles also provided a good fit, though the χ^2 was slightly higher). This provides the template for the CH absorption, while the ice feature is given by the residuals smoothed to provide a template, shown in cyan in the figure. The silicate profile is also given by smoothing the residuals.

2.3.4 Full model

The resulting full model is given by

$$f_\nu(\lambda) = \left[\sum_{i=1}^{N_{\rm Lines}} I^{(i)}_{\nu,\rm Line}(\lambda) + \sum_{i=1}^{N_{\rm PAH}} I^{(i)}_{\nu,\rm PAH}(\lambda) + (1-\beta)C_{\rm SF}(\lambda)\right]\frac{1-e^{-\tau_\lambda}}{\tau_\lambda} + \beta C_{\rm Nuc}(\lambda)e^{-(\tau_{\rm Ice}(\lambda)+\tau_N(\lambda))}, \quad (2.1)$$

where $C_{\rm SF}(\lambda)$ is the star-forming unobscured continuum, β is the nuclear fraction, and $C_{\rm Nuc}(\lambda)$ is the nuclear unobscured continuum. These unobscured continua multiplied by their respective extinction factors are normalised by the integrated flux between 5 - 14 μm to ensure that the scale factor, β, gives the fractional contribution of the nucleus to the total continuum flux (between 5 - 14 μm). This integration is calculated numerically during the fitting process.

To aid in the decomposition, we enforced a prior on the ratio of the total PAH flux, $f_{\rm PAH}$, to the integrated continuum flux of the star-forming continuum, $f_{\rm SF}$, between 5 - 14 μm. From the PAHFIT results for the star-forming calibration sample we found this ratio to be $f_{\rm PAH}/f_{\rm SF} \approx 1.92$. We use a very wide normal prior with a standard deviation of 10.0. This wide prior is designed to discourage solutions with zero contribution from the star-forming component as the large apertures of *Spitzer* will contain at least some extended contribution. The large width of this prior was chosen arbitrarily such that the prior discourages zero star-forming component where $f_{\rm PAH}/f_{\rm SF} \to \infty$ but does not heavily bias the results.

2.3.5 Bayesian inference

To fit these models to the spectra, I used a Bayesian approach to provide accurate posterior probabilities for the galaxy properties of interest. We used Markov chain Monte Carlo (MCMC) sampling from NUMPYRO (Phan et al., 2019) to sample the relative posterior probability of the model given the data, $\Pr(M|D)$, which is given by

$$\ln \Pr(M|D) = \ln \Pr(M) + \ln \Pr(D|M) + \text{const}, \quad (2.2)$$

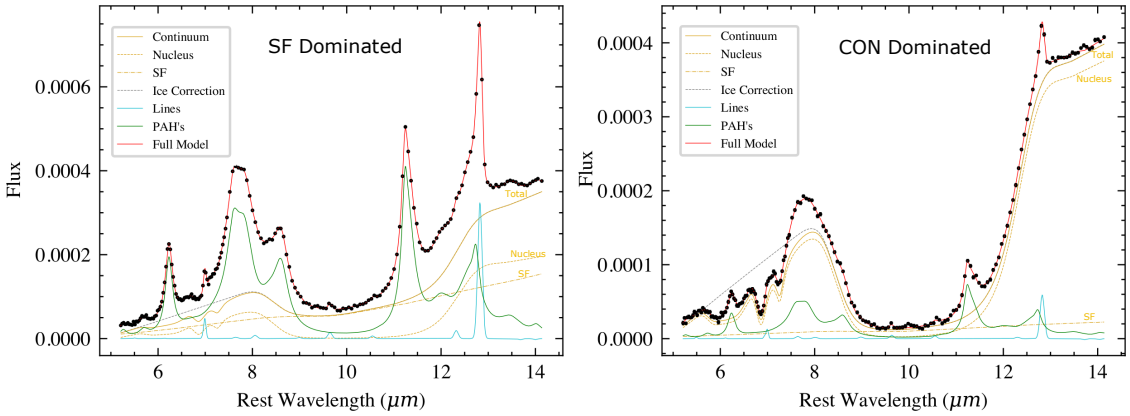

Figure 2.4: Example of our spectral decomposition fit (described in Sect. 2.3) to simulated data of a galaxy that hosts a CON. The left panel shows a highly diluted nucleus ($\beta = 0.42$) with a spectrum dominated by star formation, and the right panel shows a CON-dominated source ($\beta = 0.89$). The full model, shown in red, is composed of the various components shown in the legend. The continuum is shown as the solid gold line and is a sum of the nuclear and star-forming (SF) components, which are shown as dashed lines. The flux is in arbitrary units. The equation of the full model is given in Eq. (2.1).

where the prior, $\Pr(M)$, is uniform between sensible limits as discussed in the previous sections and the log-likelihood, $\ln \Pr(D|M)$, is effectively just the chi-squared as the error bars are fixed by the data:

$$\ln \Pr(D|M) = \sum_{i=1}^{N} \left(\frac{(f_i - f_\nu(\lambda))^2}{\sigma_i^2} \right) + \text{const}, \tag{2.3}$$

where there are N flux data f_i, with error σ_i. From NUMPYRO, we used the No-U-Turn Sampling (NUTS), a Hamiltonian Monte Carlo method that allows for faster sampling through parallelisation compared to traditional MCMC methods. After a burn-in of 2000 samples we take another 2000 samples to obtain marginalised posteriors for each of the parameters.

From the MCMC samples, posterior probability distributions for the properties derived from the spectra were constructed. For example, the EW of the PAH features, can be calculated numerically for each sample of the parameters using

$$\text{EW} = \int \frac{\text{f}_\nu^{\text{PAH}}}{\text{f}_\nu^{\text{cont}}} \text{d}\lambda, \tag{2.4}$$

where f_ν^{PAH} is the PAH profile and f_ν^{cont} is the continuum. The EW ratios of the various PAH features are then calculated with associated error bars. The continuum

used is the ice-corrected continuum to allow comparisons with the IDEOS sample (Spoon et al., 2022), and to better determine how the silicates may affect the PAH features. The integrated flux of the PAH features is also calculated using

$$f^{\rm PAH} = \int f_{\nu}^{\rm PAH} d\nu, \tag{2.5}$$

where posteriors for the PAH flux ratios can be calculated. I do this with and without extinction applied to obtain estimates for the intrinsic ratios as well.

I also estimate the strength of the 9.8 μm silicate feature defined as (Spoon et al., 2007)

$$S_{\rm sil} = \ln \left(\frac{f_{\rm 9.8,obs}^{\rm cont}}{f_{\rm 9.8,int}^{\rm cont}} \right), \tag{2.6}$$

which is the log of the ratio of the observed to the intrinsic continuum at 9.8 μm. It should be noted that this is different from the nuclear optical depth, τ_N, in the spectral decomposition method, which allows the nuclear silicate feature to be 'filled up' by the star-forming dust continuum. Therefore, objects with a buried nucleus but with a strong extended star-forming component may have a low observed silicate depth as defined by Eq. 2.6 but a deep nuclear optical depth, τ_N.

2.3.6 Testing the method

The primary motivation for modelling the spectra using this new decomposition tool is to provide a realistic continuum to enable us to accurately determine the strength of the emission features. However, it also allows us to better constrain the physical properties of the two components (nuclear and star-forming), particularly the optical depth of the nuclear region, the fraction of the nuclear to the total continuum and, consequently, the shape of the nuclear continuum. It is therefore instructive to test the effectiveness of this decomposition method before inferring the properties of the deeply obscured galaxies studied here.

Accuracy of inferred properties

I first generated simulated data of a typical star-forming galaxy hosting a CON (with a given τ_N) with varying degrees of dilution from the host galaxy (different values of β). This was done by constructing a spectrum using a star-forming galaxy and a CON template, where different fractional contributions, β, of the CON were used. I then ran the decomposition tool on the spectra and tested its ability to recover the true nuclear fraction and nuclear optical depth.

I used NGC 1797 for the star-forming component as this shows a typical spectrum of a star-forming galaxy with some silicate absorption, and the nucleus of NGC 4418 as the CON template. The star-forming continuum was normalised to the integrated continuum flux between 5 and 14 μm. The PAH and emission lines from NGC 1797 were also included as part of the star-forming component and were normalised by the same factor as the continuum. The CON continuum from NGC 4418 was normalised by its integrated flux over the same wavelength range. The star-forming component was then scaled by $(1 - \beta)$ and the CON component by β for 20 values of β between 0 and 1. I generated two sets of simulated data, the first with a CON component with $\tau_N = 4.5$ and the second with a lower nuclear optical depth of $\tau_N = 3.0$ to test the reliability of the method for different levels of nuclear obscuration. I generated noise for the simulated spectra, comparable to the actual data, with a signal to noise of 100.

Fig. 2.4 shows two example fits to the simulated data with the left panel showing a CON highly diluted by the host galaxy ($\beta = 0.42$) and the right shows a CON-dominated source ($\beta = 0.89$). In both cases the nuclear optical depth, τ_N, and nuclear fraction, β, are successfully recovered by the model. At values of $\beta \lesssim 0.4$, the method is unable to recover the nuclear fraction and/or the optical depth as reliably, although in the case of the optical depth, the errors do a reasonably good job of accounting for this. This is demonstrated in Fig. 2.5, where the measured nuclear fraction is plotted against the true value of the nuclear fraction in the left panel. The red points shown the data set with a $\tau_N = 4.4$ whereas the blue show a lower $\tau_N = 3.0$. This plot demonstrates that even when the nuclear component has

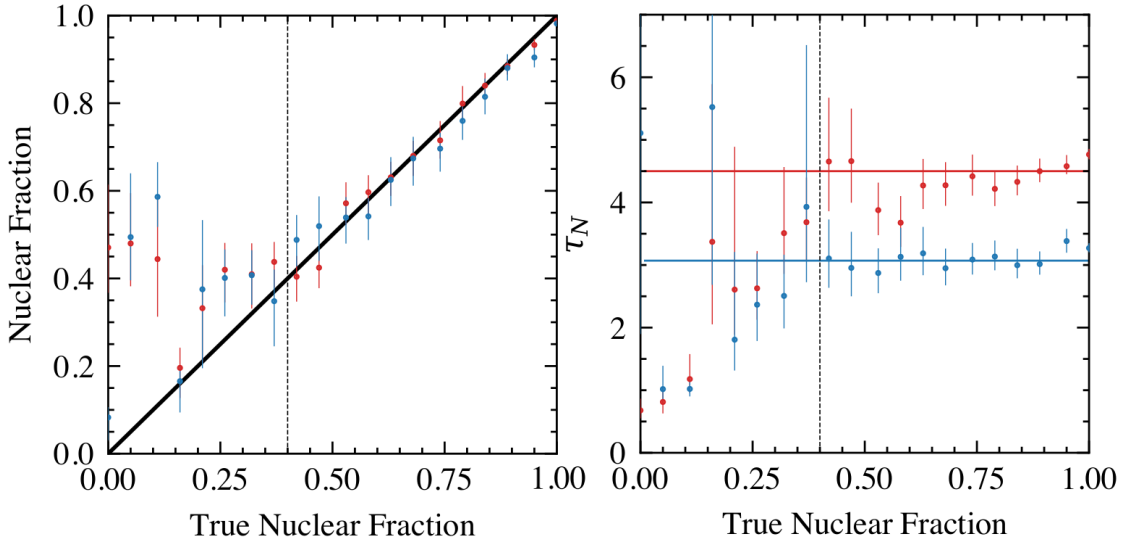

Figure 2.5: Testing the recovered properties of simulated data using the spectral decomposition fitting method. *L*eft: Measured nuclear fraction, β, against the true value. The solid black line shows where the measured equals the true value. *R*ight: Measured nuclear optical depth, τ_N, against the true nuclear fraction. The solid horizontal lines show the true optical depth of $\tau_N = 4.5$ in red and $\tau_N = 3.0$ in blue. The vertical dashed black lines show a cutoff of $\beta = 0.4$, below which the measured values become unreliable.

a lower optical depth, the nuclear component is still recovered by the model. The right panel shows the measured optical depth for each simulated spectrum with the true value of $\tau_N = 4.5$ displayed for the red points and $\tau_N = 3.0$ for the blue points.

In the cases of maximum dilution $\beta \lesssim 0.15$, the optical depth recovered is significantly below the true value but with a high measured value of β. This is likely due to the nuclear component being used to fit the star-forming component as the two components become degenerate when β is low. Therefore I conclude that the optical depth is accurately recovered for values of $\tau_N > 2.5$ (which corresponds to values greater than $> 5\sigma$ of the mean silicate depth of the star-forming calibration sample, where σ is the scatter in the silicate depths of the SF sample) and nuclear fractions of $\beta > 0.4$.

Multiple-aperture fitting

From the spectral mapping data, each aperture yields a spectrum (see Fig. 2.1) that we would like to fit. As each of these apertures has the same centre but different radii they contain the same nucleus but different contributions of the disk

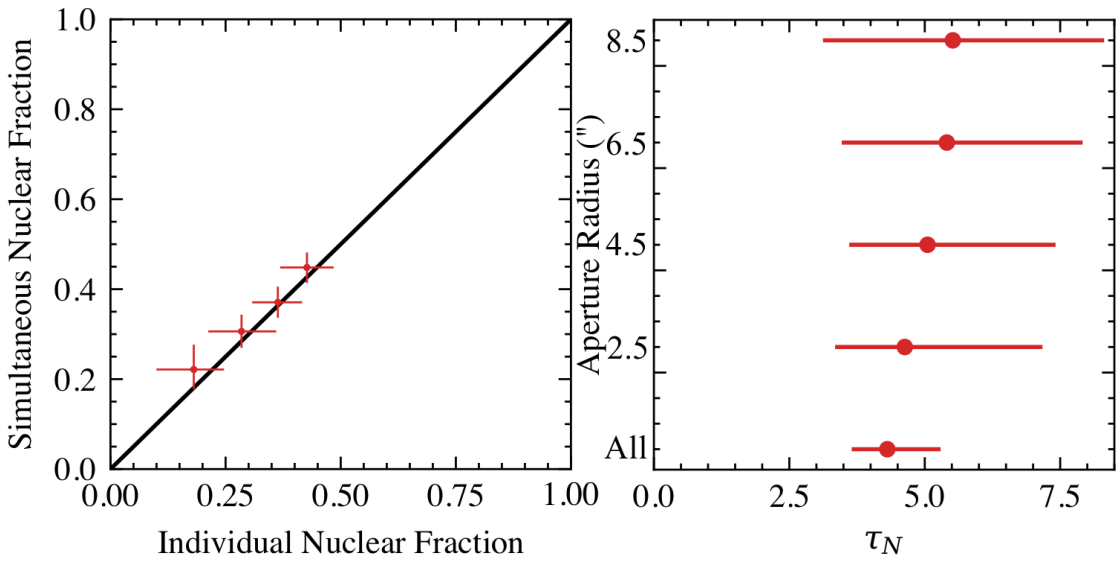

Figure 2.6: Comparison between fitting spectra from individual apertures vs fitting all apertures simultaneously with shared nuclear parameters for ESO320-G030. *L*eft: Nuclear fraction, β, measured from the simultaneous fitting on the y-axis vs the individual spectra on the x-axis. The solid black line shows where they are equal. *R*ight: Measured optical depth of the nucleus for each aperture individually and for all apertures simultaneously. Note the much smaller error when using all the spectra simultaneously.

star-forming component. It is therefore useful to fit all these spectra simultaneously assuming the same nuclear component for all the spectra but different star-forming components for each.

To test this idea, I used the spectral map of a known CON to measure the nuclear properties from the spectra of each aperture individually and then compare the results to those from fitting all the apertures simultaneously. I used ESO 320-G030, which is known to be a CON but has a strong star-forming component (Alonso-Herrero et al., 2006; González-Alfonso et al., 2021). The left panel of Fig. 2.6 compares the measured nuclear fraction for each aperture when fitting all the spectra simultaneously sharing the same nucleus against fitting each of the spectra independently. The measured values are consistent within 1σ between the two methods. The right panel of Fig. 2.6 shows the measured optical depth of the nucleus measured from each aperture individually compared to those measured from all apertures when fit simultaneously. Again, I find that the measurements are consistent between the two methods and crucially, even in the presence of significant

contribution from the host galaxy. In this case the value of τ_N does not change, instead the error bars expand accordingly. This test also demonstrates the added value in fitting all the apertures simultaneously, with tighter constraints on the nuclear optical depth. Having proved the robustness of our method, we proceed and deploy the tool to fit the spectral mapping data.

2.4 Results

Based on the spectral fits using the new decomposition tool, I first refine the CON selection criteria (Sect. 2.4.1) before investigating the physical properties of the nuclei in Sections 2.4.2. I then present results using the spectral mapping data in Sect. 2.4.3.

2.4.1 Refining the CON selection criteria

As described in Chapter 1, the PAH EW CON selection technique (García-Bernete et al., 2022b), relies on two ratios: EW(12.7)/EW(11.3) and EW(6.2)/EW(11.3), where below a certain threshold, CONs can be selected. We refine those thresholds, consistent with the fitting technique used in this work, using the HC star-forming sample (Hernán-Caballero et al., 2020).

The resulting EW ratios are shown in the top left panel of Fig. 2.7 where the 12.7/11.3 PAH EW ratio has a mean value of $\langle EW_{12.7}/EW_{11.3}\rangle = 0.427$ with a scatter of $\sigma\left(EW_{12.7}/EW_{11.3}\right) = 0.077$. Subtracting the average uncertainty of the data (0.030) in quadrature, we obtain an intrinsic scatter of $\sim 17\%$. The 6.2/11.3 PAH EW ratio shows a much larger scatter with a mean $\langle EW_{6.2}/EW_{11.3}\rangle = 0.99$ and a scatter $\sigma\left(EW_{6.2}/EW_{11.3}\right) = 0.49$.

Comparing the fitting method in this work (Drude PAH profiles) to that of IDEOS (Pearson-IV PAH profiles), I find a larger mean value in the $EW_{12.7}/EW_{11.3}$ and a higher scatter. They found a mean of 0.346 and $\sim 5\%$ intrinsic scatter (Hernán-Caballero et al., 2020).

The larger scatter in the 6.2/11.3 PAH EW ratio may be due to differences in the intrinsic properties of the continuum. Different dust temperatures will more

strongly affect the continuum between 6.2 and 11.3 than 12.7 and 11.3. This can be seen in the left panel of Fig. 2.2 where the presence of hotter dust (> 200K) will increase the continuum around 6.2 μm.

Using the newly measured PAH EW values I defined the CON selection region as follows: we take the 2σ lower boundary as the threshold for the 12.7/11.3 and the 1σ lower limit for the 6.2/11.3. The lower criteria of the 6.2/11.3 of only 1σ was due to the larger scatter in this axis where 2σ would not be able to provide a reasonable selection region. These criteria result in the purple shaded region shown in Fig. 2.7, where the thresholds are $EW_{12.7}/EW_{11.3} = 0.271$ and $EW_{6.2}/EW_{11.3} = 0.503$.

Two objects in the HC star-forming sample (Hernán-Caballero et al., 2020) fall in the CON region namely VV 283a and UGC 01845. Both of these objects are LIRGs with $\log(L_{\rm IR}/L_{\odot}) = 11.68$ and 11.12, respectively (Armus et al., 2009). These two objects are not selected in previous work (García-Bernete et al., 2022b). From our optical depth selection discussed in Sect. 2.4.2 I identify a further 5 potential CON candidates from this sample (all of them are LIRGs). Since this sample was selected only by excluding "normal" AGN, identifying additional CON candidates is therefore not unexpected.

2.4.2 Physical properties of CONs

Fitting the mid-infrared spectra with a physically motivated model allows us to recover the continuum of the nuclear component, thus providing insight into the physics of CONs, in particular the nuclear optical depth at 9.8 μm, τ_N, and the level of dilution from the host galaxy in form of the nuclear fraction, β.

It is therefore instructive to investigate further properties of the CONs. First, we examined whether there is a possible relation between the model-derived quantities and the properties of the HCN-vib line. Using PAHDecomp to fit the CONquest sample (Falstad et al., 2021), I measured the nuclear optical depth, τ_N. The measured PAH EW ratios are shown in the top right panel of Fig. 2.7. In Fig. 2.8 I show τ_N as a function of the HCN surface brightness in the left panel, and the ratio to the $L_{\rm IR}$ in the right panel. In both plots there is a clear trend for a higher

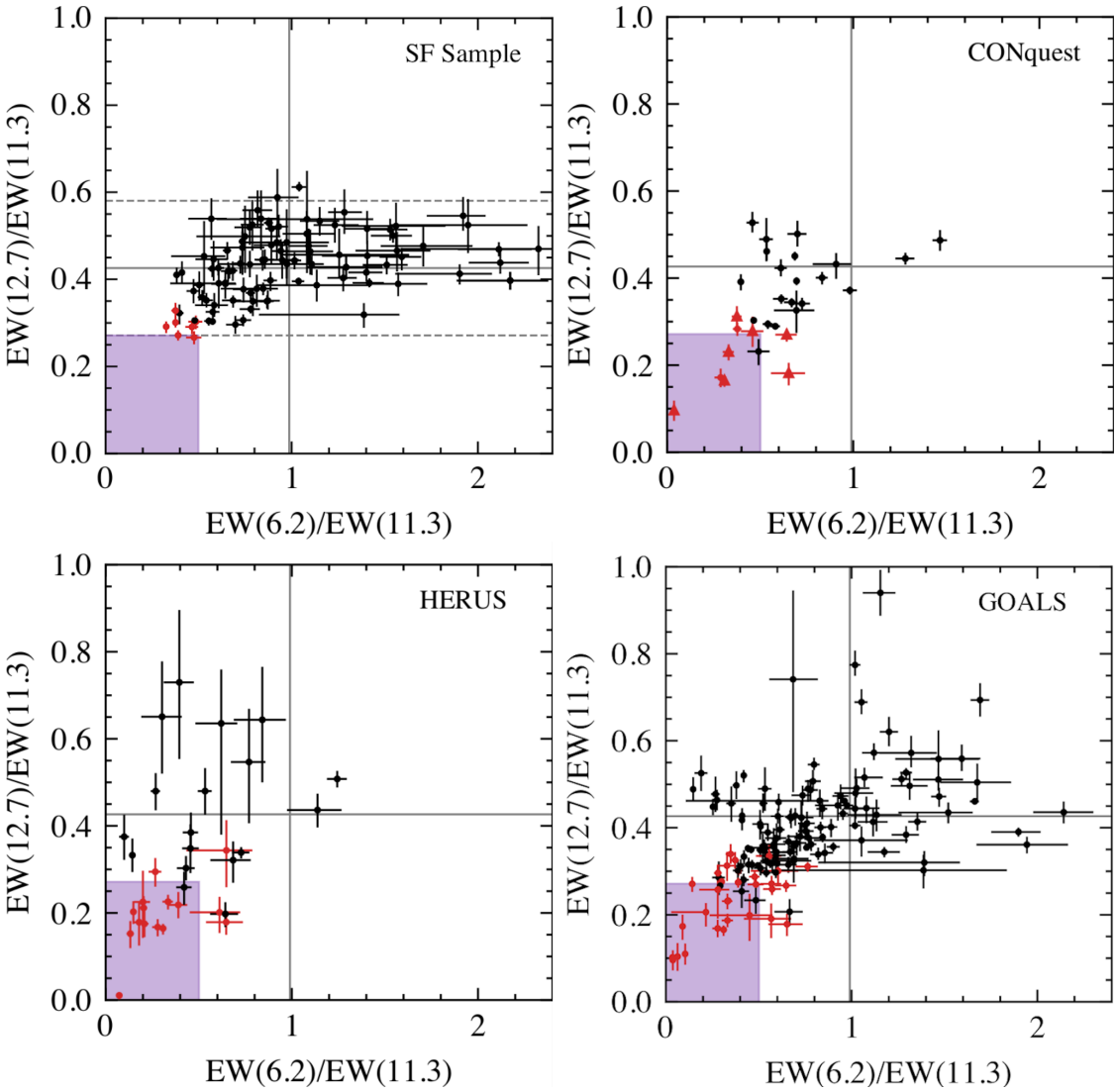

Figure 2.7: PAH EW diagram (García-Bernete et al., 2022b) of the 12.7/11.3 PAH features against the 6.2/11.3 PAH features obtained from fitting the HC star-forming sample (top left) (Hernán-Caballero et al., 2020), CONquest (top right) (Falstad et al., 2021), HERUS (lower left) (Farrah et al., 2013), and GOALS (lower right) (Armus et al., 2009). Points in red have a nuclear optical depth $\tau_N > 3.5$, and for the CONquest sample the triangle points are those identified as CONs by $\Sigma_{\rm HCN-vib} > 1 L_\odot$ pc^{-2}. The grey lines show the mean values for the star-forming sample, with the 2σ values for the 12.7/11.3 PAH shown by the dashed lines. The purple shaded area shows the CON selection region.

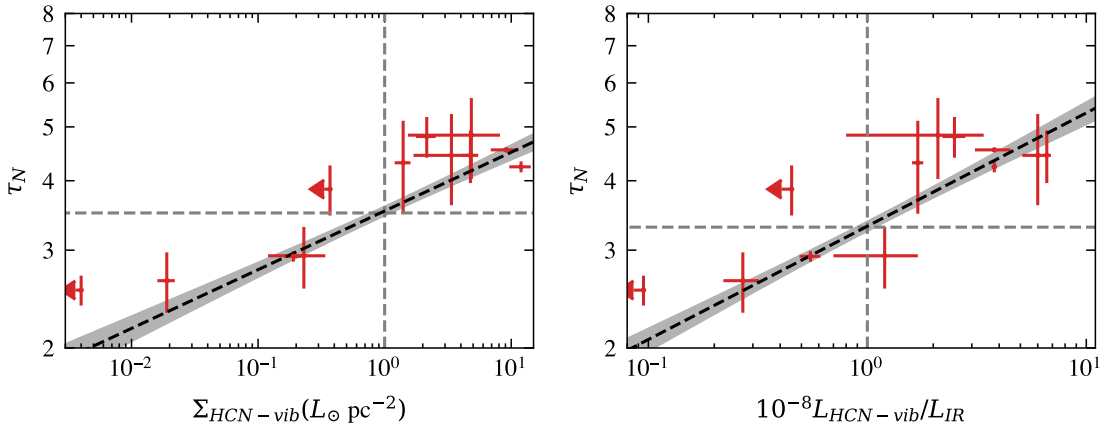

Figure 2.8: Optical depth of the nuclear component from the spectral decomposition fits to the CONquest sample (Falstad et al., 2021) against the surface brightness of HCN-vib (left) and the strength of HCN-vib to L_{IR} (right). Linear fits are shown in the dashed black lines, with 1σ confidence intervals shown in grey. The upper limits of HCN-vib measurements are shown for objects with $\tau_N > 2.5$ and $\beta > 0.4$. The dashed grey lines show the HCN-vib CON identification threshold (Falstad et al., 2021) on the x-axis and the corresponding τ_N on the y-axis.

optical depth correlating with stronger HCN-vib emission. A Pearson correlation test results in coefficients of 0.91 and 0.84 for the HCN-vib surface density plot and HCN-vib to L_{IR} plot, respectively. This correlation provides good evidence that the heat-trapping effect required to populate the vibrational states of HCN is consistent with the presence of large quantities of dust with a high internal temperature producing the mid-infrared radiation field and a cool dusty exterior to provide the high optical depths of the silicate absorption feature.

Unlike the nuclear optical depth, the apparent silicate strength as measured using Eq. 2.6 shows no trend with HCN-vib as this property is highly sensitive to dilution from the host-galaxy. I show this in Appendix A.1.2 for reference. I also show the 12.7/11.3 PAH EW ratio against the strength of HCN-vib, which does show a trend, albeit one that is weaker than that of the nuclear optical depth. This proves the importance of removing contamination by the host galaxy in order to accurately recover the obscuration properties of the nucleus.

The HCN-vib definition of a CON is based on the strength of the mm-wavelength vibrational transitions of HCN (Falstad et al., 2021). They used two definitions, the surface brightness of HCN: $\Sigma_{\mathrm{HCN-vib}} > 1 L_\odot\ \mathrm{pc}^{-2}$ and the ratio to the infrared

luminosity: $L_{\rm HCN-vib}/L_{\rm IR} > 10^{-8}$. Based on the correlation found in Fig. 2.8, it is possible to infer at what optical depth, as measured by PAHDECOMP, the HCN-vib definition is met.

To do this I fit a straight line in log-log space using SCIPY orthogonal distance regression to account for the errors in both x and y. Taking $\Sigma_{\rm HCN-vib} > 1 L_{\odot}$ pc^{-2} requires $\tau_N > 3.5$ and $L_{\rm HCN-vib}/L_{\rm IR} > 10^{-8}$ requires $\tau_N > 3.3$. As the surface brightness is a more robust definition and gives a stricter threshold, I adopt $\tau_N > 3.5$ as a criterion to select deeply obscured nuclei. In addition, I impose the extra condition that the nuclear contribution must be greater than 40% to ensure the value of τ_N is reliable from the fitting as discussed in Sect. 2.3.6.

This now means there is an additional, more physical, criterion for selection CON candidates in the mid-IR.

2.4.3 Spectral mapping sample

In this section we present the results of the fits the spectra from from the spectral mapping sample, where we fitted all the apertures simultaneously (and the shape of the nuclear spectra is the same for all of them, as discussed in Sect. 2.3.6).

Figure 2.9 shows the PAH EW ratios of this sample and how these vary with aperture size. From this figure it is clear that the PAH EW ratio values from the inner aperture deviate from the others for a number of objects, for example Arp 236 A and Mrk 938. Before analysing further we investigated the effect of the aperture correction on the spectra extracted from this aperture. The slope of the continuum is strongly dependent on this correction function and thus the PAH EWs will depend on this. Therefore, due to the aperture corrections, the CON selection box that is calibrated from staring mode spectra may not be directly applicable to spectral maps.

Aperture correction effects

To quantify if the aperture correction has a significant effect I compared the PAH EW ratios measured from the spectral mapping mode compared with those from

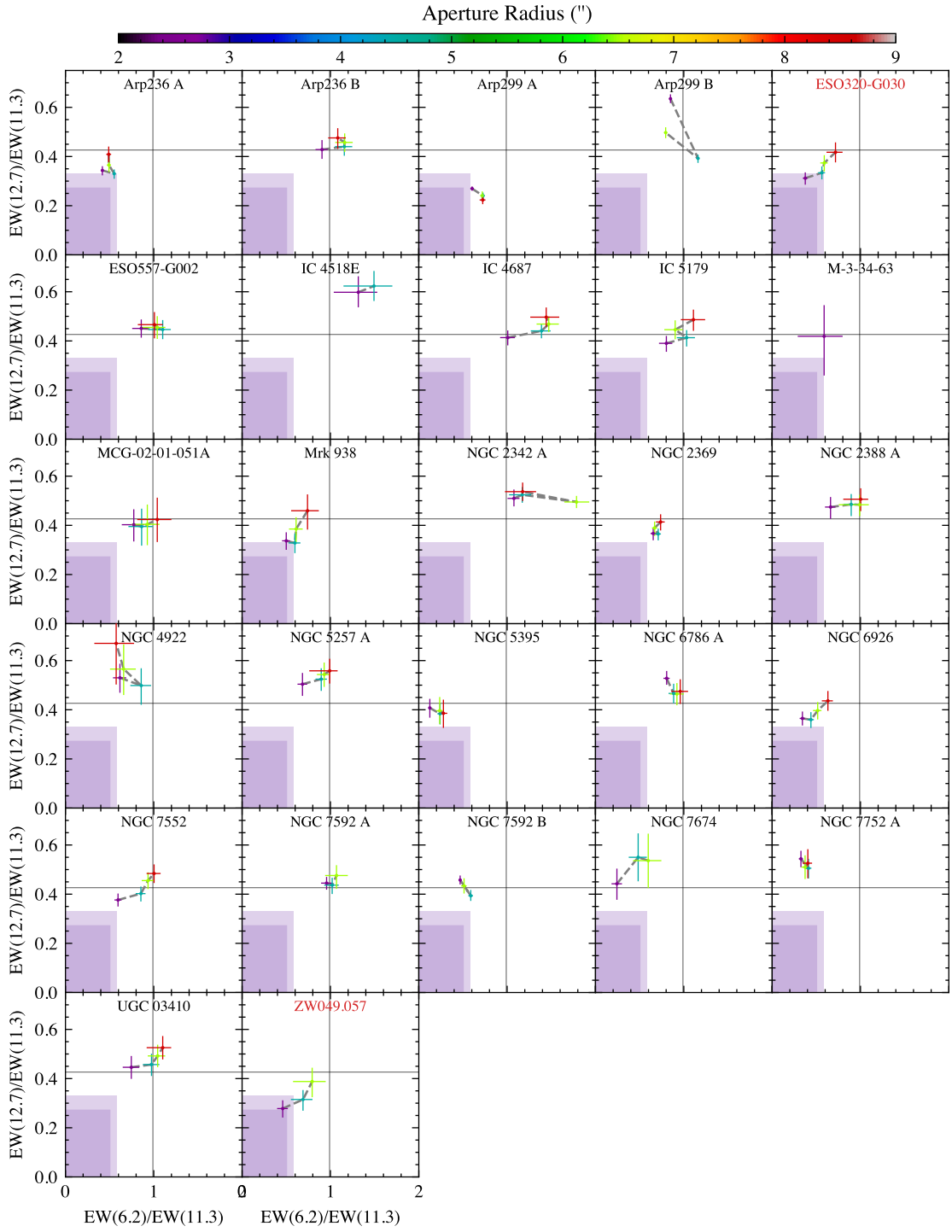

Figure 2.9: EW ratios of the 12.7/11.3 PAH and the 6.2/11.3 PAH for the spectral mapping sample. For each galaxy, values are coloured by the aperture radius used to extract the spectra; a larger aperture will contain more emission from star formation in the galactic disc. The inner purple box shows the CON selection region as defined for the staring mode spectra, and the outer box shows a larger selection region that accounts for aperture correction effects. The grey lines show the mean EW ratios for the star-forming calibration sample. The two bona fide CONs are shown with a red title.

the staring mode. I used NGC 5990 to do this as it has a significant nuclear component (AGN fraction of 0.49 (Díaz-Santos et al., 2017)). Fig. 2.10 shows the PAH EW ratios for each aperture of the spectral maps with the staring mode added as the black point. The aperture of radius 2.5" (in purple) has the aperture correction applied and shows a clear deviation from the other points in Fig. 2.10. This suggests that the aperture correction may be responsible for changing the measured PAH EW ratio values for the innermost aperture.

To account for this uncertainty I extended the CON selection criteria to a larger region using the EW ratios for NGC 5990. I used a cubic interpolation of each EW ratio against aperture radius excluding the 2.5" aperture and measured the deviation of the interpolated versus measured PAH EW ratios at 2.5". To do this I used a radius of 1.8" for the staring mode spectra as this roughly corresponds to the slit width. Using the measured deviation for the 2.5" aperture I created a larger box shown in Fig. 2.9 and 2.10 where the 12.7/11.3 EW threshold is increased by 0.058 and the 6.2/11.3 EW threshold is increased by 0.074. This creates an 'error' region where the EW ratios inferred from the innermost aperture are consistent with a CON.

CONs in the spectral mapping sample

Using the adjusted PAH EW CON selection criteria I find two objects that meet both the 12.7/11.3 and the 6.2/11.3 PAH EW criteria: ESO 320-G030 and ZW 049.057, both of which are known CONs with a HCN-vib surface brightness of $\Sigma_{\rm HCN-vib} > 1 L_{\odot}$ pc^{-2} (Falstad et al., 2021).

There are additional objects that may be CONs, selected by only one of the PAH EW criteria. The strongest candidate of these is Arp 299 A as it has a low enough 12.7/11.3 PAH EW ratio, which is more reliable than the 6.2/11.3. This object also almost meets the optical depth criterion of $\tau_N > 3.5$ with $\tau_N = 3.3$. Other objects that could be CONs are Arp 236 A and Mrk 938, which are both within 1σ of the adjusted selection region. Additionally, NGC 6926 meets both PAH EW ratios with the staring mode but this spectrum suffers from some reduction issues.

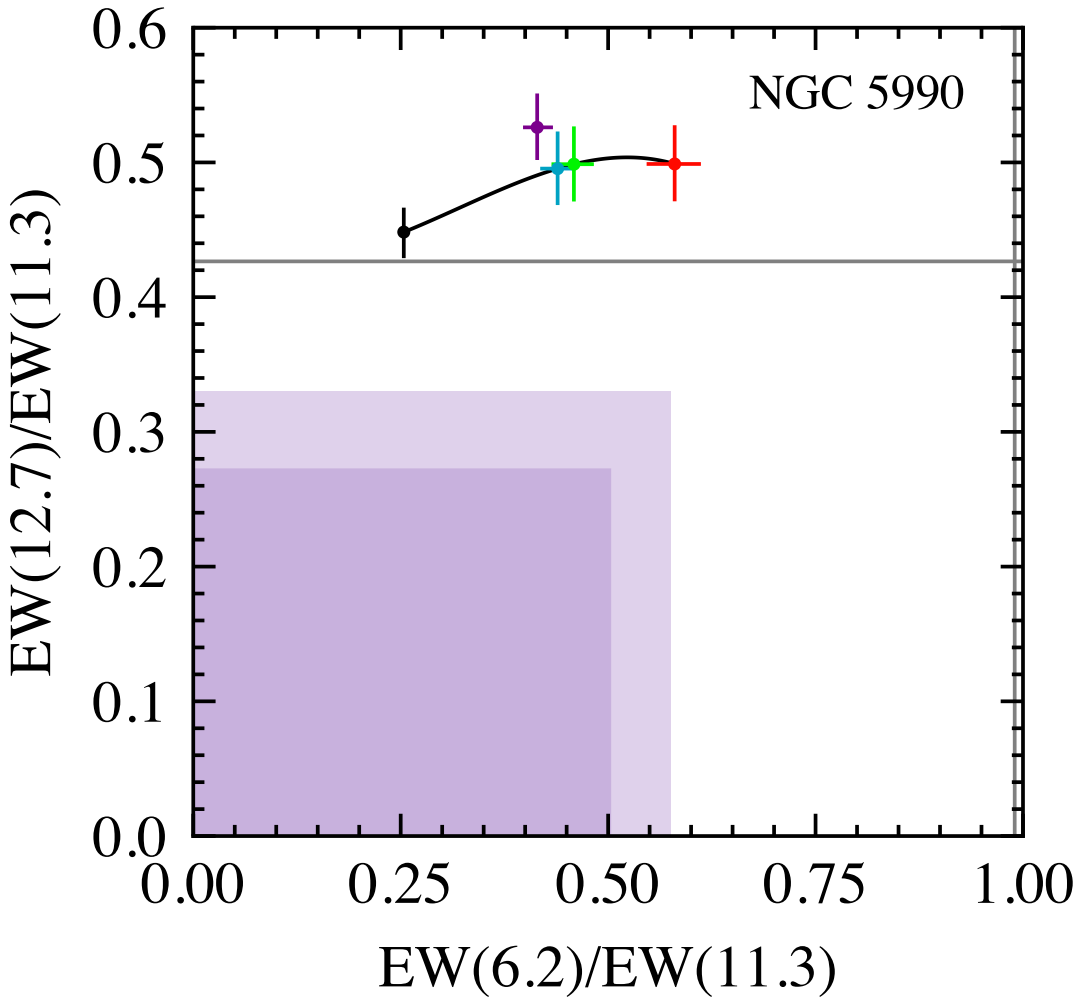

Figure 2.10: PAH EW ratios for NGC 5990. The coloured points are from spectral mapping observations and are the same as in Fig. 2.9. The additional black point is the staring mode spectra, which have a slit radius of approximately 1.8". The purple point has an aperture radius of 2.5" and has an aperture correction applied as described in Sect. 2.2. The black line shows a cubic spline interpolation that excludes this point. The inner purple box shows the CON selection region as defined for the staring mode spectra, and the outer box shows a larger selection region that accounts for aperture correction effects.

For the two known CONs (ESO 302-G030 and ZW049.057) there is a clear trend with how the EW ratios change with aperture size. As more of the galaxy disc is included within the aperture, the EW ratio moves away from the CON selection region and towards the mean values of the star-forming calibration sample. This shows that dilution from the host galaxy can cause objects to be missed by the PAH EW method; however, higher spatial resolution will overcome this issue. This last point is important considering the factor of ~ 10 increase in the spatial resolution of the Mid Infrared Instrument (MIRI) on the JWST compared to the *Spitzer* spectral maps, see Chapters 3, 4, 5.

A few other objects show trends with aperture size such as the other potential CON candidates Mrk 938 and NGC 6926 but also NGC 7552 and UGC 03410. Another interesting trend with aperture size can be seen in Arp 299 A, where the 12.7/11.3 PAH EW ratio increases as the aperture decreases. The high optical depth measured for this object means that the continuum will cause the PAH EW ratio to move in the opposite direction therefore changes in the 12.7/11.3 PAH flux ratio must drive this change and so the PAH properties may be different in the nuclear region.

The flux ratio of PAHs are known to be sensitive to changes in the properties of PAHs such as the size, charge and hardness of the incident radiation field (Li, 2020). There is evidence that the PAH molecules in the vicinity of AGN are more neutral (García-Bernete et al., 2022c; García-Bernete et al., 2022a), where it is thought that the harsh radiation field destroys the weaker ionised molecules leaving a population of neutral PAHs. It, therefore, is plausible that Arp 299 A represents an AGN that used to be completely obscured and has expelled some dust exposing PAH molecules to radiation from the central engine and therefore changing the properties of PAH molecules in the nuclear region. Arp 299 B is a known AGN (Alonso-Herrero et al., 2009) that also shows a strong increase in the 12.7/11.3 PAH EW ratio with the smallest aperture, although this is likely strongly affected by the aperture correction, as discussed in Sect. 2.4.3.

2.5 Discussion

2.5.1 How many CONs exist in the local Universe?

The first systematic search for CONs was done by Falstad et al. (2021) using the HCN-vib line; they found CONs in 38^{+18}_{-13}% of ULIRGs, 21^{+12}_{-6}% of LIRGs, and 0^{+9}_{-0}% of sub-LIRGs. This result is limited by the small sample size, hence the large errors. Using the PAH EW technique, García-Bernete et al. (2022b) found CONs in 30% of ULIRGs but only 7% of LIRGs, with the discrepancy likely due to dilution of the nuclear continuum emission by star formation in the disc of the host galaxy. To build on this work we can now use the optical depth selection criteria to recover those CONs that were missed by the PAH EW technique to achieve a more accurate estimate of the number of CONs in ULIRGs and LIRGs.

For the ULIRG sample we used HERUS (Farrah et al., 2013), as outlined in Sect. **??**. For the LIRG sample we used GOALS (Armus et al., 2009). To estimate 1σ uncertainties on the fraction of CONs in each of the sample, we followed Falstad et al. (2021) and used the Cameron (2011) method to construct a beta distribution of the CON fraction, which depends on the sample size.

From the HERUS sample of ULIRGs we identify 29^{+7}_{-7}% as CONs from the PAH EW criteria as shown in the bottom left panel of Fig. 2.7, in accordance with García-Bernete et al. (2022b). From the nuclear optical depth definition of $\tau_N > 3.5$ we select slightly more objects with 36^{+8}_{-7}% as CONs.

The EW ratios of the full GOALS sample are shown in the bottom right panel of Fig. 2.7 including the ULIRGs in that sample. From this study, we exclude objects with only spectral maps available as the required aperture corrections may bias the results. Out of the LIRGs in the GOALS sample the EW ratios select $7.7^{+2.3}_{-2.0}$% as CONs, consistent with García-Bernete et al. (2022b). The optical depth definition selects 17^{+3}_{-3}% as CONs, which is consistent with the CONquest results. In the case of LIRGs, the difference between the optical depth and PAH EW ratios techniques is larger.

Table 2.2: Fraction of CONs in ULIRGs and LIRGs in the local Universe.

Method	ULIRGs	LIRGs
HCN-vib (Falstad et al., 2021)	$38^{+18}_{-13}\%$	$21^{+12}_{-6}\%$
PAH EW (García-Bernete et al., 2022b)	30%	7.0%
PAH EW (This Work)	$29^{+7}_{-7}\%$	$7.7^{+2.3}_{-2.0}\%$
Nuclear Optical Depth, τ_N (This Work)	$36^{+8}_{-7}\%$	$17^{+3}_{-3}\%$

To understand this discrepancy we show in Fig. 2.11 the measured nuclear fraction, β, for the LIRGs selected as hosting CONs with each technique. The plot shows that the nuclear optical depth method selects additional sources with lower nuclear fractions and thus greater dilution from the host galaxy, which the PAH EW method misses. The discrepancy being larger for LIRGs compared to ULIRGs is a consequence of the fact that LIRGs contain more extended star-forming components and thus are more susceptible to dilution from the host galaxy. This is consistent with what was observed with the spectral mapping data in Sect. 2.4.3.

For both LIRGs and ULIRGs the fraction of CONs is consistent with the results of the CONquest investigation (Falstad et al., 2021) with overlapping 1σ intervals. A summary comparing the various methods is given in Table 2.2. The larger sample sizes afforded by using mid-infrared observations results in tighter constraints on these numbers. It is worth noting that the peak of the distribution for the number of CONs in LIRGs is slightly lower than the CONquest results. This may just be statistical error but it could also be due to objects where the nucleus is so diluted by the host galaxy that they are excluded by our cut requiring a nuclear contribution of 40%.

A comprehensive table of all the galaxies analysed in this work can be found in Appendix A.1.4, where measured PAH EW ratios and nuclear fraction/optical depths are reported. We also report on the detection of the HCN 14 μm absorption line (Lahuis et al., 2007). Finally, we also include information on the detections of the 23 μm, 28 μm or 33 μm crystalline silicate absorption features from Spoon et al. (2022). These features in absorption indicate heavily obscured nuclei via two methods. Method I indicates sources with the 23 μm feature and 33μm feature

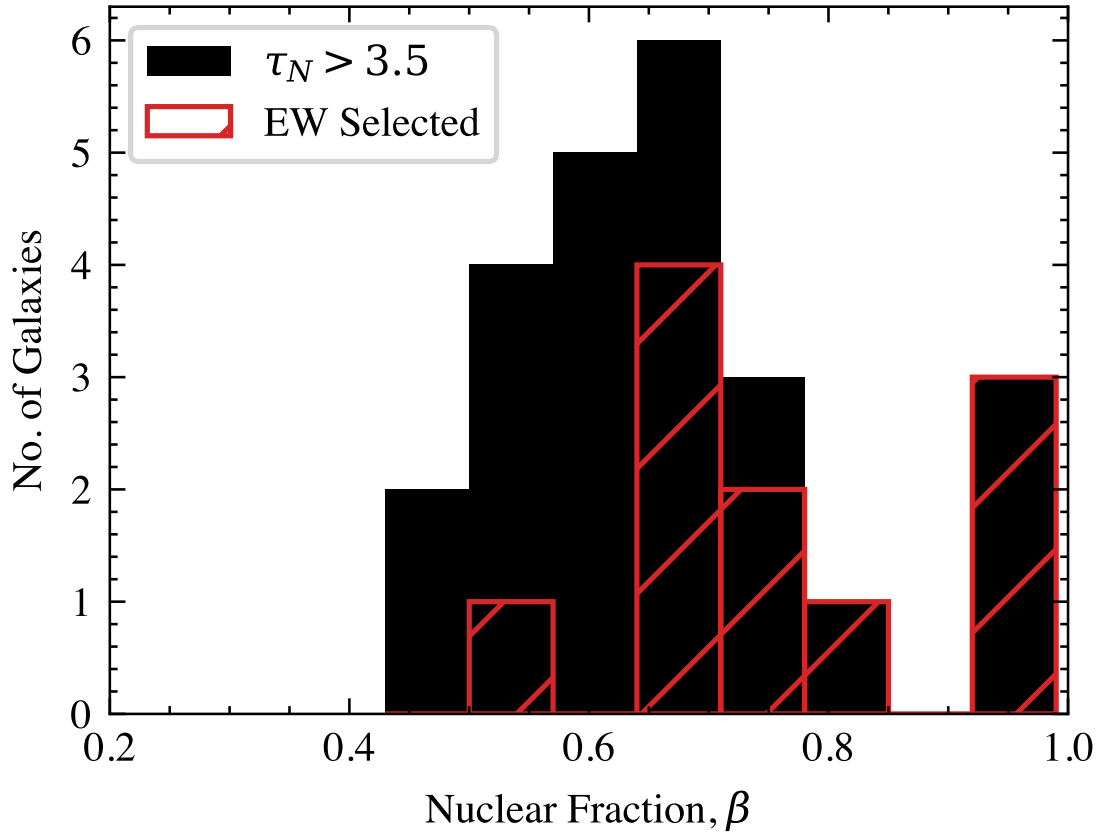

Figure 2.11: Histogram of the nuclear fraction, β, for LIRGs in the GOALS sample selected as CONs via the PAH EW method (red) and the nuclear optical depth (black). This shows that the nuclear optical depth identifies additional sources that are more heavily diluted by the host galaxy.

in absorption (i.e. $s_{23} < 0.0$ and $s_{33} < 0$). Method II indicates sources with $s_{23} < -0.09$ and $s_{23} < -0.02$. Spoon et al. (2022) also includes a method III for detection of the blue wing of the 33 μm feature where the full feature is cut due to the redshift of the source. No objects analysed in this work are classified by method III.

2.5.2 Effect of galaxy inclination

As mentioned previously, the PAH EW method can select CON candidates independent of galaxy inclination as extinction from the star-forming disc will affect both the PAH flux ratio and the continuum ratio leaving the EW ratio unchanged. However, this is not necessarily the case for the nuclear optical depth selection. In Fig. 2.7 there is one object, NGC 3628, with a $\tau_N > 3.5$ but is not selected as a CON by either

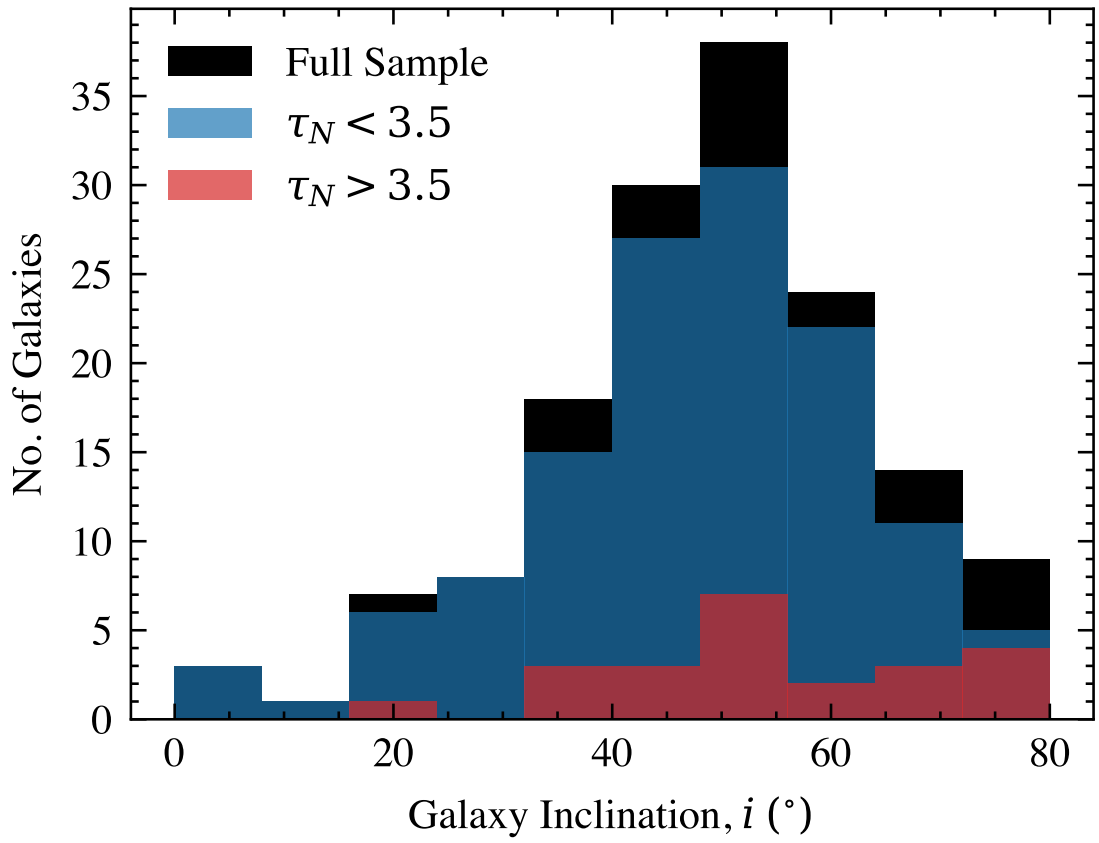

Figure 2.12: Inclination of galaxies in the GOALS sample obtained from axis ratios. The full sample is shown in black, with objects selected as obscured nuclei from the optical depth shown in red and those not as CONs in blue.

the PAH EW ratios or the HCN-vib surface brightness. This is a highly inclined galaxy, which suggests that the nuclear optical depth obtained from our spectral decomposition fitting may be sensitive to such galaxies with strong dust lanes obscuring the line of sight, which may bias our estimates of the number of CONs.

To quantify if this is an issue we obtained estimates for the inclination of galaxies in the GOALS sample from the NASA/IPAC Extragalactic Database (NED)[3] using the ratio of the minor axis, b, to the major axis, a, to estimate the inclination, i where $\cos i = b/a$. For the majority of the sample, the axis ratios were from 2MASS imaging in the K_s band (Jarrett et al., 2000) or r band imaging from SDSS (York et al., 2000). We selected a sub-sample with $\tau_N > 3.5$ and compared to the full sample. This is shown in Fig. 2.12.

[3] https://ned.ipac.caltech.edu/

Visually, the two samples look similar; however, there may be some extra galaxies selected at the highest inclinations ($i \gtrsim 65°$). To determine if there is any statistically significant difference between the samples we performed a two-sample Kolmogorov-Smirnov (K-S) test (Karson, 1968) from the SCIPY.STATS package. This tests the null-hypothesis that the two samples are drawn from the same underlying distribution, which typically requires a p-value < 0.05 to reject. We performed the K-S test on the sample with $\tau_N < 3.5$ and $\tau_N > 3.5$ to test whether there is any significant difference. We find a p-value of 0.43, which suggests there is no statistically significant difference between the two samples. It is worth noting, however, that the small sample size of the CONs may make the K-S test less likely to find a difference even if one exists and so it is worth inspecting visually. We would also only expect a difference at high inclinations where the dust lanes would obscure the line of sight towards the nucleus and so if we only compare the highest inclinations ($i \gtrsim 65°$), we do see a bias where sources may be falsely selected as CON candidates. The case of NGC 3628 is one such example; however, this case also shows the strength of the PAH EW method for selecting CON candidates.

While there may be a bias falsely selecting highly inclined sources as CON candidates, this bias may actually counteract the exclusion of the most diluted CONs by their host galaxy ($\beta < 0.4$) and so while individual objects may be misclassified, the total number of CONs likely remains accurate.

2.6 Summary

In this chapter I have presented an investigation into the effectiveness of the mid-infrared to infer the physical properties of CONs and how to identify such objects using PAH EW ratios. The main findings are:

- From the spectral modelling, the optical depth of the nuclear component at 9.8 μm, τ_N, is strongly correlated with the surface brightness of HCN-vib emission at millimetre wavelengths, suggesting the same physics is responsible for both observational signatures. This leads to a CON selection criterion of $\tau_N > 3.5$.

- Using $\tau_N > 3.5$, the CONs make up 36^{+8}_{-7}% of ULIRGs and 17^{+3}_{-3}% of LIRGs, consistent with the results of CONquest but with tighter constraints. The PAH EW method classifies fewer CONs, likely due to the low spatial resolution of *Spitzer* IRS data; it detects 29^{+7}_{-7}% of ULIRGs and $7.7^{+2.3}_{-2.0}$% of LIRGs as CONs.

- The PAH EW method is robust against false positives in highly inclined galaxies with strong dust lanes that can produce high optical depths, whereas using the nuclear optical depth to select CON sources may falsely select some objects that are highly inclined.

- From spectra extracted at different spatial scales, the PAH EW ratios move towards the CON selection criterion with smaller apertures where there is less dilution from the disc. This suggests that star formation diluting the nucleus is responsible for the EW ratios underestimating the number of LIRGs that host CONs.

This work demonstrates that the mid-infrared is effective at selecting the most obscured nuclei and allows physical properties of the dust to be inferred. This will allow these objects to be studied in great detail in the local universe, in the rest of this thesis but also beyond the local Universe, where HCN-vib emission is simply too faint to be detected, even with ALMA (Garcia-Bernete et al. 2024 submitted). Future far-infrared telescopes such as PRIMA [4] (PRobe far-Infrared Mission for Astrophysics) (Moullet et al., 2023), a concept for a 1.8 m cryogenically cooled FIR telescope which has recently been selected for Phase A study by NASA, will provide a census across cosmic time (Donnan et al. 2025 submitted).

[4] https://prima.ipac.caltech.edu/

3

An Obscured Nucleus and its Environment as seen by the JWST/MIRI.

Contents

This chapter is adapted from: F. R. Donnan, D. Rigopoulou, I. García-Bernete, M. Pereira-Santaella, A. Alonso-Herrero, P. F. Roche, A. Hernán-Caballero, H. W. W. Spoon. *The obscured nucleus and shocked environment of VV 114E revealed by JWST/MIRI spectroscopy.* 2023, MNRAS, 519, 3691

3.1 Introduction

Luminous Infrared Galaxies (LIRGs, $L_{IR} > 10^{11} L_{\odot}$) and Ultraluminous Infrared Galaxies (ULIRGs, $L_{IR} > 10^{12} L_{\odot}$) contain some of the most extreme dusty environments and disturbed morphology, with a high prevalence of major galaxy mergers (e.g. Rigopoulou et al., 1999). These obscured environments are the sites of rapid galaxy evolution with high star-formation rates and growing supermassive black holes (SMBHs). Studying such environments is a challenge at optical wavelengths due to the high levels of dust extinction and therefore requires study at longer wavelengths. The JWST Mid-InfraRed Instrument (MIRI) enables the study of these environments in the mid-infrared at a significantly improved spatial/spectral resolution and sensitivity compared to previous facilities (Rieke et al., 2015; Wright et al., 2015; Wells et al., 2015).

The most obscured galactic nuclei, so-called Compact Obscured Nuclei (CONs) show extreme column densities ($N_{H} > 10^{25} cm^{-2}, A_{v} > 1000$ mag) (e.g. Aalto et al., 2019; Falstad et al., 2021, and references therein) where either a compact starburst or an accreting supermassive black hole (SMBH) is completely obscured. These objects are prevalent among LIRGs and ULIRGs in the local universe (Donnan et al., 2023a; Falstad et al., 2021; García-Bernete et al., 2022b) and therefore represent a crucial phase of galaxy evolution where rapid SMBH growth may occur, especially considering the increased prevalence of dusty galaxies towards cosmic noon (e.g. Magnelli et al., 2011).

Detecting such objects is a challenge due to their obscured nature with most studies being confined to the sub-mm regime (e.g. Aalto et al., 2015b; Aalto et al., 2019; Falstad et al., 2021). However as I have shown in Chapter 2, the mid-infrared is effective at identifying and studying the most obscured nuclei reducing the reliance on sub-mm features which are often faint. With the launch of the James Webb Space Telescope (JWST), these techniques can now be applied to data with a significant increase in the spatial and spectral resolution over previous facilities.

In this chapter I apply the techniques outlined in Chapter 2 to JWST data for the first time with MIRI observations of the highly obscured interacting system

VV 114 (IC 1623, Arp 236). This is a local ($z = 0.02007$, $D = 84$ Mpc, Strauss et al., 1992) galaxy with a highly disturbed morphology. This object is a LIRG with $L_{\rm IR} = 10^{11.71}$ $L_{\odot}$ (Armus et al., 2009) and is in the mid-stages of a major merger as defined by Stierwalt et al. (2013). The western region of this galaxy is much more prominent in the UV/optical (e.g. Frayer et al., 1999; Evans et al., 2022) whereas the eastern region is extremely dust rich, appearing very red in the optical. Moving towards the infrared, the luminosity of the eastern region dramatically increases (e.g. Charmandaris et al., 2004) and dominates over the western region, reflecting its obscured/dusty nature.

The eastern region contains complex morphology with clumps of star formation, shocks (Rich et al., 2011) and a potential buried AGN (Saito et al., 2015). From Spitzer spectral mapping observations in Chapter 2, I found that the PAH EW ratios approached those that might indicate a CON as the aperture size was reduced towards the nucleus, however the low angular resolution meant that the spectrum was heavily diluted by the circumnuclear star-formation. The low angular resolution of Spitzer (PSF FWHM of $\sim$ 3.8" at 14 μm which corresponds to an angular size of $\sim$ 1.6 kpc) meant that the eastern region of VV 114 was completely unresolved in the spectral mapping mode with no structure visible. The almost factor of $\sim$10 increase in the spatial resolution of JWST/MIRI MRS (PSF FWHM of $\sim$ 0.48" at 14 μm which corresponds to an angular size of $\sim$ 200 pc) allows spatially resolved spectroscopic analysis of the eastern region of VV 114, where the previously unresolved region now shows multiple "nuclei" and a very complex morphology (Evans et al., 2022).

The eastern region of VV 114 has been observed with JWST as part of Early Release Science Program 1328 (PI: Lee Armus) with MIRI imaging (Evans et al., 2022) and MIRI MRS. I use this data to demonstrate the diagnostic power of mid-infrared spectroscopy to reveal highly obscured nuclei.

In Section 3.2 I describe the data and reduction steps. In Section 3.3 I outline my modified version of PAHFIT to fit JWST spectra. By applying this fitting tool I measure the obscuration and the properties of distinct regions of this galaxy.

By generating line maps I measure the distribution of fine structure lines and measure the column density of molecular hydrogen (H_2), via their rotational transitions that are tracing a shock in Section 3.4. I then discuss a possible evolutionary scenario in Section 3.5.

3.2 Observations

To illustrate the region of VV 114E I show imaging from MIRI (Evans et al., 2022) with a colour composite image in the left panel of Fig. 3.1. I used the reduced data from the MAST archive[1] to construct this image.

Two main point sources are apparent in this image, labelled A and B. Source A is significantly redder than B and is the suggested buried AGN from ALMA observations (Saito et al., 2015) where the continuum remains unresolved in the millimetre. Source B shows a stronger continuum in the F560W band relative to F1500W compared to source A. There are numerous other small clumps appearing within the image however, most of these are beyond the field of view of the MIRI-MRS observations. The F770W filter, centred on the 7.7 μm PAH shows much more extended emission and traces areas of star-formation where young stars radiatively excite PAH molecules.

3.2.1 MIRI MRS Reduction

MIRI MRS data consists of 4 sub-cubes with channel 1 (4.9–7.65 µm), channel 2 (7.51–11.71 µm), channel 3 (11.55–18.02 µm) and channel 4 (17.71–28.1 µm) with an increasing field of view towards longer wavelengths. Channel 1 has a field of view of 3.2 × 3.7 arcsecond which increases to 6.6 × 7.7 in channel 4.

The MIRI MRS data cubes were produced by Miguel Pereira-Santaella. First the level 2-b reduced data from the MAST archive were downloaded. Before running the Spec3 pipeline (version 1.6.2), the residual fringe subtraction was run offline to remove fringing still present after the fringe correction step of the pipeline. The Spec3 pipeline was then run to produce and construct the 4 sub-cubes as well as

[1] https://mast.stsci.edu/portal/Mashup/Clients/Mast/Portal.html

their corresponding background cubes. This was done using the jwst_0913.pmap context of the CRDS. The background was estimated for each wavelength channel by calculating the median in each channel of the background cubes before subtracting, following the same method as in García-Bernete et al. (2022a).

To ensure the extracted spectra are from the same spatial position, I first correct for small discrepancies in the WCS and spatially align all the sub-channels. I use the DAOStarFinder algorithm (Stetson, 1987) from the PHOTUTILS python package to find the position of point sources in the integrated intensity (moment 0) maps which trace the continuum of each of the 4 sub-channels. I then adjust the WCS header to align the measured point sources. Subsequently, I extract the spectrum using a circular aperture with a 1" diameter centred on the measured position. This is done for the two point sources in the image (A and B) and I apply the correction factor from Pereira-Santaella et al. (2022) for these apertures (García-Bernete et al., 2022a). I also extract the spectrum from a region where no source is present to represent the diffuse emission (point C). I chose an aperture placed away from the two point sources so as to not be contaminated by the PSF at the longest wavelengths but close enough such that it is within the field-of-view in the shortest wavelength channel. As the emission within aperture C is not a point source I do not apply the aperture correction factor. The three apertures are shown in the right panel of Fig. 3.1.

The three spectra are shown in Fig. 3.2 where the extended emission (source C) shows the strongest emission features compared to source A and B which both show a strong continuum. Source A is clearly the more obscured one showing very deep silicate absorption at 9.8 μm and 18 μm. There is also evidence for absorption due to water ice and aliphatic CH around 6 μm and 7.5 μm respectively. The spectrum of source B shows a strong continuum around 5 - 6 μm, consistent with the colours seen in the imaging in Fig. 3.1 and Evans et al. (2022).

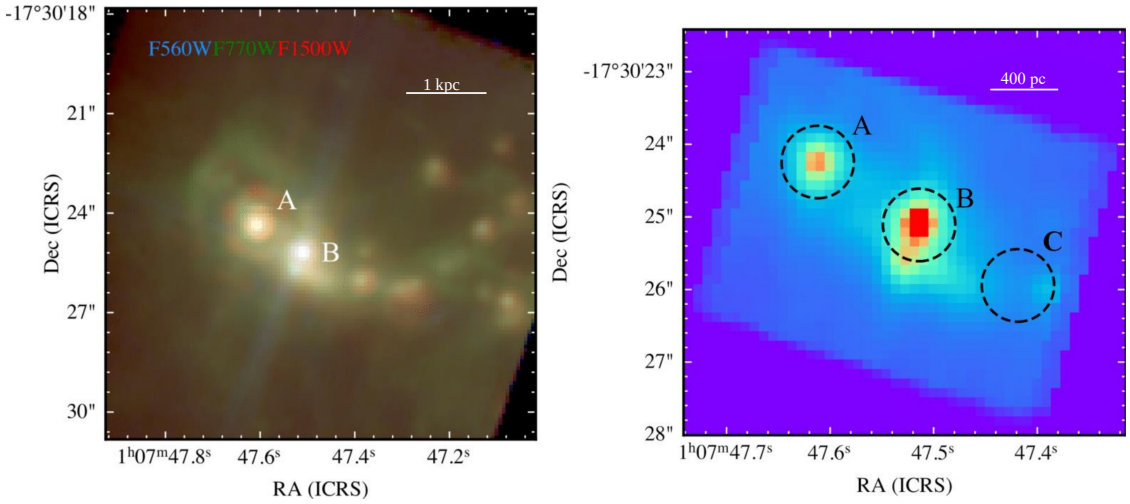

Figure 3.1: *Left:* Color composite image of VV 114E using JWST/MIRI. The F560W (blue) and F1500W (red) trace mostly continuum while the F770W (green) traces the 7.7 μm PAH feature. The two main point sources are labelled A and B. *Right:* Integrated intensity (moment 0) map of Channel 1 (4.90 μm – 7.65 μm) which is dominated by thermal continuum dust emission and the 6.2 μm PAH which is more spatially extended. The black circles show the apertures used to extract the spectra shown in Fig. 3.2, labelled A, B and C.

3.3 Methods

3.3.1 Spectral Fitting

As discussed in previous chapters, it is imperative to model the full spectrum to obtain accurate PAH fluxes. In this chapter, I use PAHFIT (Smith et al., 2007b), modified for the increased spectral resolution of JWST/MIRI MRS. I also apply PAHDECOMP, as described in the previous chapter, in section 2.3.

The following sections describe the various components of the model.

Emission Lines

With the vast increase in spectral resolution over Spitzer IRS data, the MRS spectra show more complex emission line profiles influenced by the gas kinematics. To capture this, each line is modelled with two components, a Gaussian and a Lorentzian. This allows asymmetries to be captured by the model and allows the shape to vary between being Gaussian dominated (narrow wings) or Lorentzian dominated (broad wings). Each line is therefore modelled as the sum of a Gaussian,

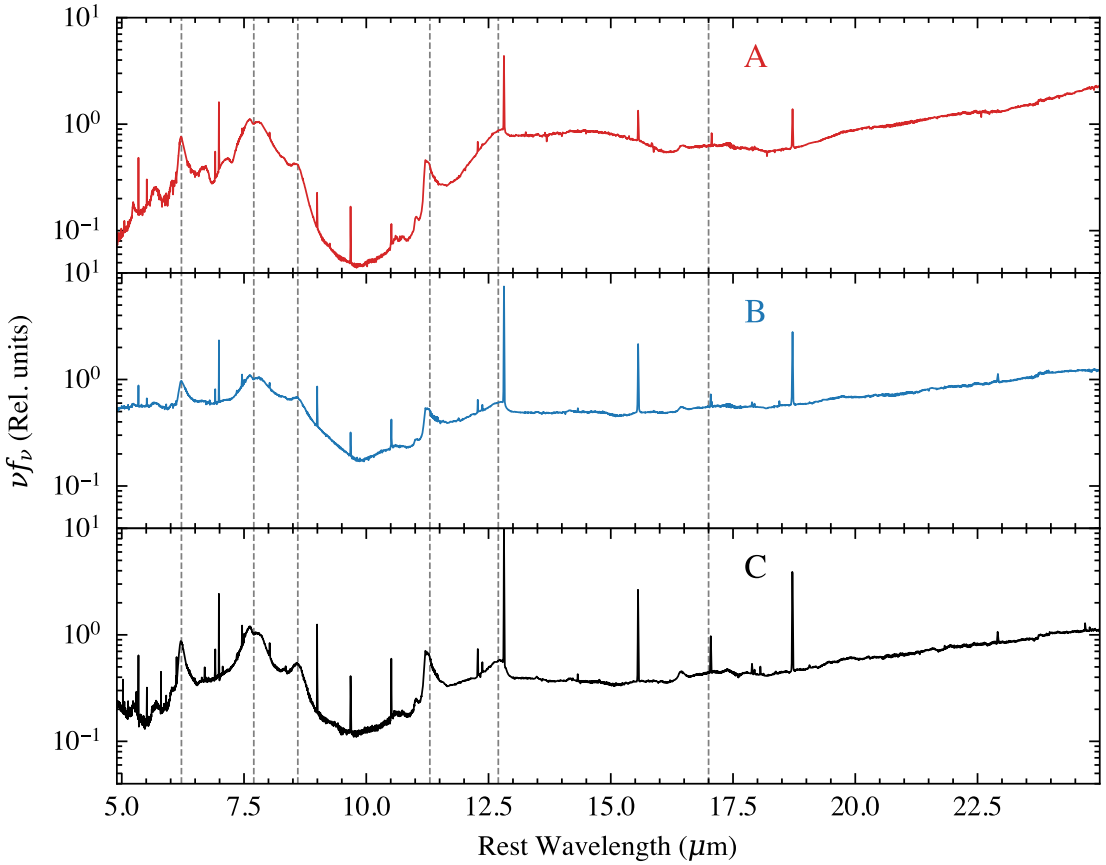

Figure 3.2: MIRI/MRS spectra of three regions in VV 114E. Spectra A and B are extracted as point sources using a 1" circular aperture with a PSF wavelength dependant correction factor applied. Source C represents extended emission without the presence of any point sources. The fluxes are normalised to 7.7 μm. The most prominent PAH features are labelled with the vertical dashed lines.

$G(\lambda_0, \gamma_G)$, and a Lorentzian $L(\lambda_0 + \delta\lambda_0, \gamma_L)$:

$$I_{\nu,\mathrm{Line}}(\lambda) = A\left[\beta G(\lambda_0, \gamma_G) + (1-\beta)L(\lambda_0 + \delta\lambda_0, \gamma_L)\right] \tag{3.1}$$

where A is the total amplitude of the line and β the fractional contribution of the Gaussian component which has a central wavelength λ_0 and a full width at half maximum (FWHM), γ_G. The Lorentzian component has a centre that is allowed to vary from the Gaussian component by $\delta\lambda_0$, restricted to $\pm 0.005\mu$m and has a FWHM γ_L. The centre of each line, λ_0 is allowed to vary by 0.01μm and each width, γ_G, γ_L can vary by 50% of its initial value. I use initial values from the FWHM of 0.0015 μm, 0.003 μm, 0.008 μm and 0.010 μm for Channels 1 to 4 respectively.

The full list of lines fitted are shown in Table 3.1 where the new lines not present in the original version of PAHFIT are highlighted in bold.

The inclusion of the Lorentzian component is required to fit the base of the lines. As the majority of the flux of the line is not contained within the wings, this has a negligible impact on the measured fluxes.

PAH Emission Features

The original PAHFIT modelled PAH features with a series of Drude profiles as shown in Table 3 of Smith et al. (2007b). With the increased spectral resolution of JWST/MIRI the PAH emission shows more resolved structure than with Spitzer data (García-Bernete et al., 2022a). I therefore update the PAH model with new additional components which I show in Table. 3.2. For example the 11.3 μm PAH feature is now comprised of four features, as shown in the middle panel of Fig. 3.3, which is necessary to properly model the shape of the profile. For each Drude feature I allow the central wavelength to vary by $\pm 0.05\mu$m to account for uncertainties in the wavelength calibration with the JWST pipeline (Rigby et al., 2022). I also allow the width of each feature to vary. In this case I allow the width to vary between +10% and −60% of the values shown in Table A.2 where this range allows the PAH features to be narrower than the previous version of the tool due to the increased spectral resolution afforded by MIRI/MRS.

Continuum

The continuum is modelled as a sum of modified blackbodies with a range of fixed temperatures [35, 40, 50, 65, 90, 135, 200, 300, 500 K] and an emissivity of ν^2. An additional blackbody at 5000K is included to account for the presence of a potential stellar continuum.

As the continuum is subject to extinction, I include a simple prescription of extinction in this Chapter. As I will demonstrate in Chapter 4, this simple model can be significantly improved. The original PAHFIT used a modified version of a Galactic centre extinction curve (Kemper et al., 2004), while subsequent versions of the code used various other extinction curves (Gallimore et al., 2010). For this

Table 3.1: Spectral Lines

Line	λ_0	FWHM (±50%)
	μm	μm
(1)	(2)	(3)
H_2 S(8)	5.053	0.0015
[**Fe II**]	5.340	0.0015
[**Fe VIII**]	5.447	0.0015
H_2 S(7)	5.551	0.0015
[**Mg V**]	5.609	0.0015
H_2 S(6)	6.109	0.0015
H_2 S(5)	6.909	0.0015
[Ar II]	6.985	0.0015
HI 6-5	7.460	0.003
[**Ar V**]	7.901	0.003
H_2 S(4)	8.026	0.003
[Ar III]	8.991	0.003
H_2 S(3)	9.665	0.003
[S IV]	10.551	0.003
H_2 S(2)	12.278	0.008
HI 7-6	12.370	0.008
[Ne II]	12.813	0.008
[**Cl II**]	14.322	0.008
[Ne III]	15.555	0.008
H_2 S(1)	17.035	0.008
[**P III**]	17.885	0.010
[**Fe II**]	17.936	0.010
[S III]	18.713	0.010
[**Fe III**]	22.925	0.010
[**Ne IV**]	24.318	0.010

Column (1): Line name, Column (2): Vacuum wavelength, Column (3): Line FWHM allowed to vary by ±50% of the value shown

Additional emission lines not present in the original PAHFIT (Smith et al., 2007b) are shown in bold.

Table 3.2: PAH Features

λ_0 ($\pm 0.05\mu$m)	Average λ_0	FWHM (+10%, −60%)	Average FWHM
μm	μm	μm	μm
(1)	(2)	(3)	(4)
5.24	5.253	0.058	0.032
5.27	5.266	0.179	0.138
5.70	5.699	0.200	0.153
5.87	5.856	0.200	0.119
6.00	6.019	0.200	0.085
6.18	6.214	0.100	0.105
6.30	6.329	0.187	0.206
6.69	6.705	0.468	0.515
7.42	7.427	0.935	0.942
7.60	7.587	0.334	0.249
7.85	7.841	0.416	0.432
8.33	8.293	0.417	0.423
8.61	8.602	0.336	0.296
10.68	10.630	0.214	0.229
11.00	10.978	0.100	0.063
11.15	11.191	0.030	0.023
11.20	11.211	0.030	0.028
11.22	11.244	0.100	0.043
11.25	11.291	0.135	0.077
11.33	11.380	0.363	0.362
11.99	11.956	0.540	0.594
12.62	12.635	0.530	0.573
12.69	12.738	0.120	0.111
13.48	13.439	0.539	0.593
14.04	13.990	0.225	0.248
14.19	14.207	0.355	0.390
14.65	14.639	0.500	0.384
15.90	15.851	0.318	0.276
16.45	16.459	0.230	0.156
17.04	17.023	1.108	0.877
17.375	17.389	0.209	0.190
17.87	17.887	0.286	0.258
18.92	18.937	0.359	0.395

Column (1): Initial central wavelength for the fit with range $\pm 0.05\mu$m. Column(2): Average best fit central wavelength. Column (3): Initial FWHM allowed to vary within +10% and −60%). Column (4): Average best fit FWHM.

Additional Drude profiles not present in the original PAHFIT (Smith et al., 2007b) are shown in bold.

work I use an extinction curve generated using templates from extremely obscured sources. I do this as many of the extinction curves in the literature (Ossenkopf et al., 1992; Kemper et al., 2004; Chiar and Tielens, 2006) do not include crystalline features at 11 μm, 16 μm, 19 μm or 23 μm, which are indeed a common component of the ISM of galaxies (Spoon et al., 2022). Moreover, their presence can be seen by eye in the spectrum for source A (e.g. absorption at 23 μm, see Fig. 3.2) and so are an imperative for the model to achieve a good fit to the data. The creation of this extinction curve is described in Appendix A.2.1. In addition I use the water ice and CH templates from Chapter 2 (Donnan et al., 2023a) derived from NGC 4418 as these features are very strong for this source. A screen of dust is assumed as the optical depth template is derived with this assumption. Therefore, the extinction has the form

$$e^{-\tau(\lambda)} = e^{-\tau_{\rm Ice}-\tau_{\rm CH}-\tau_{\rm Ext}} \tag{3.2}$$

where $\tau_{\rm Ice}$ is the optical depth of the ice template, $\tau_{\rm CH}$ is the optical depth of the CH and $\tau_{\rm Ext}$ is the optical depth of the extinction curve created in Appendix A.2.1. $\tau_{\rm Ext}$ includes the silicate features at 9.8 μm, 18 μm and a power law component.

Combining all these components gives the total model as

$$f_\nu(\lambda) = \sum_{i=1}^{N_{\rm Lines}} I^{(i)}_{\nu,{\rm Line}}(\lambda) + \sum_{i=1}^{N_{\rm PAH}} I^{(i)}_{\nu,{\rm PAH}}(\lambda) + \left(\sum_{i=1}^{N_{\rm Dust}} A_i \frac{B_\nu(T_i,\lambda)}{\lambda^2} + A_* B_\nu(5000{\rm K},\lambda) \right) e^{-\tau_\lambda} \tag{3.3}$$

where $N_{\rm Dust} = 8$ for fixed $T_i = 35, 40, 50, 65, 90, 135, 200, 300$K with scale factors A_i, B_ν is the Planck function and A_* is the scale factor for the stellar blackbody at a fixed temperature of 5000 K. The emission lines are a sum of each line function, $I^{(i)}_{\nu,{\rm Line}}(\lambda)$ (equation (3.1) for line (i) and the PAH features are a sum of each Drude function, $I^{(i)}_{\nu,{\rm PAH}}(\lambda)$ for PAH feature (i).

For each spectrum I sample the posterior probability using the No-U-Turn Sampling (NUTS) Markov-Chain Monte Carlo (MCMC) from NUMPYRO (Phan

et al., 2019). This allows posterior probabilities to be obtained from properties inferred from the spectra.

For each spectrum the integrated flux and equivalent width of each emission feature is calculated as a numeric integral. The integrated flux is simply

$$f^{\rm PAH} = \int f_\nu^{\rm PAH} d\nu, \tag{3.4}$$

for a PAH profile $f_\nu^{\rm PAH}$. Before calculating this integral I divide the feature profile by the extinction factor $e^{-\tau_{\rm Ext}}$ to recover extinction corrected fluxes. I do not include the ice plus aliphatic hydrocarbon absorption in this extinction factor as these are assumed to only affect the continuum and are not typical of star-forming regions in galaxies (Spoon et al., 2022).

To calculate the equivalent width of the PAH features I do not correct by extinction where I just use the observed flux:

$$\mathrm{EW} = \int \frac{\mathrm{f}_\nu^{\rm PAH}}{\mathrm{f}_\nu^{\rm cont}} \mathrm{d}\lambda, \tag{3.5}$$

where $f_\nu^{\rm cont}$ is the continuum, corrected by the ice plus CH absorption. This means that the EW of the 6.2 μm PAH uses a continuum only subject to the extinction curve containing the power law plus silicate absorption, in line with previous work (Spoon et al., 2022; Donnan et al., 2023a), and so this ice corrected continuum will be larger than the observed continuum.

I also measure the extinction via the strength of the 9.8 μm silicate feature as defined in Spoon et al. (2007):

$$S_{\rm sil} = \ln \left(\frac{f_{\rm 9.8,obs}^{\rm cont}}{f_{\rm 9.8,int}^{\rm cont}} \right), \tag{3.6}$$

which is simply the natural log of the observed to the underlying continuum at 9.8 μm. It is worth noting here that this definition differs slightly from Spoon et al. (2007) as I use the intrinsic continuum rather than an interpolated continuum. The intrinsic continuum here contains the power law component as well as the silicate absorption, which raises the magnitude of $S_{\rm sil}$ by 10% assuming our extinction curve

as discussed in Appendix A.2.1. This value is in-fact equal to the negative of the optical depth at 9.8 μm when I model the extinction as a screen.

I fit the spectra of the three regions as described in Section 3.2. I show these fits in Fig. 3.4. In columns (2) and (4) of Table 3.2 I show the average PAH centres and average FWHMs from these three fits which can be used to update future PAH models in various spectral fitting codes. I also fit various star-forming clumps from the the MRS spectra of NGC 7469 (García-Bernete et al., 2022b) to provide a small but representative reference sample of pure star-forming regions.

In Fig. 3.3 I show the 6.2 μm, 7.7 μm, 11.3 μm, 12.7 μm and 17 μm PAH bands for region C with the best-fit model. I show region C as it showed the strongest PAH emission features. With the increased spectral resolution of JWST/MIRI I can reveal new resolved features in the PAH profiles. In particular the 6.2 μm PAH is now asymmetric which I now fit with two Drude profiles rather than a single one. This asymmetry can be somewhat seen in ISO (Infrared Space Observatory) observations (Verstraete et al., 2001), which had a higher spectral resolution ($\sim$ 1500) than Spitzer in its low resolution mode ($\sim$ 100). The 11.3 μm feature also shows more resolved structure which I fit with four profiles compared to two in the original PAHFIT (Smith et al., 2007b). I note that the individual profiles are not necessarily real distinct components but rather serve to provide sufficient flexibility for the model to fit the profile and thus provide an accurate integrated flux. I will show a more elegant way of modelling the 11.3 μm PAH in Chapter 4.

I typically found that the errors of measured properties from the MCMC routine were very small. This is because the errors from the MCMC are largely driven by the noise of the data which is very small due to the high quality of the data. The largest source of error is the assumptions built into the model which are not accounted for. To obtain a more conservative estimate for the uncertainties of the PAH fluxes and EWs, I calculate the normalised residuals by subtracting the model from the data and dividing by the error bars. For a well fitted model, the normalised residuals should have a standard deviation of 1 however in this case it was much greater than 1 for all of the model fits. This suggests the errors

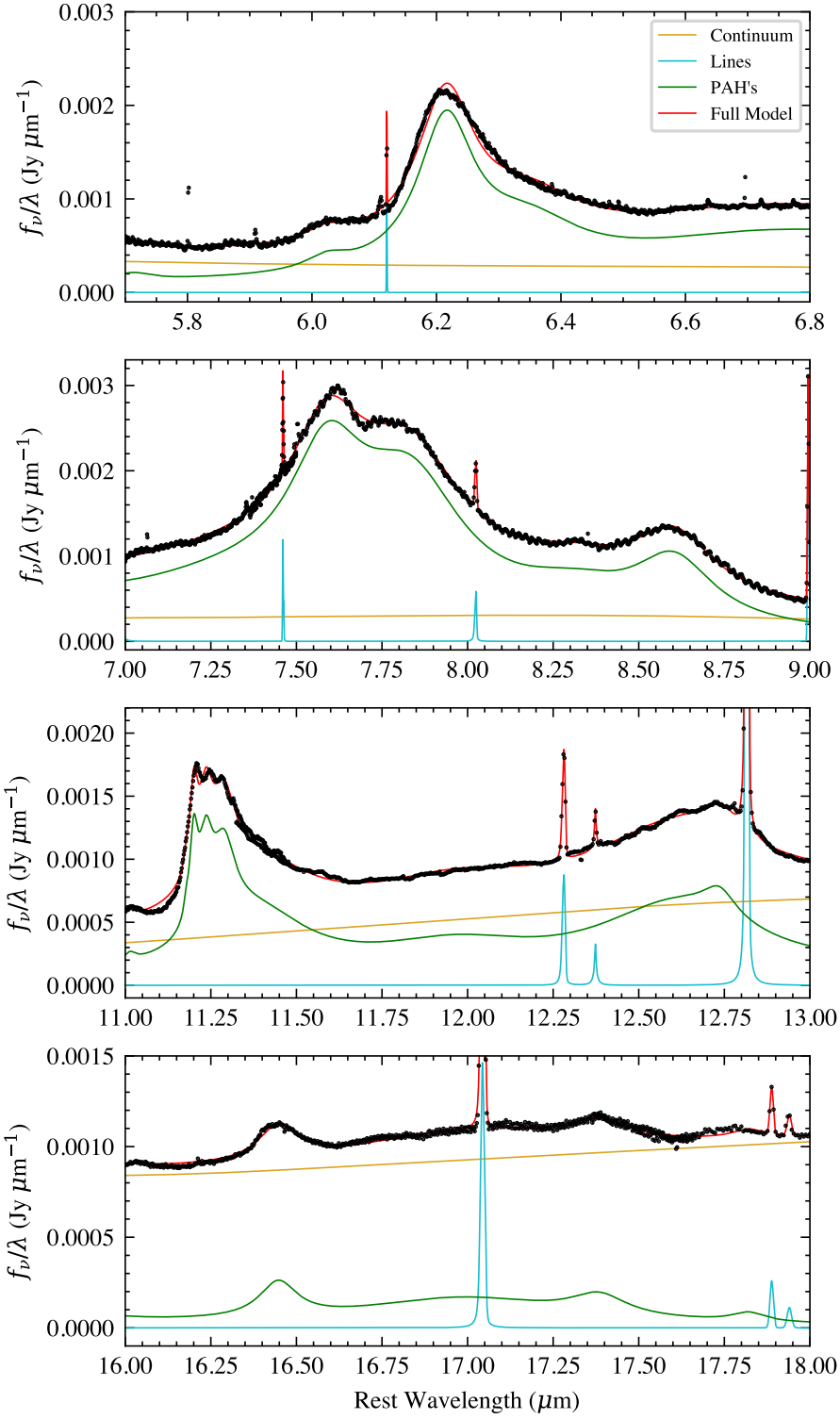

Figure 3.3: Panels showing the main PAH bands at 6.2 μm, 7.7μm, 8.6 μm, 11.3 μm, 12.7 μm and 17 μm for region C. The best fitting PAHFIT model is shown in red with its constituent components labelled in the legend. The emission lines are identified in Table 3.1.

of the data are underestimated and thus our parameter errors are too small. I therefore scaled the measured parameter errors by the factor required to achieve normalised residuals with a standard deviation of 1.

3.3.2 Emission Line Maps

To study how the emission line fluxes are spatially distributed I generate maps using a local continuum which I subtract and integrate to obtain the line flux. For each spaxel I extract a spectrum at wavelengths around the emission line. I mask the data points of the emission line, smooth the data using a Gaussian kernel and interpolate across the masked region with a cubic spline to produce a local continuum. I then subtract the local continuum from the data and integrate to measure a line flux. This is done for each spaxel to produce a map of the emission line flux.

To estimate error maps for these lines, I first estimate the noise in the flux data ($f_\nu(\lambda)$) by finding the standard deviation of the data after subtracting the local continuum and masking the emission line. I do this rather than using the flux error bars as these are likely underestimated as noted in the previous section and so this provides a more accurate estimate of the noise. As this is done for each spaxel, the noise for each is measured independently which may not be the case as correlated noise may be introduced during the resampling process in the pipeline. I then propagate the errors in f_ν to find the error in the integrated flux of the emission line for each spaxel to obtain an error map.

To ensure accurate line fluxes in such a heavily obscured environment extinction corrections need to be applied. Obtaining accurate extinction corrections is a challenge in such a complex environment as different components of the spectrum may be affected by different levels of extinction.

To do this I generate a map of the optical depth at each spaxel by measuring the silicate depth at 9.8 μm. This is done by linearly interpolating between 6.7 μm and 13 μm to approximate an underlying continuum from which the silicate depth was measured using equation (3.6). I assume a 10% contribution at 9.8 μm from a power law component and increase the measured silicate depth by a factor $1/0.9$ to estimate

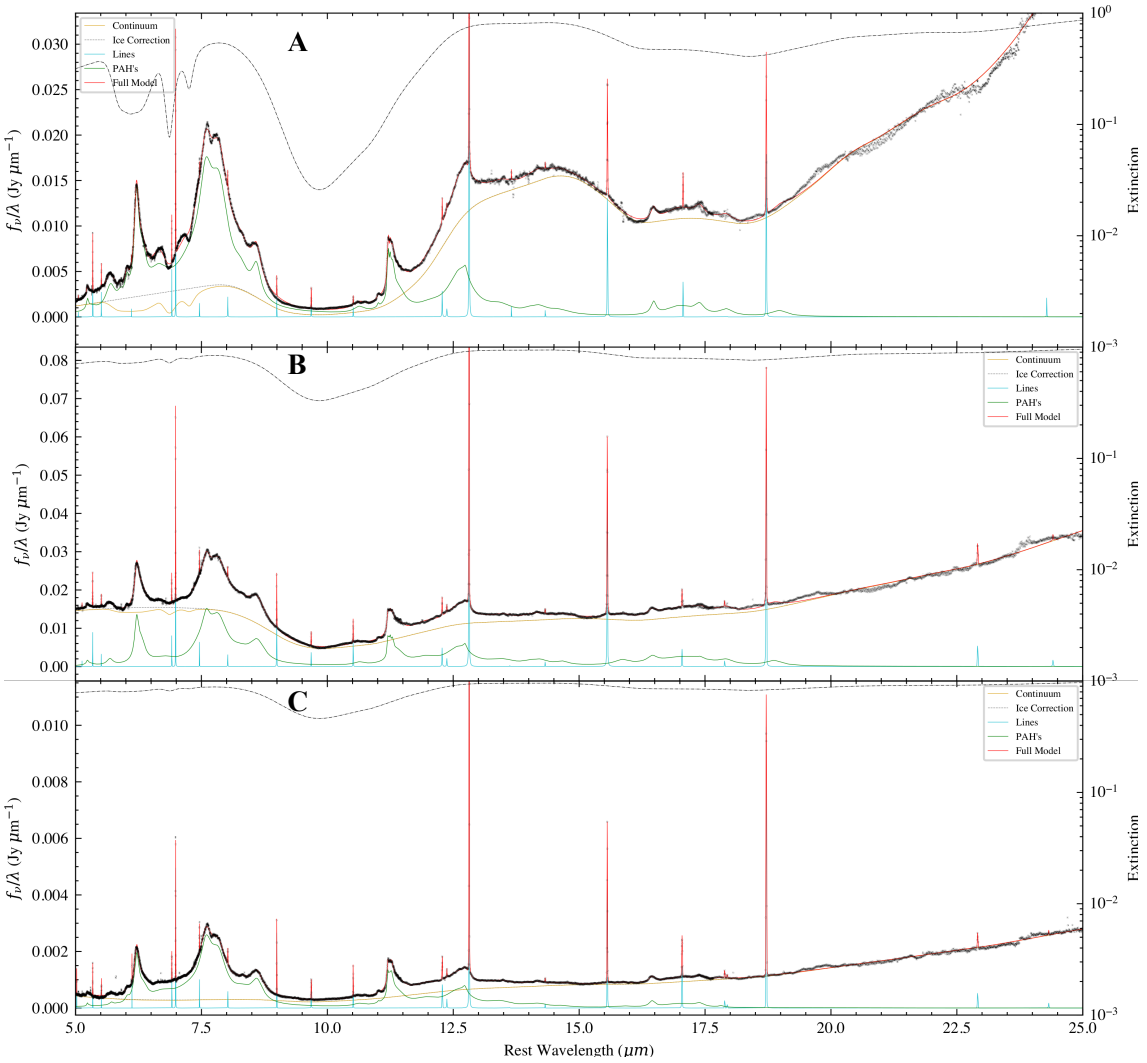

Figure 3.4: Fits to the spectra of VV 114E with our modified PAHFIT model from regions A (top), B (middle) and C (bottom) as shown in Fig. 3.1. The full model is shown in red with its constituent parts labelled in the legend. The right axis of each plot shows the extinction factor, $e^{-\tau_\lambda}$, with the dashed black line.

$\tau_{9.8}$. This results in the map shown in Fig. 3.5, which I use to correct any emission line map for extinction using our extinction curve as discussed in Appendix A.2.1. This correction is applied by dividing the value of each spaxel of a given emission feature by $e^{-\tau_{9.8}\tau(\lambda_0)}$, where λ_0 is the central wavelength of the emission feature.

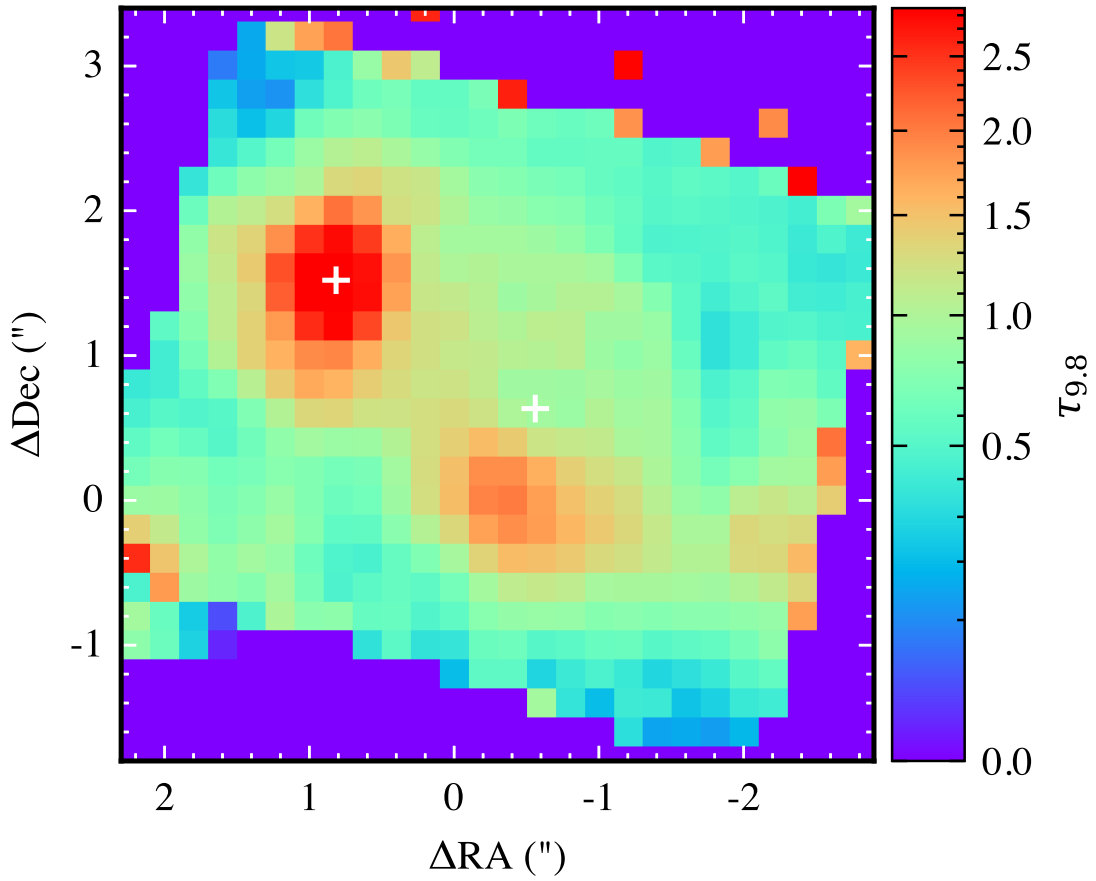

Figure 3.5: Extinction map. Optical depth at 9.8 μm derived from the silicate depth using an interpolated continuum as discussed in Section 3.3.2. This map is used to correct any emission line maps by extinction. The white crosses show the position of the continuum from source A and B. There is a peak in the extinction south of source B, consistent with the shock front (see section 3.4.4). This may be due to a third nucleus (González-Alfonso et al., 2024).

3.4 Results

3.4.1 Obscuration

PAH EW Ratios

To investigate the nature of the two nuclei and the extended emission, in particular the presence of a highly obscured nucleus, I follow Chapter 2 and García-Bernete et al. (2022b) and measure the PAH EW ratios of the 12.7 μm over the 11.3 μm and the 6.2 μm over 11.3 μm PAH features in order to construct a PAH EW diagram. On this plot Hernán-Caballero et al. (2020) showed that star-forming regions have a constant PAH EW ratio while, García-Bernete et al. (2022b) showed that highly

obscured nuclei show a lower PAH EW ratio. As all of this work used Spitzer spectra, the enhanced spectral/spatial resolution afforded by JWST MIRI/MRS, requires redefining the CON selection criteria using JWST reference spectra of star-forming regions. This is due to the increased spectral resolution resulting in different values of the PAH EW ratios, and thus recalibration of the CON selection criteria is required. In particular, the 12.7 μm PAH is better resolved, which leads to a higher measured EW than in the Spitzer data. This is because fitting the 12.7 μm PAH in lower spectral resolution data results in more of the flux being attributed to the continuum rather than the feature. With the better resolved feature and higher signal-to-noise, the fitting routine attributes more flux to the PAH feature. To recalibrate the CON selection region I use the clumps observed in the starburst ring of NGC 7469 (García-Bernete et al., 2022a). These are shown as the grey points in Fig. 3.6. As more targets are observed with MIRI MRS, the sample of star-forming regions will expand and thus improve the CON selection criteria.

From these star-forming clumps I measure the mean and standard deviation, σ, of the EW(12.7)/EW(11.3) and EW(6.2)/EW(11.3) ratios where the obscured nuclei selection region is defined as values lower than $n\sigma$ from this mean. I show 3σ, 4σ and 5σ thresholds in Fig. 3.6.

I also show the expected 12.7/11.3 PAH flux ratio as a function of the extinction as measured by the silicate strength (equation 3.6) in the right panel of Fig. 3.6. To construct this, I first measure the intrinsic flux ratio from the star-forming clumps of NGC 7469 as these show practically no extinction with a silicate strength of very close to zero (García-Bernete et al., 2022a). I then apply extinction to this ratio using our extinction curve and measure the resulting PAH flux ratio. This is shown as the black line with the dashed lines denoting ±20%. Obscured star-formation is expected to lie along this line assuming the PAH emission traces star-formation (Hernán-Caballero et al., 2020; García-Bernete et al., 2022b).

Source A shows lower EW(12.7)/EW(11.3) and EW(6.2)/EW(11.3) with both values below 3σ of the star-forming clumps. This indicates the potential presence of an obscured nucleus. This is further shown in the right panel of Fig. 3.6 where the

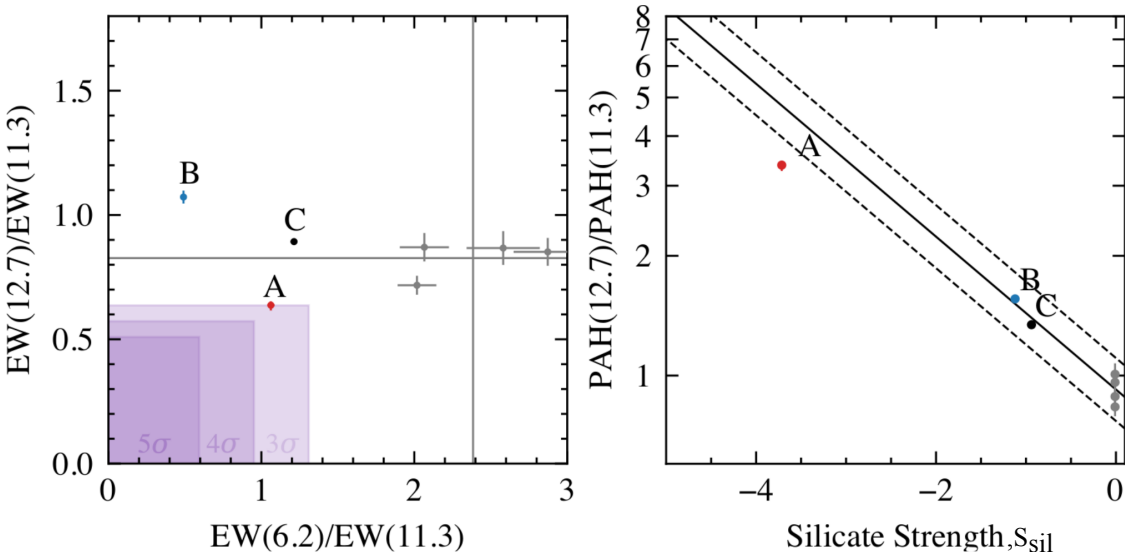

Figure 3.6: *Left:* PAH EW diagram (García-Bernete et al., 2022b) for the three regions in VV 114E, labeled A, B and C. The grey points show the values found for star-forming clumps in NGC 7469 (García-Bernete et al., 2022a) with means shown as the grey lines. The selection criteria for highly obscured nuclei are shown as the purple box defined as either 3σ, 4σ or 5σ from the mean of the star-forming clumps. *Right:* Plot of the 12.7/11.3 PAH flux ratio as a function of extinction as measured by the strength of the 9.8 μm absorption feature as given by equation 3.6. The grey points show the star-forming clumps for NGC 7469, from which the mean flux ratio subject to extinction from our custom extinction curve (see App. A.2.1) is plotted as the black line with $\pm$20% intervals shown as the dashed lines. This line shows how the flux ratio is expected to change as a function of extinction.

12.7/11.3 PAH flux ratio is lower than expected for the level of extinction (indicated by the silicate strength) measured on the continuum. This suggests the presence of additional extinction affecting the continuum compared to the extinction affecting the PAH emission and thus the presence of a deeply buried nucleus.

Source B shows a raised EW(12.7)/EW(11.3) but a significantly lower EW(6.2)/EW(11.3). This is where typical AGN are observed in the PAH EW ratio diagram in (García-Bernete et al., 2022b), which was attributed to a flatter continuum around the 11.3 μm PAH, due to contribution from silicates in emission. The low EW(6.2)/EW(11.3) is also expected for AGN as the presence of hot dust elevates the continuum around 6 μm resulting in a low 6.2 PAH EW. This is consistent with the blue MIRI image which Evans et al. (2022) point out is typical of AGN.

Region C shows an EW(12.7)/EW(11.3) consistent with the star-forming clumps as expected as this aperture traces the extended PAH emission which is likely pure

star-formation. It does however show a significantly lower EW(6.2)/EW(11.3) which could be due to a bluer continuum, raising the EW of the 6.2 μm PAH.

Spectral Decomposition

To further assess whether nucleus A contains a highly obscured source, I use PAHDECOMP (Chapter 2 Donnan et al., 2023a), to decompose the spectrum into a star-forming and nuclear component. This allows the optical depth, τ_N, of the nucleus to be inferred, removing dilution from circumnuclear star-formation. Unlike in Chapter 2, I use the silicate template derived from IRAS 08572+3915. I do this to be consistent with the extinction law used in this Chapter, which also uses the silicate template derived from IRAS 08572+3915. I also found this template to produce deeper measured optical depths, which suggests this profile is "purer", in the sense that more nuclear dominated. As I demonstrated in Appendix A.1.1, the choice of silicate template simply shifts the measured silicate depth but does not change the slope of the relation with HCN-vib surface brightness.

To properly decompose the spectra, I use priors to aid in the separation of the star-forming and nuclear component. In particular, I assume that the PAH emission is associated with star-formation (the PAH ratios in Section 3.4.2 are consistent with this) and therefore I place a tight prior on the total PAH flux, $f_{\rm PAH}$, to the star-forming continuum flux, $f_{\rm SF}$, between 5.2 - 14.2 μm. I use a normal prior of $f_{\rm PAH}/f_{\rm SF} = 1.92 \pm 0.56$ as inferred from the Hernán-Caballero et al. (2020) calibration sample in Chapter 2. I use the silicate profile of IRAS 08572+3915 for the nuclear component, where this component is constrained through its contribution to the total flux where the star-forming continuum is tied to the total PAH flux via the aforementioned prior.

This results in the decomposition in Fig. 3.7 where I measure a nuclear optical depth of $\tau_N = 5.581^{+0.006}_{-0.007}$ and a nuclear fraction of $\beta = 0.772^{+0.001}_{-0.001}$ (β is defined as the fractional contribution to the total continuum flux between 5.2 - 14.2 μm). It is worth noting that the uncertainties on these parameters are likely underestimated by a factor of ~ 10 as mentioned previously. This is due to the signal-to-noise of the

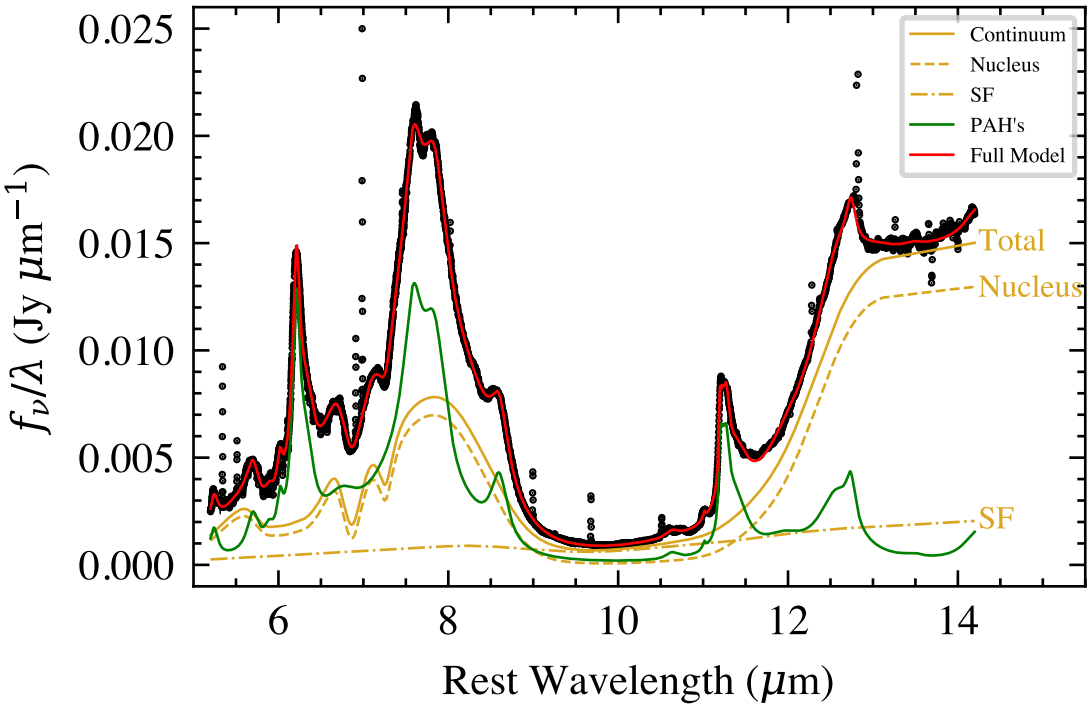

Figure 3.7: Fit to the spectrum of source A using the decomposition model described in Section 3.4.1 and Donnan et al. (2023a). This model fits the spectrum up to 14.2 μm by decomposing the continuum into star-forming and nuclear where the relative contributions are constrained by restricting the total PAH flux to the total star-forming continuum flux. The total continuum is given by the solid line and is the sum of the two components.

data being extremely high and so the dominant source of error is the assumptions of the model which are not accounted for when using the MCMC routine. These results show that the spectrum of source A can be explained by a low contribution from less obscured star-formation in the foreground in addition to a highly obscured nucleus with a deep silicate absorption feature, which dominates the spectrum. To place this optical depth in context I show a modified plot from 2.8 in Chapter 2, where the measured nuclear optical depths from Spitzer spectra of the CONquest sample (Falstad et al., 2021) are plotted against the HCN-vib surface brightness as measured in the millimetre, using the same IRAS 08572+3915 silicate template used here. This is shown in Fig. 3.8. Placing the value measured from the spectrum of nucleus A of VV 114, $\tau_N = 5.6$, onto this plot finds a HCN-vib surface brightness of $\Sigma_{\mathrm{HCN-vib}} \gtrsim 1 L_\odot$ pc^{-2}, which tentatively on the limit of the threshold to be considered a CON (Falstad et al., 2021).

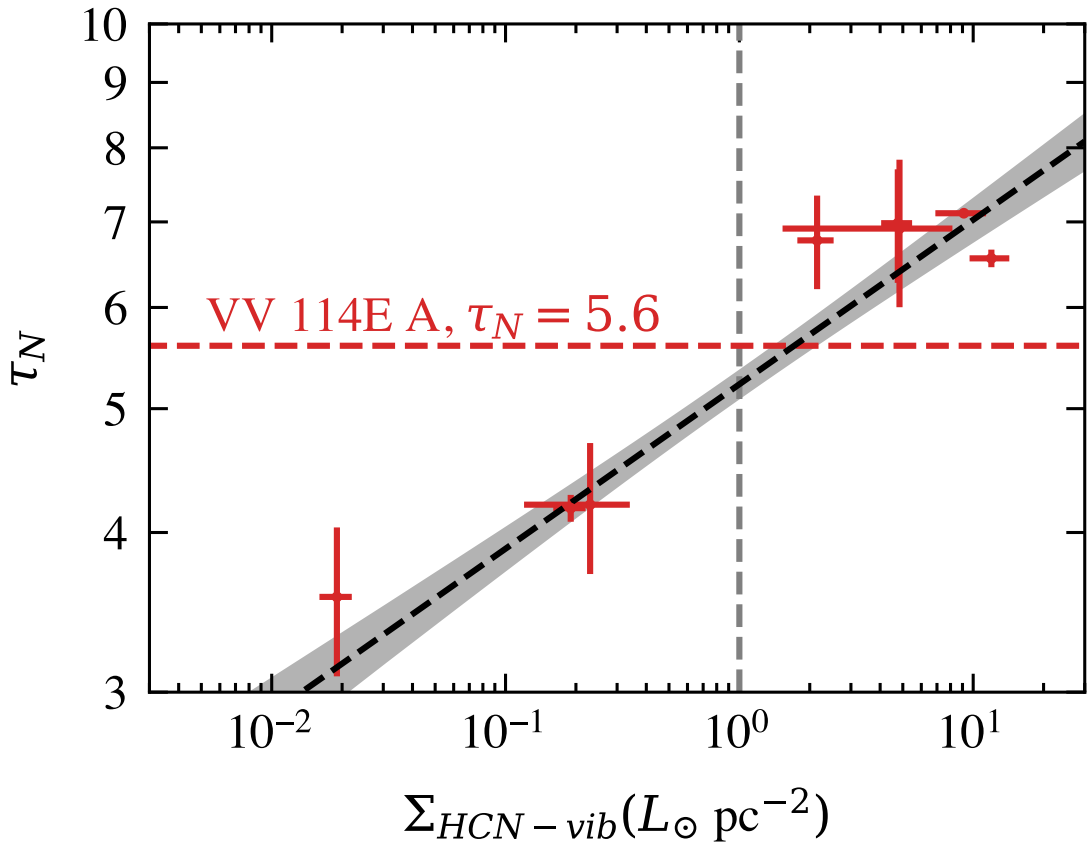

Figure 3.8: Plot modified from Donnan et al. (2023a) which shows the nuclear optical depth of the CONquest sample (Falstad et al., 2021) measured using the spectral decomposition method and plotted against the surface brightness of HCN-vib. I show the CON definition of $\Sigma_{\mathrm{HCN-vib}} > 1 L_\odot$ pc^{-2} with the vertical dashed grey line. The horizontal red line shows the value of $\tau_N = 5.6$ found for VV 114E A, which predicts a $\Sigma_{\mathrm{HCN-vib}} > 1 L_\odot$, meeting the CON definition.

3.4.2 PAH Properties

The relative fluxes between different PAH emission features are known to change with the properties of the PAH molecules and the incident radiation field (Li, 2020).

In the immediate vicinity of AGN, PAH molecules are thought to be destroyed (Roche et al., 1991; Voit, 1992; Siebenmorgen et al., 2004) however there is evidence that they can survive close to the AGN, in particular the 11.3 μm feature (Hönig et al., 2010; Alonso-Herrero et al., 2014; Alonso-Herrero et al., 2016; Jensen et al., 2017). Most recently García-Bernete et al. (2022a) found that PAHs can survive in the innermost region of luminous Seyfert galaxies using JWST/MRS data but that

these PAHs are different to typical star-forming galaxies, where they are observed to be more neutral (García-Bernete et al., 2022c; García-Bernete et al., 2022a).

For measuring the PAH properties in VV 114E, I avoid using the 7.7 μm PAH as the continuum around this feature is difficult to constrain properly due to both the CH absorption at $\sim 7.3\mu$m and the tail of the silicate absorption feature. I therefore employ the 11.3/6.2 ratio as a tracer of the ionisation state of the PAH population (Rigopoulou et al., 2021). This was shown in García-Bernete et al. (2022c) to show distinct differences in the ratios between AGN and pure star-forming galaxies.

In Fig. 3.9 I show the 11.3/6.2 μm flux ratio after correcting for extinction. This ratio is expected to decrease with a greater fraction of ionised PAH molecules (Rigopoulou et al., 2021; García-Bernete et al., 2022c). I plot the measured ratios against the [Ne III]/[Ne II] line ratio which traces the hardness of the radiation field (these lines are investigated further in the following section) and compare against the average ratios for star-forming galaxies and AGN from García-Bernete et al. (2022c). I find all three sources to be consistent with typical star-forming galaxies where the PAH molecules are less neutral (higher fraction of ionised molecules) than typical AGN. This means that if any AGN is present then it must be extremely obscured leaving the PAH emission unaffected.

It is also worth noting that the extinction is likely over-corrected for nucleus A, as the continuum receives a greater extinction than the circumnuclear PAH emission. This would change the 11.3/6.2 ratio, where over-correcting for extinction would boost the 11.3 more than the 6.2. This would imply that the true 11.3/6.2 ratio is slightly lower than plotted which moves it more in line with the other points, further from the AGN average.

3.4.3 Fine Structure Lines

To investigate the hardness of the radiation field within VV 114E I generated maps of [Ne II] (12.813 μm, IP of 21.56 eV) and [Ne III] (15.555 μm, IP of 40.96 eV).

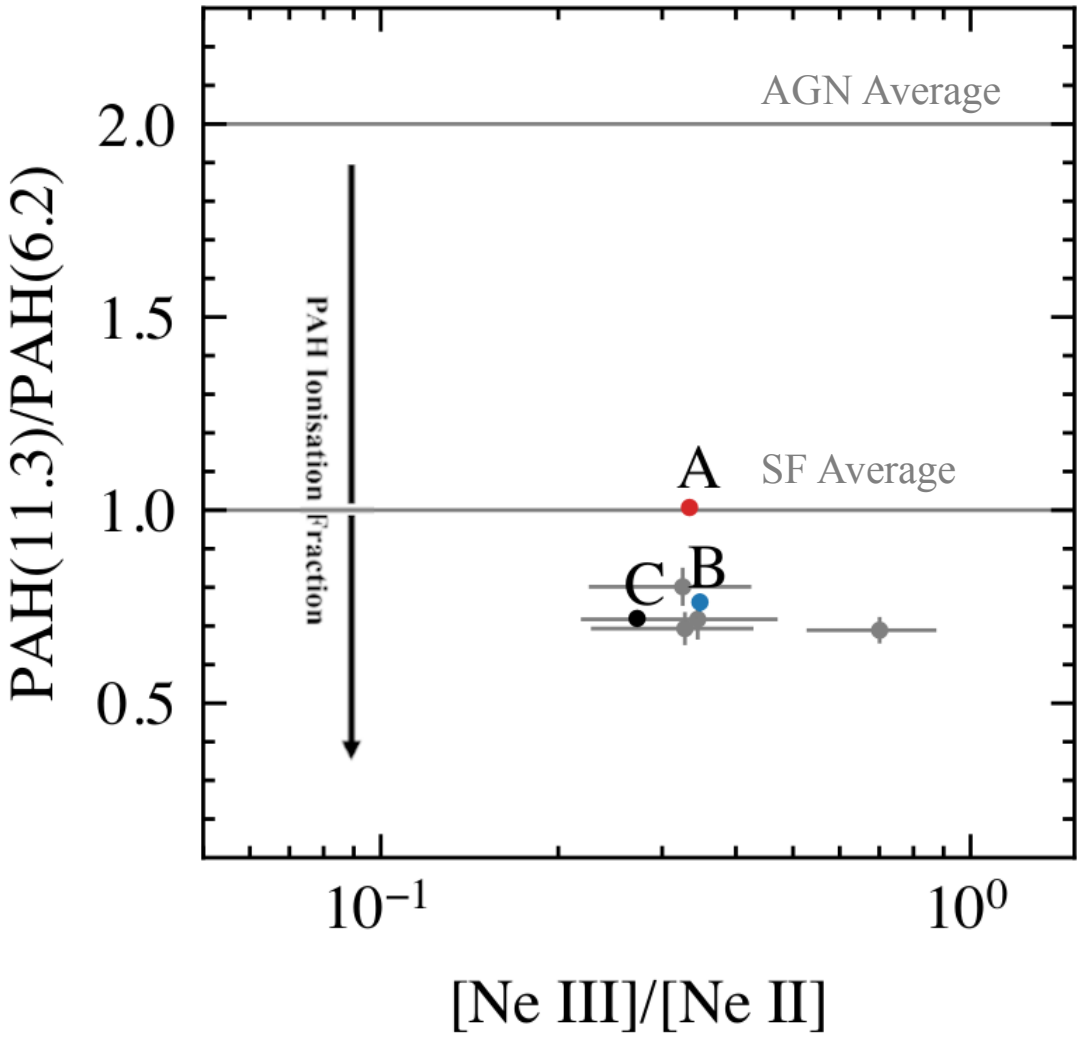

Figure 3.9: PAH flux ratios of the 11.3 μm PAH over the 6.2 μm against the [Ne II]/[Ne II] line ratio which traces the hardness of the radiation field. A greater fraction of ionised PAHs will result in a lower value. The values labelled A, B and C show those obtained from the three regions in VV 114E while the grey points show 4 star-forming clumps from NGC 7469 (García-Bernete et al., 2022a). The solid grey lines show the average value for star-forming galaxies ($\sim$ 1) and AGN ($\sim$ 2) from García-Bernete et al. (2022c). These ratios have been corrected for extinction.

The lower ionisation potential lines [Ne II] and [Ne III] are excellent tracers of star-formation due to their high relative brightness. These maps are shown in Fig. 3.10. The errors in these lines are very low as seen in the error maps in the same figure.

I do not detect any of the higher ionisation potential lines such as [Ne V] (14.322 μm, 97.1 eV) or [Ne VI] (7.652 μm, 126.2 eV), which are typical tracers of AGN activity (Sturm et al., 2002; Armus et al., 2006; Inami et al., 2013). This suggests that there is no opening angle to any potential AGN present and therefore if an AGN does exist, it must be highly obscured. I discuss this further in Chapter 5, in the context of different geometries of the dusty obscuring material.

The [Ne III]/[Ne II] line ratio is higher for source B compared to source A and the immediate surrounding region. This points towards a harder radiation field within this cluster where the lack of [Ne V] suggests that this is likely a star-forming clump with a young stellar population rather than an AGN. This is consistent with the much bluer colours seen in the imaging in Fig. 3.1 and Evans et al. (2022). The [Ne III]/[Ne II] ratio for source A may trace the foreground star-formation as found by the spectral decomposition in Section 3.4.1 as it appears similar to the surrounding environment.

I additionally detect the faint [Cl II] (14.37 μm, 12.97 eV) line which has a very low ionisation potential. Due to its faintness it was difficult to detect with Spitzer however the line has been observed in NGC 4945 (Pérez-Beaupuits et al., 2011) where it appeared to be more diffuse than [Ne II]. This is indeed the case with VV 114E where in Fig. 3.10 the emission is more extended. The [Ne III]/[Cl II] ratio is also plotted and clearly shows an increase for source B, consistent with the [Ne III]/[Ne II] ratio. It is worth noting that the error in this line ratio is significantly larger than for [Ne III]/[Ne II] due to the relative faintness of the [Cl II] line.

In Fig. 3.11 I show a map of [Fe II] (5.34 μm) which is a strong tracer of shocks (Allen et al., 2008). This is because iron is released when shocks break apart dust grains. There is a clear increase in [Fe II] emission south of source B which indicates a shock front. Comparing the line to the other transitions of similar ionisation potential such as [Cl II], it is clear that there is an enhancement

of [Fe II] at the shock front relative to [Cl II]. The errors in this map are very low as seen in the lower panel of Fig. 3.11 and therefore the spatial variations in the flux of this line are statistically significant. This map has not been corrected for extinction, however if it were corrected the shock front would be even more prominent as this region has a higher optical depth than behind the shock, resulting in a larger correction than behind the shock.

I also find the kinematics of the [Fe II] line to be dominated by the bulk rotation of the galaxy, matching the larger scale velocity field from CO observations with ALMA (Saito et al., 2015). This suggests that any motion connected to the shock is low, consistent with the interpretation in section 3.4.4.

3.4.4 Molecular Hydrogen (H_2)

In the 5 μm to 17 μm range there are the H_2 rotational transitions (e.g. Sturm et al., 1996; Rigopoulou et al., 2002). Unlike the CO rotational lines in the sub-mm, the H_2 rotational transitions are populated by hotter gas and are therefore sensitivity to higher temperatures (e.g. Valentijn et al., 1996). This makes them good tracers of shocked molecular gas.

I generated maps of the rotational transitions of H_2 in Fig. 3.12 where the S(1) to S(8) transitions are shown. These have been corrected for extinction using the map in Fig. 3.5. It is worth noting that this likely leads to an over-correction of the extinction for source A as the extinction map was inferred from silicate depth and thus measures the extinction from the continuum. As discussed in section 3.4.1 the continuum of source A is more embedded and therefore using this extinction I am over-correcting the H_2 line fluxes, in particular the S(3) J=5, 9.665 μm transition, which sits in the 9.8 μm silicate absorption band. This is seen in Fig. 3.12 where for S(3), source A appears relatively brighter than in the other lines which are less sensitive to the extinction correction. I therefore also show the uncorrected line maps in Appendix A.2.2. In Chapter 4, I investigate the different layers of extinction present in these obscured nuclei, where I show that the H_2 emission is less obscured than the dust continuum.

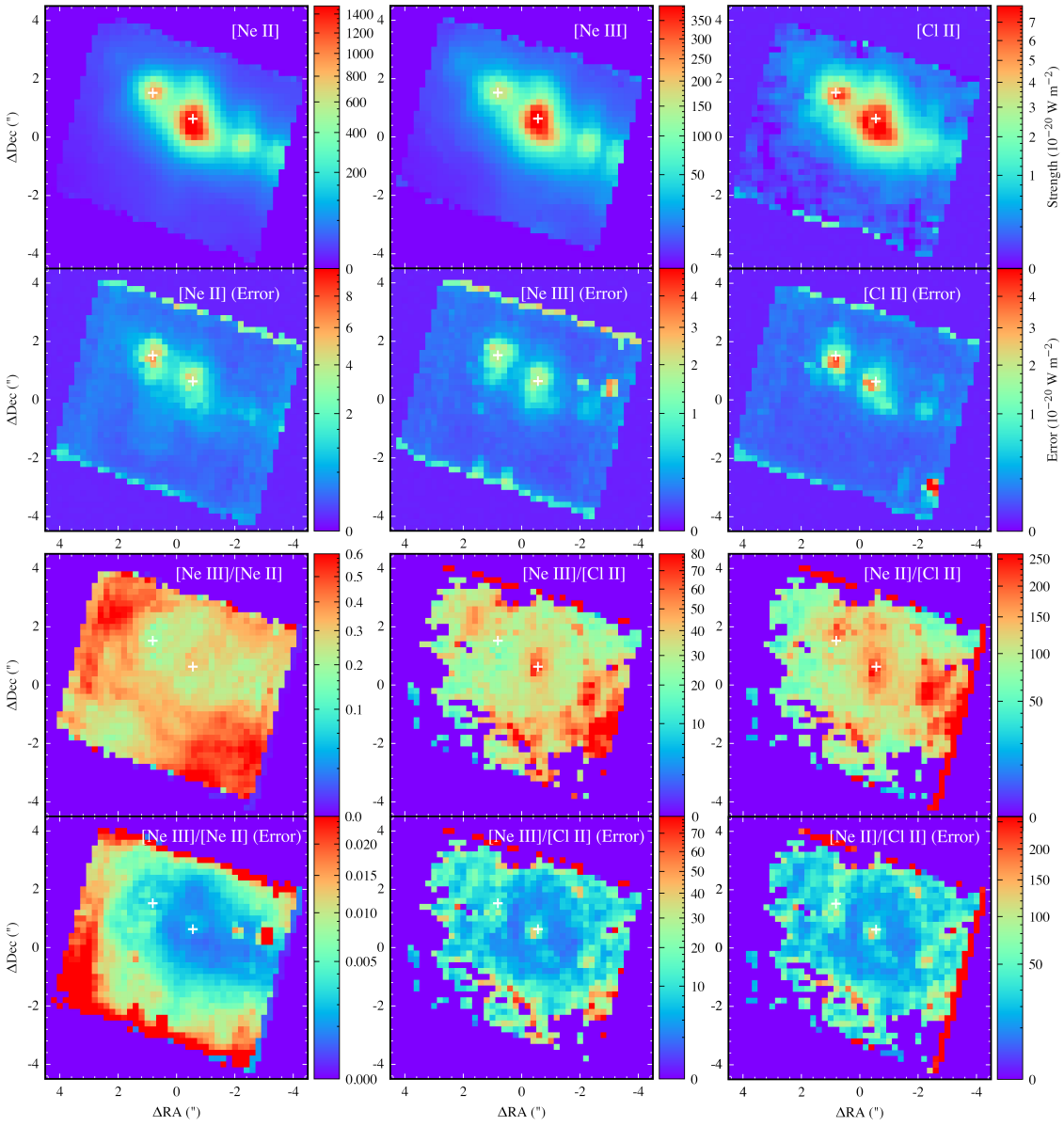

Figure 3.10: Low ionisation potential line maps and their ratios. The top panels shows [Ne II] (12.813 μm, 21.56 eV), [Ne III] (15.555 μm, 40.96 eV), and [Cl II] (14.37 μm, 12.97 eV) from left to right. The bottom panels show ratios of these lines. For each map the associated error map is shown directly below. Flux units are in 10^{-20} Wm^{-2} pixel^{-1}. The continuum positions of sources A and B are shown with the white crosses.

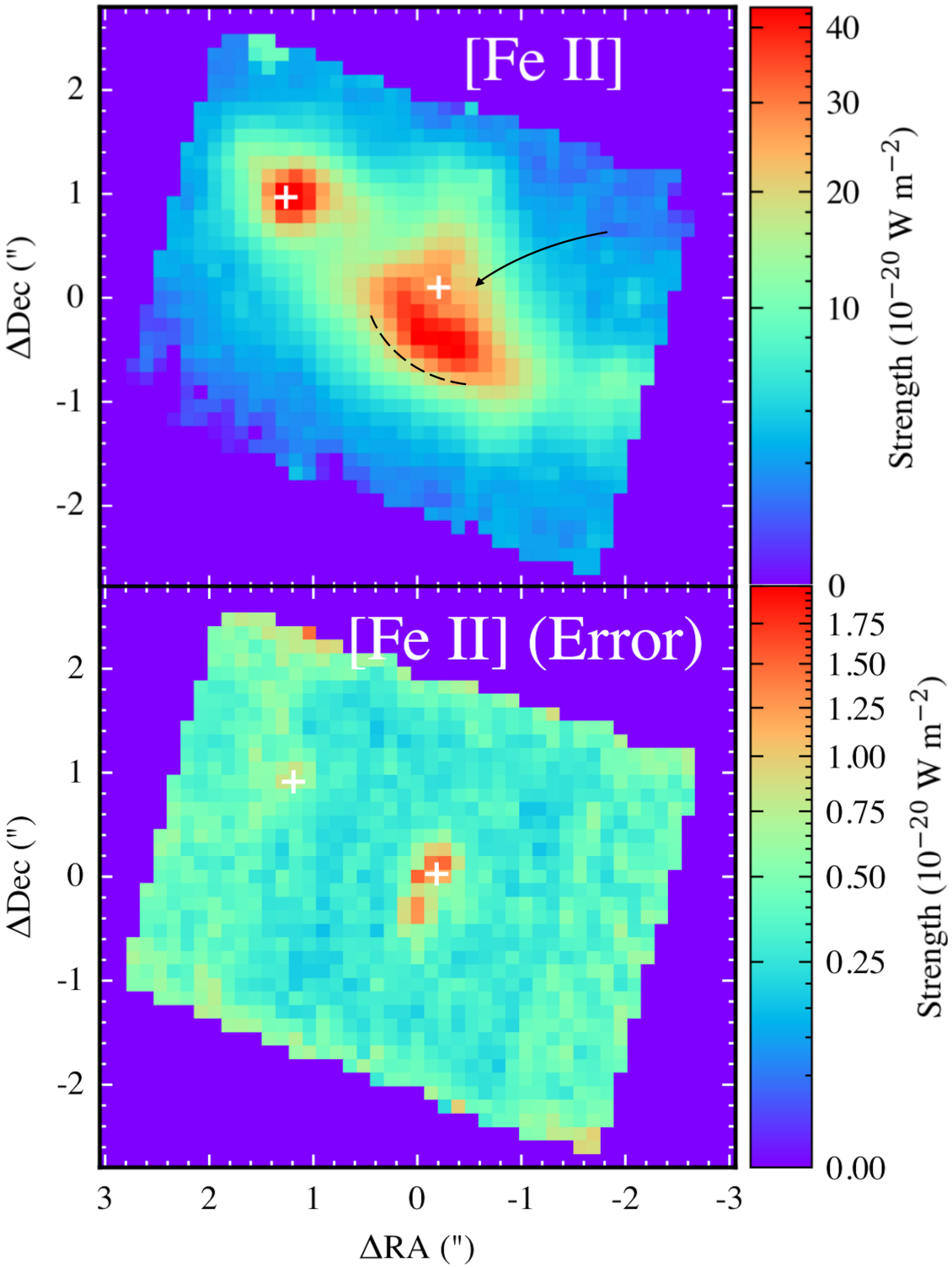

Figure 3.11: Map of the shock tracer [Fe II] (5.34 μm) line. I labelled the shock front with the dashed black line and the potential direction as discussed in Section 3.4.4. The continuum positions of sources A and B are shown with the white crosses. This map has not been corrected for extinction. In the lower panel I show the error map. Flux units are in 10^{-20} Wm^{-2} pixel^{-1}

Fig. 3.12 illustrates a clear shock with a front south of source B as suggested by the [Fe II] emission in Fig. 3.11. Moving to the lower energy transitions the peak moves behind the shock front tracing the cooler gas. I also show a map of the 6.2 μm PAH emission as contours in Fig. 3.12 which traces regions of star-formation. For most of the structure the molecular hydrogen is consistent with the PAH emission as stars are expected to form from the molecular gas and young stars excite the PAH molecules. However behind the shock front there is a clear region of molecular hydrogen which devoid of any 6.2 μm PAH emission.

Shocks are expected to destroy PAH molecules (Micelotta et al., 2010) where the shock heated gas can produce high energy collisions with the PAH molecules. Micelotta et al. (2010) showed that at velocities of $\gtrsim 100$ kms^{-1}, PAHs are destroyed while at lower velocities, the molecules are only denatured. Interestingly the 6.2 μm PAH band is strong at the shock front and only diminishes behind the front. This may suggest that the velocity of the gas is higher behind the shock front, reaching a sufficient velocity to destroy the PAH molecules. "Slow" shock fronts have been suggested in previous works (e.g. Leftley et al., 2024; Villa-Vélez et al., 2024) which can explain the lack of PAH destruction at the front itself. Behind the front the flow experiences turbulence resulting in an increased speed, capable of destroying the PAHs.

H_2 Excitation

Under the assumption of local thermodynamic equilibrium (LTE), the relative fluxes of these transitions can be modelled where the molecular hydrogen column density and temperature determine the relative population of the energy levels and thus the relative fluxes observed.

The column density, N_u, of each level is expressed as $\log\left(\frac{N_u}{g_u}\right)$, where g_u is the statistical weight of the upper energy level, u. Each of these quantities is given by

$$N_u = 4\pi \frac{f}{A_u \left(E_u - E_l\right)}; \quad g_u = (2J+1)(2I+1), \tag{3.7}$$

where f is the integrated line flux, A_u is the Einstein A coefficient for the transition, and E_u, E_l are the upper and lower energy levels respectively. The statistical weight

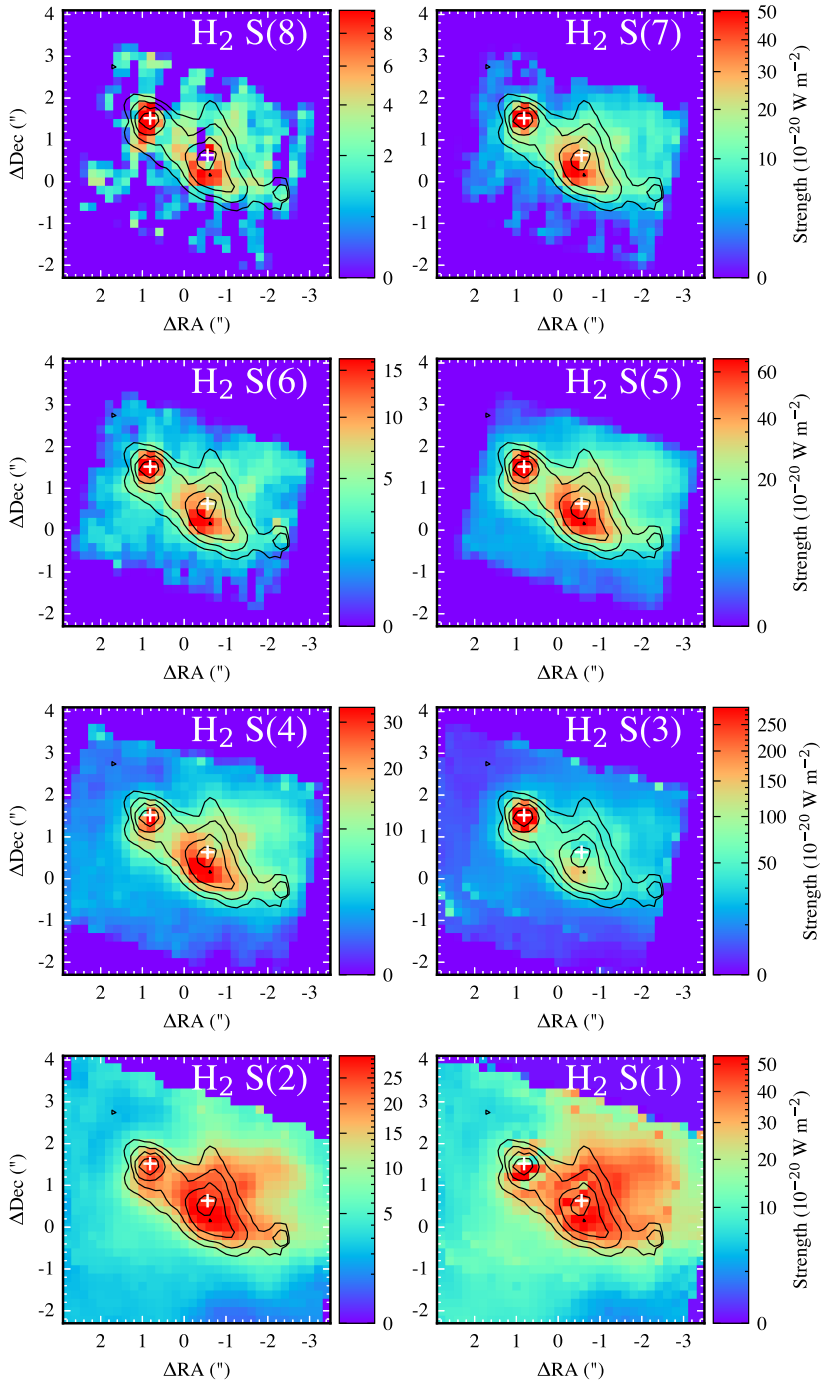

Figure 3.12: Maps of the integrated flux of the molecular Hydrogen transitions from the highest energy H_2 S(8) (5.053 μm) to the lowest energy H_2 S(1) (17.0 μm). The white crosses mark the continuum positions of sources A and B. These maps have been corrected for extinction using the optical depth map shown in Fig. 3.5. The contours show the 6.2 μm PAH emission. Flux units are in 10^{-20} Wm^{-2} pixel^{-1}

depends on the rotational quantum number, J, and the nuclear spin, I. For "Ortho" molecules, each nuclei has spin in the same direction ($I = 1$) and even values of J. "Para" molecules consist of nuclei with opposite spin ($I = 0$) and odd numbers of J. We assume an ortho-to-para ratio of 3 (e.g. Rigopoulou et al., 2002), which is reasonable under LTE conditions with $T > 200$ K, which is indeed the case in VV 114. By plotting the $\log\left(\frac{N_u}{g_u}\right)$ as a function of the upper energy of each transition, E_u, we obtain the rotation diagram in Fig. 3.13.

I model the observed rotation diagram for each spaxel using the PHOTODISSOCIATION REGION TOOLBOX code[2] (Kaufman et al., 2006; Pound and Wolfire, 2008; Pound and Wolfire, 2011). This assumes a two temperature gas model where total model is

$$\log\left(\frac{N_u}{g_u}\right) = C_{\rm hot} + C_{\rm cold} \tag{3.8}$$

where $C_{\rm hot}$ and $C_{\rm cold}$ are the hot and cold components respectively. Each component is given by

$$C_{\rm hot} = \log\left(\frac{N_{\rm hot}}{Z(T)}\right) + \frac{E_u}{k_b T} \tag{3.9}$$

where $N_{\rm hot}$ is the total column density of the hot component, $Z(T)$, is the partition function and T is the excitation temperature. The total H_2 column density is simply $N_{\rm total} = N_{\rm hot} + N_{\rm cold}$. The partition function is approximated (Herbst et al., 1996) as

$$Z(T) = 0.0247T\left(1 - e^{-\frac{6000}{T}}\right)^{-1}. \tag{3.10}$$

As the S(3) transition occurs at 9.665 μm which sits in the peak of the silicate absorption, it is highly sensitive to the extinction correction and so I include this point but with a large (50%) error to ensure it does not bias the fits. As the S(0) J=2 transition lies outside the observing range of MIRI (28.21 μm), I use the anchor point from Spitzer observations (Petric et al., 2018) to act as a guide for the model to prevent nonphysical solutions. To match the flux with the JWST/MIRI data I scale the S(0) flux by matching the S(1) measurement from Spitzer to the

[2] https://github.com/mpound/pdrtpy

median of the S(1) map from MIRI. I give the value a 50% error to account for this large uncertainty and to make it act as simply an anchor point. For the two point sources, A and B, I fit the sum of the line fluxes in a 3x3 pixel grid around the continuum position to avoid PSF effects.

In Fig. 3.13 I show the measured total column density of molecular hydrogen, the temperature of the cold gas component and the temperature of the hot gas component from these fits for each spaxel. Along the shock front there appears to be a cavity in the column density coinciding with an increased temperature in both the cold and hot gas. It is worth noting that these two quantities are somewhat degenerate from the fitting process and so should not be taken as two independent measures of the gas properties. Behind the shock the molecular hydrogen column density increases approaching $N_{H_2} \rightarrow 10^{21}$ cm^{-2} as the temperature drops. This is expected for a fast molecular shock where the gas behind the shock reforms (See Fig. 1 of Hollenbach and McKee, 1989). The H_2 column densities are lower but of a similar order of magnitude ($\sim 10^{21}$ cm^{-2}) to those found by Saito et al. (2015) using CO observations however their value is sensitive to the $\alpha_{\rm CO}$ conversion factor used.

The lower panels of Fig. 3.13 show the fits for the two nuclei A (left) and B (right). As can be seen in these plots the S(0) (J=2) is not predicted by the model but does act to prevent the solution from being non-physical. This suggests that with just two components the model is only able to fit the hotter gas and an additional cold component may be required to fit this transition. Adding this additional component to the model would add 2 more parameters which may be too many as the J=2 transition is highly uncertain and therefore the constraints on this cooler component would be very weak. For source A, the over-correction of the extinction where the S(3) J=5 transition appears too high.

The temperatures measured are high ($T_{\rm hot} > 1000$ K) as it is sensitive to the high energy transitions in the fitting. Calculating a temperature from the S(7) and S(5) fluxes (Lambrides et al., 2019) using a 4.5" aperture from Spitzer spectral mapping data (Donnan et al., 2023a), finds a temperature of 1078 K. Considering this is over a larger spatial scale and is still $\gtrsim 1000$ K, reinforces this result.

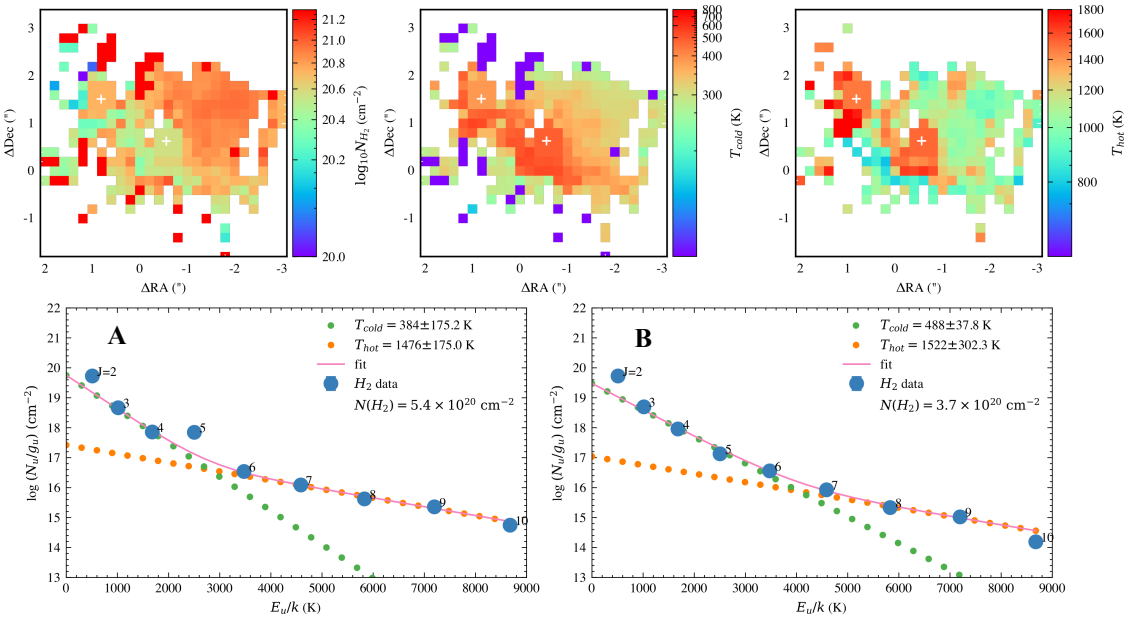

Figure 3.13: Results from modelling the S(1) to S(8) molecular hydrogen transitions. I show the total molecular hydrogen column density (left), the temperature of the cold gas component (middle) and the hot gas component (right). The continuum positions of sources A and B are shown with the white crosses. In the lower panels I show the fits to the two point sources A (left) and B (right) where each is fitted to a 3x3 region around the continuum position. In these plots the best fit is is shown with the solid line composed of the cold (green) and hot (orange) gas components. These fits assume an ortho-to-para ratio of 3. The S(0) (J=2) point for these fits is from Spitzer observations (Petric et al., 2018) and acts as a loose anchor to prevent non-physical solutions. Error bars are present but too small to see behind the markers.

3.5 Discussion

CONs are rare amongst all galaxy types which suggests this is a short-lived phase in galaxy evolution, however the high obscuration may hide extreme SMBH growth and/or compact starburst activity. CONs are commonplace among LIRGs and ULIRGs (Falstad et al., 2021; Donnan et al., 2023a) and are prevalent in major mergers. The evolutionary picture of these objects is relatively unknown, in particular its origin and subsequent evolution. The obscured source A in VV 114E is an interesting object to study to ask this question.

Our analysis in Section 3.4.1 finds that the PAH EW ratios for source A are low, indicative of a buried continuum source. The decomposition model finds a nucleus which just reaches optical depth $\tau_N = 5.6$ to satisfy the CON definition (see Chapter 2). The lack of high ionisation lines such as [Ne V] suggests if an

AGN is present, the radiation field is completely obscured and unable to affect the surrounding environment. This is confirmed by looking at the imprint on the PAH molecules that the central source makes. AGN are known to affect PAH molecules very close to the central engine or alter their properties in the circumnuclear region (García-Bernete et al., 2022c; García-Bernete et al., 2022a; García-Bernete et al., 2024b) where there is a higher fraction of neutral PAHs. This suggests that the imprint of AGN feedback can be traced through the PAH properties.

For source A I found the 11.3/6.2 PAH flux ratio to indicate a population of ionised PAHs, typical of star-forming regions. This suggests that there may not be any AGN present or that it must be extremely obscured such that the PAHs have not been affected by the AGN. The latter explanation is required to be consistent with the prediction from Saito et al. (2015) which suggested the possible presence of a hidden AGN through an elevated HCN/HCO+ ratio.

X-ray emission has been observed from this source however only upper limits have been placed on the X-ray luminosity of an intrinsic AGN (Ricci et al., 2021) with $\log L_{2-10} < 41.11$ erg s^{-1} and $\log L_{10-24} < 40.95$ erg s^{-1}. These values are typical of CON dominated sources.

In summary, I detect a deeply obscured nucleus for source A which may be powered by a hidden AGN as suggested by Saito et al. (2015). Considering its high obscuration, this object may be in an early phase of evolution, where the central engine will eventually clear the surrounding dust. To test any such scenario requires a larger sample of targets and a more comprehensive analysis of the nature of the dusty structure. This is something I will explore further in Chapter 5.

From [Fe II] emission and analysis of the transitions of molecular hydrogen, H_2, I detect a shock front south of nucleus B (illustrated in Fig. 3.11). The origin of this shock is unclear. Our analysis suggests that source B is a compact star-forming region and so supernovae (Reach et al., 2019) or winds from massive stars (Hollenbach, 1997) may be responsible if the shock originates from this region. However it appears more extended which suggests that this shock may simply be a product of the galaxy-galaxy interaction. This may form part of a larger

shock, where in Fig. 3.1 the 7.7 μm PAH emission traces this region and extends to the west. Indeed, Saito et al. (2017) detect CH_3OH emission across $\sim$ 3 kpc which extends between the two merging components of VV 114. They therefore suggest this is due to a large scale shock from the galaxy-galaxy interaction. It is also interesting to note that the shock front appears very dusty as seen in Fig. 3.5 where the optical depth increases.

3.6 Summary

I have used spatially resolved mid-infrared spectroscopy from JWST/MIRI MRS observations to investigate the obscured environment of VV 114E. I model the spectrum from 5 - 28 μm within three apertures (shown in Fig. 3.1) from which I measured the properties of the PAH molecules. I also construct maps of various molecular and ionised lines. My main findings are:

- From the low 12.7/11.3 and 6.2/11.3 PAH EW ratios I find that source A is heavily obscured and hosts a buried nucleus. The PAH EW ratios are elevated for source B while source C is typical of star-forming regions. By decomposing the spectrum into nuclear and star-forming components I measure a nuclear optical depth of $\tau_N = 5.6$, which is large enough to meet the threshold required for CONs.

- The 11.3/6.2 PAH flux ratios suggests an ionised population of PAHs typical of star-forming regions for all three sources.

- I do not detect any high ionisation potential lines such as [Ne V] or [Ne VI] which is consistent with the high obscuration of source A. However, considering the hot dust continuum of source B, for which Rich et al. (2023) suggests this source hosts an AGN, and its significantly lower obscuration, one would expect to observe high-IP lines.

- I detect clear evidence of shock south of source B with elevated [Fe II] emission. The molecular hydrogen lines trace this shock where the higher

energy transitions peak at the shock front and move behind towards the lower energy transitions.

- The 6.2 PAH emission does not trace the low energy H_2 emission lines which may suggest the ionised PAH molecules are destroyed in the post-shock gas. This may be a delayed process as the PAH emission is strong at the shock front and only subsides behind the shock.

- From modelling the transitions of molecular hydrogen I detect clear evidence of a shock front south of source B with a ridge of increased gas temperatures resulting in higher column densities behind the shock front where gas is expected to reform.

These results suggest that nucleus B is likely star-forming dominated while source A contains an extremely obscured nucleus. This nucleus shows typical characteristics of CONs and may be powered by an AGN. This initial analysis shows the power of the JWST for studying these highly obscured environments.

4

Peeling Back Layers of Extinction in the Era of JWST.

Contents

This chapter is adapted from: F. R. Donnan, D. Rigopoulou, I. García-Bernete, M. Pereira-Santaella, P. F. Roche, A. Alonso-Herrero. *Peeling back the layers of extinction of dusty galaxies in the era of JWST: modelling joint NIRSpec + MIRI spectra at rest-frame 1.5-28 μm.*, 2024, MNRAS, 529, 1386

4.1 Introduction

The mid-infrared spectra of galaxies are complex and feature rich, with dust emission and absorption signatures, Polycyclic Aromatic Hydrocarbons (PAHs), and numerous emission lines from ionised and molecular gas (e.g. Brandl et al., 2006; Smith et al., 2007b; Gallimore et al., 2010).

As discussed in previous chapters, extracting the emission features and determining accurately the level of the continuum emission is a challenge. This is particularly true in obscured sources, where strong absorption features from water ice ($\sim 6\mu$m), CH ($\sim 7\mu$m) and silicates ($\sim 9.8\mu$m) create a complex continuum (e.g. Spoon et al., 2007; Spoon et al., 2022; Veilleux et al., 2009; García-Bernete et al., 2024c).

In the era of JWST, with both NIRSpec and MIRI MRS data, modelling the spectra over a large wavelength range is challenging. This may be a consequence of differential extinction, where multiple regions of different dust obscuration all contribute within a single aperture. The resulting spectrum is therefore a combination of different intrinsic spectra with varying levels of obscuration.

Previous approaches to model mid-IR spectra assume a single level of extinction i.e a single value for column density where the difference in extinction with wavelength is purely due to the chosen extinction law. Popular choices include PAHFIT (Smith et al., 2007b), which models the full spectrum with a series of blackbodies subject to extinction and a series of PAH emission features, with flexible profiles. This works well for relatively unobscured star-forming galaxies which are dominated by PAH emission but can struggle to fit AGN and/or obscured

galaxies (e.g. Gallimore et al., 2010). Another code, CAFE (Marshall et al., 2007), similarly uses modified blackbodies but is restricted to only three where each has a different extinction.

If an AGN is present, one approach is to model the dust from AGN using a template, typically produced from radiative transfer simulations of the torus (e.g. Ramos Almeida et al., 2009; Alonso-Herrero et al., 2011; Alonso-Herrero et al., 2012; Martínez-Paredes et al., 2015; Martínez-Paredes et al., 2020; Martínez-Paredes et al., 2021; González-Martín et al., 2019a; González-Martín et al., 2019b; García-Bernete et al., 2019; García-Bernete et al., 2022d). This approach is valuable in providing constrains on physical parameters of the torus such as opening angle, inclination etc. However as this is often highly model dependent, one often needs to fit multiple libraries to obtain a complete picture of the torus for a given object. A wide variety of libraries exist in the literature, with different geometries, dust distributions etc. These include smooth torus models (e.g. Fritz et al., 2006; Efstathiou et al., 2013), clumpy models (e.g. Nenkova et al., 2008a; Nenkova et al., 2008b; Hönig et al., 2010), two-phase models (e.g. Stalevski et al., 2016) and models incorporating dust outflows (e.g. Hönig and Kishimoto, 2017). These models are discussed further in Chapter 5 in section 5.3. These templates can also struggle to fit the data in certain cases such as for the most obscured nuclei, where the deep silicate feature is difficult to reproduce (García-Bernete et al., 2022b), with only the most obscured smooth tori able to generate the deep silicates. Additionally, these models tend to lack ices which are clearly present in obscured nuclei. The most success has come from QUESTFIT (Veilleux et al., 2009), however this uses a fixed PAH template, limiting its flexibility to infer PAH properties.

While the techniques outlined above are extremely valuable, there is a need for a more general, data driven approach that can fit a wide range of objects such as star-forming regions, type 1/2 AGN, extremely obscured nuclei, etc, but still provide inference of interesting/useful physical parameters of the dusty structure in these galaxies such as the degree of obscuration and dust temperature. This is especially true in the era of JWST where the much higher data quality of NIRSpec/MIRI

(e.g. Wells et al., 2015; Wright et al., 2015; Rieke et al., 2015; Jakobsen et al., 2022; Argyriou et al., 2023; Böker et al., 2023) over previous instruments such as Spitzer IRS or Akari FIS, means the current models can struggle to fit the data due to an increase in spectral resolution and sensitivity. Additionally, the significant improvement in spatial resolution enables better isolation of the nuclei of galaxies, and therefore the spectra are less diluted by star-formation. As a consequence, the spectra are more dominated by the nucleus which tends to have a more complex dust continuum.

In this chapter I present a new model, where the continuum is generated using a generalised differential extinction model to fit combined NIRSpec and MIRI MRS spectra from 1.5 μm to 28 μm of 4 local LIRGs, where the continuum from dust of different temperatures is subject to different levels of extinction. The structure of this Chapter is as follows. I first describe the model in detail in Section 4.3. I then test the model with simulated data in Section 4.4 to verify the model before applying it to JWST data in Section 4.2. Subsequently I compare the dust extinction model with other tracers of extinction, namely the stellar continuum, Hydrogen recombination lines and H_2 lines for the 4 LIRGs observed with NIRSpec and MIRI MRS and discuss the inferred dusty structure in Section 4.7.

4.2 Observations

4.2.1 Targets

In this Chapter I use NIRSpec-IFS and MIRI MRS data from Director's Discretionary Early Release Science Program 1328 (PI: Lee Armus & Aaron Evans) of four local LIRGs, namely NGC 7469, NGC 3256, IIZw96 and VV 114. The NIRSpec-IFS data were taken with the high spectral resolution of $R \sim 2700$, with all four of the disperser/grating combinations, namely, G140H/F070LP, G140H/F100LP, G235H/F170LP, G395H/F290LP. RGB NIRCam images are shown in Fig. 4.1 for the 4 galaxies, with the F120W, F200W filters tracing stellar continuum and the F335M/F356W filters tracing the 3.3 μm PAH emission. The fully reduced files for the NIRCam imaging were downloaded from the MAST archive.

NGC 7469 is a barred spiral galaxy hosting a type 1 AGN (Osterbrock and Martel, 1993) with a compact nuclear starburst and starburst ring (Díaz-Santos et al., 2007; García-Bernete et al., 2022c; Lai et al., 2022; Lai et al., 2023). The AGN drives a wide, highly ionised outflow towards the SE (García-Bernete et al., 2022c; U et al., 2022; Bianchin et al., 2023), coinciding with a gap in the star-forming ring. This object has been subject to much analysis of the PAH population with JWST (e.g. García-Bernete et al., 2022c; Zhang and Ho, 2023b; Lai et al., 2023).

NGC 3256 is a late-stage merger consisting of a face-on spiral galaxy (NGC 3256 N Sakamoto et al., 2014) with a bright nuclear starburst (Lira et al., 2008). The southern component of the merger (NGC 3256 S) is an edge-on galaxy hosting a highly obscured, Compton Thick AGN (Ohyama et al., 2015) which drives a highly collimated outflow (Sakamoto et al., 2014; Pereira-Santaella et al., 2023).

VV114, as discussed in detail in Chapter 3, is a mid-stage major merger (Stierwalt et al., 2013) where the eastern component appears extremely dusty outputting a large infrared luminosity (Armus et al., 2009). The region is complex, with multiple nuclei and a large scale shock resulting from the interaction (Saito et al., 2017; Donnan et al., 2023b; Rich et al., 2011; Rich et al., 2023; González-Alfonso et al., 2024; Buiten et al., 2023).

Finally, IIZw96 is also a major merger, with a dusty eastern region consisting of numerous compact, dusty star-forming clumps (Inami et al., 2010; Inami et al., 2022a), separate from the two main nuclei of the interacting galaxies. The SW nucleus is thought to host a buried AGN from modelling IR rovibrational lines of the molecular bands (García-Bernete et al., 2024a).

4.2.2 Data Reduction

The MIRI data was reduced by Miguel Pereira-Santaella, using the standard MRS pipeline, v 1.9.4, (Labiano et al., 2016) up to the stage 2 data, using the 1041 calibration context. In addition to the fringe correction applied during the Spec2 pipeline, the additional residual fringe correction was applied offline before the Spec3 pipeline. An additional step was introduce to remove bad pixels still present

in the data. This was done by first generating background frames to determine the mean flux for every wavelength channel. Any pixel that deviated more than $\pm 6\sigma$ from the mean flux was masked before linearly interpolating to recover the flux of the masked pixel. Linear interpolation was only done if the SNR>30. The Spec3 pipeline was then run without the background subtraction which produces both science cubes and background cubes. The background subtraction was then performed afterwards by calculating the median flux in each background frame before subtracting it from the science cubes.

The NIRSpec-IFS data were reduced by Ismael Garcia-Bernete using pipeline version 1.9.4 with the 1063 calibration context files. The uncalibrated level 1 data was downloaded from the MAST archive. These were then processed using the detector1 pipeline to produce count rate files. The pipeline struggled to remove bad pixels in the data and so during this stage, bad pixels were masked by interpolating based on the neighbouring pixels. The count rate files were then calibrated using the Spec2 pipeline which includes the flat-fielding, flux calibration and world coordinate system (WCS) calibration. The data cubes were then build using the Spec3 pipeline.

All the cubes produced are in the IFU alignment, which means the spatial axes are aligned with the position angle of the telescope when the observations were taken. I extract the spectra with this alignment and only rotate into the sky orientation (north is up, east is left) when plotting to reduce any further errors that may be introduced when reprojecting the data.

I extract spectra of each target through a 0.3" radius aperture. To ensure the region is identical between the sub-channels I correct for small spatial misalignments due to errors in the astrometry. I do this by measuring the position of the aperture I wish to extract the spectrum from, relative to the brightest point source in the data. Measuring relative positions to a point source avoids re-sampling the entire cube which may introduce further errors into the data. After extraction of the spectra, I run an additional residual fringe correction on the 1D spectra to remove the remaining fringing. Additionally, a PSF wavelength dependent correction factor was used for a point-like extraction for the nuclear apertures (Pereira-Santaella

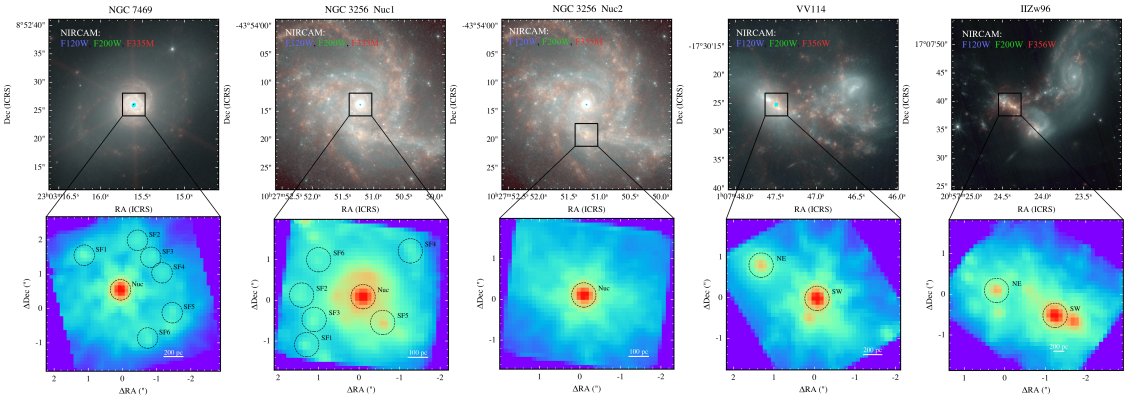

Figure 4.1: Images of the 4 LIRGs used in this work and the apertures used to extract the spectra. The upper panels show RGB images with NIRCam. The F335M/F356W filters (red) show the 3.3 μm PAH emission while the F120W and F200W filters mainly trace stellar continuum. Most of the nuclei show some saturation at the brightest points in the NIRCam imaging, but this is not present in the NIRSpec data. The field of view of the NIRSpec data is shown by the black box. The lower panels show the integrated NIRSpec detector 2 G395H/F290LP channel, integrated between 4.08 - 5.27 μm, tracing continuum (stellar and/or dust). The apertures used in this work to extract the spectra are shown and labelled. Each aperture has a radius of 0.3" and those labelled SF do not have any PSF correction applied as their emission appears extended.

et al., 2022; García-Bernete et al., 2022c; Donnan et al., 2023b). This was obtained using a standard star for both NIRSpec and MIRI where the PSF correction factor is calculated as the ratio of the spectrum within 0.3" to the total spectrum as obtained from CALSPEC (Bohlin et al., 2014; Bohlin and Lockwood, 2022). For NIRSpec I use TYC 4433-1800-1 while for MIRI I use HD 163466.

To estimate errors for the fluxes at each wavelength I avoided those generated by the pipeline for the MIRI data as I found them to be underestimated. Instead I used the dedicated background exposures and calculate the rms in each frame. For the NIRSpec data, I found the data reduction process described previously, produced reasonable errors for the purpose of this work.

Fig. 4.1 shows the positions of the apertures used in this work for each object. I extract six star-forming regions from each of NGC 7469 and NGC 3256, chosen based on near-IR bright regions. For NGC 7469, SF2, SF3 and SF4 lie on the redshifted region of the nuclear outflow (García-Bernete et al., 2022c; U et al., 2022; Bianchin et al., 2023) while a nuclear bar extends (see Fig. 10 of Díaz-Santos et al. (2007)) from SF1 to the southwest.

For IIZw96 SW (south-west), there is a secondary nucleus to the west, with a very small separation. At long wavelengths, the PSFs of each source overlap, leading to contamination. To mitigate this effect I extract the spectra of each nucleus, applying the aperture correction as discussed above. I then extract a total spectrum using a 0.6" aperture centred on the midpoint between the two nuclei. For this aperture I also apply a PSF correction factor by calculating the flux loss within a 0.6" aperture centred between two standard stars. I find the sum of the individual nuclei spectra to be larger than the 0.6" total spectrum, particularly at long wavelengths, due to contamination by each of the nuclei. To correct the SW (south-west) nuclear spectrum, I subtract a fraction of the excess flux (where excess = sum of the nuclei - total), where the fraction is the contribution of the second nuclei to the sum of the nuclei. I find the correction to be small but significant at long wavelengths. For reference this is shown in Appendix A.3.2.

4.3 Model

In this section I will describe the fitting procedure, starting with the simplest extinction model and building up to the differential extinction model.

The simplest way to predict the observed spectrum of a galaxy, f_ν, is to model the intrinsic spectrum, $f_\nu^{\rm Int}$, with a sum of modified blackbodies in the infrared, which is then subject to a single screen of extinction of the form

$$\frac{f_\nu}{f_\nu^{\rm Int}} = e^{-\tau_{9.8}\tau(\lambda)} \tag{4.1}$$

where $\tau(\lambda)$ is an assumed extinction law that is normalised to 1 at 9.8 μm. The level of extinction is then controlled by the optical depth at 9.8 μm, $\tau_{9.8}$, which scales the extinction law to increase the extinction. This is equivalent to A_V, which is often used for rest-frame UV/optical data. For reference $\tau_{9.8} \sim 0.1 A_V$ (Draine, 1989). While mathematically simple, the screen geometry is not well physically motivated, as the obscuring dust and source dust are assumed to be separate, where the obscuring dust does not emit. I demonstrate this in the top panel of Fig. 4.2, where one requires the obscuring dust to not emit while the emitting dust does not obscure.

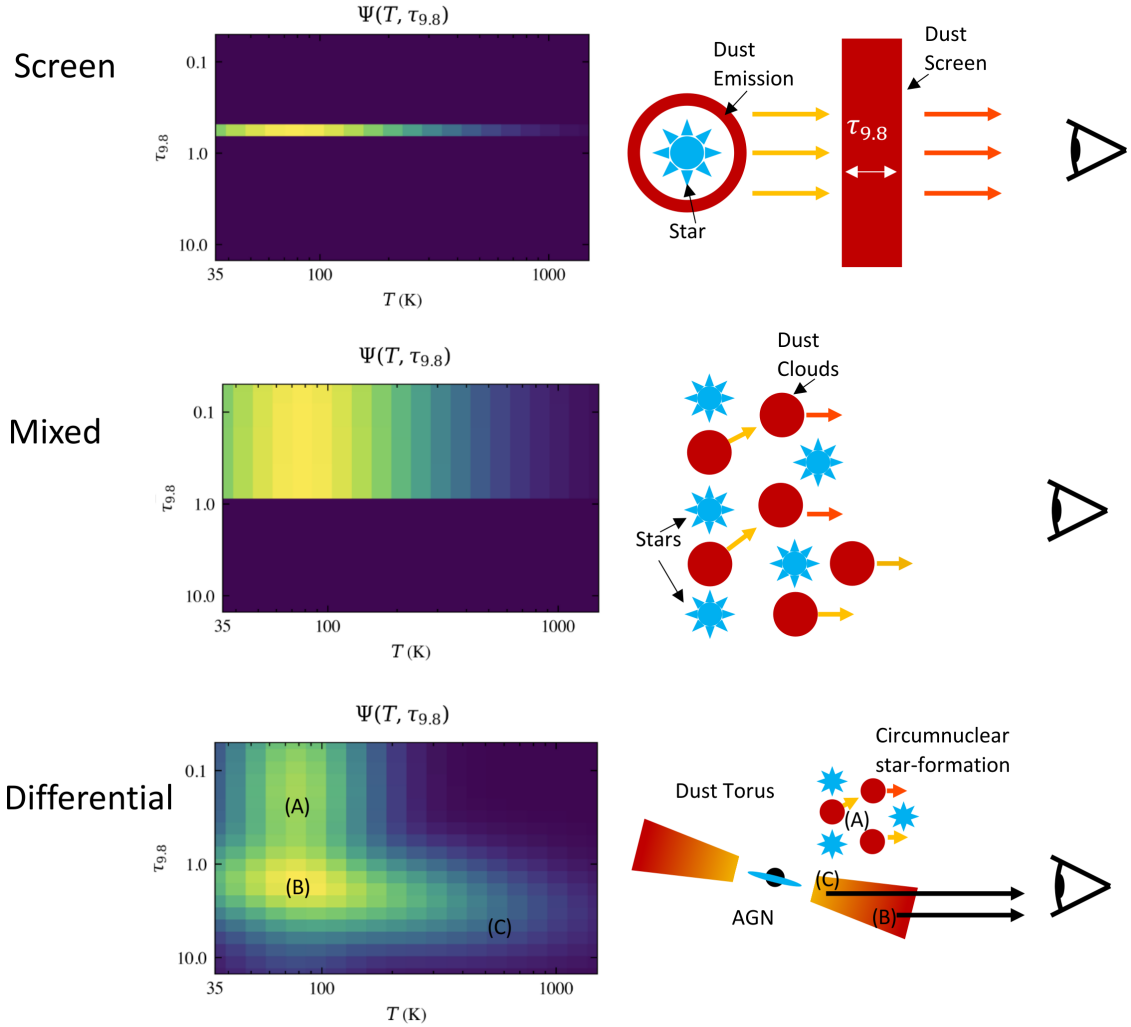

Figure 4.2: Diagrams demonstrating three different dust geometries discussed in this work. The left panels show the dust distribution, $\Psi\left(T, \tau_{9.8}\right)$, defined in section 4.3.1, corresponding to the geometry in the right panels. In each case the observer is on the right. The differential case is just one example where differential extinction is present.

Alternatively, one can assume a mixed geometry where the emitting and obscuring dust is uniformly mixed (Smith et al., 2007b), which has the form

$$\frac{f_\nu}{f_\nu^{\rm Int}} = \frac{1 - e^{-\tau_{9.8}\tau(\lambda)}}{\tau_{9.8}\tau(\lambda)}. \tag{4.2}$$

This is more physically motivated for star-forming regions compared to a simple screen, as demonstrated in Fig. 4.2. In this scenario, there is emission from dust at different obscurations up to a limit of $\tau_{9.8}$. One may imagine a star-forming region where the emission from the outside of the dust cloud is unobscured while emission from within is more obscured. However in this scenario one would expect the more

obscured emission to be hotter, where the newly born stars heat the dust, whereas the mixed model still assumes the same temperature distribution at each obscuration.

These simple approaches tend to fail when modelling highly obscured galaxies, particularly over a long wavelength range, where the emergent spectrum at < 5 μm may originate from a much less obscured environment (with a different intrinsic spectrum) compared to longer wavelength emission. A simple solution is to model two components, a relatively unobscured star-forming component and an obscured nucleus, such as that implemented in PAHDecomp (Donnan et al., 2023a), described in Chapter 2. This is also the approach of Hernán-Caballero et al. (2016) and references therein. This however does not work for sources where there may be varying degrees of extinction as different layers are probed as a function of wavelength. An example where such a geometry may be present is shown in the lower panel of 4.2. In this example, the continuum in the observed spectrum is the combination of dust from an edge-on AGN torus, where there is hot obscured dust, cooler less obscured dust and circumnuclear star-formation. Therefore in order to be able to fit the spectrum of any (U)LIRG, a flexible/general model is required to capture "differential extinction". This is described in detail in Section 4.3.1.

In addition to the differential extinction model for the continuum emission, I model the PAH emission features following a similar procedure to that of PAHFIT (Smith et al., 2007b) and include additional molecular absorption features (Imanishi et al., 2010; Lai et al., 2020; Lai et al., 2023). The full model, f_ν, is given by

$$f_\nu = \sum_{i=1}^{N_{\rm PAH}} I^{(i)}_{\nu,{\rm PAH}}(\lambda) + C_\nu e^{-\tau_{\rm ices(Dust)}(\lambda)} + S_\nu e^{-\tau_{\rm ices(Stellar)}(\lambda)} \tag{4.3}$$

where the first term is a sum over $N_{\rm PAH}$ PAH profiles $I_{\nu,{\rm PAH}}(\lambda)$ and the second is the total continuum comprising of the dust model incorporating differential extinction, C_ν, defined in section 4.3.1, and a stellar continuum, S_ν, both of which are subject to screen extinction of the following absorption features. For the dust continuum I include absorption from water ice at ~ 3 μm and 6μm, CO_2 at 4.0 μm and CH at $\sim 7\mu$m while for the stellar continuum I only apply the near-IR

absorption features of water ice at ~ 3 μm and CO_2 at 4.0 μm. These are described in detail in the following sections.

I show five examples of fits with this model to a variety of spectra in Fig. 4.3 to demonstrate the ability to fit a range of different objects with varying obscuration, where the components comprising the model in equation 4.3 are shown.

To fit this model to data I use a Bayesian approach, where I maximise the following log probability

$$\ln \text{Prob} = -\chi^2 - \sum \ln \sigma^2 - \Gamma P + \text{const.}, \tag{4.4}$$

where χ^2 is simply the sum of the squared normalised residuals between the model and the data, σ is the data error bars, and P is a penalty for complex models of the dust distribution, scaled by a regularisation scale, Γ. This factor controls the level of regularisation, where a larger value increases the penalty for non-smooth dust distributions. This term is described in detail in Section 4.3.1.

4.3.1 Continuum

Differential Extinction

A general model of dust emission and extinction can be written as a 2D weighted average of modified blackbodies, $\epsilon_\nu B_\nu$, and screens of extinction, $e^{-\tau_{9.8}\tau(\lambda)}$, where the weights are parametrised by a 2D distribution, $\Psi(T, \tau_{9.8})$, of dust temperature, T, and extinction, $\tau_{9.8}$. The modified blackbodies are given by the product of the Planck function, $B(T)$, and a wavelength dependent emissivity term, ϵ_ν. The dust continuum is therefore given by

$$C_\nu(\lambda) = A \int_0^\infty \int_{35\text{K}}^{1500\text{K}} \Psi\left(T, \tau_{9.8}\right) e^{-\tau_{9.8}\tau(\lambda)} \frac{\epsilon_\nu B_\nu(T, \lambda)}{B_0(T)} dT d\tau_{9.8}, \tag{4.5}$$

where the sum of the weights, $\Psi(T, \tau_{9.8})$, is unity and $B_0(T)$ is a normalisation factor for each modified blackbody. I choose $B_0(T)$ to be the integrated flux between 1.5μm and 28μm with some emissivity, ϵ_ν. I do not consider temperatures below 35K as dust this cold will not contribute significantly to the flux below 30 μm. I use a maximum temperature of 1500K as this is approximately the

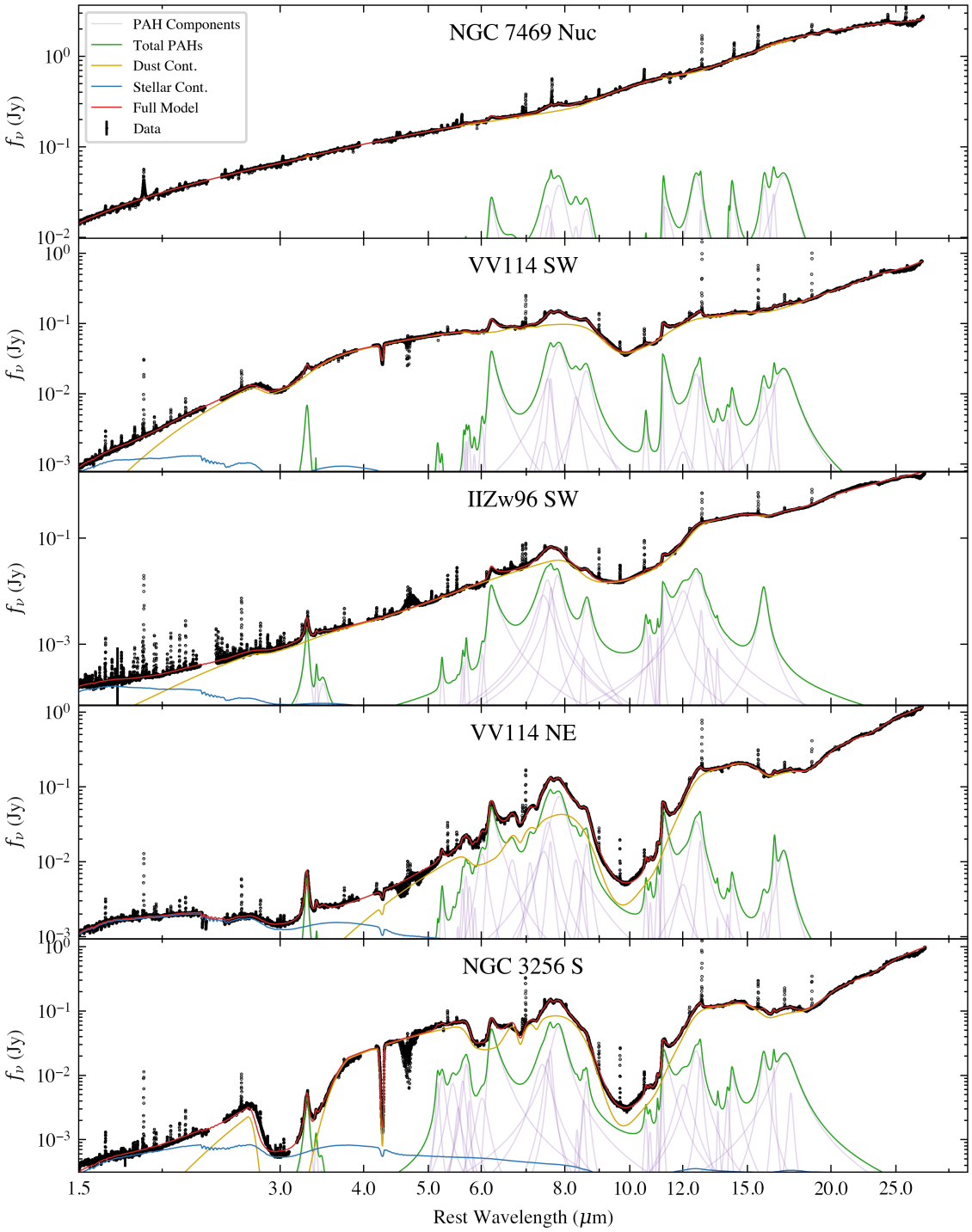

Figure 4.3: Five examples of fits to combined NIRSpec and MIRI spectra for different types of nuclei. From top to bottom is NGC 7469 (type 1 AGN - see Section 4.7.4), VV114 SW (Potential Type 2 AGN (Rich et al., 2023) - see Section 4.7.4), IIZw96 SW (Obscured AGN (García-Bernete et al., 2024a) - see Section 4.7.4), VV114 NE (Obscured AGN (Donnan et al., 2023b) - see Section 4.7.4) and NGC 3256 S (Type 2 (Compton Thick) AGN (Ohyama et al., 2015) - see Section 4.7.4). Note the CO band at ~ 4.6 μm is masked in the fitting.

average dust sublimation temperature for a mix of silicate and graphite grains (Kishimoto et al., 2007).

In this work I assume a fixed extinction law, $\tau(\lambda)$, using that presented in Donnan et al. (2023b) and in Chapter 3 and Appendix A.2.1, which consists of a power law and absorption from silicates at ~ 9.8 and ~ 18 microns. I choose this law as the silicate features include absorption from crystalline features, necessary for highly obscured spectra (Spoon et al., 2022; Donnan et al., 2023b). As the weighted average describes only the shape of the model, the entire continuum is scaled by a factor A to match the data.

In the simplest case where there is a single screen of extinction, the dust distribution has a form

$$\Psi(T, \tau_{9.8}^{'}) = \rho(T)\delta\left(\tau_{9.8}^{'} - \tau_{9.8}\right), \tag{4.6}$$

where $\rho(T)$ describes the distribution of blackbodies of different temperatures (see Fig. 4.2). The single screen is represented by a Dirac delta function which simplifies the integral into

$$C_\nu(\lambda) = e^{-\tau_{9.8}\tau(\lambda)} \int_{35\mathrm{K}}^{1500\mathrm{K}} \rho(T) \frac{\epsilon_\nu B_\nu(T, \lambda)}{B_0(T)} dT \tag{4.7}$$

where the observed continuum, $C_\nu(\lambda)$, is the intrinsic multiplied by a factor of $e^{-\tau_{9.8}\tau(\lambda)}$, recovering equation (4.1).

For the mixed case there is a uniform dust distribution between 0 and $\tau_{9.8}$ (see Fig. 4.2):

$$\Psi(T, \tau_{9.8}^{'}) = \rho(T) \begin{cases} \frac{1}{\tau_{9.8}} & 0 \leq \tau_{9.8}^{'} \leq \tau_{9.8} \\ 0 & \text{otherwise} \end{cases} \tag{4.8}$$

which simplifies the integral to

$$C_\nu(\lambda) = \frac{1 - e^{-\tau_{9.8}\tau(\lambda)}}{\tau_{9.8}\tau(\lambda)} \int_{35\mathrm{K}}^{1500\mathrm{K}} \rho(T) \frac{\epsilon_\nu B_\nu(T, \lambda)}{B_0(T)} dT, \tag{4.9}$$

where the observed continuum is the intrinsic continuum multiplied by a factor $\frac{1-e^{-\tau_{9.8}\tau(\lambda)}}{\tau_{9.8}\tau(\lambda)}$, recovering equation (4.2). This is the original PAHFIT model (Smith

et al., 2007b), where the amplitude of different blackbodies is allowed to vary, comprising $\rho(T)$, and is then subject to the extinction factor.

To implement the differential extinction model, instead of fixing the dust distribution, $\Psi(T, \tau_{9.8})$, I constrain the distribution from the data by fitting the continuum with a flexible model for $\Psi(T, \tau_{9.8})$. I do this under some prior restrictions, to prevent nonphysical solutions for $\Psi(T, \tau_{9.8})$, by ensuring the distribution is smooth and only applies differential extinction when necessary to fit the data.

To implement this model one could choose a parametric form of $\Psi(T, \tau_{9.8})$ such as a 2D Gaussian or a 2D Lorentzian, however there is no obvious/physically motivated choice for the form of this distribution. Assuming a given parametric form may therefore bias the results. I therefore opt for a non-parametric approach where I bin $\Psi(T, \tau_{9.8})$ into a 20x20 grid and allow each grid element to vary individually. This approach is similar to the stellar population modelling of pPXF (Cappellari, 2023), where a non-parametric 2D distribution of stellar metalicity and age is used to generate the model continuum.

I choose the grid carefully to ensure that each grid element gives a similar weight to the continuum. I bin $\tau_{9.8}$ into 20 evenly spaced values in natural log space between, $\tau_{9.8} = 0.05$ and $\tau_{9.8} = 15$. By binning in ln space, I am evenly sampling different screens of extinction of the form $e^{-\tau_{9.8}\tau(\lambda)}$. For the temperature axis I bin in $\log_{10}$ space between 35K and 1500K. To ensure each grid element has equal weighting when fitting, I normalise the spectrum of each grid element by the integrated flux over the wavelength range of the data. After fitting, I re-scale each grid element such that the normalisation matches that in equation 4.5 to obtain the $\Psi(T, \tau_{9.8})$ in that equation.

The wavelength dependent extinction factor is given by the ratio of the observed to the intrinsic continuum such as those shown in equation (4.1) and (4.2) for the screen and mixed cases respectively. From the model, the intrinsic continuum is defined as

$$f_\nu^{\rm Int} = S_\nu^{\rm Int} + A \int_0^\infty \int_{35{\rm K}}^{1500{\rm K}} \Psi(T, \tau_{9.8}) \frac{\epsilon_\nu B_\nu(T, \lambda)}{B_0(T)} dT d\tau_{9.8}, \tag{4.10}$$

where $S_\nu^{\rm Int}$ is the stellar population model defined in equation (4.14). From this I calculate the wavelength dependent extinction factor

$$\frac{f_\nu}{f_\nu^{\rm Int}} = \frac{S_\nu + C_\nu}{f_\nu^{\rm Int}} \tag{4.11}$$

where S_ν and C_ν are defined in equations (4.5) and (4.14) respectively while $f_\nu^{\rm Int}$ is given above. In general $\frac{f_\nu}{f_\nu^{\rm Int}} \neq e^{-\tau_{9.8}\tau(\lambda)}$, as this only holds for a single screen geometry. Rather, the extinction factor depends on the inferred $\Psi\left(T, \tau_{9.8}\right)$ and therefore can vary between objects. For example, if there is a buried hot dust component compared to the cool dust, the extinction factor will drop at $\sim$ 5 μm compared to long wavelengths. This is demonstrated with simulated data in Section 4.4.

Regularisation

Allowing each grid element to vary on a 20x20 grid, effectively adds 400 parameters to the model (typical NIRSpec+MIRI spectra contain thousands of data points). This provides the flexibility to fit complex, obscured galaxy spectra, however the best fit solution for $\Psi\left(T, \tau_{9.8}\right)$ may not be physically meaningful with so many parameters. While I find MCMC sampling returns reasonably smooth solutions compared to a simple maximisation of the ln Prob (equation (4.4)), I introduce some additional regularisation to favour solutions where the distribution is simple/smooth.

I follow the approach of Cappellari (2017) and Cappellari (2023) where I add a penalty factor to the log-likelihood to disfavour complex models of $\Psi\left(T, \tau_{9.8}\right)$. In particular I use the sum of the Laplacian for each row and column of Ψ:

$$P = \int_0^\infty \int_{35\rm K}^{1500\rm K} \Psi''\left(T, \tau_{9.8}\right) dT d\tau_{9.8} = \sum_i \left(\Psi_{i-1,j} - 2\Psi_{i,j} + \Psi_{i+1,j}\right)^2 + \sum_j \left(\Psi_{i,j-1} - 2\Psi_{i,j} + \Psi_{i,j+1}\right)^2 \tag{4.12}$$

where the integral of the 2$^{\rm nd}$ derivative of Ψ is calculated numerically on the 20x20 grid in each axis as shown by the second line of the equation. This factor must scale with the number of data points to be comparable to the other terms in equation (4.4). I therefore choose $\Gamma = 1000N$, where there are N data points in a given spectrum.

In addition to the preference for smooth solutions, I include additional regularisation on the "effective" $\tau_{9.8}$ as function of wavelength. During the fit, the effective $\tau_{9.8}$ is calculated for 20 wavelength bins across the spectrum, evenly spaced in $\log_{10}\lambda$. This is done by computing the extinction factor ($f_\nu^{\rm Obs}/f_\nu^{\rm Intr}$) at each wavelength bin and converting to an effective $\tau_{9.8}$ where $\tau_{9.8}^{\rm Eff} = -\ln\left(f_\nu^{\rm Obs}/f_\nu^{\rm Intr}\right)$ at 9.8 μm. $\tau_{9.8}^{\rm Eff}$ is then converted into units to match the grid elements of $\Psi\left(T, \tau_{9.8}\right)$, such that I am smoothing in steps of $e^{-\tau_{9.8}}$. I then place a Gaussian prior on the differences between successive $\tau_{9.8}^{\rm Eff}$ with a mean of zero and a standard deviation of 6 grid elements. I chose this prior to be wide such as to not limit the inference on $\Psi\left(T, \tau_{9.8}\right)$, but restrictive enough to prevent the model fitting for differential extinction where it is not needed. Therefore this prior ensures that the fit defaults to no differential extinction and only deviates from this when necessary to fit the data.

Emissivity

The shape of the blackbody profile for a given temperature, T, is modified by an emissivity factor, ϵ_ν. Typically this factor takes the form of a power law

$$\epsilon_\nu \propto \lambda^{-\gamma}, \tag{4.13}$$

with values of $\gamma = 1.5 - 2$. Codes such as PAHFIT (Smith et al., 2007b), adopt $\gamma = 2$, however this approach does not account for silicates, which contribute significantly in the mid-infrared (Li and Draine, 2001). Adopting a more physically motivated emissivity that includes silicates (as well as graphite grains), results in a more realistic spectrum including intrinsic silicate emission at 9.8 μm and 18μm (Li and Draine, 2001; Draine and Li, 2007; Marshall et al., 2007). However, silicate emission is mainly observed in type 1 AGN (Gallimore et al., 2010; García-Bernete et al., 2017; Martínez-Paredes et al., 2020; García-Bernete et al., 2022c), where lines of sight of hot silicates, heated by the black hole accretion disk, are visible without a significant hot background source, requiring clumpy or low-inclination tori. In star-forming regions, the continuum is typically flat or shows moderate silicate absorption. To achieve such a continuum with intrinsic silicate emission

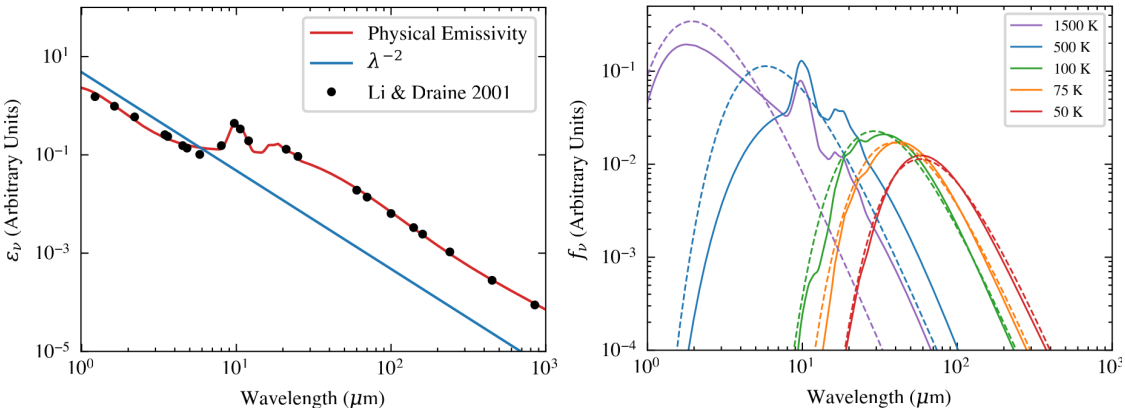

Figure 4.4: Left: Emissivity used to modify the intrinsic blackbody dust emission. The blue line shows a simple power law with index $\gamma = 2$. The black points are taken from Table 6 of Li and Draine (2001) and include silicate & carbon grains. The red line shows the physical emissivity profile (including silicates) based on these points by fitting a polynomial and a silicate template. **Right:** The corresponding modified blackbodies with the physical emissivity (solid lines) and the power law emissivity (dashed lines), at various temperatures.

requires either a cool dust temperature, where the silicates contribute less and/or extra extinction to compensate. The problem is therefore degenerate from an observational perspective, as the observed continua for star-forming regions can be reproduced by either the power law emissivity or a physically motivated emissivity.

In this work I explore both possibilities, starting with the simple power law with $\gamma = 2$ and then with a emissivity following the curve presented in Table 6 of Li and Draine (2001). To adjust to the spectral resolution of JWST, I fit these points with a polynomial and the empirical silicate templates in Donnan et al. (2023b). This is shown in the left panel of Fig. 4.4 in comparison with the simple power law. I also show the resulting modified blackbodies in the right panel of Fig. 4.4, where the silicate emission is present at high temperatures with the physical emissivity (where silicates are included).

4.3.2 Stellar Continuum

In addition to the dust continuum, stellar emission will dominate below 3 μm. Fitting the stellar component is critical to constraining any possible contribution from hot dust, $T \sim 1000K$, at around ~ 5 μm where the inclusion of NIRSpec-IFS at a high spectral resolution of $R \sim 2700$ to provide data at < 5 μm provides strong

constraints on the stellar contribution. Particular features of stellar continua can be seen such as the CO band heads from stellar atmospheres at ~ 2.2 μm.

To model the stellar continuum I use two templates with ages of 10 Gyr and 100 Myr, at solar metallicity, provided by FSPS (Conroy et al., 2009; Conroy and Gunn, 2010), with a Salpeter (1955) Initial Mass Function (IMF). At wavelengths > 1 μm, the stellar continuum is dominated by more evolved stellar populations in LIRGs (Gonzále Delgado et al., 2010; Giovannoli et al., 2011; Pereira-Santaella et al., 2015), despite these galaxies being highly star-forming. Indeed those works showed that the optical spectra is dominated by a young stellar population (10-1000 Myr) but that an evolved population does exist and contributes very little to the optical. However at wavelengths $> 1\mu$m, the evolved population dominates and so I chose a 10 Gyr and a 100 Myr template to reproduce the near-infrared stellar continuum. I find these provide a reasonable stellar continuum without doing a full stellar population model, which would be beyond the scope of this work. Such work would involve optical data at a similar angular resolutions, such as from MUSE (e.g. Perna et al., 2022), to properly constrain the contribution from young, newly formed stars.

I allow each template to be scaled individually to allow different combinations of young/older populations which relates to the star-formation history. The scaled sum of the templates is subject to its own screen of extinction, constrained by the shape of the spectrum at ~ 1.5 - 2 μm. Therefore the stellar component is simply

$$S_\nu = e^{-\tau_{9.8}\tau(\lambda)} S_\nu^{\rm Int}, \tag{4.14}$$

where $S_\nu^{\rm Int}$ is the sum of each template scaled by its corresponding scale factor.

4.3.3 Ices

In addition to the extinction present in the dust model, there are absorption features from H_2O ice, CO, CO_2 and aliphatic CH present in the spectrum as seen in equation (4.3). To account for this, I generate templates of the optical depth from highly obscured sources and apply them as a screen to the continuum. The templates for the mid-IR water ice and CH features at ~ 6 μm are taken from Donnan et al.

(2023a), which were generated from Spitzer IRS spectra of the deeply embedded source, NGC 4418 (García-Bernete et al., 2024c). I find the low resolution Spitzer data is sufficient to generate a template for fitting the data as these features are broad. However, the near-IR water ice at $\sim$ 3 μm and CO_2 at $\sim$ 4.2 μm were generated using the NIRSpec spectrum of the southern nucleus of NGC 3256. This was necessary in order to create a reliable template as the depth of this feature, with the high signal to noise of NIRSpec, much better captures the shape compared to Akari data and the higher spatial resolution better isolates the nucleus.

I do this by first creating a local continuum using a cubic spline with anchor points at [2.5, 2.6, 2.65, 3.8, 4.18, 4.48, 4.82, 4.95] μm. This is shown in red in the left panel of Fig. 4.5. I calculate an optical depth curve, $\tau_{\rm ices}(\lambda)$, using this local continuum, $C_{\rm local}$ where

$$\tau_{\rm ices}(\lambda) = \ln\left(f_{\rm data}/C_{\rm local}\right) \tag{4.15}$$

with $f_{\rm data}$ as the spectra. I mask the main emission features before computing equation (4.15), most notably the 3.3 μm and 3.4 μm PAH features. This results in the black points in the right panel of Fig. 4.5. To convert this into a usable template I simply smooth the data for the CO_2 feature. For the broad water ice feature I fit two $5^{\rm th}$ order polynomials to each side of the feature.

I do not create a template for the CO features at $\sim$ 4.6 μm as this band consists of a variety of absorption/emission features which will change shape from object to object and thus requires more complex modeling (Pereira-Santaella et al., 2023; González-Alfonso et al., 2024; García-Bernete et al., 2024a; Buiten et al., 2023). I therefore mask this region during the fitting process. However I find the extrapolated best fit continuum over this region provides a good fit to an underlying continuum (e.g. see Fig. 4.3).

I apply the near-infrared ices, namely the $\sim$ 3 μm water ice and CO_2 at $\sim$ 4.2 μm, to both the dust continuum and the stellar continuum. For both continua, the depth of the $\sim$ 3 μm water ice and the CO_2 feature are allowed to vary independently. Moreover, the depths of each feature are not necessarily the same

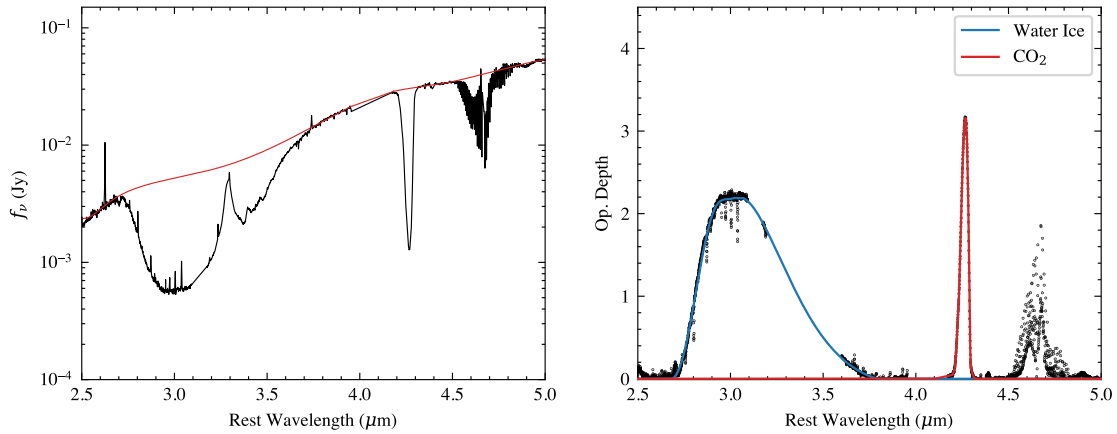

Figure 4.5: Generation of water ice and CO_2 templates from the southern nucleus of NGC 3256. **Left:** NIRSpec spectrum between 2.5 and 5 μm shown in black. The red line shows a local spline continuum, masking the main absorption features of water ice, CO_2 and CO. **Right:** Optical depth curve of the absorption features using the local continuum in the left panel and masking the main emission features in the data. The blue line shows the generated template for water ice, created using two 5^{th} order polynomials for each side of the feature. The CO_2 template in red was generated by smoothing the data. I avoid generating a template for the CO feature and simply mask this region of the spectrum in the fitting.

for each continuum as a highly obscured AGN, such as NGC 3256 S, shows much deeper ices than typical stellar continua from star-forming regions. Therefore to obtain an adequate fit for NGC 3256 S, I indeed require different optical depths for the ices applied to the stellar vs dust continuum. This can be seen in the lower panel of Fig. 4.3. I therefore allow the optical depth of the near-IR ices to vary separately as seen in equation (4.3).

For most cases, there is not enough information present in the data to constrain each component separately (unlike NGC 3256 S), as the continuum is either dominated by the stellar component or dust component rather than both. I therefore I place a Gaussian prior that the depth of the ices is the same for the dust and stellar continuum, such that these are only separate components when necessary to fit the data. The prior is on the ratio of the two components with a mean of 1 and a standard deviation of 0.2, such that $\pm 5\sigma$ varies between zero and two.

4.3.4 PAH Profiles

I model the PAH features with a series of Drude profiles, following the original approach of Smith et al. (2007b). As discussed in Donnan et al. (2023b), I add additional profiles to be able to fit the higher spectral resolution data from JWST, where more substructure within the features is visible. To fit the NIRSpec portion of the spectra, I follow Lai et al. (2020), where the original PAHFIT was extended to fit AKARI data.

In chapter 3, I used four Drude profiles to model the 11.3 μm feature to better capture the feature's shape. In this chapter I take a different approach, where I model asymmetric PAH features by introducing an asymmetry parameter to a single Drude profile to better capture the shape of the feature with fewer parameters than summing multiple components. This is applied to the 3.3, 3.4, 5.2, 6.2, 11.0, 11.3, 13.55 and 14.2 μm PAH profiles. I follow the approach of Gordon et al. (2021) and Stancik and Brauns (2008) where I introduce a parameter, a, into the following equation

$$I_{\nu,\mathrm{PAH}}(\lambda) = A\frac{(\gamma/\lambda_0)^2}{(\lambda/\lambda_0 - \lambda_0/\lambda)^2 + (\gamma/\lambda_0)^2} \tag{4.16}$$

where the original FWHM γ_0 is modified

$$\gamma = \frac{2\gamma_0}{1 + e^{a(\lambda-\lambda_0)}} \tag{4.17}$$

where A is the amplitude and λ_0 is the central wavelength.

Similar to previous iterations of PAHFIT, I restrict the width, centre and now the asymmetry parameters to a small range of values to prevent additional degeneracies.

For the majority of the features the asymmetry is simply turned off. A full list of these parameters can be found in Table. A.2. The individual Drude profiles can be seen in Fig. 4.3 for some example fits with the model.

I have additionally added some restrictions to the relative strengths of certain PAH features. In particular, the less prominent PAH features, such as those between the 6.2 μm and 7.7 μm cannot be too large relative to the 6.2 μm and 7.7 μm PAHs. This is to prevent these PAHs fitting the continuum when the PAH emission is weak.

I therefore place the following restrictions on the integrated PAH flux between certain limits: PAH[6.6, 7.3]/PAH[6.0, 6.5] $<$ 1.0, PAH[6.6, 7.3]/PAH[7.4, 8.2] $<$ 0.25, PAH[12.3, 13.0]/PAH[11.7, 12.2] $<$ 2.8, PAH[11.7, 12.2]/PAH[11.2, 11.5] $<$ 1.0, PAH[10.0, 11.1]/PAH[11.2, 11.5] $<$ 0.4, where the values in the square brackets denote the integration limits. These were chosen based on the star-forming spectra from NGC 3256 and NGC 7469, where the PAH features are bright and well resolved.

4.3.5 Emission Lines

In the Spitzer era it was possible to model emission lines with simple Gaussian profiles (Smith et al., 2007b). This was necessary, not only to obtain fluxes for each line but to properly decompose lines that may be blended with PAH features. This was particularly important for the 12.7 μm PAH feature which was heavily blended with the strong [Ne II] line at 12.81 μm.

An early modified version of PAHFIT for MIRI/MRS data was presented in Chapter 3, (also used in García-Bernete et al., 2022a) which modelled each line with a 2 component profile to capture the more complex line profile observed with the significantly higher spectral resolution of MIRI/MRS (R $\sim$ 1500 - 3500) over Spitzer/IRS data (R $\sim$ 500) (Labiano et al., 2021). Considering the abundance of lines now detected in typical MIRI MRS spectra (Pereira-Santaella et al., 2022; García-Bernete et al., 2022c; U et al., 2022; Lai et al., 2022; Armus et al., 2023; Donnan et al., 2023b; Rich et al., 2023; Young et al., 2023), and the number of parameters required per line to capture the profile, this approach is extremely inefficient. Fortunately, the high spectral resolution means that blending of emission lines and PAH features is no longer an issue as the narrow widths of the emission lines makes them easily distinguishable from the much broader PAH features. I therefore simply mask the emission lines where they are detected in the spectra, and integrate using the model subtracted data to obtain the corresponding line fluxes.

For some emission lines, particular those with low signal to noise, the model subtracted data may contain some residuals which when integrated, will cause inaccurate flux measurements. This is particularly relevant if the line is faint. An

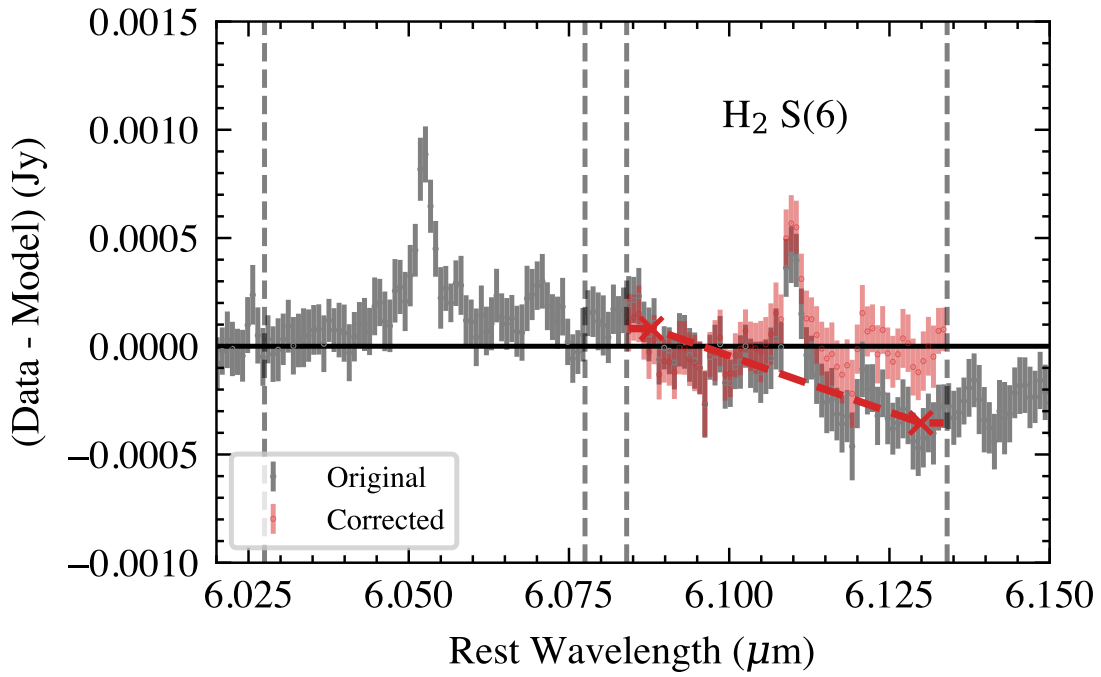

Figure 4.6: Model subtracted residuals for the fit to NGC 3256 SF1 (grey; see Section 4.2.2), to be used to integrate to obtain emission line fluxes. The red dashed line marks a local continuum correction to the H_2 S(6) line, which when subtracted from the residuals, results in the red data points. This process is applied to every emission line before calculating the integrated flux. The vertical dashed lines show the range over which the line is integrated.

example is shown in Fig. 4.6, where I show the model subtracted residuals for two lines from a fit to a star-forming region in NGC 3256 (see Section 4.2.2). The continuum around the H_2 S(6) line (6.109 μm) appears overestimated resulting in negative residuals redwards of the line, whereas the continuum around first line (H_2O ν=1-0 212-101, 6.049 μm, González-Alfonso et al. (2024) and García-Bernete et al. (2024a)) is predicted accurately. This can happen to certain emission lines, where the signal-to-noise of the line is much lower compared to the continuum/PAH features, and so small fluctuations in the model continuum/PAHs can cause the continuum around the emission line to be over or underestimated.

Before integrating to obtain a line flux, I correct the residuals by measuring a local continuum around the line and subtracting it from the residuals. I do this by calculating the median flux at either side of the line and connecting the points linearly. This creates the red dashed line in Fig. 4.6 which is subsequently

subtracted to obtained the corrected residuals. This is done for every emission line before integrating to obtain a flux. I found that this correction led to underestimated flux errors as it effectively corrects for scatter between each MCMC sample. To overcome this, I re-sample the model subtracted residuals, for each MCMC sample, using the flux error bars before integrating to obtain a flux.

4.4 Simulated Data

To assess the feasibility of this method in recovering the dust distribution from the data, I test the model with simulated data. In particular, I want to test that the model recovers accurately the input dust distribution. I also want to test that the model recovers the simple screen and mixed cases and thus does not fit for differential extinction where it does not exist.

4.4.1 Generating Mock Data

I generate three sets of mock data, a screen, mixed and a differential extinction distribution where there is a gradient of obscuration, with the hot dust appearing more obscured than the cool dust. Specifically, I generated mock spectra by inputting a dust distribution $\Psi\left(T, \tau_{9.8}\right)$ for each of the three cases. For the differential case I use three 2D Gaussians with parameters $\{x_0, y_0, \sigma_x, \sigma_y\} = \{4, 4, 2, 4\}$, $\{8, 8, 2, 4\}$ and $\{12, 12, 2, 4\}$ in units of the grid elements (pixels of the 2D dust distribution) with a position angle, of -40 °. For these tests I adopt the simple power law emissivity profile (see Section 4.3.1). This is to allow a more direct comparison to the traditional PAHFIT methods.

The dust distribution for the three sets of simulated data are shown in Fig. 4.7 with the corresponding continuum and extinction factor in the right panels. I add a stellar continuum to simulate the near-IR portion of the spectra. I use the 100 Myr template (I chose the 100 Myr arbitrarily here and test whether the model recovers the correct stellar continuum in Section 4.4.2), and apply an extinction equal to that of the dust continuum for the screen and mixed cases. For the differential case, I apply a screen of extinction to the stellar continuum, equivalent to the screen case.

I additionally add a PAH and emission line template to the continuum before generating the mock data. This template was generated as the average of all the continuum subtracted spectra of the star-forming regions in NGC 3256 and NGC 7469 (see Section 4.2.2) after fitting with the original PAHFIT-like continuum (Donnan et al., 2023b). I then generate the mock data with wavelengths equal to that of the real data and noise of 1% of the flux values. This gives a signal-to-noise comparable to the JWST data.

Each of the three simulated spectra are fitted with a fixed screen, fixed mixed and the new differential extinction model to investigate how well the true dust distribution and extinction factor can be recovered. The best fit extinction factor is shown in the right panels of Fig. 4.7, in comparison with the true, input extinction factor. The contours in the left most panel show the best fit dust distribution from the differential model.

4.4.2 Case 1: Screen Dust Distribution

For an input screen dust distribution, the screen model (see the top panel of Fig. 4.7) recovers the true extinction factor within 1 % over the entire wavelength range as expected, while the mixed model performs the worst, underestimating the extinction across the wavelength range by $\sim$ 5% up to $\sim$ 15% at $\sim$ 4 μm. The differential model recovers the true extinction well within 1 % across the majority of the wavelength range, only deviating at $\sim$ 4 μm by a maximum of 4 %. For all the fits I find the stellar continuum is recovered accurately, with the input stellar population of 100 Myr being recovered, as the near-IR is dominated by this component and so there is no difficulty in reproducing the input stellar continuum.

The recovered dust distribution in the left panel of Fig. 4.7 peaks in the correct region but shows a larger spread. This larger spread is not seen for the mixed input data where the best fit dust distribution matches the spread accurately. Physically this is a bias towards more mixed dust distributions and so while this does not change the resultant extinction factor/continuum in any significant way, one must take care when drawing any inference about the physical dusty structure from

the shape of $\Psi(T, \tau_{9.8})$. This bias towards more smooth dust distributions is a consequence of the regularisation with the non-parametric method. This is a known bias of non-parametric approaches (Leja et al., 2019; Iyer et al., 2019), for example with non-parametric SFH-histories, where sudden bursts in star-formation can be physically expected but can be difficult to reproduce with this approach.

4.4.3 Case 2: Mixed Dust Distribution

For the mixed input case I find the mixed model (see the middle panel of Fig. 4.7) performs best as expected, recovering the extinction factor within 1%. The screen and differential models also perform well in this case, both finding the true extinction factor within 1% with both only deviating by a maximum of 4% at $\sim 1.6\mu$m. These tests highlight that the differential extinction model is able to recover the extinction factor in the simple cases where there is no differential extinction.

4.4.4 Case 3: Differential Dust Distribution

The third simulated spectrum was produced using a dust distribution with a clear gradient where the hotter dust is more obscured than the colder dust (see the bottom panel of Fig. 4.7). I find that the fixed screen and mixed models fail to recover the extinction factor, and indeed fail to produce a satisfactory fit to the continuum. The differential model however reproduces the input dust continuum accurately and recovers the extinction factor well, with a deviation at ~ 5 μm by up to 15%. This deviation implies the model has difficulty recovering the most obscured hot dust, which would lower the extinction factor at ~ 5 μm. This is a limitation of the physics as these obscured blackbodies will have a minimal contribution to the flux/shape of the model and thus makes little difference to the fit. Therefore due to the regularisation of the model, the fit favours more conservative solutions by not switching on components unnecessary to fit the data, pushing the recovered extinction factor closer to a case with less extreme differential extinction. This is therefore a hard limit, where the information is simply not present to infer the most obscured hot dust that was included when generating the mock data.

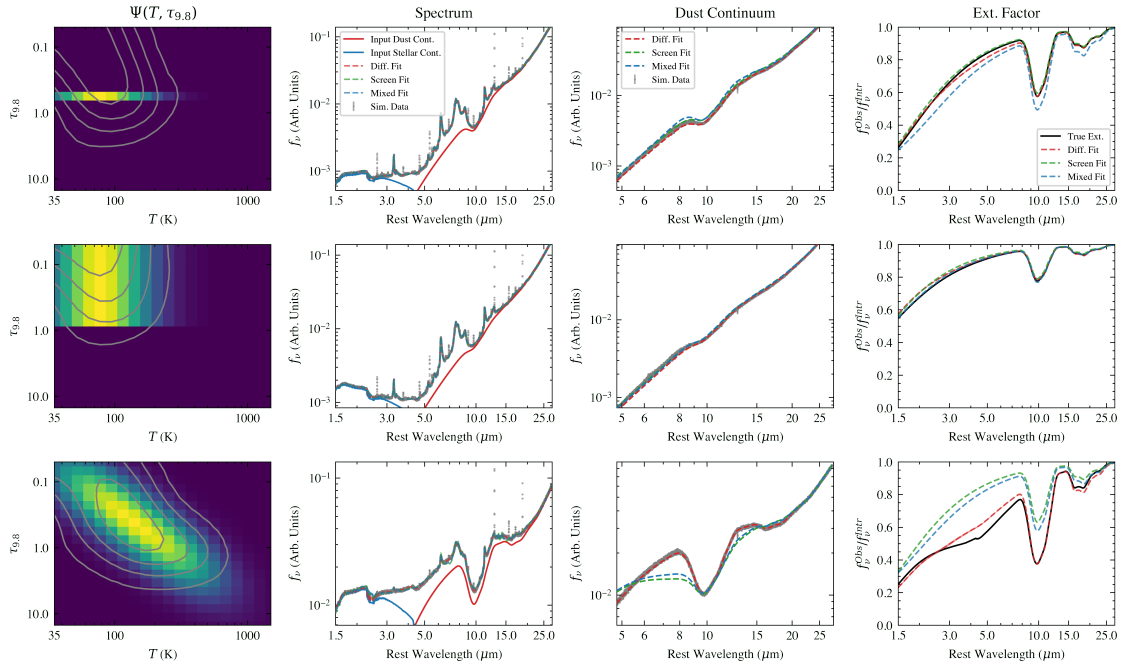

Figure 4.7: Tests with simulated data for three input dust distributions: screen (upper), mixed (middle) and differential (lower). The left panels show the dust distribution, $\Psi(T, \tau_{9.8})$, used to generate the simulated data overlayed with the best fit model in the grey contours. The colour scale is linear, with the grid elements summing to one. The 2nd column shows the resulting continuum from the input dust distribution (solid red line) and the input stellar continuum (solid blue line). The simulated data is shown with the grey points. The dashed lines show the different best fit models from the screen fit (green), mixed (blue) and the differential model (red). The 3rd column shows just the dust continuum from the simulated data in comparison with the best fit models. The right panel shows the wavelength dependent extinction factor for the input (black) and the best fit results when fitting with a single screen (green dashed), pure mixed (blue dashed) and the new differential extinction model (red dashed).

For the third case I see that the traditional fixed or screen models do not properly fit the data and predict the extinction factor incorrectly, which would lead to incorrect flux ratios from emission features. This demonstrates the need for a more complex dust distribution is required and where my new model is able to reproduce the input conditions. As discussed in Section 4.6, dust distributions similar to this are present in LIRGs (and therefore also ULIRGs), and so accounting for the effect of differential extinction is necessary to model these spectra.

4.5 Other Estimates of Extinction

With the rich MIRI MRS and NIRSpec spectra, comes additional diagnostics of extinction. These can then be compared to the differential extinction model of the dust continuum to provide insight into the physical conditions of the regions. In the following sections I discuss three different measures of extinction using the emission features in the spectra.

4.5.1 Hydrogen Recombination Lines (HI)

Hydrogen recombination lines have been used in the optical to obtain extinction measurements for decades (Salim and Narayanan, 2020). The so-called Balmer decrement measures the extinction of HII regions around young stars. This works by assuming an intrinsic Hα/Hβ ratio under case B conditions (Hummer and Storey, 1987) and inferring the optical depth required to reproduce the observed ratio. In the near and mid-infrared the same technique can be applied using the Brackett (Br, 4.05, 2.62, 2.17, ... μm), Pfund (Pf, 7.46, 4.65, 3.74, ... μm) and Humphreys (Hu, 12.4, 7.50, 5.91 ... μm) series rather than the Balmer series.

While a large number of lines can be used, I focus on the ratio of Brβ (2.62 μm) to Brγ (2.17 μm) as these lines have a high signal-to-noise and are unblended with any other lines. A more detailed analysis combining all the HI lines may provide further insight but is beyond the scope of this work.

I predict the extinction for each spectrum by applying a screen with a given $\tau_{9.8}$ that reproduces the observed flux ratio. I do this for each MCMC sample to obtain uncertainties for the extinction.

I do not apply this to the nucleus of NGC 7469 as there is significant contamination of the HI recombination lines from the broad line region of the AGN. Therefore the intrinsic flux ratio of these lines is no longer due to case B in HII regions and so would provide inaccurate extinction values.

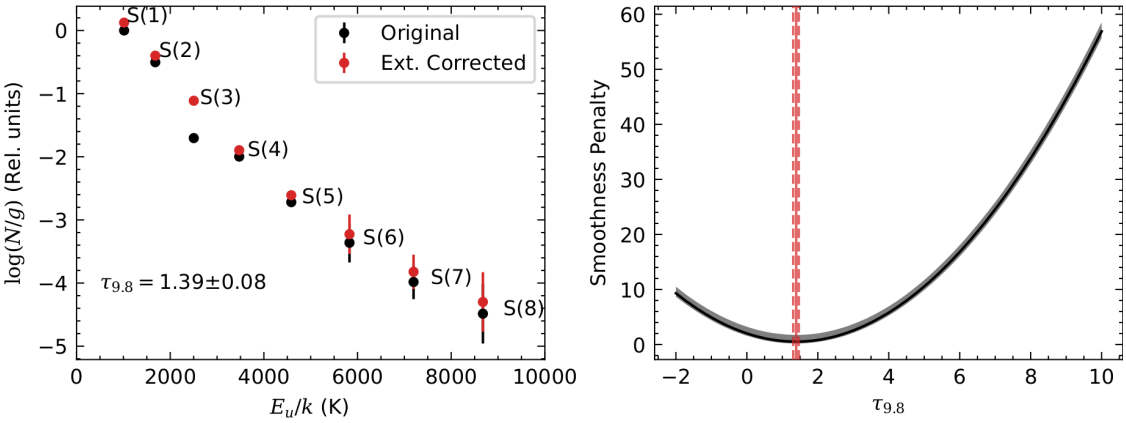

Figure 4.8: Inferring the extinction of H_2, in this case for NGC 3256 SF4, by varying the extinction correction and measuring the smoothness of the resultant rotation diagram. **Left:** Rotation diagram for H_2 for the observed fluxes (black) and the extinction corrected fluxes (red). Note the change for the S(3) transition. **Right:** Penalty factor for the smoothness of the resulting rotation diagram given an extinction correction with optical depth $\tau_{9.8}$. The best fit value is given by the minimum of this curve which is marked with the solid vertical red line. The vertical dashed red liens show the 1σ error range.

4.5.2 Molecular Gas (H_2)

The mid-infrared is populated with numerous rotational H_2 lines tracing the molecular gas. In particular the S(1) to S(8) transitions between 5 μm and 28 μm. In Donnan et al. (2023b) and Hernandez et al. (2023), it was noted that the S(3) J=5 transition is extremely sensitive to extinction as its central wavelength at 9.665 μm places it within the trough of the 9.8 μm silicate absorption (Pereira-Santaella et al., 2014). In the referenced works, this line was largely ignored as a result, however this fact also makes it ideal for predicting level of extinction affecting the molecular gas. I do this by first constructing a rotation diagram where I plot the population of each energy level, $\log(N/g)$, against the energy of the upper level, E_u/k, as shown in the left panel of Fig. 4.8. This is for a typical star forming region (NGC 3256 SF4), where the fluxes used have not been corrected for extinction (black points). As a result, the S(3) transition appears lower than expected. I can therefore estimate the extinction by varying the correction factor until this dip no longer exists.

I do this by varying the optical depth of a single screen of dust and calculating the extinction corrected rotation diagram for all the transitions. For each optical depth, I calculate the smoothness of the resulting rotation diagram using the sum

of the Laplacian, which is the 1D version of equation (4.12),

$$P_{H_2} = \sum_i \left[\log(N_{i-1}/g_{i-1}) - 2\log(N_i/g_i) + \log(N_{i+1}/g_{i+1})\right]^2 \tag{4.18}$$

where, $\log(N_i/g_i)$ is the population of transition i. The inferred extinction is that where the smoothness penalty, P_{H_2} is minimised. This is demonstrated in the right panel of Fig. 4.8 with the corresponding extinction corrected rotation diagram in the left panel in red. As before I can perform this for each MCMC sample to get an uncertainty on the inferred H_2 extinction.

The gradient of the rotation diagram is related to the temperature of the gas, where steeper curves result from cooler gas as the higher energy transitions are relatively less populated. Typically one will fit multiple (~ 2 or 3) linear components, each with a different temperature to fit the curve (Rigopoulou et al., 2002; Pereira-Santaella et al., 2022) or assume some power law distribution of temperature (Togi and Smith, 2016; Pereira-Santaella et al., 2014). To obtain an estimate without assuming a model, I calculate the median gradient of pairs of transitions to provide an average molecular gas temperature as traced by the mid-infrared.

4.5.3 PAHs

If an intrinsic ratio between two PAH bands is assumed, the extinction can be inferred by a similar method as the Hydrogen recombination lines. This method was proposed by Hernán-Caballero et al. (2020) where they showed that the 12.7/11.3 PAH ratio is intrinsically constant for star-forming galaxies with the observed ratio depending only on the extinction.

I calculate the intrinsic 12.7/11.3 PAH ratio using the star-forming regions of NGC 3256 and NGC 7469 as a calibration sample. This step is required as the increased spectral resolution of MIRI MRS over Spitzer IRS, leads to a more resolved 12.7 PAH feature as discussed in Chapter 3. I measure an intrinsic 12.7/11.3 PAH ratio of 0.72 ± 0.08, after correcting for extinction using the average continuum extinction as given in Table 4.1. As I rely on an empirical calibration, the resulting

measured PAH extinctions will largely follow that of the continuum for the star-forming regions by construction. Therefore the measured PAH extinction is not a completely independent measure but is valuable as a comparison between objects.

Taking the samples of the intrinsic ratio, I vary the extinction until the observed 12.7/11.3 PAH ratio is reproduced for each MCMC sample of the measured ratio, to obtain a posterior for the PAH extinction.

4.6 Results

I fit the model to each spectrum extracted as discussed in Section 4.2.2. I fit the entire sample with each emissivity, first with the simple power law with $\gamma = 2$ and then with the physical emissivity profile which includes a mixture of silicates and graphite based on Li and Draine (2001). I found the physical emissivity profile provides a better fit in all cases. Moreover it is necessary to fit the silicates seen in emission for the nucleus of NGC 7469 (Alonso-Herrero et al., 2020; García-Bernete et al., 2022c). I compare the choice of emissivity in detail in Section 4.7.2. The results have been obtained with the physical emissivity, as it provides a better fit and is better motivated from a theoretical perspective.

I show the best fit dust distributions for all the nuclei and a representative star-forming region in Fig. 4.9. The remaining star-forming regions are shown in Fig. 4.10. I use the physical emissivity as I found this to provide a better fit to the data and is more physically motivated.

I find the shape of the dust distribution, $\Psi(T, \tau_{9.8})$, to be largely consistent between the various star-forming regions. In particular it shows a relatively low dust temperature ($\sim$ 90 - 100 K) that is lightly obscured ($\tau_{9.8} \sim 0.2$), resulting in a steep dust continuum with little to no silicate absorption. There additionally appears to be a faint, obscured hot dust component with $\tau_{9.8} > 1$. A few of the star-forming regions, NGC 7469 SF1, SF3 and SF4, show a stronger gradient, with a stronger hot dust component resulting in moderate silicate emission. Comparing with the other estimates of extinction, the molecular gas appears the most obscured, even more obscured than the dust continuum. I discuss possible reasons for this in Section 4.7.1.

As expected, the nuclei generally show more complex dust distribution, where multiple dust components contribute to the observed spectrum. I discuss each individually in detail in Section 4.7.4.

I display the inferred properties of each fitted spectrum in Table 4.1. The temperature, T, and extinction, $\tau_{9.8}$, are given for the total continuum and individual components of the dust distribution for those cases as described in Section 4.7.3. To obtain this, I sum over one of the axes of the dust distribution to collapse the 2D distribution into a 1D distribution either of temperature, T, and extinction, $\tau_{9.8}$ (by summing over the other axis). I then determine the median and 16%/84% upper and lower bounds of the 1D distributions. These values reflect the shape/spread of $\Psi(T, \tau_{9.8})$ rather than the statistical uncertainties, which are negligible by comparison.

I additionally show the measured extinction from the other tracers as outlined in Section 4.5. For the molecular gas I also show the measured gas temperature.

For NGC 7469 Nuc and IIZw96 SW, the 12.7/11.3 PAH ratio is not well constrained, and therefore cannot measure the extinction accurately.

I note that the uncertainties on the inferred properties are dominated by the priors on the intrinsic PAH ratio as the statistical uncertainties are very small due to the high signal-to-noise of the data. This is reflected in the errors on the stellar extinction. These are likely underestimated as I have not folded in errors based on the assumption of the chosen stellar population templates, which for example, assumed solar metallicity.

4.7 Discussion

4.7.1 Layers of Extinction

From Fig. 4.9 and Fig. 4.10, I find that the molecular gas and HII regions are the most obscured while the PAHs and stellar continuum are less obscured. This is consistent with a picture where the molecular gas is the most buried within dust clouds which will collapse to form stars. The HII regions are similarly

Table 4.1: Inferred properties from each spectrum

Spectrum	Total Cont.		SF Cont.		AGN Warm		AGN Hot		HI	H_2		PAHs	Stellar
	$\tau_{9.8}$	T	$\tau_{9.8}$	T	$\tau_{9.8}$	T	$\tau_{9.8}$	T	$\tau_{9.8}$	$\tau_{9.8}$	$\bar{T}$	$\tau_{9.8}$	$\tau_{9.8}$
		K		K		K		K			K		
NGC 7469 SF1	$0.49^{+1.2}_{-0.38}$	$111.0^{+120.0}_{-50.0}$	-	-	-	-	-	-	$0.56^{+0.17}_{-0.18}$	$0.86^{+0.05}_{-0.074}$	$716.0^{+100.0}_{-100.0}$	$0.88^{+0.27}_{-0.23}$	$0.3767^{+0.0033}_{-0.0031}$
NGC 7469 SF2	$0.43^{+1.6}_{-0.34}$	$100.0^{+79.0}_{-41.0}$	-	-	-	-	-	-	$1.09^{+0.13}_{-0.14}$	$0.72^{+0.084}_{-0.072}$	$664.0^{+69.0}_{-74.0}$	$0.56^{+0.28}_{-0.24}$	$0.3513^{+0.0039}_{-0.0039}$
NGC 7469 SF3	$0.40^{+1.2}_{-0.3}$	$104.0^{+66.0}_{-40.0}$	-	-	-	-	-	-	$1.56^{+0.29}_{-0.28}$	$1.11^{+0.096}_{-0.11}$	$654.0^{+54.0}_{-56.0}$	$0.54^{+0.25}_{-0.24}$	$0.2436^{+0.0036}_{-0.0037}$
NGC 7469 SF4	$0.41^{+1.4}_{-0.31}$	$100.0^{+65.0}_{-38.0}$	-	-	-	-	-	-	$1.20^{+0.20}_{-0.28}$	$0.87^{+0.11}_{-0.13}$	$660.0^{+76.0}_{-70.0}$	$0.55^{+0.27}_{-0.21}$	$0.2401^{+0.0027}_{-0.0027}$
NGC 7469 SF5	$0.50^{+1.9}_{-0.4}$	$93.0^{+75.0}_{-43.0}$	-	-	-	-	-	-	$0.55^{+0.15}_{-0.21}$	$1.1^{+0.11}_{-0.084}$	$629.0^{+45.0}_{-46.0}$	$0.70^{+0.24}_{-0.24}$	$0.2578^{+0.0022}_{-0.003}$
NGC 7469 SF6	$0.53^{+1.7}_{-0.41}$	$105.0^{+87.0}_{-43.0}$	-	-	-	-	-	-	$0.55^{+0.15}_{-0.16}$	$1.21^{+0.084}_{-0.084}$	$654.0^{+46.0}_{-42.0}$	$0.49^{+0.25}_{-0.24}$	$0.3233^{+0.0059}_{-0.0056}$
NGC 7469 Nuc	$1.02^{+2.8}_{-0.89}$	$154.0^{+62.0}_{-40.0}$	-	-	$1.04^{+3.0}_{-0.92}$	$149.0^{+47.0}_{-37.0}$	$0.97^{+0.75}_{-0.48}$	$634.0^{+390.0}_{-160.0}$	-	$0.34^{+0.012}_{-0.024}$	$712.0^{+5.9}_{-5.9}$	-	-
NGC 3256 SF1	$0.33^{+1.5}_{-0.25}$	$87.0^{+68.0}_{-33.0}$	-	-	-	-	-	-	$0.85^{+0.28}_{-0.29}$	$1.26^{+0.048}_{-0.06}$	$538.0^{+92.0}_{-21.0}$	$0.15^{+0.29}_{-0.23}$	$0.1862^{+0.0035}_{-0.0033}$
NGC 3256 SF2	$0.55^{+2.2}_{-0.44}$	$90.0^{+68.0}_{-33.0}$	-	-	-	-	-	-	$1.10^{+0.24}_{-0.22}$	$1.45^{+0.048}_{-0.048}$	$684.0^{+29.0}_{-34.0}$	$0.55^{+0.24}_{-0.34}$	$0.4949^{+0.0058}_{-0.0059}$
NGC 3256 SF3	$0.38^{+1.6}_{-0.29}$	$91.0^{+62.0}_{-33.0}$	-	-	-	-	-	-	$0.72^{+0.16}_{-0.15}$	$1.43^{+0.036}_{-0.024}$	$722.0^{+20.0}_{-24.0}$	$0.64^{+0.26}_{-0.24}$	$0.3288^{+0.0034}_{-0.0035}$
NGC 3256 SF4	$0.41^{+1.7}_{-0.33}$	$89.0^{+69.0}_{-36.0}$	-	-	-	-	-	-	$0.83^{+0.19}_{-0.19}$	$1.39^{+0.072}_{-0.084}$	$634.0^{+58.0}_{-77.0}$	$0.39^{+0.26}_{-0.24}$	$0.2575^{+0.0052}_{-0.0052}$
NGC 3256 SF5	$1.07^{+1.9}_{-0.81}$	$116.0^{+84.0}_{-46.0}$	-	-	-	-	-	-	$1.01^{+0.060}_{-0.064}$	$1.63^{+0.024}_{-0.024}$	$765.0^{+14.0}_{-8.9}$	$0.40^{+0.28}_{-0.22}$	$0.4173^{+0.004}_{-0.0041}$
NGC 3256 SF6	$0.47^{+1.7}_{-0.38}$	$93.0^{+61.0}_{-33.0}$	-	-	-	-	-	-	$0.81^{+0.17}_{-0.17}$	$1.33^{+0.048}_{-0.048}$	$658.0^{+29.0}_{-52.0}$	$0.68^{+0.25}_{-0.25}$	$0.3821^{+0.0045}_{-0.0043}$
NGC 3256 N	$1.07^{+1.3}_{-0.83}$	$109.0^{+62.0}_{-29.0}$	-	-	-	-	-	-	$1.35^{+0.036}_{-0.036}$	$2.38^{+0.012}_{-0.012}$	$436.0^{+19.0}_{-3.2}$	$1.18^{+0.26}_{-0.23}$	$0.2937^{+0.0017}_{-0.0012}$
NGC 3256 S	$4.66^{+6.4}_{-3.6}$	$83.0^{+43.0}_{-27.0}$	$0.66^{+0.61}_{-0.54}$	$77.0^{+30.0}_{-22.0}$	$6.1^{+6.4}_{-3.4}$	$83.0^{+40.0}_{-27.0}$	$6.6^{+2.7}_{-1.8}$	$1274.0^{+230.0}_{-290.0}$	$2.49^{+0.040}_{-0.036}$	$2.24^{+0.012}_{-0.024}$	$540.0^{+38.0}_{-39.0}$	$2.07^{+0.27}_{-0.22}$	$1.3971^{+0.0018}_{-0.0018}$
VV114 NE	$5.27^{+4.4}_{-2.6}$	$93.0^{+68.0}_{-32.0}$	$1.02^{+0.46}_{-0.88}$	$64.0^{+23.0}_{-14.0}$	$5.48^{+4.4}_{-2.5}$	$95.0^{+68.0}_{-33.0}$	-	-	$1.76^{+0.058}_{-0.059}$	$1.98^{+0.026}_{-0.012}$	$591.0^{+11.0}_{-7.3}$	$2.03^{+0.27}_{-0.23}$	$0.7016^{+0.00056}_{-0.00056}$
VV114 SW	$0.95^{+2.1}_{-0.81}$	$84.0^{+100.0}_{-29.0}$	$0.25^{+0.36}_{-0.17}$	$71.0^{+27.0}_{-20.0}$	$2.1^{+2.2}_{-1.0}$	$93.0^{+66.0}_{-33.0}$	$2.29^{+1.4}_{-0.83}$	$732.0^{+260.0}_{-200.0}$	$1.46^{+0.038}_{-0.039}$	$1.51^{+0.024}_{-0.024}$	$656.0^{+92.0}_{-56.0}$	$1.47^{+0.28}_{-0.22}$	$0.7309^{+0.0046}_{-0.0043}$
IIZw96 NE	$0.69^{+1.8}_{-0.55}$	$72.0^{+70.0}_{-30.0}$	-	-	-	-	-	-	$1.11^{+0.14}_{-0.14}$	$0.69^{+0.24}_{-0.31}$	$461.0^{+120.0}_{-75.0}$	$1.49^{+0.27}_{-0.24}$	$0.5045^{+0.0037}_{-0.0038}$
IIZw96 SW	$2.25^{+3.3}_{-1.7}$	$91.0^{+58.0}_{-30.0}$	$0.69^{+0.56}_{-0.54}$	$76.0^{+35.0}_{-21.0}$	$3.59^{+3.2}_{-1.5}$	$104.0^{+60.0}_{-37.0}$	$13.11^{+1.9}_{-9.5}$	$774.0^{+340.0}_{-240.0}$	$1.30^{+0.020}_{-0.019}$	$2.08^{+0.036}_{-0.024}$	$902.0^{+9.2}_{-7.8}$	-	$0.194^{+0.0096}_{-0.0090}$

obscured, resulting from newly formed stars that still remain deeply buried within the star-forming region.

The dust continuum appears highly mixed ranging from unobscured ($\tau_{9.8} \sim 0.2$) to obscured ($\tau_{9.8} > 1$), with the most buried dust consistent with the molecular gas and HII regions. This suggests the dust exists throughout star-forming regions where a significant fraction of the flux is from the outer layers, where the dust emission is unobscured towards the line of sight of the observer. A significant portion of the heating of this unobscured dust may therefore originate from old stars that exist outside the obscured molecular clouds where stars are actively forming. This is confirmed by the extinction from the stellar continuum, which at these wavelengths is dominated by evolved stars, and appears less buried than the more obscured molecular gas and HII regions. This is also true for the PAHs, where previous studies have shown that some excitation can be attributed to more evolved stellar populations (Peeters et al., 2004; Zhang and Ho, 2023a), which is an important consideration when determining star-formation rates.

PAHs experience similar obscuration as the cooler dust continuum. This is

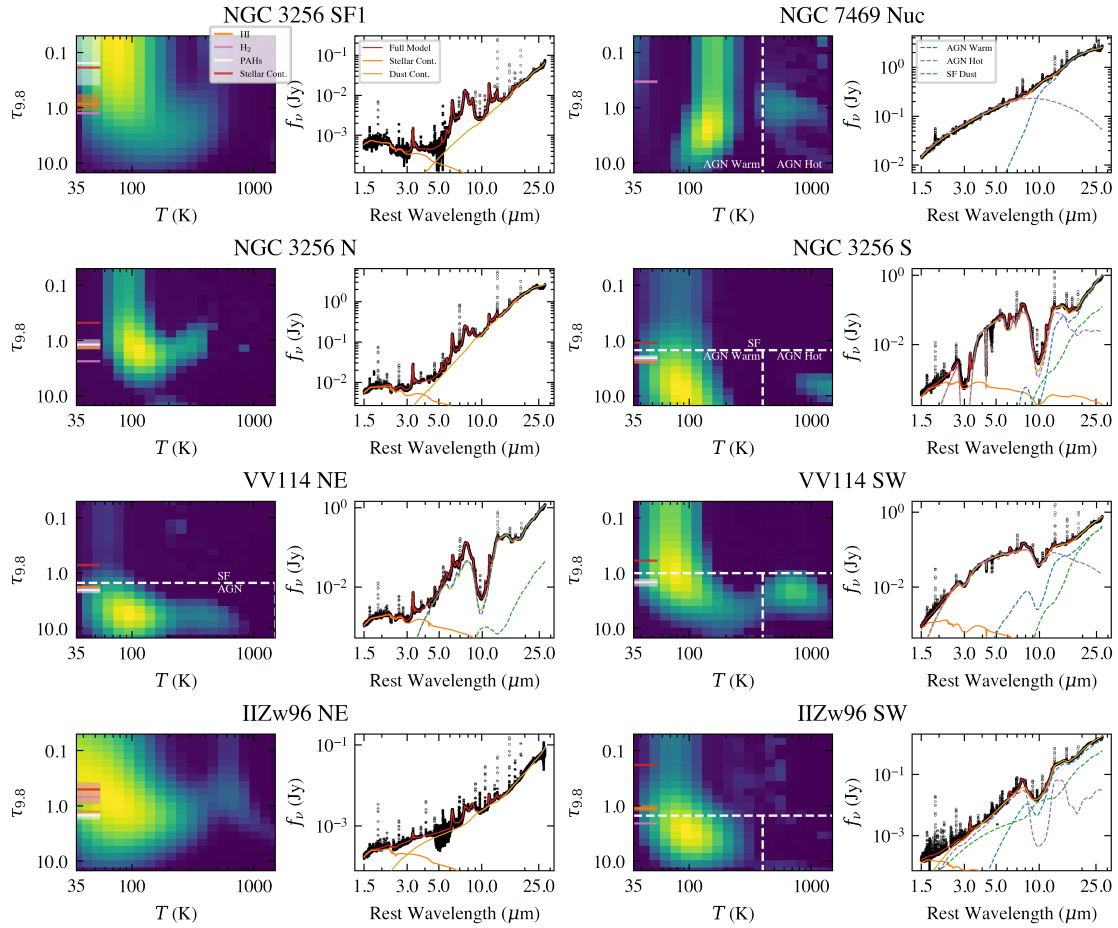

Figure 4.9: Fits to eight of the spectra in this work. I show a star-forming region (NGC 3256 SF1) and the 7 nuclei. Each panel shows the best fit dust distribution, $\Psi\,(T, \tau_{9.8})$, on the left and the corresponding fit to the data in the right panel. The horizontal coloured lines show the extinction measurements for the molecular gas, PAHs, HI lines and the stellar continuum, as described in Section 4.5. The dashed white lines show a decomposition of the best fit distribution into star-forming and AGN warm and hot components for those cases where applied. The resulting continuum for each component is plotted in the right panels.

however, largely by construction, as the intrinsic 12.7/11.3 ratio is empirically calibrated using the average extinction of the continuum (see Section 4.5.3). However, one would expect the PAHs to be somewhat less obscured than the HII regions as they are known to exist in Photodissociation Regions (PDRs), where the PAHs exist on the boundary between ionised and molecular gas (e.g. See Fig. 1 of Chown et al., 2023) and therefore the measured values (in Table 4.1) are not unexpected.

I find that the molecular gas temperature is generally high, likely due to these lines being sensitive to the warm molecular gas. If the S(0) transition was also

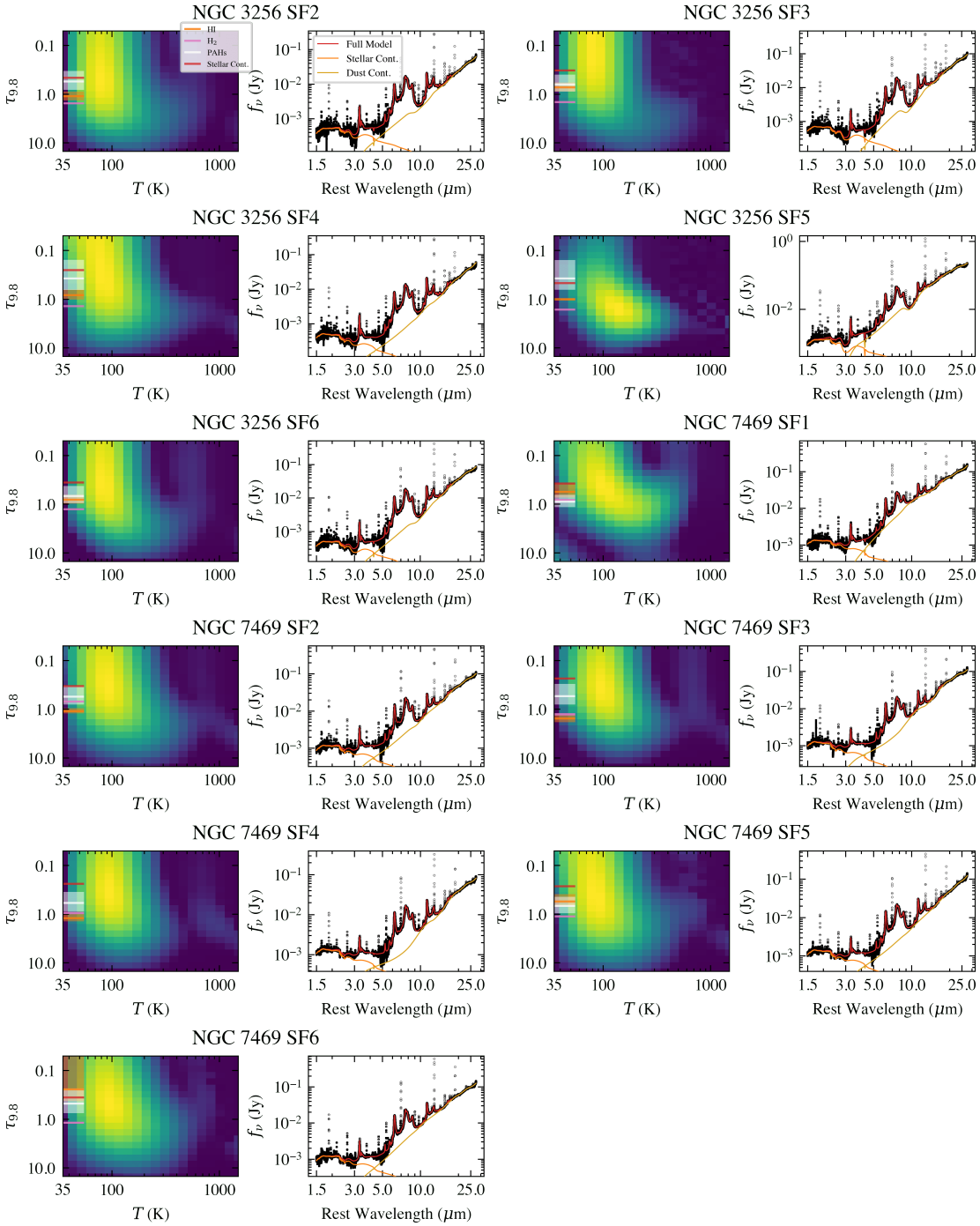

Figure 4.10: Same as Fig. 4.9 but for the remaining spectra, all of which are star-forming regions.

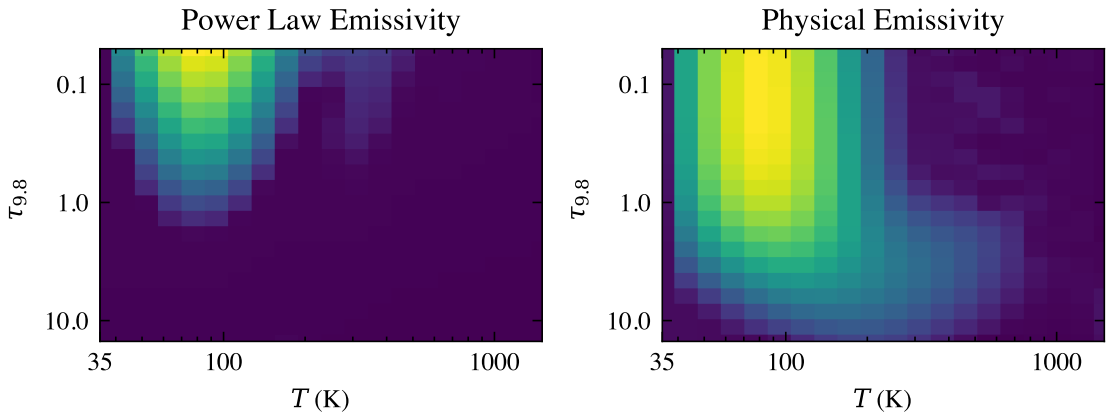

Figure 4.11: Comparison of the inferred dust distribution for a typical star-forming region (NGC 3256 SF3) depending on the chosen emissivity function as shown in Fig. 4.4. The left is for $\epsilon_\nu \propto \lambda^{-2}$ while the right is a physically motivated emissivity function, including silicates, based on Li and Draine (2001).

included, the measured average temperature would likely be lower as this transitition is sensitive to cooler molecular gas. I measure generally similar gas temperatures of $\sim 500 - 700$ K for all of the regions with the exception of IIZw96 SW, which shows a higher temperature of ~ 900 K. Interestingly, the known AGN, NGC 7469 Nuc and NGC 3256 S both show temperatures consistent with the star-forming regions. This is likely because the mid-IR transitions of H_2 originate from gas at temperatures around those shown in Table 4.1 and so are sensitive to molecular gas heating by stars rather than AGN. This has been found in previous studies (Rigopoulou et al., 2002) where AGN and star-forming dominated galaxies show similar molecular gas temperatures as traced by the mid-IR.

4.7.2 Choice of Emissivity

I found a more physically motivated emissivity, which includes silicates, provides a better fit to the data over a simple power law. In Fig. 4.11 I show a comparison of the inferred dust distribution for a star-forming region depending on the choice of emissivity.

For the power law emissivity, the dust is almost completely unobscured and shows no sign of any differential extinction, as to create a smooth continuum with little silicate absorption requires close to zero extinction. By contrast the dust distribution

for the physically motivated emissivity shows a greater average extinction compared to the power law emissivity, with evidence of differential extinction, with a more obscured hot dust component relative to the cooler dust.

The latter case is physically more reasonable, as the dust extinction is more consistent with the other extinction tracers, where the buried hot dust is consistent with the obscured molecular gas where stars are actively forming. I therefore conclude that the physically motivated emissivity is closer to reality.

4.7.3 Decomposing the Dust Distribution

For objects that show a complex dust distribution such as IIZw96 SW, I can decompose it into multiple components. For this example, there is a clear component of relatively unobscured cold dust that is consistent with the HI, H_2 and stellar continuum extinction measures. Additionally there is an obscured component with a gradient, where the hotter dust appears more obscured. This is potentially the signature of an AGN torus (García-Bernete et al., 2024a) and so if I split the dust distribution into two, I can extract individual continua for each component.

As I find the majority of the dust distribution for star-forming regions lie at $\tau_{9.8} < 1 \sim 1.5$, I define a cutoff around these values for NGC 7469 Nuc, VV114 NE, VV114 SW, IIZw96 SW and NGC 3256 S, as these show complex dust distributions with clear components. Firstly, I select dust from star-formation by using grid elements below $\tau_{9.8} < 1.5$ for NGC 3256 S, VV114 NE and IIZw96 SW and $\tau_{9.8} < 1.0$ for VV114 SW. I then note that NGC 7469 Nuc, NGC 3256 S and VV114 SW show a clear separate component in the $T, \tau_{9.8}$ space at high temperatures. I isolate this with a temperature cutoff of $T > 400$ K. I also apply this to IIZw96 SW, which tentatively shows a separate component here.

One interpretation is that the obscured high temperature component is heated very close to the AGN, near the dust sublimation zone. This may be the inner rim of a torus or polar dust, where dusty grains are driven as a wind by radiation pressure from the AGN accretion disk (Hönig and Kishimoto, 2017; García-Bernete et al., 2022d).

I have presented a simple interpretation of the best fit dust distribution, but the reality may be more complex. For example if there is dust at a similar temperature and obscuration in both an AGN torus and star-forming regions, the two cannot be disentangled by a simple cutoff.

4.7.4 Nature of the Individual Sources

From the best fit dust distributions and the extinction predicted from the different emission features, I can infer the nature of these sources in terms of layers of extinction. I briefly summarise my findings for each object here in the context of the literature. Beyond the scope of this work, the rich data of these targets allows much more analysis into the nature of these objects (Inami et al., 2022a; García-Bernete et al., 2022a; Donnan et al., 2023b; Rich et al., 2023; Armus et al., 2023; Lai et al., 2023; Zhang and Ho, 2023b; Pereira-Santaella et al., 2023; González-Alfonso et al., 2024; García-Bernete et al., 2024a; Buiten et al., 2023).

NGC 7469

I find the nuclear dust continuum to be dominated by the AGN, with relatively weak PAH emission and no significant contribution from stellar continuum, consistent with previous analysis of this target (Alonso-Herrero et al., 2020; García-Bernete et al., 2022c; Armus et al., 2023). The dust distribution shows a large spread of extinction with an average extinction of $\tau_{9.8} \sim 1$ with a significant hot dust component with $T > 400$ K. Considering its classification as a type 1 AGN, it is expected to have clear lines of sight to very hot dust close to the sublimation radius at T $>$ 1000 K. Interestingly, this dust is moderately obscured which may suggest that there is some intervening dust that obscures the very hot inner regions of the AGN torus.

For three of the star-forming regions (see Section 4.2.2 and Fig. 4.1) I find the HII regions to be more obscured than the molecular gas, contrary to the other SF regions. Namely SF2, SF3 and SF4 show this behaviour and lie on the north-west section of the star-forming ring. Additionally, these regions show silicates in emission (along with SF1) due to a combination of low obscuration and higher dust

temperatures. From Díaz-Santos et al. (2007), these regions show slightly more evolved stellar populations and lack molecular gas (via CO (2-1)) compared to SF1, SF5 and SF6. This offers a potential explanation as to why the H_2 lines appear less obscured than the HII regions, where the relative lack of CO but presence of the mid-IR H_2 lines would suggest a high molecular gas temperature.

For NGC 7469 SF1, the comparative lack of cool obscuring dust, resulting in the silicate emission, may be related to the nuclear bar, as this region is placed on the boundary between the bar and the star-forming ring.

VV 114

VV 114 NE shows a significant highly obscured dust continuum appearing more obscured than the PAHs, molecular gas or HII regions. This is consistent with initial analysis of this target in Chapter 3 where there is likely an extremely buried AGN considering its obscuration and compact nature (<100 pc). Additionally, the ro-vibration molecular bands of CO and H_2O, show a high excitation temperature (Buiten et al., 2023). From the dust distribution, high temperatures are reached up to $\sim$ 800 K but unlike the SW nucleus, there is no clear isolated hot dust component.

VV 114 SW also shows a strong continuum but it is significantly less obscured than the NE nucleus. There is a significant isolated hot dust component that dominates the continuum between 2-10 μm. This is consistent with the claim that this is an AGN by Rich et al. (2023), due to its low 3.3 μm and 6.2 μm PAH equivalent widths, where the hot dust continuum dominates over the emission features. From the decomposition, the warm AGN component shows a gradient where the obscuration increases with temperature. This may indicate a high covering factor smooth torus. This picture can explain the lack of high ionisation potential lines (Donnan et al., 2023b; Rich et al., 2023) that would be expected for an AGN with the observed level of obscuration.

An alternative explanation is that the isolated hot dust component is a result of the shock front that has passed through the region (Saito et al., 2017; Donnan et al., 2023b) and that the nucleus is simply an obscured star-forming region. This

may explain the lack of high-ionisation lines, and the low excitation temperature of the ro-vibration molecular bands (Buiten et al., 2023). However, similar to the NE core, the source is very compact ($<$ 100 pc in the near-IR) and so reaching such a high infrared surface brightness is difficult to explain without an AGN.

NGC 3256

NGC 3256S hosts a low luminosity, Compton Thick AGN (Ohyama et al., 2015) which has a collimated molecular outflow (Sakamoto et al., 2014; Emonts et al., 2014; Pereira-Santaella et al., 2023) detected through CO, HCN, HCO+ and H_2 transitions. From the dust distribution I see a clear signature of a buried continuum source which shows a gradient of extinction, with the extinction increasing with temperature in the warm component. This suggests a smooth torus rather than a clumpy one, as the hot dust is buried and not leaking through low density lines of sight. In addition, the dust distribution shows an isolated hot dust component that is also highly obscured. This hot dust, as shown in Fig. 4.9, dominates the continuum between 2 - 10 μm.

The stellar continuum, PAHs and HI extinction show a similar pattern to the star-forming regions and VV114 NE, where these trace different phases of the circumnuclear star-formation. However, the H_2 appears less obscured as it is likely tracing the molecular outflow dominating the H_2 emission over circumnuclear star-forming molecular clouds. Indeed, the kinematics of these lines as presented in Pereira-Santaella et al. (2023) trace the outflow.

The northern nucleus shows a dust distribution that is hotter with higher extinction than the star-forming regions but does not show any significant hot component that would be consistent with AGN heating. This is consistent with the literature, that this is a star-forming nucleus (Lira et al., 2008).

Interestingly, the star-forming region to the southwest, SF5, shows a higher obscuration and dust temperature unlike the other star-forming regions as well as deeper near-IR ices. This may suggest an additional heating source such as supernovae and/or X-ray binaries. This is not unexpected considering LIRGs are

believed to have high supernovae rates (many per year) owing to their high star-formation rates. Multiple supernovae have been detected in NGC 3256 (Kankare et al., 2018), however none match this specific source.

With the exception of SF5, all the star-forming regions in NGC 3256 are remarkably similar, with all showing the same pattern of obscuration where the stellar continuum, PAHs, HII regions and molecular gas exist from least obscured to most obscured respectively. The star-forming regions in NGC 3256 appear slightly cooler than those in NGC 7469 and therefore do not show any silicate emission.

A detailed analysis of the PAH properties, comparing to theoretical spectra, is discussed in Rigopoulou et al. (2024).

IIZw96

The spectrum of the SW nuclei of IIZw96 is highly unusual (Inami et al., 2022a; García-Bernete et al., 2024a), with very weak PAH features and a plethora of emission features in the near-infrared (< 3 μm). Indeed, Shipley et al. (2016) noted this object as an outlier in the PAH vs SFR correlation, due to its weak PAH emission as probed by Spitzer.

From the dust distribution I find evidence for a cold, buried continuum source, which shows a gradient, which would again suggest a smooth obscuring structure. The star-forming component is strong, which dilutes this obscured source, filling up the silicate feature. Additionally, the star-forming component is hot, leading to silicate emission at 9.8 μm, consistent with the higher molecular gas temperature of $\sim$ 900 K.

The $\sim 4.6\mu$m CO band appears in emission rather than absorption (García-Bernete et al., 2024a). This is the case for NGC 3256 S, where the nucleus shows CO absorption while the outflow shows emission (Pereira-Santaella et al., 2023). I tentatively detect a very hot dust component in the dust distribution and thus contributing to the continuum at ~ 3 μm. Unlike NGC 3256 S and VV114 SW, this is not as clearly isolated from the warm component and so the temperature/extinction is not well constrained, however this component dominates the continuum in the

near-IR band. The values for the extinction and temperature for this hot component in Table 4.1 are consequently very uncertain, in particular the extinction, as the other dust components dominate in the silicate bands.

The NE nuclei appears to be a relatively unobscured star-forming region, however the PAH features appear a-typical. Most notably is the extremely strong 8.6 μm feature. Additionally, the molecular gas appears less obscured than the HII regions and PAHs.

4.7.5 Effective Extinction Curve

For each object, the extinction correction factor, defined as the ratio of the observed to the intrinsic spectrum (equation (4.11)), varies depending on the shape of the best fit dust distribution, $\Psi(T, \tau_{9.8})$. In general this dust distribution is not a screen and therefore cannot be converted into an optical depth as $\frac{f_\nu}{f_\nu^{\rm Int}} \neq e^{-\tau_{9.8}\tau(\lambda)}$. However, to compare the inferred dust correction factors with known extinction curves from the literature, I calculate an "effective" extinction curve by inverting this equation. This can be thought as "locally" assuming a screen at each wavelength and stitching together an extinction curve. It is worth noting that I am not deriving a new extinction law, as in general $\frac{f_\nu}{f_\nu^{\rm Int}} \neq e^{-\tau_{9.8}\tau(\lambda)}$ and therefore the variation I see between targets is purely due to the shape of $\Psi(T, \tau_{9.8})$. In this work I have assumed a fixed law of that given in Donnan et al. (2023b), which governs the intrinsic properties of the dust grains.

Fig. 4.12 shows the "effective" optical depth normalised at 9.8 μm for a variety of the targets.

All of the targets show a shallower gradient in the near-infrared compared to a single screen from any of the extinction laws. This highlights the effect of differential extinction, where the mid-infrared traces more obscured activity than the near-infrared. This is particularly true for VV114 NE, where I observe a turnover at $\lambda < 4\mu$m, where the relatively less obscured stellar continuum dominates over the highly buried dust continuum. IIZw96 also shows an unusual shape, where the

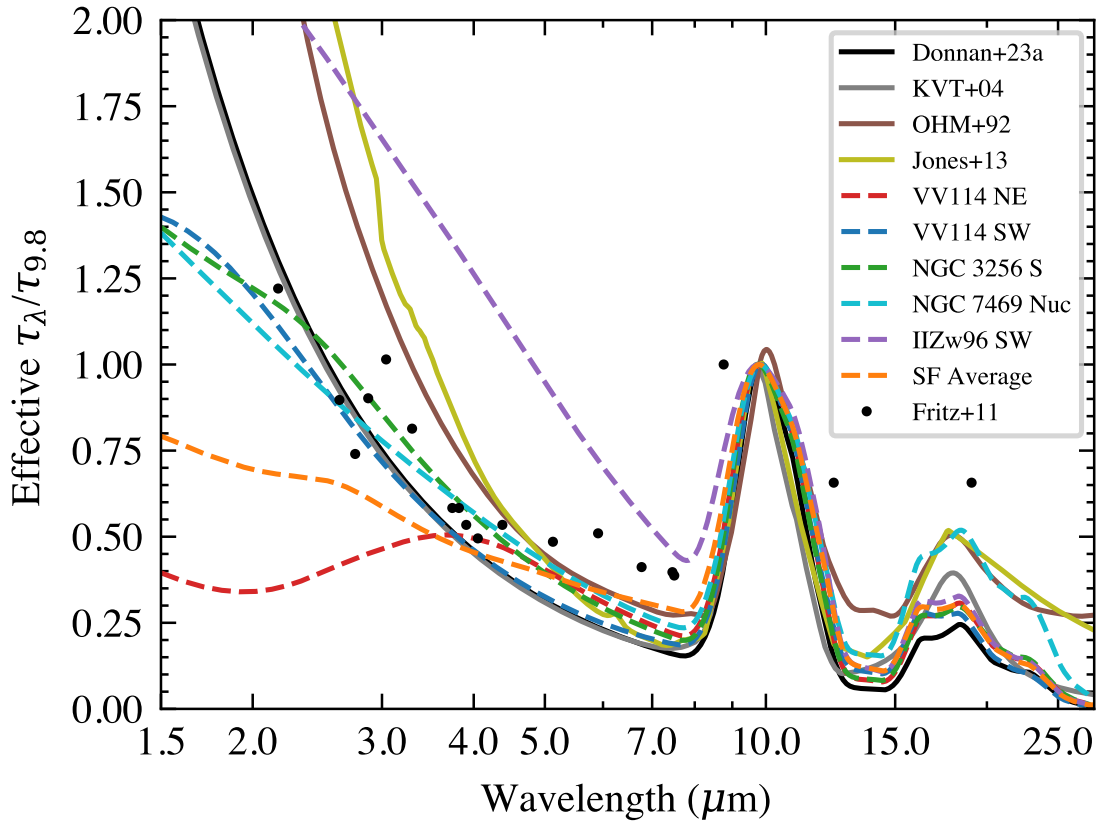

Figure 4.12: Comparison of the inferred extinction factor (equation (4.11)) for each target, converted to an "effective" optical depth, normalised at 9.8 μm. I show the targets in Fig. 4.3 as well as the average for the star-forming regions NGC 3256 and NGC 7469. I compare to the extinction law used in this work from Donnan et al. (2023b) and others from the literature, namely Ossenkopf et al. (1992), Kemper et al. (2004), Fritz et al. (2011), and Jones et al. (2013).

silicate feature is "filled up" by the hot dust emission and thus the shorter wavelength portion appears at a relatively higher optical depth compared to the silicate band.

Extinction curves with flatter optical depths at ~ 5 μm, have been observed in the literature (see Fig. 4 of Draine (2003) or Fig. 2 of Li et al. (2015)), deviating from the expected power law. Differential extinction offers a potential explanation, where the mid-infrared traces more obscured dust while the near-infrared traces less obscured stellar-continuum, flattening the "effective" extinction curve. When the near-infrared is dominated by buried hot dust instead, such as for NGC 3256 S, the "effective" extinction curve becomes steeper, better resembling a power law.

The ratio of the 9.8 μm and 18 μm silicate bands also varies between targets,

depending on the relative obscuration and temperature of different dust components. This can relate to the clumpiness of AGN tori (Hatziminaoglou et al., 2015; Martínez-Paredes et al., 2020; García-Bernete et al., 2024c).

4.8 Summary

I have presented a model to reproduce the joint NIRSpec and MIRI spectra between 1.5 - 28 μm for a variety of LIRGs. The main findings are

- By testing with simulated data, I show that the model is able to reproduce the dust distribution and thus extinction correction factor for input data with and without differential extinction, where in the latter case, the traditional screen/mixed approaches fail, highlighting the need for differential extinction to model the spectra of obscured (U)LIRGs.
- I find evidence for differential extinction from fitting the spectra of LIRGs where star-forming regions show dust distributions dominated by relatively unobscured cool dust with some buried hot dust.
- I find a deeply buried continuum component in the dust distribution for VV114 NE, NGC 3256 S and IIZw96 SW, with the latter two showing a hot isolated dust component at T$\sim$ 1000 K, likely due to AGN heating. Similarly, VV114 SW shows a significant hot component, either due to AGN heating or a shock front passing through as a result of the galaxy-galaxy merger.
- I compare the dust extinction with that of the stellar continuum, PAHs, HII regions (HI lines) and molecular gas (H_2) lines. For star-forming regions I find that the molecular gas, and HII regions are the most obscured consistent with the hottest dust. The stellar continuum and PAHs are significantly less obscured, consistent with the cooler dust.
- By constructing an "effective" extinction curve, I find the near-infrared to be much shallower than the mid-infrared which is indicative of differential

extinction, where the near-infrared traces less obscured emission than the mid-infrared. This can explain flatter extinction curves in the literature.

I have shown that by modelling the distribution of dust I am able to reproduce the spectrum for a variety of objects from star-forming regions to highly obscured AGN. Such detailed modelling is imperative considering the high frequency of dusty galaxies being observed with JWST.

5

Unveiling the Nature of Dusty Obscured Nuclei: Insights from a sample of galaxies observed with JWST.

Contents

5.1 Introduction

The growth of SMBHs takes place their active phase, where accretion generates vast amounts of radiation, visible in the UV/optical when unobscured (e.g. Hickox and Alexander, 2018). However, the majority of AGN activity is obscured, with high column densities of $N_{\rm H} > 10^{22}$ cm^{-2}, with at least 1/3 exceeding column densities of $N_{\rm H} > 10^{24}$ cm^{-2} (e.g. Boorman et al., 2025). This fact, combined with the need for AGN feedback to explain the evolution of galaxies, suggests that a key phase of growth is hidden behind vast quantities of dust.

The nature/geometry of the obscuring dusty structure and how it evolves as the SMBH grows/feedbacks, is unknown. From the earliest suggestion of a simple torus (Antonucci and Miller, 1985; Antonucci, 1993) to explain the presence/lack of broad emission lines in AGN spectra, the dust in/around AGN is thought to be dynamic (e.g. Wada, 2012), showing extended dust in the polar direction (e.g. López-Gonzaga et al., 2016; Haidar et al., 2024), possibly existing as an outflow from the AGN itself.

The idea that ULIRGs are the progenitors of quasars is not new (Sanders et al., 1988; Hopkins et al., 2006; Veilleux et al., 2009), considering that local ULIRGs are predominantly major mergers, which allows the disruption of angular momentum, feeding the central black hole(s). As the SMBH grows, it is likely to radiatively drive winds that clear the obscuring material, revealing an unobscured quasar. This "blowout" phase succeeding the obscured feeding stage, may cause the extended polar dust seen through infrared interferometry (e.g. López-Gonzaga et al., 2016; Hönig et al., 2012; Hönig et al., 2013). However the observational evidence for polar dust is tentative and it is not clear how it is linked to the most obscured nuclei found in ULIRGs.

Studying the dust continuum directly which appears through the near, mid and far-infrared, depending on the distribution of dust temperature and/or extinction, provides a direct measure of the nature of the dust. However interpreting the observed continuum can be challenging. The approach has often been to use libraries of torus models to fit the data, which works reasonably well for Seyfert galaxies (e.g. Ramos Almeida et al., 2009; Alonso-Herrero et al., 2011; Alonso-Herrero et al., 2012;

Martínez-Paredes et al., 2015; Martínez-Paredes et al., 2020; Martínez-Paredes et al., 2021; González-Martín et al., 2019a; González-Martín et al., 2019b; García-Bernete et al., 2019; García-Bernete et al., 2022d). However, this often requires fitting different libraries to different objects and can be particularly challenging for the most obscured objects (e.g. García-Bernete et al., 2022b; Efstathiou et al., 2022; Varnava and Efstathiou, 2024). Moreover, the presence of ice absorption features of H_2O, CO, CO_2 etc, in both ULIRGs (e.g. Spoon et al., 2002) and Seyferts (e.g. García-Bernete et al., 2024c), is particular clear now with JWST. As torus models typically do not include these features, fitting the data directly with these libraries proves challenging.

Since the advent of JWST, there have been many studies of both obscured nuclei (e.g. Donnan et al., 2023b; Buiten et al., 2023; García-Bernete et al., 2024a; Rich et al., 2023) and AGN (e.g. García-Bernete et al., 2024b; Zhang et al., 2024), however these works tend to focus on individual objects or small samples. With the large volume of objects now observed, the use of significant samples is now possible.

In this chapter, I will use the tools and techniques outlined in previous chapters, in particular Chapter 4, to infer the properties of dust in the nuclei of a significant sample of ULIRGs, LIRGs and crucially more "normal" Seyfert galaxies. With a consistent approach to modelling the dust continua for this wide range of nuclei, I aim to infer the nature of the obscuring dust and any evolution to test the scenario proposed in Sanders et al. (1988).

In section 5.2 I outline the samples and data I use in this work. In section 5.3 I describe four libraries of torus models to interpret my findings. In section 5.4 I provide a summary of the fitting technique in Chapter 4, with some updates. I then present my results in Section 5.5 before some discussion in Section 5.6.

5.2 Sample and Observations

5.2.1 JWST Data

In this work, I use data from multiple observing programs with JWST. The majority is public archival data from cycles 1, 2 and GTO programs. Details of all the data

used in this work is shown in Table 5.1.

Namely, I use the GOALS ERS program 1328 (P.I. Lee Armus & Aaron Evans) providing NIRSpec IFU and MIRI MRS data of four local LIRGs. The MIRI MRS data provides spectral cubes between 5 and 28 μm with an increasing FOV from 3.2" $\times$ 3.7" at 5μm to 6.6" $\times$ 7.7" at 28 μm. The NIRSpec IFU data is varies depending on the object/observing program. This is either the high spectral resolution of $R \sim$ 2700, with all four of the disperser/grating combinations, namely, G140H/F070LP, G140H/F100LP, G235H/F170LP, G395H/F290LP providing coverage from 1-5 μm, or the medium spectral resolution of $R \sim$ 1000 with the disperser/grating combinations G140M/F070LP, G140M/F100LP, G235M/F170LP, G395M/F290LP. Many of the observing programs only include the longest wavelength disperser, only providing data from 2.87 - 5.27 μm. I find this coverage is sufficient to constrain the stellar continuum reasonably well.

To complete the LIRG sample I include cycle 1 data from GO 1991 (P.I. George Privon) of two local CONS, NGC 4418 and IC 860 as well as NGC 6240 from GTO 1265 (P.I. Almudena Alonso-Herrero).

The majority of the ULIRG sample is from the GOALS cycle 2 ULIRG survey, GO 3368 (P.I. Lee Armus & Aaron Evans), which provides 12 ULIRGs, some with multiple pointings depending on the separation of the nuclei. I supplement this sample with Arp 220 and Mrk 231 from the GTO programs 1267 (P.I. Daniel Dicken) and 1268 (P.I. Roberto Maiolino). I also use GO 1717 (P.I. Vivian U) to obtain MIRI MRS data of UGC 5101 with the NIRSpec IFU data provided by GO 2186 (P.I. Shunsuke Baba). I also use this program for the NIRSpec portion of Mrk 273 and IRS 10565+2448. I excluded IRAS 09022-3615 from the GOALS ULIRG survey, as it contains two nuclei that are separated at short wavelengths but not at long wavelengths making extracting a spectrum of each difficult.

The Seyfert sample comes from GATOS cycle 1 and 2 programs. These are GO 1670 (P.I. Taro Shimizu) and GO 3535 (P.I. Ismael Garcia-Bernete). Those from GO 3535 have both NIRSpec IFU and MIRI MRS while GO 1670 only has MIRI MRS data. I additionally include NGC 7319 which comes from the

Early Release Observation ERO 2732 (P.I. Klaus Pontoppidan). It is important to note that the luminoisity and host galaxies of Seyferts differs from the (U)LIRGs, which are much more luminous. The purpose here is to have a sample of AGN tori but is far from complete.

5.2.2 Data Reduction

In this chapter I use both NIRSpec IFU and MIRI MRS data. The data reduction process is identical to that in Chapter 4 and described in Section 4.2.2.

I extract spectra from the reduced data cubes in the same way as Chapter 4. This involves a 0.3" radius aperture, applying a fringe correction on the 1D spectrum after extraction and applying a PSF wavelength correction using a standard star. More details can be found in in Section 4.2.2. The only exception is Mrk 231, where the longest wavelength channel of the NIRSpec data, g395h-f290lp, between 2.9 μm and 5 μm, proved to show an unusual continuum which I deemed unreliable. In particular, erroneous features appear in the extracted continuum and the flux level does not match the MIRI or the shorter wavelength NIRSpec data. By comparing to archival data of Mrk 231 from the AGNSEDATLAS [1] (Brown et al., 2019), the first two channels appeared reliable, providing data up to 2.9 μm, which is sufficient to constrain the near-IR continuum from this target.

While in the previous chapter, I used the background frames to estimate the error bars for the extracted spectra, I instead calculate the errors for each spectra separately. The main motivation over using the background frames, was to add this as an initial step in my fitting tool to ensure all users of the tool use consistent method of predicting the noise for a given spectrum. This ensures that the regularisation is weighted properly when calculating the log-probability (equation (4.4)) during the fitting process. The noise levels predicted via this method are consistent with the method in the previous chapters.

To produce errors for the fluxes I calculate the noise as a function of wavelength. I do this by first masking all the emission lines before applying a median filter to

[1] archive.stsci.edu/hlsp/agnsedatlas

Table 5.1: Summary of Targets

Name	RA	Dec	z	Nuclei	Observing Program
		LIRGs			
VV 114	01h07m47.1800s	-17d30m25.300s	0.020	NE, SW	ERS 1328
NGC 3256	10h27m51.0300s	-43d54m18.200s	0.009	N, S	ERS 1328
NGC 4418	12h26m54.6075s	-00d52m39.292s	0.007	Nuc	GO 1991
IC 860	13h15m03.5083s	+24d37m07.791s	0.013	Nuc	GO 1991
NGC 6240	16h52m58.8708s	+02d24m03.333s	0.024	N, S	GTO 1265
IIZw96	20h57m23.9400s	+17d07m39.500s	0.036	NE, SW	ERS 1328
NGC 7469	23h03m15.6142s	+08d52m26.100s	0.016	Nuc	ERS 1328
		ULIRGs			
IRAS 05189-2524	05h21m01.3969s	-25d21m45.229s	0.044	Nuc	GO 3368
IRAS 07251-0248	07h27m37.5835s	-02d54m54.185s	0.088	Nuc	GO 3368
IRAS 08572+3915	09h00m25.3828s	+39d03m54.298s	0.058	Nuc	GO 3368
IRAS 09111-1007	09h13m38.8450s	-10d19m20.037s	0.054	Nuc	GO 3368
UGC 5101	09h35m51.5979s	+61d21m11.721s	0.039	Nuc	GO 1717, GO 2186
IRAS 10565+2448	10h59m18.1335s	+24d32m34.549s	0.043	Nuc	GO 2186, GO 3368
Mrk 231	12h56m14.2340s	+56d52m25.237s	0.042	Nuc	GTO 1268
IRAS 13120-5453	13h15m06.3348s	-55d09m22.773s	0.031	Nuc	GO 3368
Mrk 273	13h44m42.1110s	+55d53m12.651s	0.037	N, S	GO 1717, GO 2186
IRAS 14348-1447	14h37m38.4909s	-15d00m19.117s	0.082	NE, SW	GO 3368
IRAS 15250+3609	15h26m59.4136s	+35d58m37.286s	0.055	Nuc	GO 3368
Arp 220	15h34m57.2064s	+23d30m13.262s	0.018	E, W	GTO 1267
IRAS 19542+1110	19h56m35.3900s	+11d19m03.000s	0.065	Nuc	GO 3368
IRAS 20551-4250	20h58m26.8048s	-42d39m00.431s	0.043	Nuc	GO 3368
IRAS 22491-1808	22h51m49.3505s	-17d52m23.984s	0.078	Nuc	GO 3368
IRAS 23128-5919	23h15m46.7628s	-59d03m15.692s	0.045	N, S	GO 3368
		Seyferts			
MCG-05-23-016	09h47m40.1290s	-30d56m55.992s	0.009	Nuc	GO 1670
NGC 3081	09h59m29.5431s	-22d49m34.720s	0.008	Nuc	GO 1670
NGC 3227	10h23m30.5748s	+19d51m54.340s	0.004	Nuc	GO 3535
NGC 4051	12h03m09.6073s	+44d31m52.709s	0.002	Nuc	GO 3535
NGC 5506	14h13m14.8756s	-03d12m27.698s	0.006	Nuc	GO 1670
NGC 5728	14h42m23.8735s	-17d15m10.855s	0.009	Nuc	GO 1670
ESO 137-G034	16h35m14.0026s	-58d04m47.869s	0.009	Nuc	GO 1670
NGC 7172	22h02m01.8945s	-31d52m10.525s	0.009	Nuc	GO 1670
NGC 7582	23h18m23.6280s	-42d22m13.512s	0.005	Nuc	GO 3535
NGC 7319	22h36m03.5453s	+33d58m32.593s	0.023	Nuc	ERO 2732

smooth the spectrum. I then measure the standard deviation of the data around the smoothed spectrum in bins of 100 wavelength pixels to calculate the noise as a function of wavelength. This function is then also smoothed with a median filter to prevent spikes in the noise. We find that this produces accurate errors for any input spectrum, suitable for fitting with my tool and measuring the fluxes of emission features. One caveat, is that the presence of ro-vibrational CO at $\sim 4.6\mu$m can artificially inflate the standard deviation in bins that contain these features. Smoothing the noise function helps, but the errors can be overestimated if one wants to analyse the ro-vibrational transitions of CO. Such analysis is beyond the scope of this work however.

5.3 Torus Models

In order to interpret the inferred 2D dust distributions I obtain from fitting the JWST spectra, I use radiative transfer torus models from the literature. The aim here is to generate mock data through different parameter combinations for a range of torus libraries and fit the mock data with the fitting tool to infer the 2D dust distribution for each torus model. I can therefore link features I see in the inferred 2D dust distribution from the real data to physical parameters of the torus models.

I use the CYGNUS models (Efstathiou et al., 2013; Varnava and Efstathiou, 2024), SKIRTOR (Stalevski et al., 2016), Fritz (Fritz et al., 2006) and the Siebenmorgen (Siebenmorgen et al., 2015) models. With these models, one can generate spectra with different physical parameters of the AGN torus such as viewing angle, opening angle etc. By fitting these spectra with my tool, I will infer what kinds of models reproduce the dust distribution that is seen in the (U)LIRGs and Seyfert galaxies and what parameters are most important in reproducing different features of this distribution.

The four libraries make different assumptions about the geometry and dust properties of the torus. I chose these specific libraries as they are implemented in a single code from Varnava and Efstathiou (2024) and use full radiative transfer.

I show the models form each of the four libraries in Fig. 5.1, with a diagram illustrating the different geometry for each.

The first library is the CYGNUS models (Efstathiou et al., 1995) which assume a tapered disk with a smooth distribution of dust with a standard mixture of silicates and carbon based grains. The tapered disk is defined as one that has a maximum scale height, h, which decreases only in the inner regions of the disk. As a result, the fraction of grains exposed to the central power source is reduced, where the outer regions of the disk contribute more cold dust. These models are governed by four parameters, the UV (0.1 μm) equatorial optical depth, τ_{UV}, which relates to the column density along the mid-plane of the disk, the outer to inner radius, r_2/r_1, the opening angle as measured from the polar axis, OA, and the inclination measured from the equator, i. For these models the value of h/r_1 is fixed at 10, to keep the inner structure of the torus the same irrespective of the value of r_2/r_1. These parameters are illustrated in Fig. 5.1 and described in more detail in Efstathiou et al. (1995).

The Fritz models (Fritz et al., 2006) are similar but instead assume a flared disk. This disk is defined as one that linearly increases its scale height from the centre and therefore has a larger surface exposed to the central radiation producing a higher fraction of hot dust over the tapered disk models. This library shares the same four parameters as the CYGNUS models and is also illustrated in Fig. 5.1.

The SKIRTOR library (Stalevski et al., 2016) is also a flared disk but instead assumes a two-phase medium with a low density smooth component and a high density clumpy medium consisting of individual clouds of dust. With a clumpy medium, different lines of sight have different column densities depending on the presence of a high density cloud. This allows hot dust from the inner regions of the disk to be visible even when looking edge-on through the midplane of the disk. This library also shares the same four parameters as the previous two libraries and is described in Fig. 5.1.

The Siebenmorgen models (Siebenmorgen et al., 2015) use a two phase medium with a smooth disk embedded within a spherical clumpy envelope comprised of high

density clouds. Additionally Siebenmorgen assumes "fluffy" dust grains which have a higher emissivity in the sub-mm. Unlike the other three libraries the four parameters governing these models are the volume filling factor, which is the percentage of volume occupied by the high density clumps, the optical depth of the clouds, τ_C, the midplane optical depth, τ_{mid}, and the inclination at which the the torus is viewed at, i. This library is illustrated in Fig. 5.1, where more details can be found in Siebenmorgen et al. (2015).

To be able to measure the dust distribution for different torus models, I generate mock JWST (NIRSpec + MIRI) data for a variety of different parameter combinations. As the spectral resolution of these models are significantly lower than JWST spectra, I use a cubic spline interpolation in log space (to prevent negative fluxes), interpolated onto the NIRSpec and MIRI wavelength values from one of the real spectra. I also generate noise for the mock spectra, equivalent to the signal to noise of a typical JWST spectra of a galaxy nucleus.

5.4 Spectral Fitting

In Chapter 4 and Donnan et al. (2024), I presented a new fitting technique that is able to fit the complex spectra of a variety of objects observed with JWST. Below I summarise the methodology of this technique. More details can be found in Chapter 4.

To fit the combined NIRSpec + MIRI spectra, I use a differential extinction model to generate the dust continuum. The continuum is generated using a 2D distribution of extinction (given by the optical depth at 9.8 μm, $\tau_{9.8}$), and dust temperature, where the resulting continuum is a 2D weighted average of blackbodies at a given temperature subject to a screen of extinction at a given $\tau_{9.8}$. The weights are the 2D distribution, which is constrained by the data under some regularisation to ensure it is physically meaningful and does not over-fit the data. In addition to the dust continuum, I also fit the stellar continuum at short wavelengths, using two templates from FSPS (Conroy et al., 2009; Conroy and Gunn, 2010), a 10 Gyr and a 100Myr population. This assumes a Salpeter (1955) IMF at solar metallicity. In

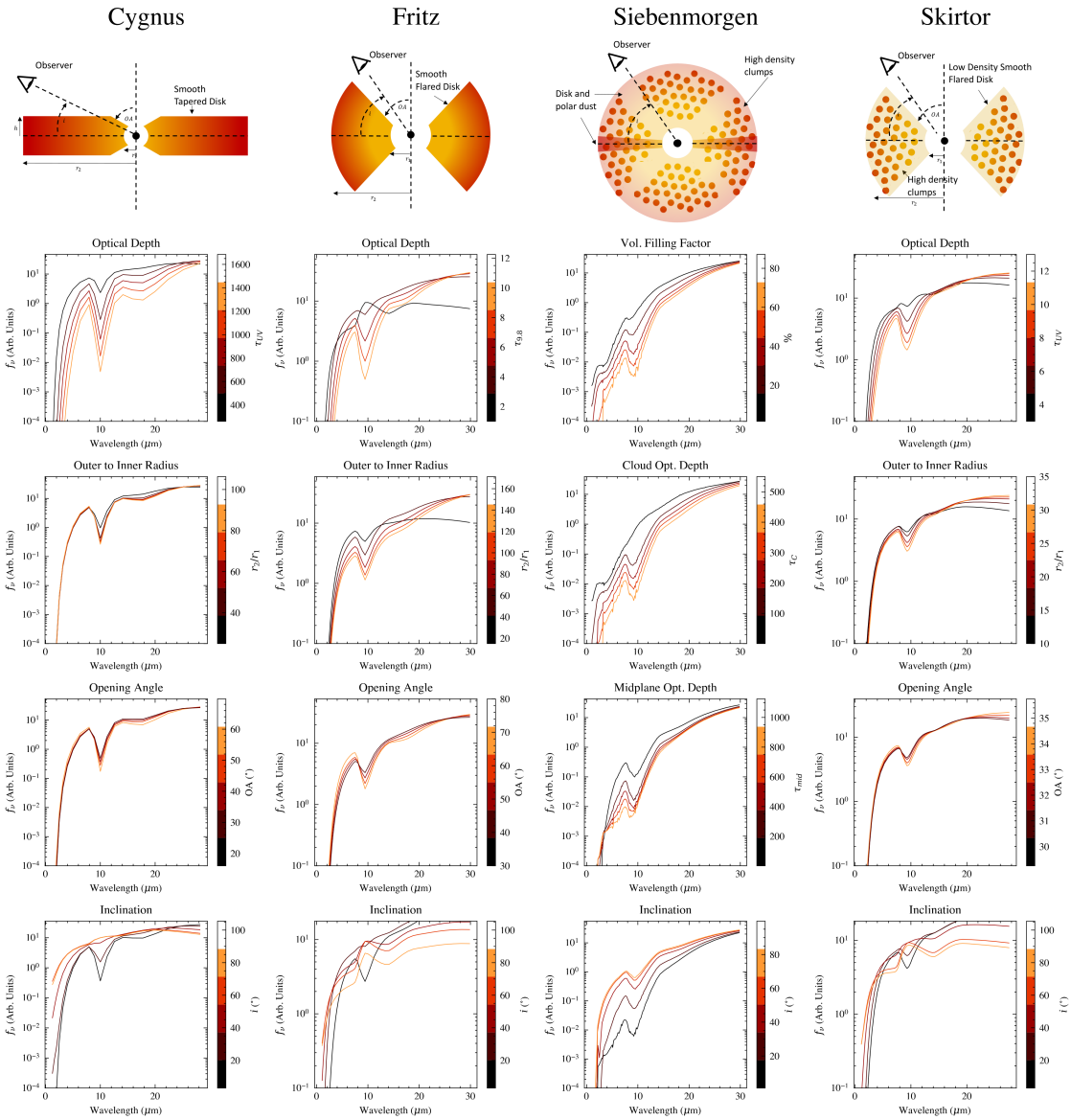

Figure 5.1: Overview of the 4 libraries of torus models we test in this work. Each column is a different library, with each panel showing the variety of spectra produced for different physical parameters. In each case only one parameter is changed with the others set to some default. These are, Cygnus: $\tau_{\rm UV} = 500$, $r_2/r_1 = 50$, $OA = 40°$, $i = 5°$, Fritz: $\tau_{9.7} = 5$, $r_2/r_1 = 50$, $OA = 30°$, $i = 5°$, Seibenmorgen: $V_{ff} = 50\%$, $\tau_C = 300$, $\tau_{mid} = 500$, $i = 5°$, Skirtor: $\tau_{\rm UV} = 500$, $r_2/r_1 = 50$, $OA = 40°$, $i = 5°$. The top panels show a diagram, illustrating the geometry of each kind of model. The definitions of the inclination, i, opening angle, OA, and radii, r_1, r_2 are shown.

this work I update the stellar templates to match the spectral resolution of NIRSpec using the X-shooter Spectral Library (Verro et al., 2022), still using a Salpeter (1955) IMF at solar metallicity, and degrading the resolution to match that of JWST. As X-shooter is limited to $\lambda < 2.5\mu$m, I use the FSPS template beyond 2.5 μm. This is not an issue as the majority of absorption features present in the stellar continuum are at wavelengths less than 2.5 μm, where the spectral resolution becomes relevant.

The PAH features are also fitted using a series of Drude profiles, these are shown in Table. A.2. In Chapter 4, I described some restrictions on certain PAH features to prevent the continuum being unphysically fit by the PAH features. This was only a problem when the PAH emission was weak, such as in AGN. In this chapter I update these restrictions, to now use a prior on the profile of the PAH emission within certain wavelength bins. This way, if the signal to noise of the PAH emission is low and there is not enough information within the data to properly constrain the shape of the PAH features, the model will instead default to a template of typical PAH emission rather than trying to fit features in the continuum with the PAH profiles.

I generate the PAH prior templates by taking the average of the PAH emission from the 12 star-forming regions from NGC 7469 and NGC 3256, in Chapter 4.

As described in Chapter 4, the fitting tool calculates the flux of emission lines after the fit is completed. As the lines are masked during the fitting process, this is done by integrating the residuals between two limits around each line. For the purposes of this work, I found that this method of integrating did not produce accurate fluxes for the [Ne V] (14.32 μm) line, as it is often faint and blended with the nearby [Cl II] (14.36 μm) line. I therefore opted to fit the [Ne V] + [Cl II] lines with two component Gaussians.

As I am primarily interested in the [Ne V]/[Ne II] ratio, I also fit the [Ne II] line simultaneously with the [Ne V] + [Cl II]. Each line is fitted with two components, a broad and a narrow Gaussian component. The dispersion and velocity offset is restricted to be the same for each line with only the amplitude varying. I employ MCMC to perform the fit to enable uncertainties of the integrated fluxes of each line.

I show an example fit for NGC 6240 N, where the [Ne V] + [Cl II] lines are fitted.

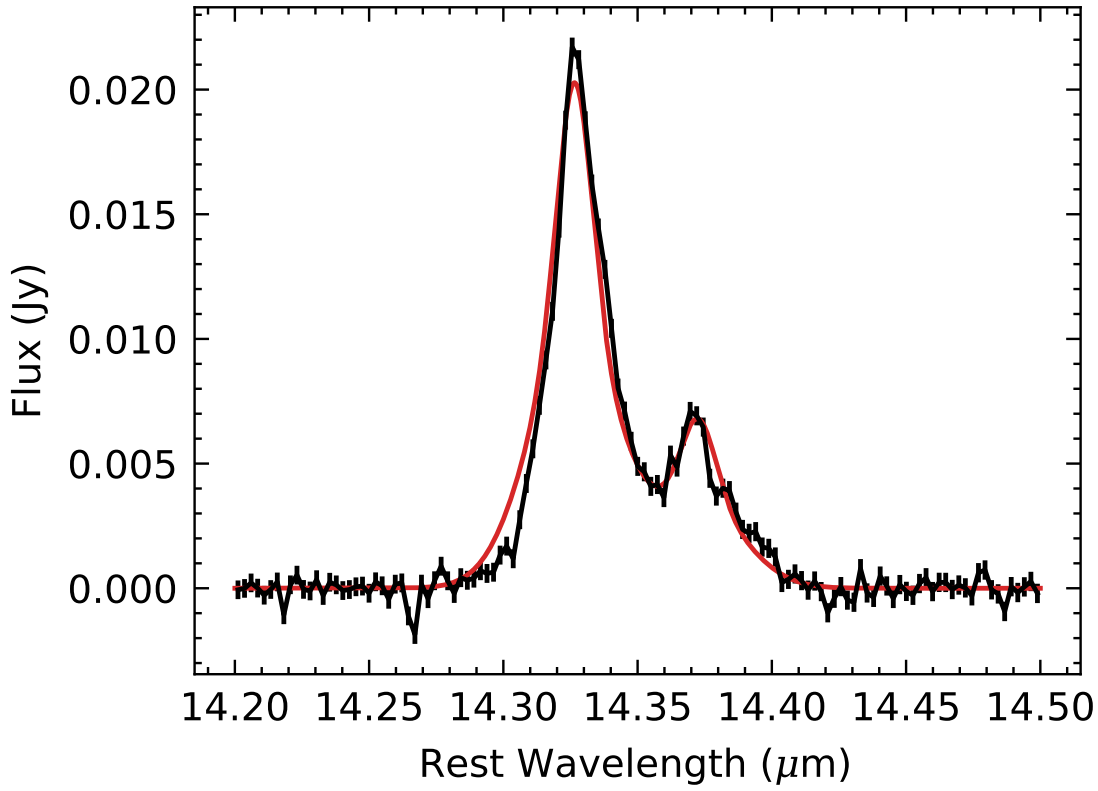

Figure 5.2: Example fit of the [Ne V] (14.32 μm) and [Cl II] (14.36 μm) lines in NGC 6240 N, where each line is fitted with two Gaussian components. This process is used to extract the flux of [Ne II], [Ne III] and [Ne V], to produce the ratios shown in Fig. 5.6. The continuum subtracted spectrum is shown, with the fitted lines in red.

5.5 Results

5.5.1 JWST Spectra

By fitting the samples of ULIRGs, LIRGs and Seyfert galaxies, I infer the 2D distribution of dust temperature and extinction. I show these in three separate plots for each sample. The LIRGs are shown in Fig. 5.3, the ULIRGs in Fig. 5.4 and the Seyferts in Fig. 5.5. It is clear that there is a wide variety of shapes of the dust distribution amongst the objects, particularly for the Seyfert galaxies. In the following sections I discuss each sample in more detail.

Dust Distribution

Amongst the ULIRG sample the shape of the dust distribution appears much less varied than the Seyfert sample. This likely suggests that AGN tori are much more

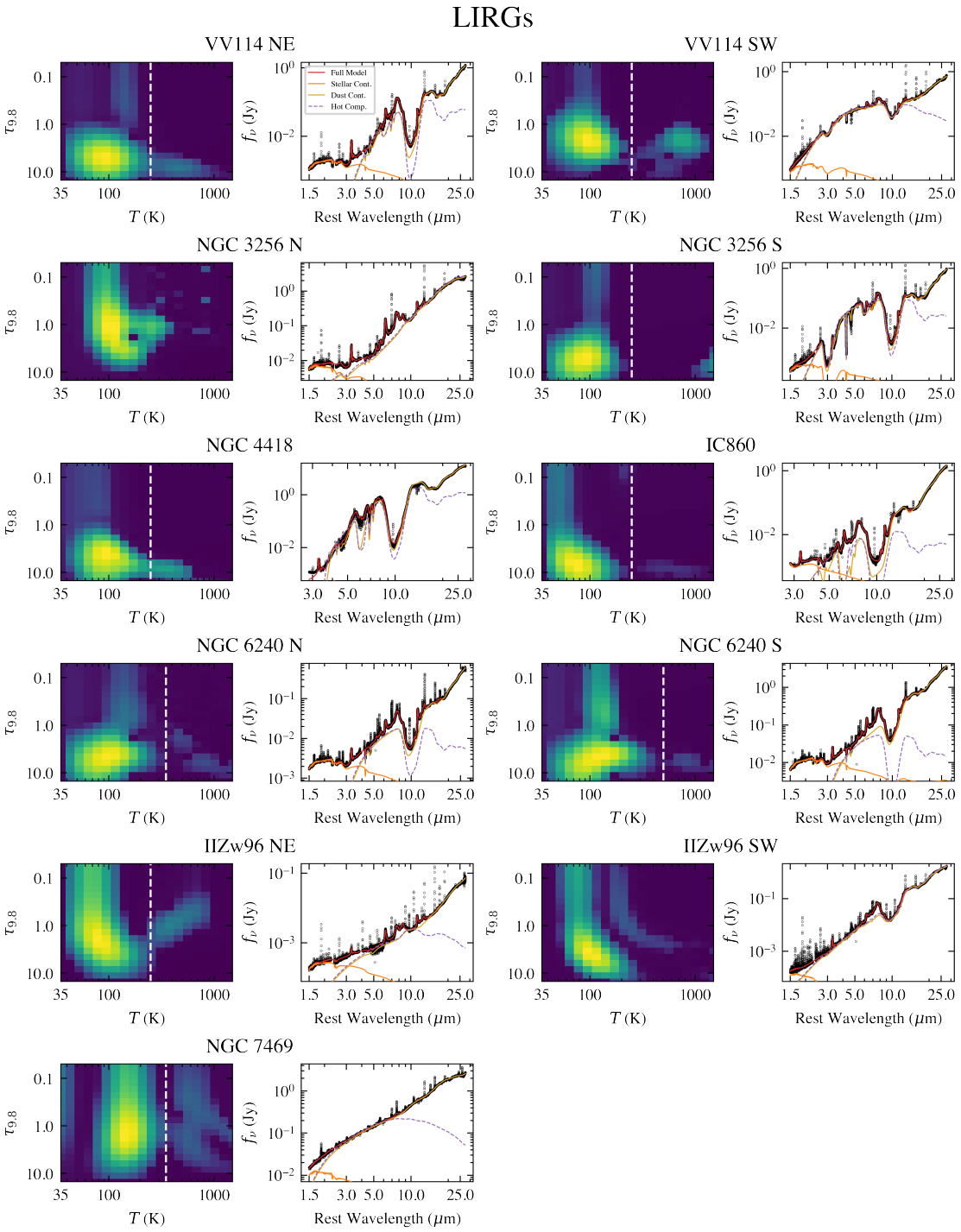

Figure 5.3: Results of the fitting for the LIRG sample. The left panel in each case shows the inferred 2D dust distribution of temperature and extinction. The vertical white dashed line shows the cut-off to measure the temperature and extinction of the hot dust component where present. The right panel shows the data with the model fit. The stellar and dust continuum components are also shown. In cases where a hot dust component is present, the isolated continuum of this component is shown with the purple dashed line.

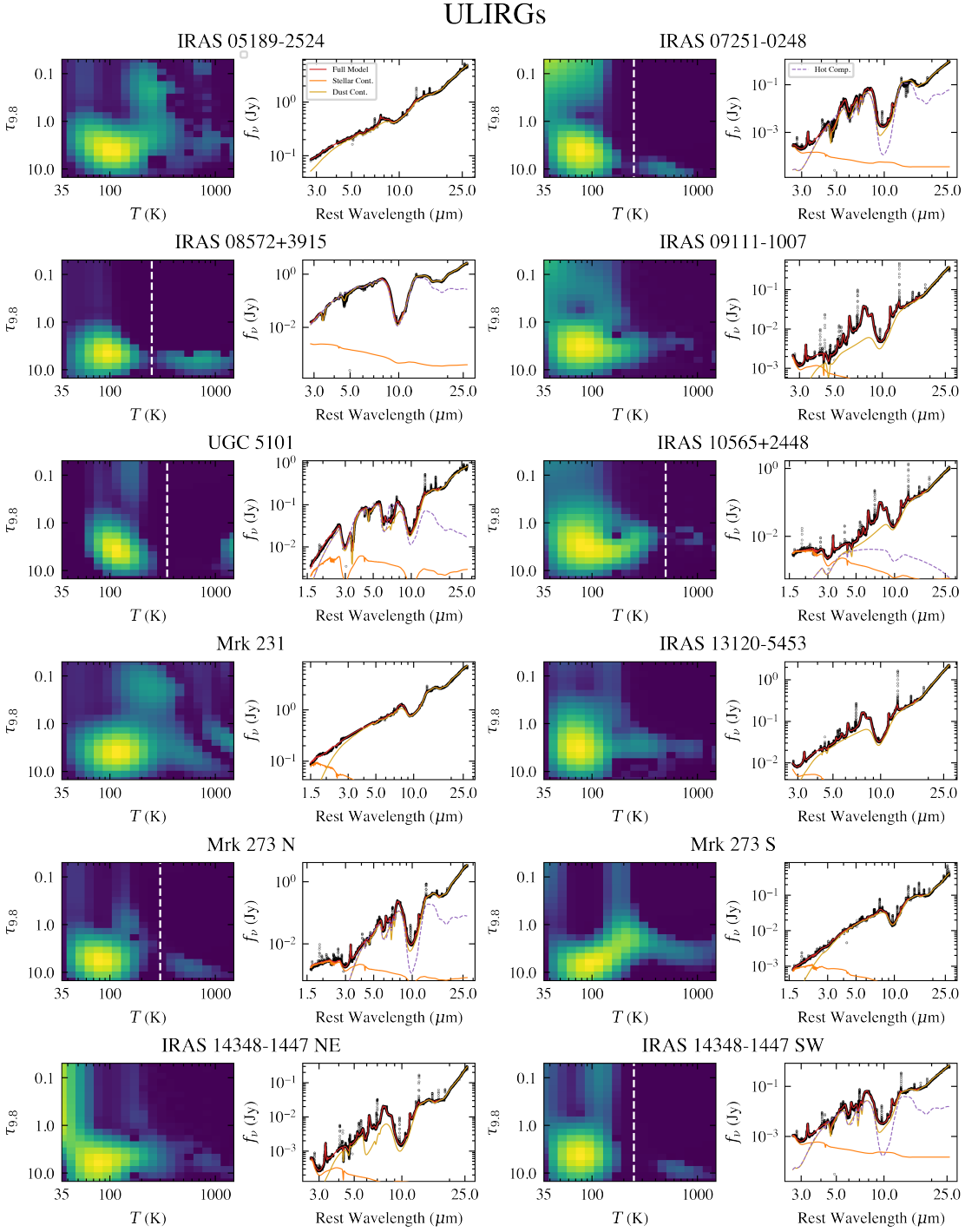
ULIRGs
IRAS 05189-2524
IRAS 07251-0248
IRAS 08572+3915
IRAS 09111-1007
UGC 5101
IRAS 10565+2448
Mrk 231
IRAS 13120-5453
Mrk 273 N
Mrk 273 S
IRAS 14348-1447 NE
IRAS 14348-1447 SW
Full Model
Stellar Cont.
Dust Cont.
Hot Comp.
$\tau_{9.8}$
T (K)
f_ν (Jy)
Rest Wavelength (μm)

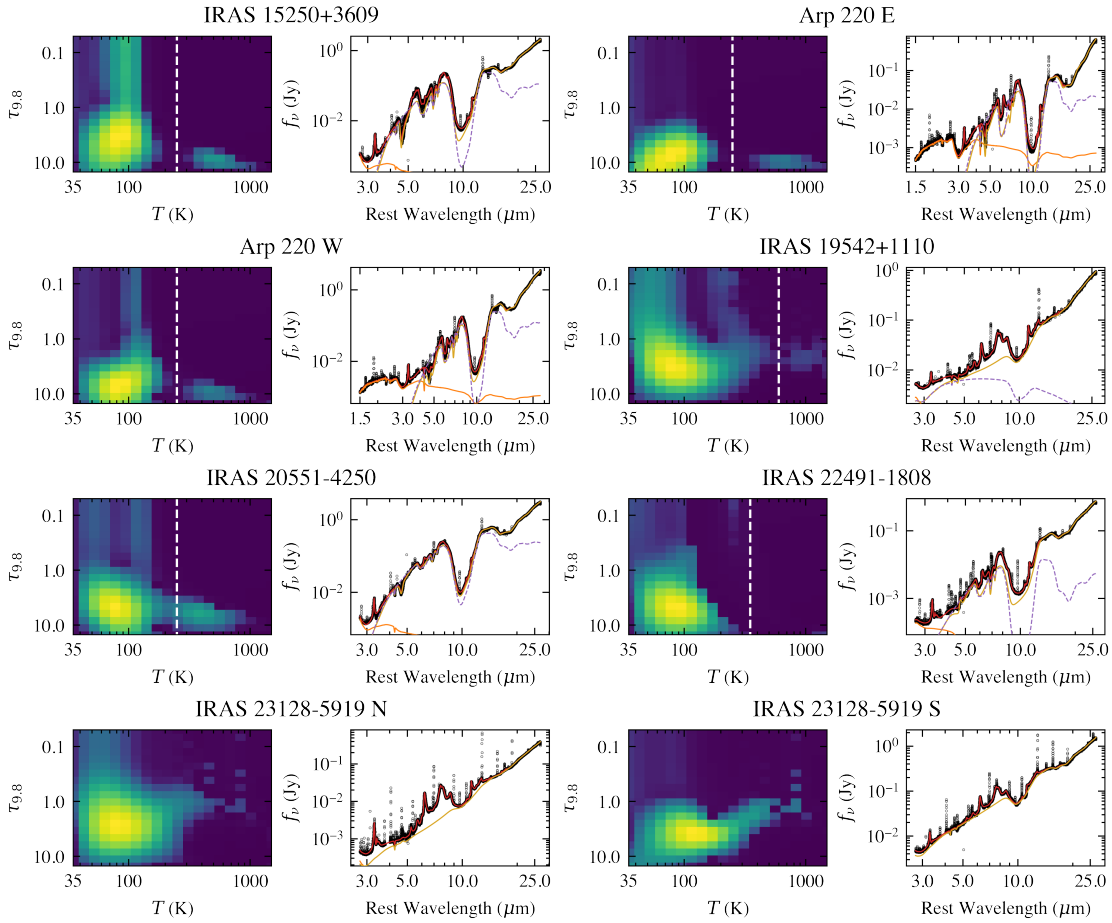

Figure 5.4: Results of the fitting for the ULIRG sample. The left panel in each case shows the inferred 2D dust distribution of temperature and extinction. The vertical white dashed line shows the cut-off to measure the temperature and extinction of the hot dust component where present. The right panel shows the data with the model fit. The stellar and dust continuum components are also shown. In cases where a hot dust component is present, the isolated continuum of this component is shown with the purple dashed line.

diverse amongst the wider AGN population compared to what we see in ULIRGs which may contain an extreme subsection of the total population of AGN.

One particular shape of the dust distribution stands out amongst the sample, which has a distinct "warm" and "hot" component, similar to what was found in Chapter 4. In fact, a majority of the ULIRGs show this kind of dust distribution. For those objects, I placed a cut off temperature and measured the mean extinction, $\tau_{9.8}$, and temperature, T. This threshold is shown in Fig. 5.3 and Fig. 5.4 with a vertical white dashed line.

I plot the temperature and extinction of each component in Fig. 5.6. As before

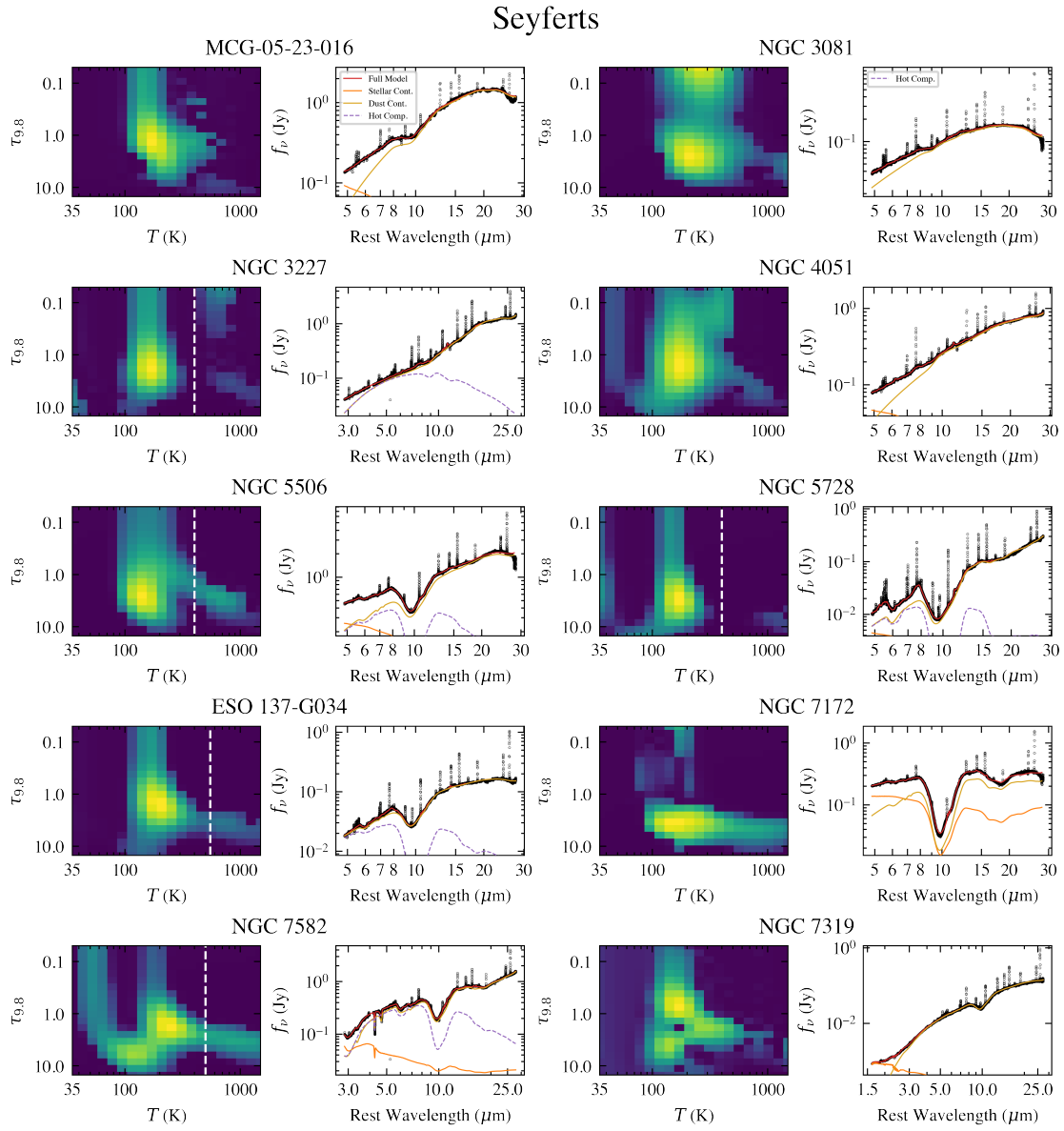

Figure 5.5: Results of the fitting for the Seyfert sample. The left panel in each case shows the inferred 2D dust distribution of temperature and extinction. The vertical white dashed line shows the cut-off to measure the temperature and extinction of the hot dust component where present. The right panel shows the data with the model fit. The stellar and dust continuum components are also shown. In cases where a hot dust component is present, the isolated continuum of this component is shown with the purple dashed line.

in Chapter 4, the error bars in this plot represent the spread of the hot component rather than statistical uncertainties. This plot reveals some interesting behaviour. Firstly, the most obscured sources (CONs) appear to occupy the top left of the plot. Amongst these are bona fide CONs from the HCN-vib surface brightness in Falstad et al. (2021). Interestingly, these sources all lie above $\tau_{9.8} > 5$ which was defined as the CON criteria in Chapter 2 when using the same silicate template (IRAS 08572+3915) as used in the extinction curve in this work (see Appendix A.1.1).

Sources such as Arp 220 E and IRAS 08572+3915 show similarly high levels of obscuration, also with $\tau_{9.8} > 5$, but show a higher temperature hot component. They also drop below the HCN-vib threshold of $\Sigma_{\rm HCN-vib} > 1 L_{\odot}$ pc^{-2} (Falstad et al., 2021). This suggests that the physical conditions required to achieve a high HCN-vib surface brightness also requires this hot dust component to be cool at temperatures of $T_{\rm hot} < 600$K.

Moving from the CONs in the top left corner of the plot, as the temperature increases the extinction appears to decrease. A majority of the Seyfert galaxies occupy the lower right quadrant of the plot. This may suggest some sort of evolution where the torus opens up revealing more hot dust. To test this I use the inferred dust distributions of the torus models. This is described in section 5.3.

I additionally plot the ratio of the [Ne V] (14.32 μm) and [Ne II] (12.81 μm) lines in Fig. 5.6. I choose this ratio as the [Ne V] line has a high ionisation potential (126.2 eV) compared to the [Ne II] (41 eV). This makes [Ne V] a relatively unambiguous tracer of AGN activity (e.g. Sturm et al., 2002; Pereira-Santaella et al., 2010), while [Ne II] is more strongly dominated by circumnuclear star-formation. As a large number of objects do not show any [Ne V] detection ($< 3\sigma$), the [Ne V]/ [Ne II] ratio becomes an upper limit. As different targets have different levels of noise, for clarity I plot any non-detections as a line ratio of zero in Fig. 5.6. I also found it difficult to fit [Ne V] in Mrk 273 N, where there is a broad blueshifted line present. Inspecting other high-IP lines at shorter wavelengths where the spatial resolution is greater, suggests that this is simply contamination from the nearby south nucleus which shows strong [Ne V]. There additionally appears to be a clump to the south west of

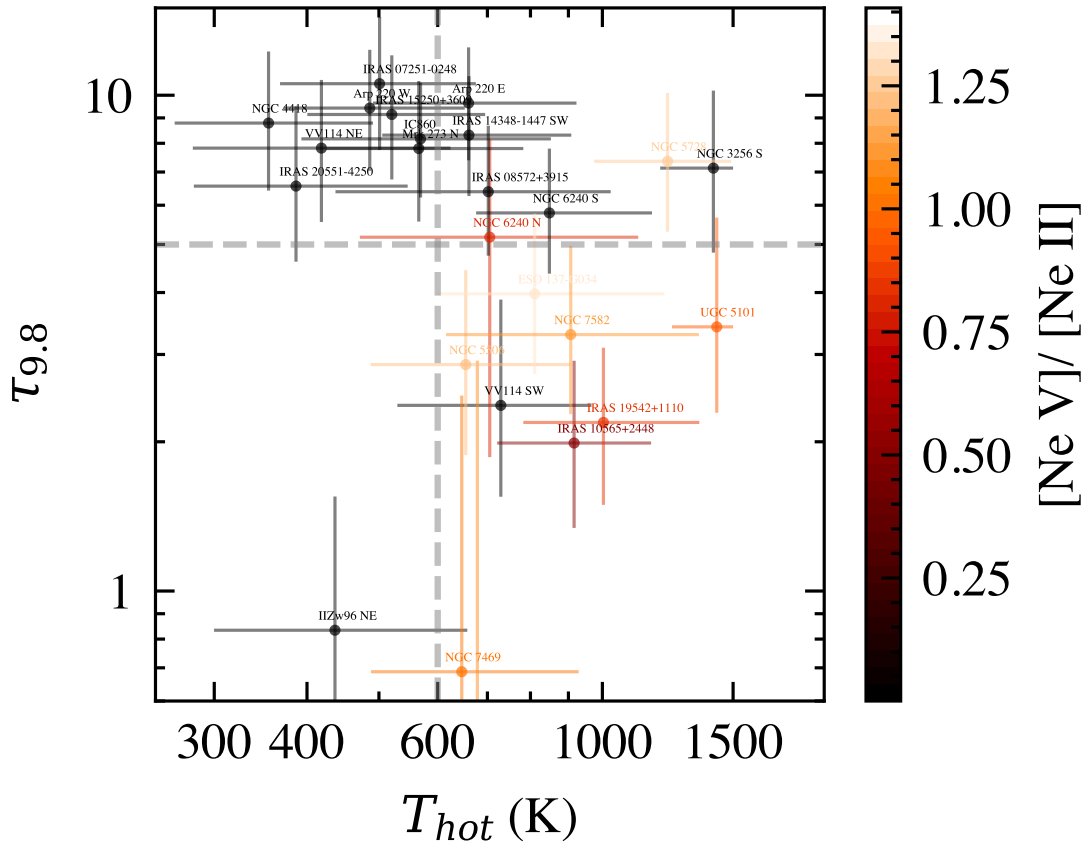

Figure 5.6: The extinction, $\tau_{9.8}$, and temperature, T, of the hot dust component where present in the inferred dust distribution. The colour of each point represents the [Ne V]/[Ne II] flux ratio. The vertical dashed line shows a cut-off at 600 K between the "cold" nuclei and the "hot" nuclei. The horizontal dashed line shows the optical depth threshold of 5, as defined in Chapter 2, to select CONs, in particular for the IRAS 08572+3915 silicate template as discussed in section A.1.1 and Fig. A.1.

the northern nucleus that shows very strong ionisation potential lines. The physical origins of this clump is unclear, however it may also contaminate the line detection in the northern nucleus. It is clear from this plot that the hotter, less obscured targets show relatively stronger [Ne V] emission, indicative of ionisation by an AGN.

5.5.2 Torus Models

In Section 5.3, I described the four libraries of radiative transfer simulations of different AGN tori. As each library contains 4 free parameters and I vary each of them 5 times, there is a total of 80 model spectra to fit. To easily digest all the information, I present the fits to each library separately, in Figs. 5.7, 5.8,

5.9, 5.10. In each figure, each column shows the inferred 2D dust distribution for varying a given parameter.

Cygnus

The first are the Cygnus models, which represents a smooth tapered disk geometry. The inferred dust distributions are shown in Fig. 5.7. For each fit, one of the parameters of the torus model is varied while the other parameters are fixed at some default value. These are: $\tau_{\rm UV} = 500$, $r_2/r_1 = 50$, $OA = 40°$, $i = 5°$. This means the majority of the fits displayed in Fig. 5.7 are viewed edge-on, with the exception of the fourth column where the inclination explicitly varies. As I will discuss in section 5.6.2, the edge-on models better reproduce the obscured nuclei.

These models produce a dust distribution most similar to the highly obscured nuclei, where the shape of the distribution matches and contains a "warm" and a "hot" dust component. Depending on the parameters of the model, these components can appear more or less distinct, with the opening angle having the greatest effect. As the opening angle increases (becomes more disk like), the hot component increases in temperature and increases in obscuration. This behaviour may imply an evolution in obscuration and/or dust temperature, moving from cold/obscured to hot/obscured, between the two top quadrants of Fig. 5.6.

The Cygnus models however have two shortcomings, namely, it predicts increasing obscuration as the opening angle is increased and does not reach high enough temperatures to explain objects such as NGC 5728 and UGC 5101. To address the first issue, one can simply lower the τ_{UV} parameter as the opening angle is increased. I do this in section 5.6.1. Physically this could be explained as a lowering of the column density as the dust is expelled. The second point may be addressed by including an explicit polar dust component within the Cygnus models (Varnava and Efstathiou, 2024), however this component is comprised of unobscured dust blackbodies which cannot explain the obscured but hot components found for objects such as UGC 5101. Therefore, one may need the flared and/or clumpy models to reach a sufficiently high temperature.

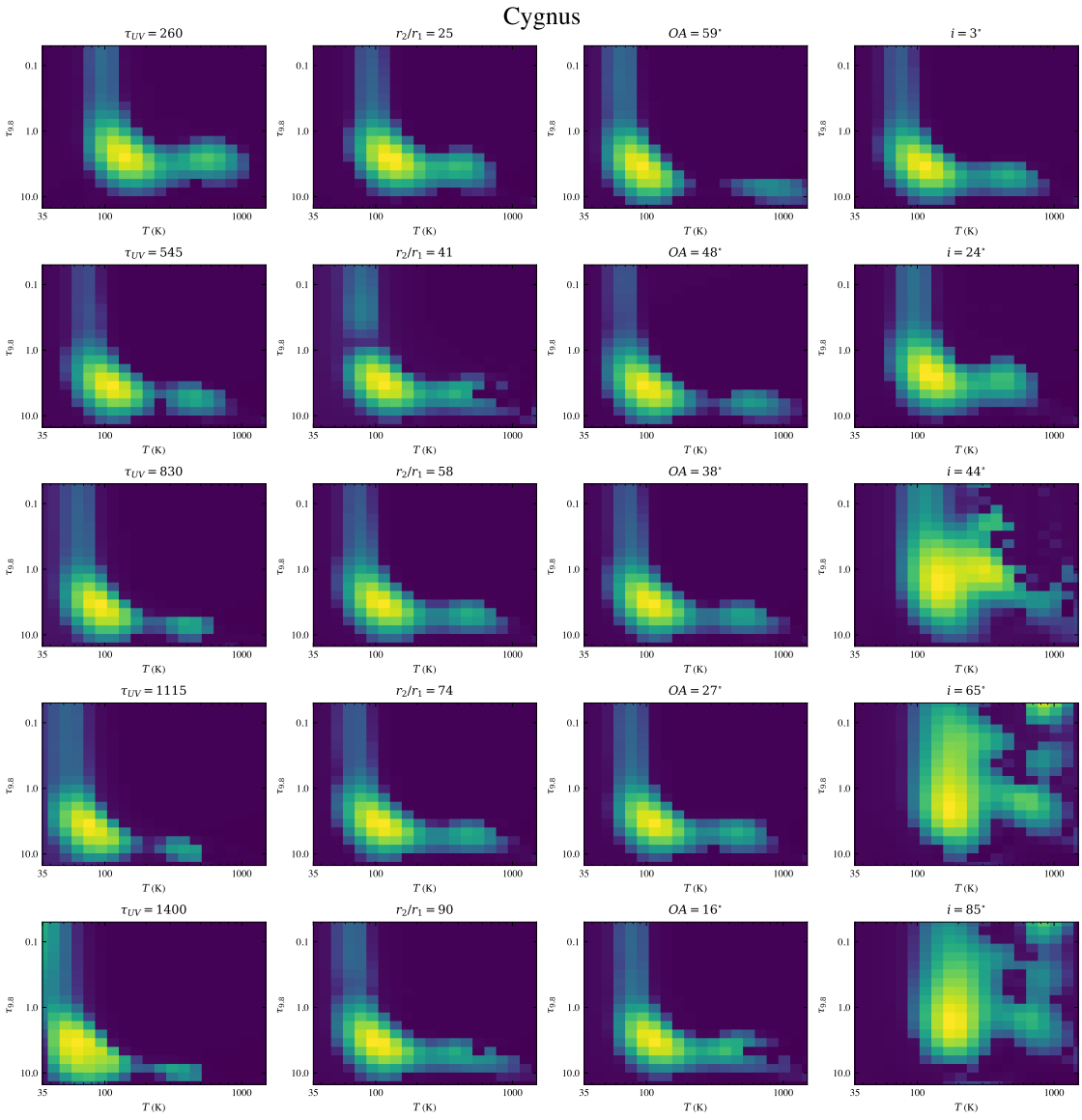

Figure 5.7: The inferred 2D dust distributions for the Cygnus (Efstathiou et al., 2013; Varnava and Efstathiou, 2024) library of torus models of a smooth tapered disk. Each column varies one of the four parameters. For each the other three parameters are set to a default of $\tau_{\rm UV} = 500$, $r_2/r_1 = 50$, $OA = 40°$, $i = 5°$ (edge-on).

It is also worth noting that the cooler component moves to lower temperatures as the optical depth is increased. This may be because more of the cooler dust is visible when the column density is increased where the hot dust contributes relatively less to the total emission. This may also be because the model struggles to fit the spectra accurately once the optical depth, $\tau_{\rm UV}$, increases above 1000, where there is simply a lack of pixels in the dust distribution grid to reproduce such a high optical depth. The grid can be extended to larger values of $\tau_{9.8}$ if necessary however none of the real data required such high optical depths.

The success of this model in reproducing the most obscured targets is unsurprising as a smooth dusty medium produces deeper silicate features than clumpy models (e.g. Efstathiou et al., 2022; García-Bernete et al., 2024c). Additionally, viewing a tapered disk edge-on provides a sufficiently high column density to produce the deep silicate absorption feature. However the main caveat of these models is that all the obscured nuclei must be viewed edge-on where even a moderate increase in inclination changes the dust distribution dramatically and no longer appears obscured, with the silicates in emission. This raises a key question: are all the obscured nuclei viewed edge-on? I discuss this further in section 5.6.2.

Fritz

The Fritz models describe a smooth flared tapered disk. The inferred dust distributions are shown in Fig. 5.8. Like the Cygnus models, each column shows one parameter being varied with the others defaulting to $\tau_{9.7} = 5$, $r_2/r_1 = 50$, $OA = 40°$, $i = 5°$. Similarly this means the majority of models show in Fig. 5.8 are viewed edge-on with the exception of the fourth column where the inclination is explicitly varied.

The shape of the dust distribution produces matches more closely to the Seyfert galaxies such as NGC 7582, NGC 7319, ESO 137-G034 and NGC 5506. Mrk 273 S in the ULIRG sample also matches this shape. For the Fritz models there is less of a clear separate hot component, however at large opening angles (more disk-like), the hot component separates, similar to the Cygnus models. Moreover,

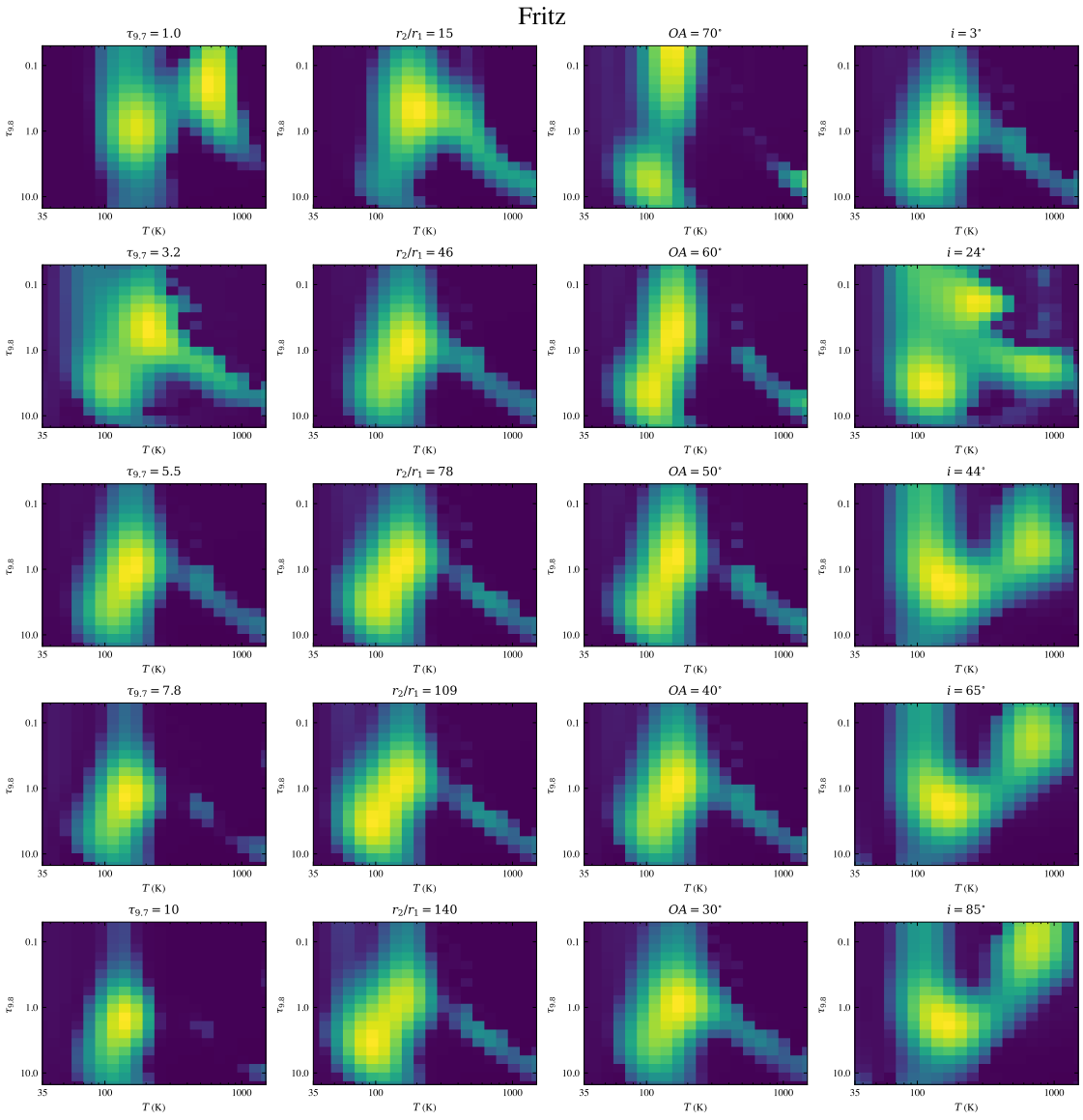

Figure 5.8: The inferred 2D dust distributions for the Fritz (Fritz et al., 2006) library of torus models of a smooth flared disk. Each column varies one of the four parameters. For each the other three parameters are set to a default of $\tau_{9.7} = 5$, $r_2/r_1 = 50$, $OA = 40°$, $i = 5°$.

when the opening angle increases (becomes more disk-like), the temperature of the hot component increases.

The dust distribution also changes as the ratio of the outer to inner radius, r_2/r_1 changes. This behaves as expected, where a larger ratio causes the distribution to be dominated more by lower temperature dust, as relatively more dust is at larger radii.

When viewed at higher inclinations, the shape once again changes dramatically, where the silicate feature diminishes or appears in emission. For example NGC 7469 matches the more face-on shape produced by the Fritz models, consistent with its type 1 classification (e.g. Wanders et al., 1997). As I will discuss in section 5.5.2, the Skirtor models providing a clumpy flared disk produce similar dust distributions and may be a better match for some targets such as NGC 7469.

Seibenmorgen

The Seibenmorgen models are the most unique in this work. These consist of two components, a smooth disk within a clumpy spherical medium. Unlike the other libraries, the opening angle cannot be varied, instead the models are controlled by the optical depth of the disk and the clouds separately, as well as the filling factor of the clouds. The inferred 2D dust distributions are shown in Fig. 5.9, where each column shows one parameter being varied where the others are set to a default of $V_{ff} = 50\%$, $\tau_C = 300$, $\tau_{mid} = 500$, $i = 5°$. As before, this means a majority of the panels in the figure are for an edge-on case.

The shape of the dust distribution appears to not vary as much as the other libraries. This is consistent with the SED shapes in Fig. 5.1, where the silicate feature never appears strongly in emission unlike the other libraries. This makes sense, especially when the volume filling factor and/or cloud optical depth are high, as the model is more spherically symmetric than the classical "torus" geometry.

Skirtor

The Skirtor library consists of a flared disk comprised of high density individual clouds within a low density smooth medium. The inferred 2D dust distributions

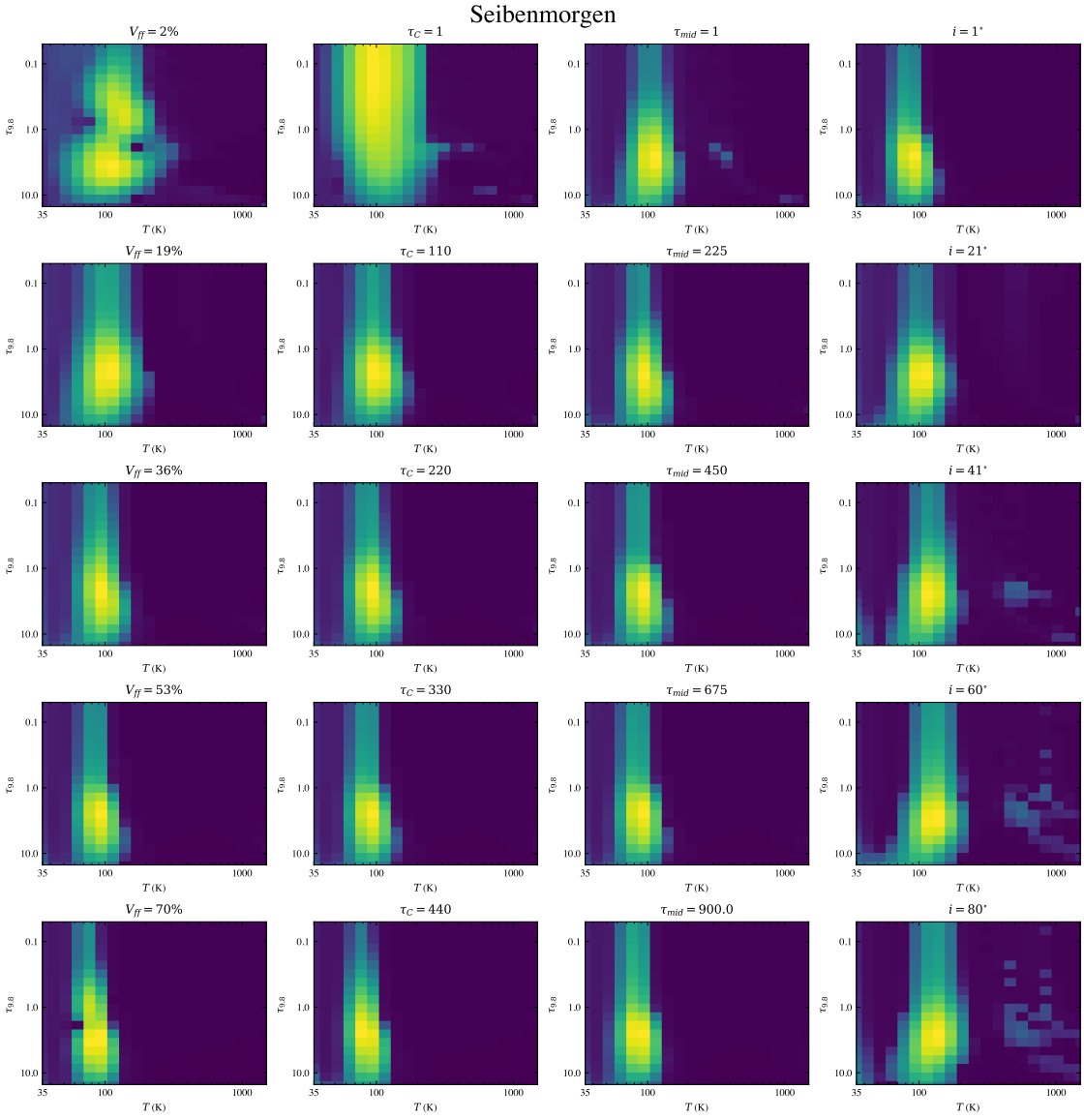

Figure 5.9: The inferred 2D dust distributions for the Seibenmorgen (Siebenmorgen et al., 2015) library of torus models of a smooth disk within a spherically volume consisting of individual clouds. Each column varies one of the four parameters. For each the other three parameters are set to a default of $V_{ff} = 50\%$, $\tau_C = 300$, $\tau_{mid} = 500$, $i = 5°$.

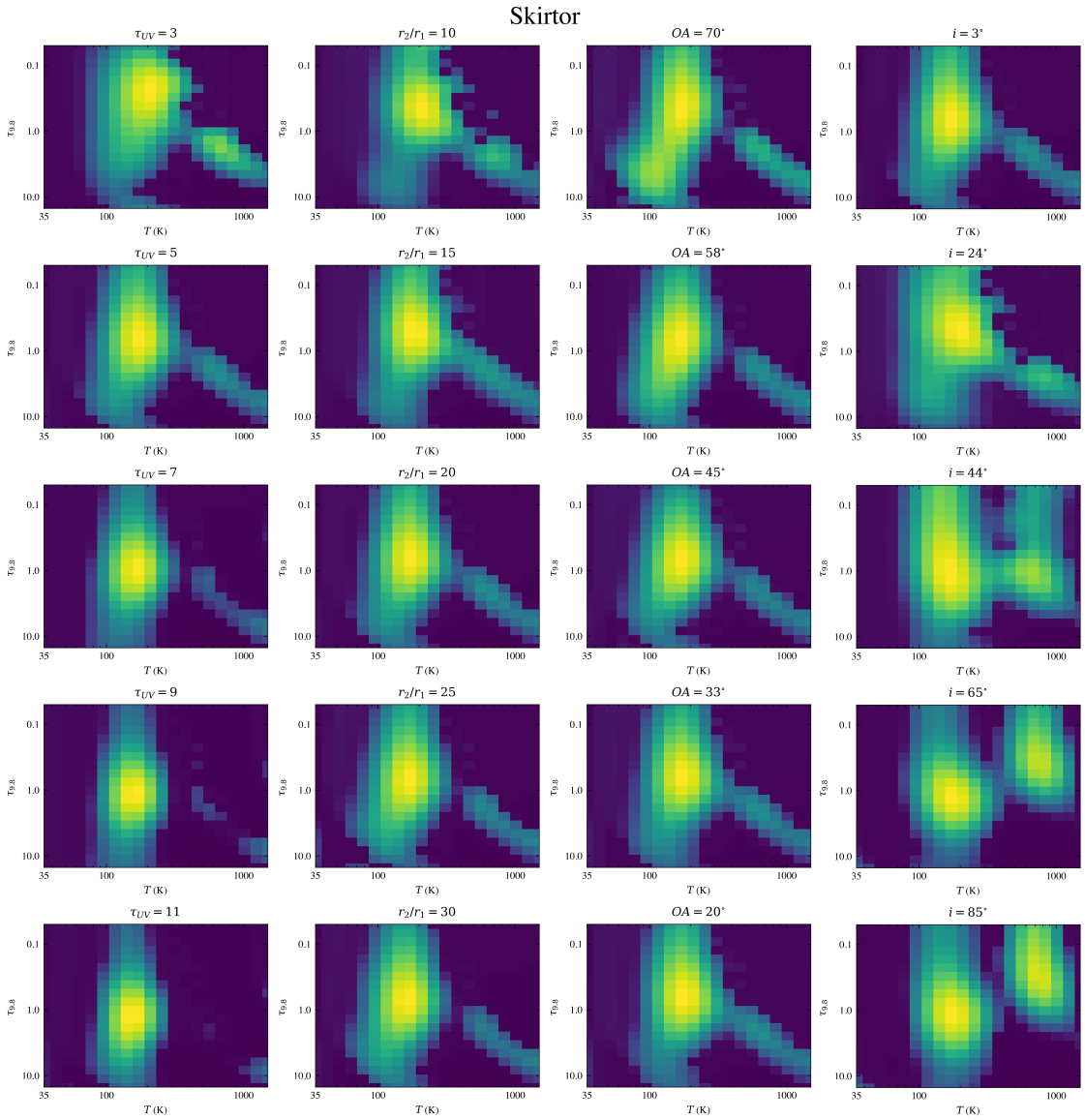

Figure 5.10: The inferred 2D dust distributions for the Skirtor (Stalevski et al., 2016) library of torus models of a clumpy flared disk. Each column varies one of the four parameters. For each the other three parameters are set to a default of $\tau_{\rm UV} = 5$, $r_2/r_1 = 50$, $OA = 40°$, $i = 5°$.

are shown in Fig. 5.10. The default parameters for this library are $\tau_{\rm UV} = 5$, $r_2/r_1 = 50$, $OA = 40°$, $i = 5°$.

I find the shape of the dust distribution to be similar to that of the Fritz models. Both the Fritz and Skirtor models are flared disks with the former being fully smooth while the latter is more clumpy. The lack of significant differences likely reflects the fact that the Skirtor models are not fully clumpy but rather also contain

a smooth component. It may also suggest that the geometry of the torus has a more significant impact than the clumpiness of the medium.

While the shape of the dust distributions are a poorer match to the most obscured targets, the Skirtor library does predict a distinct hot component. These are similar to the hot component seen in the AGN in our sample.

5.6 Discussion

5.6.1 Evolution of Dusty Nuclei

It is widely thought that the nuclei of ULIRGs are the progenitors of more typical unobscured quasars (e.g. Sanders et al., 1988; Hopkins et al., 2006), where the obscured phase is a rapid period of SMBH growth. With the joint approach of fitting the JWST spectra to infer the properties of the dusty obscuring structure and how well torus models can reproduce those properties, I can test this scenario directly using the dust properties itself.

Obscured Phase

From the variety of torus models, it is clear that the smooth tapered disk provided by the Cygnus models provide the closest match in terms of the shape dust distribution to the most obscured nuclei, when viewed edge-on. As I showed in Fig. 5.6, there are three distinct quadrants where objects appear based on the inferred extinction and temperature of the hot dust component. The majority of the obscured sources appear in the top left with $\tau_{9.8} > 5$ and $T_{\rm hot} < 600$K, where a majority also show a high surface brightness of HCN-vib emission (e.g. Falstad et al., 2021). As discussed in Chapters 1 and 2, a high surface brightness of HCN-vib is thought to require an enclosed dusty structure, such as a torus with a low opening angle, to create a greenhouse effect and populate the vibrational states of HCN (González-Alfonso and Sakamoto, 2019).

The second quadrant also shows a high obscuration ($\tau_{9.8} > 5$) but the temperature is higher ($T_{\rm hot} > 600$K). Objects here, such as Arp 220 E, and IRAS 08572+3915, show a lower HCN-vib surface brightness and are consistent with a higher opening

angle smooth tapered disk. This suggests there is a possible evolution, where the dusty structure opens up, lowering the HCN-vib surface brightness and raising the dust temperature. This would suggest that the track in the $\tau_{9.8}$ vs $T_{\rm hot}$ plot shows some evolution.

To investigate this further, I re-ran the Cygnus models where I generate models of different opening angles for three more inclinations of 15°, 30°, 50°. I then extract the temperature and extinction of the hot dust component and plot it in the top left panel of Fig. 5.11. The blue line shows the hot component in the edge-on case as presented in Fig. 5.7, showing an increase in temperature as the opening angle is increased. However, the extinction appears to also increase, which is not seen in the real data. To compensate for this effect I re-run the experiment also changing τ_{UV} as the opening angle changes. For the lowest opening angle I use a $\tau_{UV} = 1000$, moving down to $\tau_{UV} = 450$ for the highest opening angle. This results in the grey line in the top left panel of Fig. 5.11 which matches the observed trend better. However only the top left quadrant into the top right can be explained by the Cygnus models as they fail to reach a sufficiently high temperature to explain objects such as UGC 5101 or NGC 5728. Moreover, when the inclination is increased, the obscuration is reduced dramatically, with the points occupying the lower left quadrant. No objects are found in this region of the plot which suggests the tapered disk model is rarely viewed face-on. I investigate the inclination further in the following section where I take a statistical approach using the ULIRG sample to provide more insight.

I also plot some SEDs of the Cygnus library in the lower left panel of Fig. 5.11. These are the face-on ($i = 90°$) and edge-on ($i = 0°$) of two tapered disk models with a low opening angle (OA= 31°) which is more enclosed (dashed lines) and a high opening angle (OA= 74°), which is more disk-like (solid lines). Interestingly, the silicate feature in the face-on case changes from emission to mild absorption by only changing the opening angle, where the lower opening angle model shows absorption.

All the models in the lower left panel of Fig. 5.11 share the same intrinsic AGN luminosity but clearly have different infrared luminosities. This effect is discussed in Efstathiou (2006), where viewing the same torus face-on results in a larger infrared

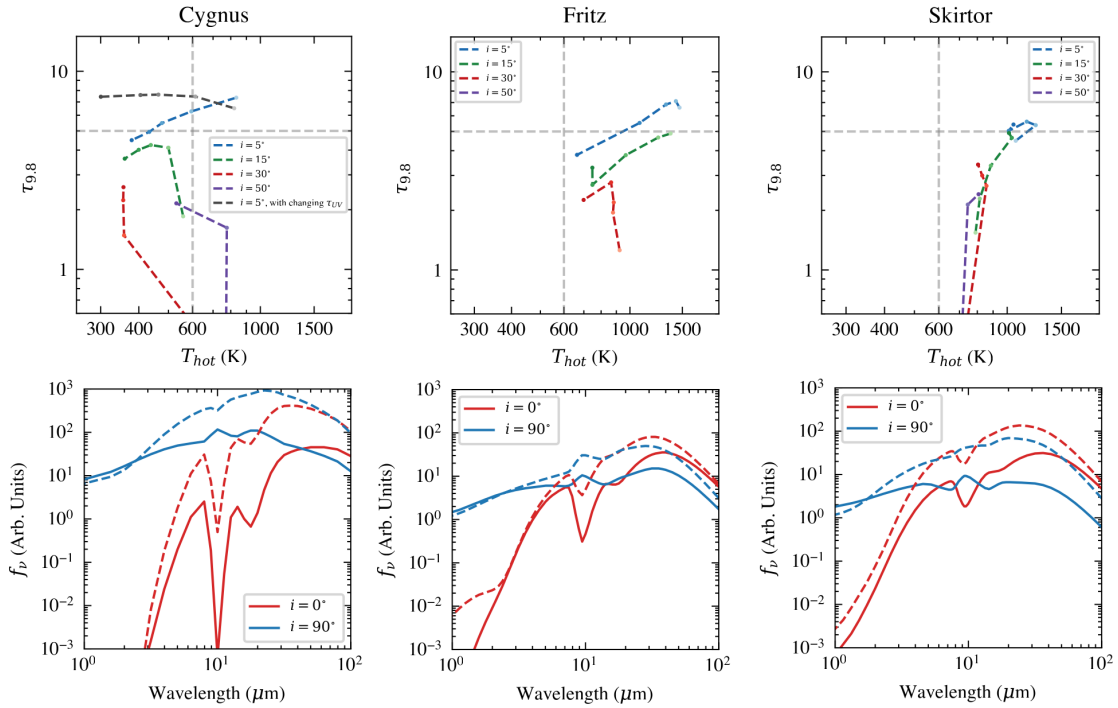

Figure 5.11: Plot of the extinction and temperature of the hot dust component of the Cygnus, Fritz and Skirtor torus models where the opening angle is varied. The brightness of each point indicates the opening angle, where lighter is a higher angle (more open/disk-like). Each colour shows a different inclination. In the middle panel, the $i = 50°$ track is at obscurations below the limit of the graph. The lower panels show SEDs for an edge-on case ($i = 0°$) and a face-on case ($i = 90°$), where the solid line corresponds to a high opening angle (more disk-like) while the dashed line is a lower opening angle (more enclosed). Each model in a given panel have the same intrinsic AGN luminosity, accounting for the anisotropy correction (Efstathiou, 2006).

luminosity. This difference can be accounted for through an anisotropy correction factor as presented in Efstathiou (2006). The effect of anisotropy contributes to the inclination problem, as a ULIRG CON viewed face-on, assuming the tapered disk model, would be classified as a HLIRG quasar ($L_{\rm IR} > 10^{13} L_\odot$), none of which are observed in the local universe. The lack of HLIRG quasars in the local universe may just be due to the relative low number statistics of CONs in the local universe. I investigate this further in section 5.6.2.

This exercise shows that the range of obscured nuclei observed with JWST can be explained by an evolving tapered disk, viewed edge-on, that gradually opens up.

AGN Phase

To explain the hotter obscured objects such as UGC 5101, NGC 5728 or the less obscured AGN, requires models from the Firtz (smooth flared disk) or Skirtor (two phase clumpy & smooth flared disk) libraries. I show in Fig. 5.11, the impact of increasing the opening angle at different inclinations for both libraries. As noted previously, the Fritz models show a similar behaviour to the Cygnus models where the temperature increases as the opening angle is increased (more disk-like). The opposite is true however for the Skirtor models, where there is very little change in temperature with opening angle or even a decrease for $i = 15°$. Both libraries occupy both the obscured and less obscured quadrants of the hot region of the extinction/temperature plot, consistent with those objects that show [Ne V] emission. This suggests that for more typical AGN, the flared disk is a good prescription, with the clumpiness, orientation and opening angle explaining the wide range of temperatures and extinctions observed.

Similar to the Cygnus models, I plot SEDs of the Fritz and Skirtor models in the lower panels of Fig. 5.11, where the range of models in each panel share the same intrinsic AGN luminosity. The effect of anisotropy on the measured infrared luminosity is less pronounced compared to the tapered disk, but is still present.

5.6.2 Inclination Problem

While the smooth tapered disk reproduces the top left quadrant of the $\tau_{9.8}$ vs $T_{\rm hot}$ plot, we do not observe any objects consistent with a face-on tapered disk in the ULIRG sample. Before drawing any significant conclusions on a possible evolutionary scenario, the issue of inclination needs further investigation. It is evident from Fig. 5.7, that even with a relatively high covering factor torus, with an opening angle of 40°, the dust distribution begins to fail to reproduce the observations, when the inclination even moderately increases. If the CONs are indeed required to be viewed edge-on, then the objects that show a hot component and are shown in Fig. 5.6 must have face-on counterparts within the ULIRG sample.

To approach this problem from another angle, I perform a simple statistical test to quantify if face-on CONs exist. I first assume that all of the ULIRGs host CONs (they are all intrisnically the same but viewed at different inclinations) and that the $\sim 40\%$ of ULIRGs that are identified as CONs (Falstad et al., 2021; Donnan et al., 2023a, see also Chapter 2) are simply those that are viewed sufficiently edge-on. I can test this assumption by generating a random distribution of inclinations and opening angles before measuring how many "CONs" would be identified. From this I can calculate the opening angle required to identify $\sim 40\%$ as "CONs".

I first generate a uniform distribution of $\sin i$ where i is the inclination measured from the equator to the pole (90° is face-on). This results in a distribution of inclinations, where edge-on tori are more likely than face-on as shown in Fig. 5.12. This makes sense as an equally random distribution of the normal vector of a circular disc, pointing to the inside of a sphere, will result in more edge-on cases than face-on.

I then loop through all values of opening angle from 0° (enclosed) to 90° (thin disk), calculating the number of CONs one would measure with the criteria of (90-OA)$> i$. This criteria is simply that for type 2 compared to type 1, where 90-OA is the angle from the equator, which when larger than the inclination, means the line of sight is through the torus i.e. type 2. From this criteria, I find an opening angle of $\sim 68°$ to measure 40% of the total as CONs. This criteria ((90-OA)$> i$) simply defines type 1 vs type 2, however from the results in Fig. 5.7, the inferred/predicted dust distributions begin to fail to match the CONs when $i > 24°$ where the opening angle has a value of OA $= 40°$, which would meet the above criterion. A stricter criterion to define "edge-on" is therefore needed. If one chooses (90-OA)$> 2i$, the opening angle required to detect $\sim 40\%$ as CONs increases to $\sim 45°$. The requirement of a stricter condition for an orientation to be considered edge-on suggests that a relatively low opening angle is required (a fairly enclosed structure). These simple tests suggest that the number of CONs detected is consistent with a relatively edge-on disk with a low opening angle of $\lesssim 45°$, under the assumption that all the ULIRGs are intrinsically CONs but just viewed at different inclinations.

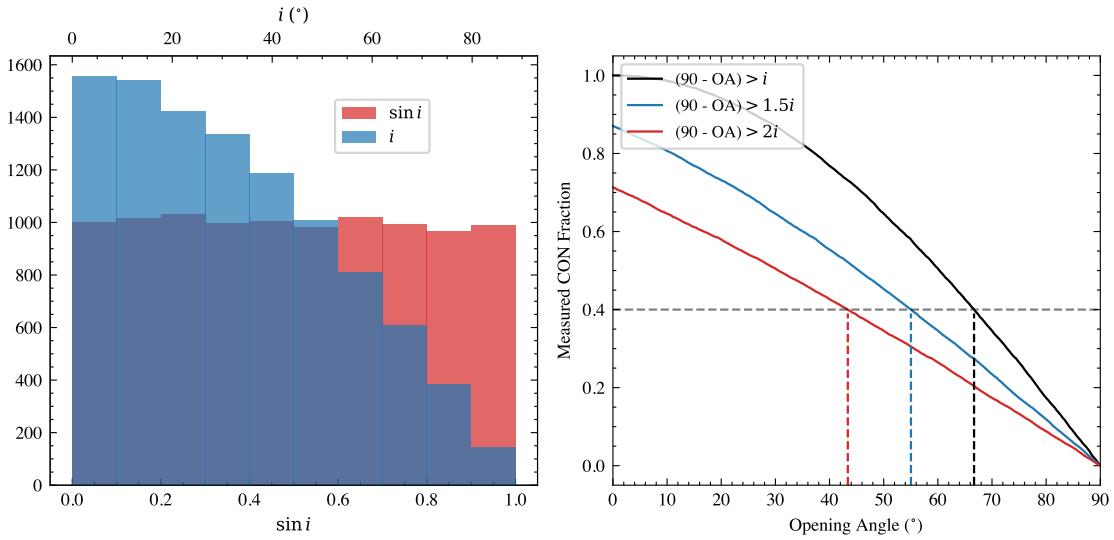

Figure 5.12: Left: Distribution of random orientations of a circular disk. In red is a uniform distribution of $\sin i$ which results in a distribution of inclinations, i, that prefers lower inclinations (more edge-on), shown in blue. **Right:** The measured fraction of CONs for a given opening angle, OA, for different CON criteria depending on how strict the condition is. The OA is measured from the polar axis where a larger OA is a more open torus. The dashed lines show the required opening angle for each criteria to match the observed $\sim 40\%$ of ULIRGs that are CONs.

This assumption is unlikely to be true but rather that the ULIRGs consist of a range of nuclei at different evolutionary stages. This would then therefore lower the total sample of intrinsic CONs of any orientation, and so the required $\sim$ 40% that would need to be viewed relatively edge-on would require an even lower opening angle. If we assume that half of the ULIRGs are intrinsic CONs (to provide a more conservative estimate), then this increases to $\sim 80\%$ that need to show high obscuration and so and opening angle of $\sim 10°$ would be required to meet a criteria of OA$> 1.5i$.

There are therefore two potential scenarios inferred from this simple experiment:

- The CONs are relatively edge-on tori with a small opening angle of $\lesssim 45°$, where a majority of the ULIRGs are intrinsically CONs of any orientation where the 40% observed as CONs are the edge-on objects. This means there are face-on counterparts in the ULIRG sample.

- ULIRGs contain a number of intrinsically different nuclei e.g. AGN at different

stages of evolution, and therefore the total number of intrinsic CONs is lower, requiring a lower opening angle. This would mean the torus is a much more enclosed structure and so no face-on counterparts exist in the ULIRG sample.

If the reality is somewhere between these scenarios, this would place the opening angle of the CON torus between OA$\sim 0^\circ - 45^\circ$, depending on how many of the ULIRGs are intrinsically CONs of any orientation. Based on the results shown in Fig. 5.6 and discussion in section 5.6.1, an evolution of the torus where the opening angle increases moving from a relatively spherical/closed structure to a more disk-like structure would suggest the latter scenario is true, where different ULIRGs are not intrinsically the same. With the upper left quadrant of the extinction/temperature plot in Fig. 5.11 occupied by tapered disk models with opening angles of $\sim 0^\circ - 50^\circ$, the range of $\sim 0^\circ - 45^\circ$ is entirely consistent.

Another key observational piece of evidence is the lack of high-ionisation potential lines in the CONs as shown in Fig. 5.6 (see also. Donnan et al., 2023b; Perna et al., 2024, Chapter 3). This has been used to suggest that the obscuring torus must be close to spherical to prevent any highly ionising photons escaping and ionising the surrounding gas. The lack of detection of high-IP lines is therefore a combination of a small opening and hence intrinsically weak ionising photon fraction as well as the bright dust continuum reducing the equivalent width of the lines if they are indeed present.

5.6.3 Face-on CONs?

As discussed in the previous section, it is worth identifying if any of the ULIRGs in the sample could be a face-on CON. If face-on CONs exist, finding and studying them would be invaluable as this would allow a much less obscured view of the central engine. To obtain a quantitive estimate of how many might exist in the local universe, I take the distribution of inclinations in Fig. 5.12 and calculate the proportion with $i > 60^\circ$, where this threshold is chosen arbitrarily. I therefore expect $\sim 13\%$ of a given sample of intrinsic CONs to be viewed relatively face-on. If one assumes that all the ULIRGs are intrinsically CONs, I would expect ~ 2 in my

sample to be face-on CONs. As mentioned previously, this assumption is unlikely and so if I reduce the fraction of ULIRGs that are intrinsic CONs by half, I therefore expect ~ 1 to be a face-on CON. In the larger HERUS sample (Farrah et al., 2013, see also Chapter 2) of local ULIRGs I would expect $\sim 2-3$ objects to be face-on CONs.

With these probabilities, I expect that one of the targets may be a face-on CON. If one assumes the tapered disk model, then one would expect to see silicate emission or moderate silicate absorption as demonstrated in the lower left panel of Fig. 5.11. None of the ULIRGs in our sample show silicate emission, which is a characteristic most commonly found in quasars (e.g. Netzer et al., 2007; Veilleux et al., 2009), however there are those with silicate emission in the HERUS sample, namely IRAS 07598+6508 and Mrk 1014.

Perhaps the best candidate in my sample (Table 5.1) is Mrk 231, a Broad Absorption Line (BAL) Quasar (e.g. Boksenberg et al., 1977; Feruglio et al., 2015; Rupke and Veilleux, 2011), which is thought to be viewed face-on and critically also shows emission from HCN-vib (Aalto et al., 2015a) although does not reach the surface brightness threshold. All the sources that are identified as CONs via this criterion all appear within the top left quadrant of Fig. 5.6 and therefore through the analysis using torus models, would all be viewed somewhat edge-on. If a face-on CON does exist, would it also show a high HCN-vib surface brightness or is the area dependent on projection effects? Interestingly, this object shows a relatively deep silicate feature and shows no high-ionisation lines despite its quasar classification, even with the high sensitivity of the MIRI MRS data (Alonso Herrero et al., 2024). This may suggest that there is still a large column density of obscuring material along the line of sight of the poles of the torus, possibly within the molecular outflow (e.g. Aalto et al., 2015a).

5.6.4 Is there a Clear Evolutionary Scenario?

Bringing together all the pieces of evidence that have been presented in this chapter and throughout the thesis, is it possible to say there is a clear evolutionary scenario?

I have shown that obscured nuclei show a buried hot dust component indicative of AGN heating which is distributed in a plane of extinction and temperature. There are three quadrants to this plot moving from cold/obscured ($\tau_{9.8} > 5$ and $T_{\rm hot} < 600$K) to hot/obscured $\tau_{9.8} > 5$ and $T_{\rm hot} > 600$K and then hot/less obscured $\tau_{9.8} < 5$ and $T_{\rm hot} > 600$K. This can be reproduced by an evolving torus moving from a smooth tapered disk to a flared disk that may be clumpy. The increase in dust temperature from cold/obscured to hot/obscured is explained by an edge-on smooth tapered disk that gradually opens. At some point the disk must transition into a flared shape. A possible physical mechanism to do this is the fountain model (Wada, 2012), where failed dusty outflows fall back towards the disk, inflating the torus from a tapered disk into a flared disk. This is just one possibility but is by no means at all constrained.

This picture is also consistent with the [Ne V]/[Ne II] ratio, where the hotter, less obscured objects show stronger [Ne V] emission. As the torus moves from a more enclosed structure to an open disk (opening angle increases), the hard radiation field from the accretion disk becomes visible, producing [Ne V] emission. There are a few outliers however. Most noticeably is VV 114 SW, which lacks any high-IP lines. This has been noticed in previous works (Chapter 3, Donnan et al., 2023b; Rich et al., 2023) as an unexpected result considering the hot dust continuum which would suggest AGN heating. Another object of note is IIZw96 NE, which is likely a pure star-forming region. As discussed in García-Bernete et al. (2024a), and shown in Fig. 8 of Rigopoulou et al. (2024), this object exhibits a hard radiation field, possibly due to an abundance of HII regions from intense star-formation. The final outlier in terms of the lack of high-IP lines is NGC 3265 S, which appears in a very similar region of the plot to NGC 5728 which has one of the highest [Ne V] fluxes. This is peculiar and may suggest that the AGN is no longer active, but the dust remains heated. As discussed in Chapter 4, NGC 3256 S has a collimated molecular outflow (Sakamoto et al., 2014; Emonts et al., 2014; Pereira-Santaella et al., 2022) but no ionised counterpart is detected. Sakamoto et al. (2014) indeed suggests that NGC 3256 S was once active but has since weakened.

5.7 Summary

In this Chapter I have presented results by fitting the near to mid-infrared spectra of samples of galaxy nuclei from ULIRGs, LIRGs and Seyfert galaxies. I have inferred the dust distribution (extinction and temperature) from the JWST spectra and interpreted my results using four libraries of torus models. My main findings are

- Most of ULIRGs show an isolated hot dust component in the inferred dust distribution. Plotting the extinction and temperature of this component reveals a trend of increasing temperature before the obscuration reduces, moving from cold/obscured (CONs) to hot/obscured (CT AGN) and finally hot/less obscured (AGN).

- The increase in the temperature of the hot dust component is reproduced by an edge-on smooth tapered disk that increases its opening angle i.e moves from a more enclosed structure to an open disk. This is consistent with an evolution where the central AGN clears/expels its dust. During this stage of evolution, the central AGN still remains obscured and no high ionisation potential lines are detected.

- The hot/obscured and hot/less obscured sources are well represented by a flared disk that is either completely smooth or somewhat clumpy. The level of obscuration is highly dependent on the inclination of the torus, in line with the classical type 1/2 picture. Objects in this regime show the presence of high-ionisation potential lines, where the AGN has ionised the surrounding gas.

- While the most obscured objects (CONs) are consistent with the tapered disk models, they are required to be viewed edge-on. By simulating a distribution of random inclinations, I showed that the number of CONs detected is consistent with a low opening angle disk ($\lesssim 45°$) viewed edge-on, implying the existence of at least ~ 1 face-on CON in the ULIRG sample.

- Mrk 231 provides a potential candidate for a face-on CON, due to its face-on molecular disk, presence of HCN-vib emission and lack of high-ionisation lines, however further work is required to confirm if it is indeed a face-on CON.

One key piece of observational evidence to investigate further the issue of inclination and the potential existence of face-on CONs, is through high resolution ALMA data, to observe kinematics on extremely small scales as this is the only true way to constrain the inclination. This has been possible for a few objects (e.g. Aalto et al., 2015a; Gorski et al., 2023) which shows a consistent picture with this work, where objects identified as CONs appear edge-on. It is unclear that if a face-on CON were to exist, it would show a sufficiently high HCN-vib surface brightness to be classified as a CON. It is also worth expanding the sample of AGN to include a significant quasar sample as seen by JWST, similar to QUEST (Schweitzer et al., 2006; Netzer et al., 2007; Veilleux et al., 2009), which would increase the parameter space of AGN to higher luminosities/Eddington ratios etc.

6
Conclusions.

Contents

The most fundamental processes in galaxy evolution, namely star-formation and SMBH growth are ubiquitous with large quantities of dust, obscuring much of this activity. This thesis presents analysis of the most obscured galaxy nuclei in the local universe, with the aim of understanding the nature of these objects undergoing a hidden but critical phase of galaxy evolution. In the following section I summarise the key results of each chapter.

6.1 Summary of Results

In Chapter 2, I first analysed archival Spitzer data to investigate the effectiveness of the mid-infrared to identify and study deeply obscured nuclei. I showed that by carefully decomposing the spectra into a star-forming and nuclear component, one can account for contamination by the host galaxy. The optical depth of the nucleus can therefore be recovered which I find correlates with the surface brightness of HCN-vib in the sub-mm. I also demonstrate the effect of this contamination using

spectral mapping data. Using the HERUS and GOALS samples, I constrain the fraction of deeply obscured nuclei to be $36^{+8}_{-7}\%$ of ULIRGs and $17^{+3}_{-3}\%$ of LIRGs, consistent with previous results but better constrained.

In Chapter 3 I presented analysis of an obscured nucleus, VV 114, as seen by JWST/MIRI MRS. I extracted spectra of the two nuclei and found the NE nucleus to be highly obscured, consistent with the criteria laid out in Chapter 2. The second nucleus in the SW, shows a hot dust continuum, possibly due to AGN heating but lacks the expected high-IP lines. Finally, with the increased spatial resolution over Spitzer, I detected a shock front south of the SW nucleus, likely due to the galaxy-galaxy interaction, which shows elevated [Fe II] emission and H_2 temperatures. Behind the shock front, there is a lack of 6.2 μm PAH emission, possibly indicative of a delayed destruction due to the shock.

In Chapter 4, I studied the various layers of extinction one can probe over a wide wavelength range combining NIRSpec and MIRI data of a variety of nuclei and star-forming regions. I did this by implementing a differential extinction model, where the dust continuum is determined by a 2D distribution of dust extinction and temperature. I found evidence for differential extinction in both star-forming regions and obscured nuclei, consistent with other tracers of extinction. In particular I found the PAHs and stellar continua to be less obscured than the molecular gas and HI lines. Additionally the obscured nuclei appeared to show an isolated hot dust component in their dust distribution, indicative of AGN heating. This work has produced a new tool that has the flexibility to fit a variety of different objects while also providing physical constraints on the nature of the obscuring dust.

In Chapter 5, I applied the fitting techniques outlined in chapter 4 to a considerable sample of ULIRGs, LIRGs and Seyfert galaxies observed with JWST NIRSpec IFU and MIRI MRS. By inferring the 2D dust distribution for this sample, I observe a spread in the temperature and extinction of the hot dust component, from cold/obscured to hot/obscured and hot/unobscured. There is a trend where emission from [Ne V] is detected at hotter temperatures and/or lower extinctions. By employing four libraries of torus models, I showed that the increase in temperature

can be explained by the opening of a smooth tapered disk viewed edge-on while the hottest obscured objects requires a flared disk that may be clumpy. The requirement that CONs are tapered disks viewed edge-on is consistent with the number of CONs detected however would require $\sim 1-3$ face-on CONs to exist in the local universe. It is not clear which specific objects could be face-on CONs.

6.2 Open Problems and Future Work

With the large number of high quality spectra produced by JWST of ULIRGs/AGN in the local universe and the complexity present in their spectra, there is a need to advance the current state of torus models. Firstly the clear presence of ices of H_2O, CO, and CO_2 produces broad absorption features and are not currently reproduced by existing torus models.

There is also a need to explore more geometries, in particular to explain the continuum of the most obscured nuclei. While I have shown that the tapered disk models of Efstathiou et al. (1995) provide a good fit, the issue of inclination is not perfectly resolved. Solving this will require a more comprehensive test of different geometries as well involving high resolution studies with ALMA, to resolve the dense gas kinematics on parsec scales. Considering the use of protoplanetary disk models to explain the kinematics of molecular gas on parsec scales (e.g. Gorski et al., 2023), pursuing associated radiative transfer models may provide more success than AGN torus models.

The focus of this thesis and much of the work in the literature is to study the nature and role of the most obscured nuclei in the local universe. However a majority of star-formation and AGN activity takes place at cosmic noon at $z \sim 1-3$. As I have demonstrated in this thesis, observations in the mid-infrared are crucial for revealing the majority of AGN and star-forming activity, particularly at cosmic noon where ULIRGs dominate the peak of cosmic star-formation (e.g. Zavala et al., 2021).

With JWST it is possible to study the role of the most obscured nuclei at cosmic noon for the first time. By first selecting candidates from MIRI imaging surveys by detecting objects with deep silicate features (García-Bernete et al., 2025), one can

follow-up targets to obtain spectroscopy. With the increased sensitivity of JWST over previous telescopes, obscured nuclei are being detected in much lower luminosity galaxies, something which is not seen in the local universe (Falstad et al., 2021).

More long term there is a need for a new far-infrared space telescope, that can enable a complete view of dust in the local universe, but more crucially unlock the restframe mid-infrared into the epoch of reionisation ($z > 5$). The most promising is PRIMA (PRobe far-Infrared Mission for Astrophysics) (Moullet et al., 2023), which is a concept for a 1.8 m cryogenically cooled FIR telescope which has recently been selected for Phase A study by NASA. If built, this telescope would launch relatively quickly, in 2032, providing observations between 25 - 235 μm bridging the gap between JWST and ALMA. The telescope will contain two instruments, PRIMAger and FIRESS, which will enable both imaging and spectroscopy respectively. While the relatively low angular resolution will require de-blending techniques (Donnellan et al., 2024), the high sensitivity will allow many obscured nuclei to be detected up to $z \sim 7$, providing a complete (flux limited) census of the most obscured nuclei over cosmic time (Donnan et al., 2025). Moreover, follow-up spectroscopy of obscured nuclei up to $z \sim 7$ is possible with modest time investment.

6.3 Closing Remarks

With the launch of JWST, the quality of data in terms of sensitivity, spatial and spectral resolution has dramatically improved enabling much of the science presented in this thesis. However this is only the beginning, with at least 10 years of operating time, JWST will continue to observe and unlock the secrets of the obscured universe. The work and techniques developed in this thesis lays the foundation for a bright future with JWST and beyond.

Appendices

A
Supplementary Material

Contents

A.1 Chapter 2:

A.1.1 Choice of silicate template

In my analysis I chose to use an empirical template for the 9.8 μm silicate absorption feature, derived from NGC 4418 as described in Appendix 2.3.3. I chose this source as it is highly obscured with minimal emission features and is a well studied CON with strong HCN-vib emission (e.g. Sakamoto et al., 2010). However, as noted in Sect. 2.3.2, ground based observations with a smaller beam find a higher

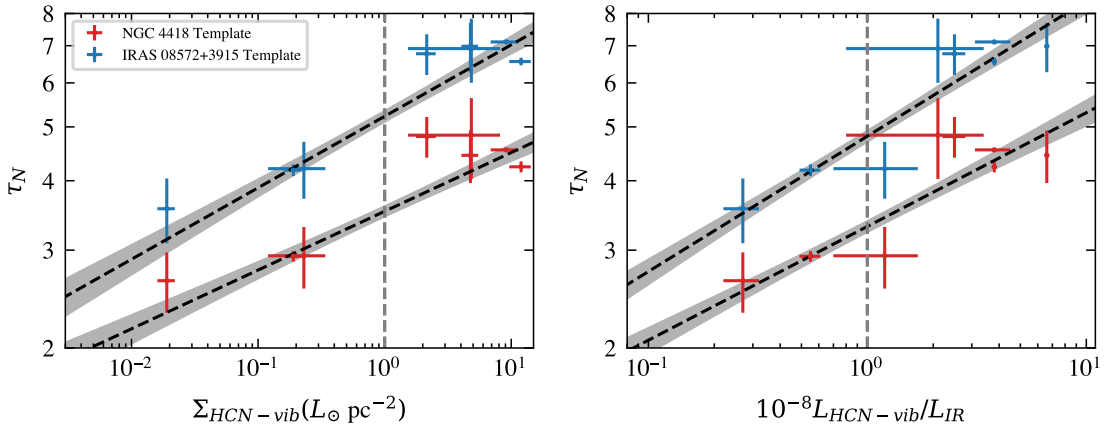

Figure A.1: Comparison of the measured nuclear optical depths of the CONquest sample with different silicate templates. In red are the measured τ_N against the surface density of HCN-vib (left) and HCN-vib luminosity to L_{IR} (right) using the NGC 4418 profile. In blue are the results using the template from IRAS 08572+3915.

peak optical depth than with *Spitzer* IRS, which suggests the template contains some contribution from the relatively unobscured continuum from circumnuclear star formation. I therefore test another template derived from another highly obscured galaxy, IRAS 08572+3915.

The profile for this galaxy is narrower, which suggests less contamination by any unobscured continuum, consistent with a total absence of emission features. I tested the model using this template on the CONquest sample and compared the resulting decomposition. In Fig. A.1 I compare the measured optical depths using the IRAS 08572+3915 template in blue to the NGC 4418 template in red. As expected the IRAS 08572 template produces higher nuclear optical depths requiring more contribution from the star-forming component to fit the data. Crucially this is a constant offset in optical depth with the same correlation found but shifted to higher values. Therefore, the conclusions of this paper are not strongly affected by the choice of silicate template.

While this template may be advantageous for future work, I chose not to use it as this object is not a CON by the HCN-vib definition.

A.1.2 Silicate strength versus HCN-vib

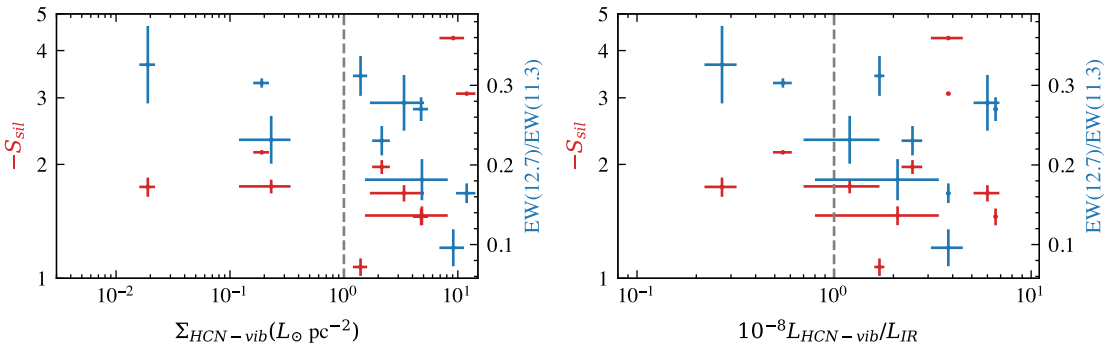

Figure A.2: Same as Fig. 2.8 but with the apparent silicate strength as calculated by Eq. 2.6 (red), which shows no trend. The 12.7/11.3 PAH EW ratio is also shown (blue) against HCN-vib on the right-hand axis of each plot and shows a very weak trend. A comparison with Fig. 2.8 shows the value in accounting for the star-forming contribution to properly recover properties of the obscured nucleus.

A.1.3 Continuum ratios of the spectral mapping sample

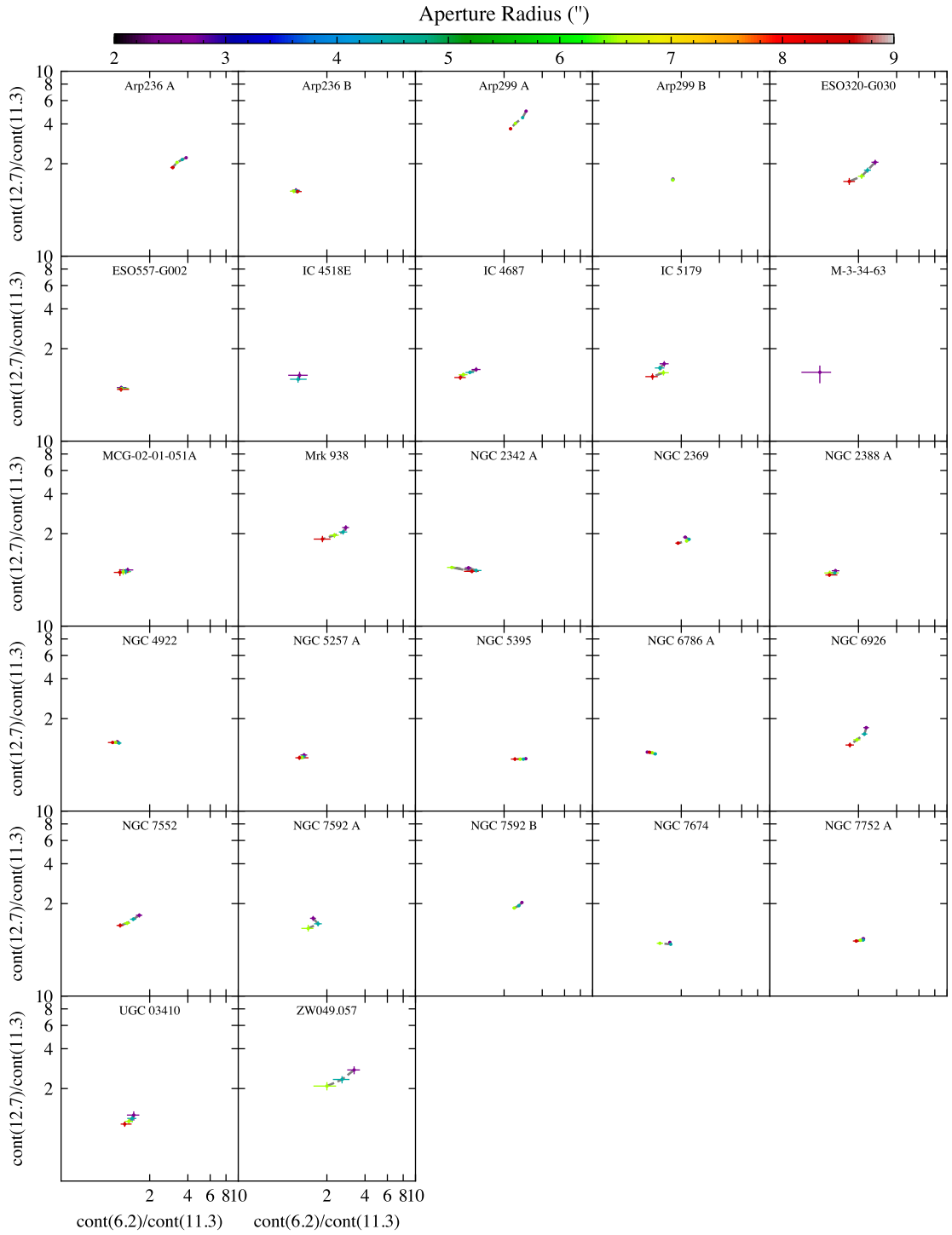

Figure A.3: Continuum ratios at 12.7 μm to 11.3 μm against the 6.2/11.3 continuum ratio for the spectral mapping sample. For each galaxy, values are coloured by the aperture radius used to extract the spectra; a larger aperture will contain more emission from star formation in the galactic disc.

A.1.4 Table of spectral properties

Table A.1: Spectral properties of all the galaxies used in Chapter 2.

Name	EW(6.2)/EW(11.3)	EW(12.7)/EW(11.3)	$S_{\rm Sil}$	τ_N	β	HCN (14 μm)	Crystallines?
(1)	(2)	(3)	(4)	(5)	(6)	(7)	(8)
2MASS J03574895-1340458	$0.923^{+0.114}_{-0.157}$	$0.588^{+0.065}_{-0.068}$	$-0.462^{+0.083}_{-0.104}$	-	-	-	-
2MASX J00480675-2848187	$0.792^{+0.083}_{-0.103}$	$0.350^{+0.031}_{-0.034}$	$-1.061^{+0.092}_{-0.100}$	-	-	-	-
2MASX J02245768-0414182	$1.082^{+0.356}_{-0.486}$	$0.538^{+0.111}_{-0.124}$	$-0.661^{+0.221}_{-0.146}$	-	-	-	-
2MASX J02253645-0500123	$1.081^{+0.15}_{-0.129}$	$0.505^{+0.052}_{-0.047}$	$-0.433^{+0.106}_{-0.099}$	-	-	-	-
2MASX J05583717-7716393	$0.776^{+0.075}_{-0.085}$	$0.434^{+0.032}_{-0.029}$	$-1.402^{+0.079}_{-0.08}$	-	-	-	-
2MASX J08182925+3717481	$0.973^{+0.226}_{-0.256}$	$0.485^{+0.076}_{-0.083}$	$-0.641^{+0.217}_{-0.096}$	-	-	-	-
2MASX J09192731+3347270	$0.974^{+0.196}_{-0.37}$	$0.435^{+0.040}_{-0.049}$	$-0.725^{+0.182}_{-0.304}$	-	-	-	-
2MASX J10363621+6322224	$2.325^{+0.486}_{-0.742}$	$0.470^{+0.053}_{-0.061}$	$-0.444^{+0.117}_{-0.096}$	-	-	-	-
2MASX J11182408+5602074	$1.947^{+0.319}_{-0.418}$	$0.525^{+0.06}_{-0.065}$	$-0.445^{+0.112}_{-0.099}$	-	-	-	-
2MASX J14081899+2904474	$1.56^{+0.266}_{-0.292}$	$0.523^{+0.053}_{-0.058}$	$-0.542^{+0.172}_{-0.153}$	-	-	-	-
2MASX J14094683-0820036	$1.566^{+0.18}_{-0.224}$	$0.466^{+0.043}_{-0.048}$	$-0.428^{+0.103}_{-0.089}$	-	-	-	-
2MASX J14255448+3446026	$1.405^{+0.13}_{-0.125}$	$0.516^{+0.041}_{-0.035}$	$-0.192^{+0.08}_{-0.072}$	-	-	-	-
2MASX J14520570+3810593	$1.091^{+0.102}_{-0.11}$	$0.477^{+0.040}_{-0.042}$	$-0.221^{+0.087}_{-0.076}$	-	-	-	-
2MASX J15574349+2727530	$1.134^{+0.294}_{-0.326}$	$0.386^{+0.036}_{-0.038}$	$-0.789^{+0.206}_{-0.104}$	-	-	-	-
2MASX J16070059+5538090	$1.706^{+0.265}_{-0.229}$	$0.477^{+0.043}_{-0.047}$	$-0.129^{+0.056}_{-0.040}$	-	-	-	-
2MASX J16140266+5330358	$1.15^{+0.105}_{-0.106}$	$0.534^{+0.032}_{-0.034}$	$-0.069^{+0.046}_{-0.026}$	-	-	-	-
2MASX J16164521+5502305	$0.735^{+0.119}_{-0.173}$	$0.473^{+0.051}_{-0.063}$	$-0.589^{+0.146}_{-0.183}$	-	-	✓	-
2MASX J18003399-0401443	$1.283^{+0.094}_{-0.088}$	$0.554^{+0.053}_{-0.050}$	$-0.14^{+0.077}_{-0.061}$	-	-	-	-
2MASX J18113842+0131397	$0.78^{+0.050}_{-0.060}$	$0.332^{+0.009}_{-0.010}$	$-0.861^{+0.037}_{-0.039}$	-	-	-	-
2MASX J18324117-3411274	$0.575^{+0.015}_{-0.017}$	$0.303^{+0.007}_{-0.008}$	$-1.531^{+0.020}_{-0.022}$	-	-	-	-
2MASX J19565118+1633389	$0.608^{+0.090}_{-0.262}$	$0.391^{+0.040}_{-0.058}$	$-0.752^{+0.111}_{-0.247}$	-	-	-	-
2MASX J21270303+2355456	$0.774^{+0.065}_{-0.082}$	$0.519^{+0.039}_{-0.040}$	$-0.396^{+0.087}_{-0.084}$	-	-	-	-
2MASX J22382548-1646485	$1.232^{+0.128}_{-0.115}$	$0.525^{+0.04}_{-0.041}$	$-0.173^{+0.098}_{-0.057}$	-	-	-	-
2MFGC 13321	$0.529^{+0.114}_{-0.177}$	$0.453^{+0.081}_{-0.087}$	$-0.869^{+0.230}_{-0.183}$	-	-	-	-
3C 273	$\mathbf{0.396^{+0.078}_{-0.084}}$	$0.730^{+0.166}_{-0.176}$	$0.126^{+0.011}_{-0.011}$	-	-	-	-
AM 0702-601 NED02	$0.891^{+0.030}_{-0.033}$	$0.517^{+0.025}_{-0.025}$	$-0.686^{+0.033}_{-0.034}$	-	-	-	-
Arp 148	$0.509^{+0.034}_{-0.036}$	$0.307^{+0.014}_{-0.017}$	$-1.379^{+0.037}_{-0.043}$	$3.430^{+0.621}_{-0.442}$	$0.589^{+0.032}_{-0.030}$	-	-
Arp 220	$\mathbf{0.308^{+0.016}_{-0.016}}$	$\mathbf{0.164^{+0.010}_{-0.014}}$	$-3.078^{+0.020}_{-0.020}$	$\mathbf{4.237^{+0.098}_{-0.094}}$	$0.89^{+0.006}_{-0.006}$	✓	I
Arp 256 NED01	$1.401^{+0.086}_{-0.098}$	$0.416^{+0.016}_{-0.02}$	$-0.624^{+0.037}_{-0.036}$	-	-	-	-
Arp 295 B	$0.739^{+0.043}_{-0.048}$	$0.306^{+0.013}_{-0.014}$	$-0.919^{+0.04}_{-0.044}$	-	-	-	-
Arp236 A*	$\mathbf{0.418^{+0.011}_{-0.012}}$	$0.343^{+0.017}_{-0.02}$	$-1.611^{+0.017}_{-0.019}$	-	-	-	-
Arp236 B*	$0.904^{+0.065}_{-0.073}$	$0.428^{+0.039}_{-0.038}$	$-0.549^{+0.061}_{-0.062}$	-	-	-	-
Arp299 A*	$0.603^{+0.02}_{-0.02}$	$\mathbf{0.269^{+0.009}_{-0.009}}$	$-2.412^{+0.026}_{-0.027}$	$3.256^{+0.049}_{-0.047}$	$0.881^{+0.007}_{-0.007}$	-	-
Arp299 B*	$0.849^{+0.015}_{-0.016}$	$0.635^{+0.018}_{-0.018}$	$-0.874^{+0.003}_{-0.003}$	-	-	-	-
CGCG 011-076	$\mathbf{0.446^{+0.019}_{-0.021}}$	$0.315^{+0.016}_{-0.02}$	$-1.031^{+0.038}_{-0.04}$	-	-	-	-
CGCG 052-037	$0.782^{+0.029}_{-0.034}$	$0.362^{+0.012}_{-0.016}$	$-0.879^{+0.027}_{-0.030}$	-	-	-	-
CGCG 058-009	$\mathbf{0.142^{+0.007}_{-0.007}}$	$\mathbf{0.271^{+0.016}_{-0.018}}$	$-1.798^{+0.049}_{-0.048}$	$\mathbf{4.905^{+0.389}_{-0.329}}$	$0.653^{+0.023}_{-0.025}$	-	-
CGCG 141-034	$\mathbf{0.403^{+0.024}_{-0.027}}$	$0.312^{+0.016}_{-0.018}$	$-1.626^{+0.064}_{-0.061}$	$3.004^{+0.219}_{-0.203}$	$0.638^{+0.036}_{-0.039}$	-	-
CGCG 142-034	$\mathbf{0.349^{+0.027}_{-0.028}}$	$0.340^{+0.023}_{-0.023}$	$-1.401^{+0.061}_{-0.054}$	$\mathbf{3.750^{+0.762}_{-0.507}}$	$0.491^{+0.056}_{-0.048}$	-	-
CGCG 152-070	$0.812^{+0.114}_{-0.193}$	$0.378^{+0.032}_{-0.041}$	$-0.507^{+0.114}_{-0.188}$	-	-	-	-
CGCG 290-067	$0.835^{+0.091}_{-0.113}$	$0.539^{+0.065}_{-0.072}$	$-0.515^{+0.088}_{-0.082}$	-	-	-	-
CGCG 436-030	$0.660^{+0.045}_{-0.048}$	$0.315^{+0.018}_{-0.019}$	$-1.588^{+0.047}_{-0.049}$	-	-	-	-
CGCG 453-062	$0.592^{+0.054}_{-0.067}$	$0.337^{+0.025}_{-0.031}$	$-1.043^{+0.086}_{-0.099}$	$2.654^{+0.967}_{-0.534}$	$0.476^{+0.071}_{-0.071}$	-	-
CGCG 465-012	$1.120^{+0.312}_{-0.064}$	$0.572^{+0.022}_{-0.017}$	$-0.101^{+0.32}_{-0.019}$	-	-	-	-
CGCG 468-002 NED02	$0.872^{+0.064}_{-0.075}$	$0.351^{+0.024}_{-0.020}$	$-1.294^{+0.049}_{-0.050}$	-	-	-	-
CGCG 468-002	$\mathbf{0.353^{+0.025}_{-0.028}}$	$0.456^{+0.039}_{-0.042}$	$-0.121^{+0.019}_{-0.019}$	-	-	-	-
CXO J191431.2-211905	$0.576^{+0.036}_{-0.039}$	$0.325^{+0.022}_{-0.023}$	$-1.316^{+0.046}_{-0.056}$	$2.785^{+0.269}_{-0.253}$	$0.64^{+0.034}_{-0.039}$	-	-

Table A.1: Continued.

Name	EW(6.2)/EW(11.3)	EW(12.7)/EW(11.3)	$S_{\rm Sil}$	τ_N	β	HCN (14 μm)	Crystallines?
(1)	(2)	(3)	(4)	(5)	(6)	(7)	(8)
ESO 069-IG 006N	$1.269^{+0.042}_{-0.050}$	$0.512^{+0.015}_{-0.015}$	$-0.661^{+0.018}_{-0.013}$	-	-	-	-
ESO 099-G004	$1.176^{+0.085}_{-0.090}$	$0.344^{+0.011}_{-0.012}$	$-0.953^{+0.059}_{-0.052}$	-	-	-	-
ESO 138-G027	$1.354^{+0.048}_{-0.049}$	$0.414^{+0.020}_{-0.020}$	$-0.267^{+0.023}_{-0.024}$	-	-	-	-
ESO 148-IG 002	$1.244^{+0.052}_{-0.055}$	$0.508^{+0.018}_{-0.02}$	$-0.698^{+0.042}_{-0.045}$	-	-	-	-
ESO 173-G015	$\mathbf{0.496^{+0.015}_{-0.016}}$	$0.314^{+0.006}_{-0.006}$	$-2.144^{+0.020}_{-0.020}$	$2.887^{+0.071}_{-0.066}$	$0.813^{+0.011}_{-0.011}$	-	-
ESO 221-IG10	$0.908^{+0.081}_{-0.126}$	$0.432^{+0.026}_{-0.034}$	$-0.441^{+0.053}_{-0.083}$	-	-	-	-
ESO 239-IG002	$1.676^{+0.182}_{-0.199}$	$0.504^{+0.043}_{-0.043}$	$-0.442^{+0.076}_{-0.065}$	-	-	-	-
ESO 244- G 012 NED02	$1.511^{+0.112}_{-0.129}$	$0.433^{+0.021}_{-0.022}$	$-0.767^{+0.044}_{-0.044}$	-	-	-	-
ESO 255-IG 007 NED01	$2.113^{+0.177}_{-0.220}$	$0.469^{+0.017}_{-0.016}$	$-0.300^{+0.037}_{-0.025}$	-	-	-	-
ESO 255-IG 007 NED03	$1.406^{+0.217}_{-0.244}$	$0.454^{+0.034}_{-0.036}$	$-0.366^{+0.099}_{-0.082}$	-	-	-	-
ESO 255-IG007	$1.593^{+0.101}_{-0.167}$	$0.559^{+0.033}_{-0.029}$	$-0.036^{+0.035}_{-0.021}$	-	-	-	-
ESO 264-G036	$\mathbf{0.411^{+0.014}_{-0.017}}$	$0.428^{+0.017}_{-0.018}$	$-0.621^{+0.028}_{-0.030}$	-	-	-	-
ESO 264-G057	$0.675^{+0.022}_{-0.024}$	$0.423^{+0.022}_{-0.024}$	$-0.901^{+0.028}_{-0.030}$	-	-	-	-
ESO 267-G030	$0.535^{+0.017}_{-0.019}$	$0.353^{+0.013}_{-0.017}$	$-0.651^{+0.025}_{-0.029}$	-	-	-	-
ESO 286-G035	$0.669^{+0.031}_{-0.041}$	$0.344^{+0.009}_{-0.012}$	$-1.006^{+0.027}_{-0.028}$	-	-	-	-
ESO 286-IG 019	$\mathbf{0.208^{+0.022}_{-0.022}}$	$\mathbf{0.175^{+0.03}_{-0.031}}$	$-3.049^{+0.033}_{-0.033}$	$\mathbf{3.578^{+0.129}_{-0.099}}$	$0.936^{+0.009}_{-0.011}$	-	II
ESO 319-G022	$1.468^{+0.218}_{-0.233}$	$0.558^{+0.066}_{-0.069}$	$-0.393^{+0.083}_{-0.078}$	-	-	-	-
ESO 339-G011	$0.661^{+0.027}_{-0.029}$	$0.368^{+0.016}_{-0.019}$	$-0.58^{+0.032}_{-0.032}$	-	-	-	-
ESO 343-IG013	$0.541^{+0.033}_{-0.033}$	$0.323^{+0.017}_{-0.019}$	$-1.25^{+0.040}_{-0.047}$	$3.330^{+0.679}_{-0.512}$	$0.537^{+0.043}_{-0.036}$	-	-
ESO 350-IG038	$1.155^{+0.080}_{-0.095}$	$0.940^{+0.053}_{-0.053}$	$-0.433^{+0.019}_{-0.021}$	-	-	-	-
ESO 353-G020	$\mathbf{0.373^{+0.022}_{-0.023}}$	$0.326^{+0.019}_{-0.02}$	$-1.561^{+0.061}_{-0.057}$	$\mathbf{4.589^{+0.467}_{-0.381}}$	$0.551^{+0.034}_{-0.034}$	-	-
ESO 374-IG032	$\mathbf{0.036^{+0.001}_{-0.001}}$	$\mathbf{0.102^{+0.007}_{-0.008}}$	$-4.328^{+0.024}_{-0.023}$	$\mathbf{6.031^{+0.086}_{-0.081}}$	$0.959^{+0.001}_{-0.001}$	-	I
ESO 420- G 013	$\mathbf{0.442^{+0.013}_{-0.015}}$	$0.353^{+0.009}_{-0.009}$	$-0.797^{+0.029}_{-0.031}$	-	-	-	-
ESO 440-IG058	$1.321^{+0.138}_{-0.171}$	$0.572^{+0.04}_{-0.033}$	$-0.055^{+0.048}_{-0.03}$	-	-	-	-
ESO 453-G005	$0.595^{+0.076}_{-0.098}$	$0.344^{+0.027}_{-0.026}$	$-0.616^{+0.107}_{-0.116}$	-	-	-	-
ESO 467-G027	$0.696^{+0.025}_{-0.026}$	$0.428^{+0.017}_{-0.023}$	$-0.551^{+0.041}_{-0.045}$	-	-	-	-
ESO 495- G 021	$2.56^{+0.062}_{-0.072}$	$0.399^{+0.005}_{-0.005}$	$-0.151^{+0.010}_{-0.011}$	-	-	-	-
ESO 507-G070	$0.569^{+0.052}_{-0.060}$	$\mathbf{0.271^{+0.018}_{-0.021}}$	$-2.237^{+0.049}_{-0.048}$	$\mathbf{3.816^{+0.371}_{-0.292}}$	$0.724^{+0.025}_{-0.025}$	-	-
ESO 557- G 002	$0.698^{+0.048}_{-0.051}$	$0.296^{+0.02}_{-0.021}$	$-1.231^{+0.037}_{-0.041}$	$2.919^{+0.394}_{-0.335}$	$0.582^{+0.034}_{-0.030}$	-	-
ESO 602-G025	$\mathbf{0.293^{+0.013}_{-0.012}}$	$\mathbf{0.267^{+0.01}_{-0.011}}$	$-1.567^{+0.024}_{-0.025}$	$3.427^{+0.367}_{-0.3}$	$0.649^{+0.023}_{-0.021}$	-	-
ESO 203-IG001	$\mathbf{0.090^{+0.012}_{-0.014}}$	$\mathbf{0.173^{+0.027}_{-0.031}}$	$-4.084^{+0.066}_{-0.061}$	$\mathbf{5.978^{+0.262}_{-0.235}}$	$0.943^{+0.005}_{-0.005}$	-	-
ESO 320-G030*	$\mathbf{0.375^{+0.025}_{-0.027}}$	$\mathbf{0.312^{+0.024}_{-0.026}}$	$-1.071^{+0.052}_{-0.061}$	$\mathbf{4.309^{+0.983}_{-0.657}}$	$0.448^{+0.035}_{-0.033}$	-	-
ESO 557-G002*	$0.858^{+0.075}_{-0.103}$	$0.451^{+0.036}_{-0.038}$	$-0.274^{+0.095}_{-0.08}$	-	-	-	-
ESO 593-IG008	$0.574^{+0.036}_{-0.039}$	$0.319^{+0.021}_{-0.022}$	$-1.326^{+0.053}_{-0.057}$	$2.798^{+0.272}_{-0.237}$	$0.652^{+0.034}_{-0.036}$	-	-
IC 0214	$0.889^{+0.034}_{-0.039}$	$0.402^{+0.019}_{-0.023}$	$-0.726^{+0.034}_{-0.036}$	-	-	-	-
IC 0563	$0.730^{+0.065}_{-0.072}$	$0.424^{+0.040}_{-0.042}$	$-0.809^{+0.084}_{-0.096}$	-	-	-	-
IC 0860	$\mathbf{0.332^{+0.03}_{-0.032}}$	$\mathbf{0.187^{+0.016}_{-0.016}}$	$-1.733^{+0.049}_{-0.054}$	$\mathbf{4.016^{+0.334}_{-0.281}}$	$0.758^{+0.016}_{-0.018}$	✓	I
IC 2810	$0.722^{+0.062}_{-0.071}$	$0.380^{+0.031}_{-0.034}$	$-0.706^{+0.073}_{-0.083}$	-	-	-	-
IC 4280	$0.607^{+0.017}_{-0.019}$	$0.459^{+0.020}_{-0.019}$	$-0.592^{+0.037}_{-0.036}$	-	-	-	-
IC 4734	$0.555^{+0.022}_{-0.025}$	$0.304^{+0.009}_{-0.011}$	$-1.399^{+0.027}_{-0.029}$	$2.734^{+0.192}_{-0.172}$	$0.629^{+0.024}_{-0.027}$	-	-
IC 5298	$0.703^{+0.036}_{-0.04}$	$1.075^{+0.067}_{-0.065}$	$-0.259^{+0.037}_{-0.036}$	-	-	-	-
IC 4518E*	$1.315^{+0.215}_{-0.278}$	$0.598^{+0.065}_{-0.061}$	$-0.536^{+0.137}_{-0.095}$	-	-	-	-
IC 4687*	$1.007^{+0.081}_{-0.086}$	$0.413^{+0.029}_{-0.032}$	$-0.648^{+0.067}_{-0.07}$	-	-	-	-
IC 5179*	$0.802^{+0.067}_{-0.083}$	$0.390^{+0.03}_{-0.034}$	$-0.839^{+0.069}_{-0.075}$	-	-	-	-
IRAS 00188-0856	$\mathbf{0.143^{+0.016}_{-0.018}}$	$0.333^{+0.038}_{-0.039}$	$-2.341^{+0.065}_{-0.06}$	$3.235^{+0.221}_{-0.19}$	$0.850^{+0.018}_{-0.019}$	-	-
IRAS 00397-1312	$\mathbf{0.179^{+0.025}_{-0.031}}$	$\mathbf{0.179^{+0.045}_{-0.054}}$	$-2.940^{+0.043}_{-0.039}$	$\mathbf{4.059^{+0.222}_{-0.178}}$	$0.883^{+0.013}_{-0.014}$	-	-
IRAS 03521+0028	$0.648^{+0.139}_{-0.215}$	$0.344^{+0.07}_{-0.085}$	$-1.207^{+0.158}_{-0.188}$	$\mathbf{5.090^{+2.356}_{-1.600}}$	$0.485^{+0.066}_{-0.056}$	-	II
IRAS 04271+3849	$0.577^{+0.015}_{-0.016}$	$0.357^{+0.014}_{-0.015}$	$-1.181^{+0.029}_{-0.031}$	-	-	-	-

Table A.1: Continued.

Name	EW(6.2)/EW(11.3)	EW(12.7)/EW(11.3)	$S_{\rm Sil}$	τ_N	β	HCN (14 μm)	Crystallines?
(1)	(2)	(3)	(4)	(5)	(6)	(7)	(8)
IRAS 05083+2441	$0.901^{+0.035}_{-0.036}$	$0.356^{+0.01}_{-0.011}$	$-0.958^{+0.033}_{-0.032}$	-	-	-	-
IRAS 05129+5128	$0.856^{+0.045}_{-0.050}$	$0.342^{+0.022}_{-0.024}$	$-1.075^{+0.036}_{-0.037}$	-	-	-	-
IRAS 05189-2524	$0.621^{+0.086}_{-0.139}$	$0.635^{+0.124}_{-0.256}$	$-0.349^{+0.045}_{-0.063}$	-	-	-	-
IRAS 06035-7102	$\mathbf{0.455^{+0.045}_{-0.045}}$	$0.348^{+0.055}_{-0.057}$	$-1.242^{+0.072}_{-0.085}$	-	-	-	-
IRAS 06206-6315	$\mathbf{0.458^{+0.039}_{-0.044}}$	$0.385^{+0.046}_{-0.045}$	$-1.562^{+0.065}_{-0.069}$	-	-	-	-
IRAS 07027-6011	$0.736^{+0.043}_{-0.060}$	$0.475^{+0.022}_{-0.024}$	$-0.596^{+0.035}_{-0.033}$	-	-	-	-
IRAS 07251-0248	$\mathbf{0.104^{+0.012}_{-0.012}}$	$\mathbf{0.110^{+0.024}_{-0.025}}$	$-3.107^{+0.092}_{-0.085}$	$\mathbf{5.428^{+0.397}_{-0.325}}$	$0.831^{+0.025}_{-0.020}$	-	-
IRAS 07598+6508	$1.128^{+0.293}_{-0.426}$	$2.608^{+0.554}_{-0.758}$	$0.147^{+0.016}_{-0.018}$	-	-	-	-
IRAS 08355-4944	$1.019^{+0.029}_{-0.03}$	$0.774^{+0.033}_{-0.025}$	$-0.485^{+0.020}_{-0.021}$	-	-	-	-
IRAS 09022-3615	$0.534^{+0.035}_{-0.039}$	$0.480^{+0.053}_{-0.054}$	$-1.136^{+0.040}_{-0.043}$	-	-	-	-
IRAS 10378+1109	$\mathbf{0.200^{+0.038}_{-0.049}}$	$\mathbf{0.225^{+0.072}_{-0.083}}$	$-2.289^{+0.105}_{-0.113}$	$\mathbf{4.916^{+0.944}_{-0.679}}$	$0.721^{+0.039}_{-0.041}$	-	-
IRAS 10565+2448	$1.138^{+0.129}_{-0.164}$	$0.436^{+0.038}_{-0.04}$	$-0.952^{+0.109}_{-0.116}$	-	-	-	-
IRAS 11095-0238	$\mathbf{0.073^{+0.010}_{-0.011}}$	$\mathbf{0.011^{+0.006}_{-0.009}}$	$-3.764^{+0.072}_{-0.066}$	$\mathbf{5.382^{+0.278}_{-0.242}}$	$0.925^{+0.009}_{-0.010}$	-	II
IRAS 12116-5615	$\mathbf{0.301^{+0.008}_{-0.009}}$	$0.276^{+0.006}_{-0.006}$	$-1.550^{+0.031}_{-0.034}$	$\mathbf{3.742^{+0.168}_{-0.15}}$	$0.562^{+0.024}_{-0.025}$	-	-
IRAS 13052-5711	$\mathbf{0.478^{+0.026}_{-0.031}}$	$\mathbf{0.287^{+0.012}_{-0.014}}$	$-1.438^{+0.032}_{-0.035}$	$\mathbf{4.121^{+0.501}_{-0.445}}$	$0.570^{+0.019}_{-0.017}$	-	-
IRAS 13120-5453	$0.725^{+0.042}_{-0.047}$	$0.342^{+0.013}_{-0.015}$	$-1.554^{+0.045}_{-0.045}$	-	-	✓	-
IRAS 13451+1232	$\mathbf{0.303^{+0.106}_{-0.112}}$	$0.651^{+0.127}_{-0.131}$	$-0.254^{+0.018}_{-0.020}$	-	-	-	-
IRAS 14348-1447	$\mathbf{0.279^{+0.028}_{-0.030}}$	$\mathbf{0.167^{+0.018}_{-0.021}}$	$-2.066^{+0.06}_{-0.059}$	$\mathbf{3.909^{+0.452}_{-0.378}}$	$0.732^{+0.028}_{-0.027}$	-	-
IRAS 14378-3651	$0.684^{+0.095}_{-0.122}$	$0.321^{+0.043}_{-0.052}$	$-1.750^{+0.094}_{-0.110}$	$2.642^{+0.381}_{-0.265}$	$0.709^{+0.052}_{-0.057}$	-	-
IRAS 16090-0139	$\mathbf{0.132^{+0.018}_{-0.020}}$	$\mathbf{0.152^{+0.029}_{-0.033}}$	$-2.797^{+0.057}_{-0.055}$	$\mathbf{4.166^{+0.339}_{-0.26}}$	$0.834^{+0.022}_{-0.025}$	-	-
IRAS 17208-0014	$\mathbf{0.331^{+0.028}_{-0.032}}$	$\mathbf{0.230^{+0.017}_{-0.020}}$	$-1.97^{+0.086}_{-0.081}$	$\mathbf{4.805^{+0.429}_{-0.379}}$	$0.712^{+0.028}_{-0.028}$	-	I
IRAS 17578-0400	$0.643^{+0.054}_{-0.061}$	$\mathbf{0.270^{+0.014}_{-0.016}}$	$-1.455^{+0.075}_{-0.073}$	$\mathbf{4.444^{+0.522}_{-0.443}}$	$0.513^{+0.040}_{-0.039}$	-	I
IRAS 18090+0130	$0.764^{+0.055}_{-0.066}$	$0.311^{+0.010}_{-0.012}$	$-0.76^{+0.041}_{-0.046}$	$\mathbf{3.603^{+0.595}_{-0.515}}$	$0.43^{+0.020}_{-0.020}$	-	-
IRAS 19254-7245	$\mathbf{0.149^{+0.009}_{-0.01}}$	$\mathbf{0.203^{+0.024}_{-0.028}}$	$-1.353^{+0.026}_{-0.026}$	$\mathbf{4.267^{+0.304}_{-0.273}}$	$0.432^{+0.013}_{-0.011}$	-	-
IRAS 19297-0406	$0.611^{+0.111}_{-0.160}$	$\mathbf{0.201^{+0.036}_{-0.048}}$	$-1.680^{+0.133}_{-0.154}$	$\mathbf{4.746^{+1.369}_{-0.918}}$	$0.583^{+0.049}_{-0.051}$	-	-
IRAS 19542+1110	$0.581^{+0.063}_{-0.072}$	$0.362^{+0.038}_{-0.039}$	$-0.899^{+0.097}_{-0.106}$	-	-	-	-
IRAS 20087-0308	$\mathbf{0.267^{+0.032}_{-0.036}}$	$0.295^{+0.032}_{-0.034}$	$-2.077^{+0.105}_{-0.109}$	$\mathbf{4.570^{+0.929}_{-0.659}}$	$0.668^{+0.034}_{-0.033}$	-	-
IRAS 20100-4156	$\mathbf{0.204^{+0.018}_{-0.019}}$	$\mathbf{0.212^{+0.027}_{-0.030}}$	$-2.654^{+0.059}_{-0.057}$	$\mathbf{4.867^{+0.37}_{-0.317}}$	$0.794^{+0.019}_{-0.019}$	-	-
IRAS 20351+2521	$1.027^{+0.069}_{-0.088}$	$0.491^{+0.022}_{-0.021}$	$-0.587^{+0.050}_{-0.062}$	-	-	-	-
IRAS 21101+5810	$1.391^{+0.192}_{-0.571}$	$0.320^{+0.027}_{-0.031}$	$-0.926^{+0.100}_{-0.157}$	$2.630^{+0.337}_{-0.281}$	$0.553^{+0.061}_{-0.073}$	-	-
IRAS 22491-1808	$0.647^{+0.09}_{-0.108}$	$\mathbf{0.179^{+0.024}_{-0.029}}$	$-1.465^{+0.088}_{-0.088}$	$\mathbf{4.799^{+0.823}_{-0.626}}$	$0.652^{+0.036}_{-0.045}$	-	-
IRAS 23230-6926	$\mathbf{0.390^{+0.048}_{-0.054}}$	$\mathbf{0.219^{+0.030}_{-0.031}}$	$-2.348^{+0.079}_{-0.075}$	$\mathbf{3.838^{+0.400}_{-0.302}}$	$0.802^{+0.026}_{-0.027}$	-	-
IRAS 23253-5415	$\mathbf{0.432^{+0.047}_{-0.049}}$	$0.303^{+0.028}_{-0.028}$	$-1.584^{+0.050}_{-0.056}$	-	-	-	-
IRAS 23365+3604	$0.643^{+0.068}_{-0.082}$	$\mathbf{0.198^{+0.027}_{-0.030}}$	$-1.968^{+0.063}_{-0.060}$	$2.636^{+0.21}_{-0.163}$	$0.834^{+0.030}_{-0.032}$	-	-
IRAS 23436+5257	$0.779^{+0.040}_{-0.044}$	$0.487^{+0.025}_{-0.026}$	$-0.506^{+0.030}_{-0.031}$	-	-	-	-
IRAS F01364-1042	$0.605^{+0.108}_{-0.148}$	$0.301^{+0.035}_{-0.035}$	$-1.824^{+0.132}_{-0.153}$	$\mathbf{4.226^{+0.74}_{-0.549}}$	$0.668^{+0.033}_{-0.033}$	-	-
IRAS F01417+1651	$1.387^{+0.449}_{-0.815}$	$0.302^{+0.036}_{-0.042}$	$-0.907^{+0.137}_{-0.115}$	$3.159^{+0.957}_{-0.644}$	$0.527^{+0.068}_{-0.07}$	-	-
IRAS F02437+2122	$\mathbf{0.285^{+0.033}_{-0.036}}$	$0.286^{+0.037}_{-0.040}$	$-1.820^{+0.064}_{-0.065}$	$2.777^{+0.411}_{-0.297}$	$0.741^{+0.049}_{-0.05}$	-	-
IRAS F03217+4022	$0.527^{+0.019}_{-0.023}$	$0.354^{+0.013}_{-0.014}$	$-1.238^{+0.030}_{-0.034}$	-	-	-	-
IRAS F05081+7936	$0.828^{+0.048}_{-0.722}$	$0.462^{+0.026}_{-0.038}$	$-0.901^{+0.047}_{-0.62}$	-	-	-	-
IRAS F05187-1017	$\mathbf{0.329^{+0.040}_{-0.043}}$	$0.313^{+0.032}_{-0.035}$	$-1.741^{+0.116}_{-0.098}$	$\mathbf{4.292^{+0.995}_{-0.751}}$	$0.575^{+0.056}_{-0.047}$	-	-
IRAS F05189+2524	$0.685^{+0.133}_{-0.128}$	$0.741^{+0.204}_{-0.259}$	$-0.320^{+0.065}_{-0.052}$	-	-	-	-
IRAS F06076-2139	$0.596^{+0.054}_{-0.063}$	$0.376^{+0.034}_{-0.038}$	$-1.679^{+0.057}_{-0.059}$	-	-	-	-
IRAS F06592-6313	$1.080^{+0.071}_{-0.086}$	$0.445^{+0.027}_{-0.035}$	$-0.665^{+0.052}_{-0.065}$	-	-	-	-
IRAS F10173+0828	$\mathbf{0.451^{+0.124}_{-0.215}}$	$\mathbf{0.199^{+0.049}_{-0.059}}$	$-1.893^{+0.164}_{-0.194}$	$\mathbf{5.341^{+1.862}_{-1.254}}$	$0.669^{+0.050}_{-0.049}$	-	-
IRAS F10565+2448	$1.134^{+0.136}_{-0.156}$	$0.430^{+0.035}_{-0.038}$	$-0.961^{+0.094}_{-0.099}$	-	-	-	-
IRAS F12112+0305	$\mathbf{0.492^{+0.059}_{-0.060}}$	$\mathbf{0.232^{+0.028}_{-0.032}}$	$-1.750^{+0.068}_{-0.078}$	$2.931^{+0.451}_{-0.294}$	$0.683^{+0.045}_{-0.048}$	-	-
IRAS F12224-0624	$\mathbf{0.063^{+0.010}_{-0.011}}$	$\mathbf{0.104^{+0.031}_{-0.033}}$	$-3.500^{+0.089}_{-0.090}$	$\mathbf{7.129^{+0.609}_{-0.529}}$	$0.842^{+0.013}_{-0.014}$	-	-
IRAS F14348-1447	$\mathbf{0.288^{+0.030}_{-0.033}}$	$\mathbf{0.172^{+0.020}_{-0.022}}$	$-2.064^{+0.063}_{-0.070}$	$\mathbf{3.863^{+0.450}_{-0.348}}$	$0.729^{+0.027}_{-0.027}$	-	-

Table A.1: Continued.

Name	EW(6.2)/EW(11.3)	EW(12.7)/EW(11.3)	$S_{\rm Sil}$	τ_N	β	HCN (14 μm)	Crystallines?
(1)	(2)	(3)	(4)	(5)	(6)	(7)	(8)
IRAS F14378-3651	$0.688^{+0.095}_{-0.129}$	$0.324^{+0.045}_{-0.050}$	$-1.752^{+0.097}_{-0.107}$	$2.625^{+0.374}_{-0.262}$	$0.712^{+0.053}_{-0.062}$	-	-
IRAS F16164-0746	$0.556^{+0.066}_{-0.072}$	$0.335^{+0.025}_{-0.023}$	$-2.097^{+0.07}_{-0.069}$	$\mathbf{4.836^{+0.657}_{-0.533}}$	$0.652^{+0.024}_{-0.023}$	-	-
IRAS F16516-0948	$0.760^{+0.041}_{-0.049}$	$0.410^{+0.027}_{-0.028}$	$-0.628^{+0.058}_{-0.066}$	-	-	-	-
IRAS F17138-1017	$0.613^{+0.035}_{-0.044}$	$0.352^{+0.01}_{-0.012}$	$-1.106^{+0.037}_{-0.041}$	-	-	-	-
IRAS F17207-0014	$\mathbf{0.331^{+0.027}_{-0.03}}$	$\mathbf{0.231^{+0.017}_{-0.019}}$	$-1.968^{+0.074}_{-0.069}$	$\mathbf{4.804^{+0.429}_{-0.382}}$	$0.711^{+0.027}_{-0.029}$	-	-
IRAS F18293-3413	$0.600^{+0.014}_{-0.014}$	$0.318^{+0.007}_{-0.008}$	$-1.533^{+0.014}_{-0.016}$	-	-	-	-
IRAS F19297-0406	$0.567^{+0.107}_{-0.148}$	$\mathbf{0.191^{+0.035}_{-0.045}}$	$-1.697^{+0.119}_{-0.143}$	$\mathbf{4.690^{+1.381}_{-0.848}}$	$0.607^{+0.048}_{-0.055}$	-	-
IRAS F22491-1808	$0.652^{+0.084}_{-0.101}$	$\mathbf{0.178^{+0.024}_{-0.027}}$	$-1.470^{+0.071}_{-0.078}$	$\mathbf{4.767^{+0.853}_{-0.647}}$	$0.656^{+0.035}_{-0.051}$	-	-
IRAS F23365+3604	$0.667^{+0.07}_{-0.082}$	$\mathbf{0.207^{+0.029}_{-0.032}}$	$-1.964^{+0.049}_{-0.057}$	$2.605^{+0.201}_{-0.163}$	$0.834^{+0.033}_{-0.035}$	-	-
M-3-34-63	$0.588^{+0.209}_{-0.299}$	$0.419^{+0.127}_{-0.16}$	$-0.477^{+0.128}_{-0.149}$	-	-	-	-
MCG +08-11-002	$\mathbf{0.336^{+0.017}_{-0.017}}$	$\mathbf{0.232^{+0.008}_{-0.009}}$	$-2.380^{+0.046}_{-0.039}$	$\mathbf{4.705^{+0.219}_{-0.195}}$	$0.716^{+0.016}_{-0.013}$	-	-
MCG +09-27-025	$0.749^{+0.191}_{-0.261}$	$0.499^{+0.071}_{-0.084}$	$-0.831^{+0.245}_{-0.126}$	-	-	-	-
MCG +10-25-031	$0.581^{+0.077}_{-0.098}$	$0.446^{+0.042}_{-0.049}$	$-0.247^{+0.093}_{-0.077}$	-	-	-	-
MCG -02-33-098	$1.108^{+0.065}_{-0.076}$	$0.435^{+0.019}_{-0.025}$	$-0.507^{+0.047}_{-0.047}$	-	-	-	-
MCG -05-12-006	$1.592^{+0.104}_{-0.12}$	$0.452^{+0.021}_{-0.031}$	$-0.246^{+0.033}_{-0.031}$	-	-	-	-
MCG+04-48-002	$\mathbf{0.421^{+0.018}_{-0.018}}$	$0.334^{+0.015}_{-0.018}$	$-1.228^{+0.048}_{-0.051}$	$3.403^{+0.506}_{-0.389}$	$0.403^{+0.053}_{-0.052}$	-	-
MCG+12-02-001	$1.293^{+0.032}_{-0.032}$	$0.527^{+0.01}_{-0.015}$	$-0.579^{+0.015}_{-0.015}$	-	-	-	-
MCG-02-01-051A	$0.774^{+0.121}_{-0.136}$	$0.403^{+0.063}_{-0.068}$	$-0.419^{+0.084}_{-0.117}$	-	-	-	-
MCG-02-33-098	$1.691^{+0.05}_{-0.052}$	$0.694^{+0.039}_{-0.038}$	$-0.229^{+0.018}_{-0.018}$	-	-	-	-
MCG-03-04-014	$1.018^{+0.054}_{-0.063}$	$0.444^{+0.026}_{-0.031}$	$-0.684^{+0.049}_{-0.055}$	-	-	-	-
MCG-03-34-064	$0.191^{+0.034}_{-0.036}$	$0.526^{+0.04}_{-0.041}$	$-0.091^{+0.004}_{-0.004}$	-	-	-	-
Mrk 0231	$0.770^{+0.088}_{-0.097}$	$0.547^{+0.122}_{-0.141}$	$-0.689^{+0.02}_{-0.022}$	-	-	-	-
Mrk 0273	$\mathbf{0.409^{+0.04}_{-0.048}}$	$\mathbf{0.254^{+0.035}_{-0.039}}$	$-2.061^{+0.039}_{-0.038}$	$2.883^{+0.2}_{-0.175}$	$0.796^{+0.03}_{-0.031}$	-	-
Mrk 0331	$0.592^{+0.025}_{-0.026}$	$0.297^{+0.011}_{-0.013}$	$-1.030^{+0.022}_{-0.023}$	$2.725^{+0.324}_{-0.285}$	$0.55^{+0.029}_{-0.024}$	-	-
Mrk 1014	$0.841^{+0.127}_{-0.153}$	$0.644^{+0.122}_{-0.144}$	$0.205^{+0.03}_{-0.033}$	-	-	-	-
Mrk 1490	$1.116^{+0.077}_{-0.084}$	$0.414^{+0.032}_{-0.034}$	$-0.682^{+0.043}_{-0.047}$	-	-	-	-
Mrk 938*	$\mathbf{0.499^{+0.043}_{-0.048}}$	$0.337^{+0.035}_{-0.037}$	$-1.569^{+0.06}_{-0.062}$	$2.623^{+0.285}_{-0.207}$	$0.639^{+0.041}_{-0.042}$	-	-
NGC 0023	$0.665^{+0.019}_{-0.021}$	$0.418^{+0.014}_{-0.017}$	$-0.448^{+0.028}_{-0.031}$	-	-	-	-
NGC 0232	$0.545^{+0.015}_{-0.016}$	$0.335^{+0.006}_{-0.007}$	$-1.021^{+0.021}_{-0.022}$	$2.606^{+0.238}_{-0.211}$	$0.476^{+0.027}_{-0.024}$	-	-
NGC 0354	$0.683^{+0.025}_{-0.03}$	$0.420^{+0.021}_{-0.023}$	$-0.709^{+0.048}_{-0.049}$	-	-	-	-
NGC 0633	$0.734^{+0.015}_{-0.017}$	$0.487^{+0.023}_{-0.033}$	$-0.505^{+0.033}_{-0.036}$	-	-	-	-
NGC 0660	$0.582^{+0.025}_{-0.028}$	$0.289^{+0.007}_{-0.008}$	$-1.659^{+0.026}_{-0.027}$	$2.798^{+0.16}_{-0.14}$	$0.665^{+0.024}_{-0.027}$	-	-
NGC 0695	$0.842^{+0.028}_{-0.032}$	$0.444^{+0.023}_{-0.024}$	$-0.613^{+0.033}_{-0.035}$	-	-	-	-
NGC 0828	$\mathbf{0.459^{+0.01}_{-0.01}}$	$0.350^{+0.009}_{-0.009}$	$-1.144^{+0.014}_{-0.014}$	-	-	-	-
NGC 0838	$1.292^{+0.196}_{-0.207}$	$0.428^{+0.03}_{-0.028}$	$-0.266^{+0.098}_{-0.053}$	-	-	-	-
NGC 0877	$\mathbf{0.275^{+0.017}_{-0.021}}$	$0.464^{+0.024}_{-0.024}$	$-0.463^{+0.044}_{-0.051}$	-	-	-	-
NGC 0958	$\mathbf{0.380^{+0.017}_{-0.02}}$	$0.497^{+0.033}_{-0.032}$	$-0.526^{+0.055}_{-0.058}$	-	-	-	-
NGC 0992	$0.844^{+0.018}_{-0.019}$	$0.378^{+0.009}_{-0.011}$	$-0.769^{+0.022}_{-0.023}$	-	-	-	-
NGC 1067	$0.949^{+0.089}_{-0.103}$	$0.444^{+0.041}_{-0.043}$	$-0.192^{+0.076}_{-0.053}$	-	-	-	-
NGC 1365	$\mathbf{0.419^{+0.01}_{-0.011}}$	$0.520^{+0.013}_{-0.016}$	$-0.183^{+0.021}_{-0.023}$	-	-	-	-
NGC 1572	$1.202^{+0.049}_{-0.05}$	$0.621^{+0.034}_{-0.033}$	$-0.327^{+0.044}_{-0.04}$	-	-	-	-
NGC 1614	$1.471^{+0.038}_{-0.043}$	$0.472^{+0.02}_{-0.024}$	$-0.698^{+0.015}_{-0.016}$	-	-	-	-
NGC 1797	$0.942^{+0.043}_{-0.049}$	$0.465^{+0.027}_{-0.033}$	$-0.712^{+0.03}_{-0.033}$	-	-	-	-
NGC 1808	$0.696^{+0.013}_{-0.013}$	$0.393^{+0.009}_{-0.01}$	$-0.796^{+0.021}_{-0.027}$	-	-	-	-
NGC 1961	$\mathbf{0.147^{+0.01}_{-0.011}}$	$0.489^{+0.028}_{-0.026}$	$-0.518^{+0.051}_{-0.046}$	-	-	-	-
NGC 2146	$1.417^{+0.078}_{-0.089}$	$0.392^{+0.011}_{-0.01}$	$-0.707^{+0.02}_{-0.023}$	-	-	-	-
NGC 2342 A*	$1.077^{+0.063}_{-0.072}$	$0.510^{+0.036}_{-0.032}$	$-0.321^{+0.079}_{-0.074}$	-	-	-	-
NGC 2342	$0.769^{+0.067}_{-0.078}$	$0.377^{+0.02}_{-0.025}$	$-0.660^{+0.053}_{-0.059}$	-	-	-	-
NGC 2369*	$0.654^{+0.031}_{-0.03}$	$0.367^{+0.022}_{-0.028}$	$-1.329^{+0.041}_{-0.04}$	-	-	-	-

Table A.1: Continued.

Name	EW(6.2)/EW(11.3)	EW(12.7)/EW(11.3)	$S_{\rm Sil}$	τ_N	β	HCN (14 μm)	Crystallines?
(1)	(2)	(3)	(4)	(5)	(6)	(7)	(8)
NGC 2388 A*	$0.661^{+0.055}_{-0.063}$	$0.474^{+0.041}_{-0.048}$	$-0.346^{+0.095}_{-0.098}$	-	-	-	-
NGC 2388	$0.750^{+0.017}_{-0.019}$	$0.406^{+0.009}_{-0.011}$	$-0.778^{+0.021}_{-0.023}$	-	-	-	-
NGC 2544	$0.503^{+0.030}_{-0.036}$	$0.387^{+0.031}_{-0.036}$	$-0.479^{+0.055}_{-0.065}$	-	-	-	-
NGC 2623	$0.690^{+0.079}_{-0.105}$	$0.329^{+0.028}_{-0.028}$	$-1.860^{+0.073}_{-0.079}$	$3.065^{+0.302}_{-0.254}$	$0.731^{+0.032}_{-0.032}$	-	-
NGC 2903	$0.877^{+0.024}_{-0.026}$	$0.530^{+0.013}_{-0.011}$	$-0.310^{+0.023}_{-0.02}$	-	-	-	-
NGC 2993	$1.529^{+0.093}_{-0.138}$	$0.514^{+0.025}_{-0.025}$	$-0.021^{+0.022}_{-0.012}$	-	-	-	-
NGC 3110	$0.833^{+0.03}_{-0.034}$	$0.401^{+0.013}_{-0.015}$	$-0.834^{+0.036}_{-0.043}$	-	-	-	-
NGC 3188	$1.099^{+0.123}_{-0.141}$	$0.464^{+0.05}_{-0.053}$	$-0.147^{+0.087}_{-0.071}$	-	-	-	-
NGC 3256	$1.037^{+0.031}_{-0.037}$	$0.396^{+0.009}_{-0.009}$	$-0.647^{+0.022}_{-0.022}$	-	-	-	-
NGC 3628	$\mathbf{0.378^{+0.023}_{-0.024}}$	$0.283^{+0.015}_{-0.016}$	$-2.360^{+0.04}_{-0.041}$	$\mathbf{5.098^{+0.495}_{-0.401}}$	$0.669^{+0.014}_{-0.014}$	-	-
NGC 4194	$0.953^{+0.027}_{-0.03}$	$0.433^{+0.011}_{-0.014}$	$-0.723^{+0.02}_{-0.021}$	-	-	-	-
NGC 4369	$0.643^{+0.017}_{-0.019}$	$0.392^{+0.013}_{-0.015}$	$-0.362^{+0.026}_{-0.026}$	-	-	-	-
NGC 4385	$1.921^{+0.12}_{-0.196}$	$0.546^{+0.043}_{-0.034}$	$-0.079^{+0.047}_{-0.035}$	-	-	-	-
NGC 4418	$\mathbf{0.038^{+0.005}_{-0.005}}$	$\mathbf{0.096^{+0.023}_{-0.024}}$	$-4.317^{+0.019}_{-0.018}$	$\mathbf{4.546^{+0.037}_{-0.035}}$	$0.988^{+0.001}_{-0.002}$	✓	I
NGC 4666	$\mathbf{0.458^{+0.034}_{-0.032}}$	$0.527^{+0.025}_{-0.022}$	$-0.333^{+0.084}_{-0.082}$	-	-	-	-
NGC 4922*	$0.617^{+0.07}_{-0.078}$	$0.530^{+0.057}_{-0.061}$	$-0.519^{+0.034}_{-0.02}$	-	-	-	-
NGC 4922	$1.021^{+0.096}_{-0.114}$	$0.480^{+0.057}_{-0.059}$	$-0.515^{+0.064}_{-0.045}$	-	-	-	-
NGC 5010	$\mathbf{0.326^{+0.013}_{-0.014}}$	$0.291^{+0.012}_{-0.015}$	$-1.494^{+0.03}_{-0.036}$	$\mathbf{3.651^{+0.318}_{-0.292}}$	$0.616^{+0.019}_{-0.019}$	-	-
NGC 5104	$\mathbf{0.388^{+0.027}_{-0.027}}$	$0.302^{+0.022}_{-0.025}$	$-1.298^{+0.049}_{-0.081}$	$3.186^{+0.404}_{-0.311}$	$0.590^{+0.038}_{-0.04}$	-	-
NGC 5135	$0.523^{+0.024}_{-0.019}$	$0.456^{+0.023}_{-0.022}$	$-0.717^{+0.029}_{-0.031}$	-	-	-	-
NGC 5257 A*	$0.683^{+0.053}_{-0.056}$	$0.504^{+0.046}_{-0.048}$	$-0.455^{+0.073}_{-0.089}$	-	-	-	-
NGC 5331	$0.614^{+0.025}_{-0.027}$	$0.396^{+0.026}_{-0.024}$	$-1.136^{+0.038}_{-0.038}$	-	-	-	-
NGC 5394	$0.687^{+0.027}_{-0.03}$	$0.358^{+0.014}_{-0.016}$	$-0.648^{+0.023}_{-0.025}$	-	-	-	-
NGC 5395*	$\mathbf{0.125^{+0.016}_{-0.017}}$	$0.408^{+0.037}_{-0.04}$	$-0.355^{+0.026}_{-0.024}$	-	-	-	-
NGC 5430	$1.040^{+0.037}_{-0.041}$	$0.612^{+0.012}_{-0.01}$	$-0.263^{+0.018}_{-0.02}$	-	-	-	-
NGC 5607	$1.015^{+0.036}_{-0.039}$	$0.443^{+0.018}_{-0.02}$	$-0.522^{+0.026}_{-0.028}$	-	-	-	-
NGC 5643	$0.611^{+0.032}_{-0.034}$	$0.423^{+0.02}_{-0.019}$	$-0.309^{+0.032}_{-0.033}$	-	-	-	-
NGC 5734	$\mathbf{0.396^{+0.017}_{-0.019}}$	$0.391^{+0.017}_{-0.02}$	$-0.603^{+0.027}_{-0.029}$	-	-	-	-
NGC 5743	$\mathbf{0.397^{+0.023}_{-0.026}}$	$0.323^{+0.02}_{-0.026}$	$-0.804^{+0.055}_{-0.059}$	-	-	-	-
NGC 5936	$0.752^{+0.044}_{-0.042}$	$0.392^{+0.019}_{-0.021}$	$-0.742^{+0.031}_{-0.033}$	-	-	-	-
NGC 5990	$\mathbf{0.254^{+0.005}_{-0.006}}$	$0.448^{+0.018}_{-0.019}$	$-0.639^{+0.024}_{-0.023}$	-	-	-	-
NGC 6090 NED01	$2.174^{+0.205}_{-0.287}$	$0.397^{+0.02}_{-0.021}$	$-0.145^{+0.038}_{-0.028}$	-	-	-	-
NGC 6090	$1.943^{+0.222}_{-0.271}$	$0.361^{+0.018}_{-0.02}$	$-0.207^{+0.03}_{-0.025}$	-	-	-	-
NGC 6161	$1.255^{+0.376}_{-0.317}$	$0.456^{+0.06}_{-0.053}$	$-0.663^{+0.277}_{-0.131}$	-	-	-	-
NGC 6240	$0.820^{+0.042}_{-0.044}$	$0.339^{+0.016}_{-0.013}$	$-1.438^{+0.038}_{-0.034}$	-	-	-	-
NGC 6286	$\mathbf{0.389^{+0.018}_{-0.019}}$	$0.274^{+0.011}_{-0.012}$	$-1.557^{+0.026}_{-0.03}$	$\mathbf{3.939^{+0.384}_{-0.349}}$	$0.628^{+0.018}_{-0.017}$	-	-
NGC 6670A	$0.867^{+0.036}_{-0.038}$	$0.350^{+0.014}_{-0.017}$	$-0.844^{+0.037}_{-0.039}$	-	-	-	-
NGC 6701	$0.520^{+0.026}_{-0.025}$	$0.359^{+0.017}_{-0.017}$	$-0.807^{+0.025}_{-0.026}$	-	-	-	-
NGC 6786 A*	$0.806^{+0.034}_{-0.036}$	$0.528^{+0.03}_{-0.026}$	$-0.383^{+0.016}_{-0.016}$	-	-	-	-
NGC 6786	$0.931^{+0.049}_{-0.048}$	$0.521^{+0.028}_{-0.024}$	$-0.348^{+0.056}_{-0.054}$	-	-	-	-
NGC 6926*	$\mathbf{0.343^{+0.028}_{-0.031}}$	$0.365^{+0.028}_{-0.029}$	$-1.120^{+0.049}_{-0.052}$	-	-	-	-
NGC 6926	$\mathbf{0.280^{+0.062}_{-0.1}}$	$\mathbf{0.258^{+0.056}_{-0.067}}$	$-1.352^{+0.195}_{-0.176}$	$\mathbf{5.633^{+2.133}_{-1.465}}$	$0.502^{+0.054}_{-0.061}$	-	-
NGC 7130	$0.792^{+0.042}_{-0.043}$	$0.507^{+0.026}_{-0.023}$	$-0.462^{+0.031}_{-0.037}$	-	-	-	-
NGC 7252	$0.658^{+0.032}_{-0.039}$	$0.419^{+0.021}_{-0.024}$	$-0.474^{+0.05}_{-0.056}$	-	-	-	-
NGC 7469	$0.975^{+0.017}_{-0.018}$	$0.451^{+0.006}_{-0.006}$	$-0.053^{+0.002}_{-0.002}$	-	-	-	-
NGC 7552*	$0.595^{+0.039}_{-0.041}$	$0.376^{+0.026}_{-0.027}$	$-0.735^{+0.068}_{-0.076}$	-	-	-	-
NGC 7591	$0.521^{+0.074}_{-0.081}$	$0.354^{+0.032}_{-0.037}$	$-1.038^{+0.096}_{-0.1}$	$2.818^{+1.159}_{-0.695}$	$0.409^{+0.104}_{-0.092}$	-	-
NGC 7592 A*	$0.956^{+0.06}_{-0.062}$	$0.445^{+0.025}_{-0.027}$	$-0.745^{+0.044}_{-0.047}$	-	-	-	-
NGC 7592 B*	$\mathbf{0.468^{+0.017}_{-0.016}}$	$0.458^{+0.018}_{-0.018}$	$-1.446^{+0.024}_{-0.024}$	-	-	-	-

Table A.1: Continued.

Name	EW(6.2)/EW(11.3)	EW(12.7)/EW(11.3)	$S_{\rm Sil}$	τ_N	β	HCN (14 μm)	Crystallines?
(1)	(2)	(3)	(4)	(5)	(6)	(7)	(8)
NGC 7674*	$\mathbf{0.243^{+0.057}_{-0.061}}$	$0.442^{+0.062}_{-0.065}$	$-0.185^{+0.012}_{-0.012}$	-	-	✓	-
NGC 7674A	$0.920^{+0.078}_{-0.055}$	$0.485^{+0.036}_{-0.04}$	$-0.35^{+0.077}_{-0.082}$	-	-	-	-
NGC 7679	$0.962^{+0.017}_{-0.016}$	$0.462^{+0.008}_{-0.009}$	$-0.195^{+0.014}_{-0.015}$	-	-	-	-
NGC 7752 A*	$\mathbf{0.326^{+0.023}_{-0.024}}$	$0.544^{+0.033}_{-0.034}$	$-0.500^{+0.037}_{-0.037}$	-	-	-	-
NGC 7752	$0.704^{+0.053}_{-0.064}$	$0.365^{+0.024}_{-0.029}$	$-0.698^{+0.051}_{-0.056}$	-	-	-	-
NGC 7771	$0.603^{+0.03}_{-0.037}$	$0.427^{+0.018}_{-0.017}$	$-0.823^{+0.046}_{-0.049}$	$2.875^{+0.635}_{-0.505}$	$0.401^{+0.049}_{-0.039}$	-	-
NVSS J211129+582307	$1.388^{+0.191}_{-0.563}$	$0.319^{+0.027}_{-0.03}$	$-0.932^{+0.09}_{-0.152}$	$2.586^{+0.342}_{-0.267}$	$0.562^{+0.056}_{-0.075}$	-	-
SBS 1132+579	$0.817^{+0.078}_{-0.083}$	$0.559^{+0.046}_{-0.042}$	$-0.212^{+0.114}_{-0.089}$	-	-	-	-
SBS 1204+579	$0.789^{+0.062}_{-0.062}$	$0.525^{+0.057}_{-0.06}$	$-0.228^{+0.104}_{-0.081}$	-	-	-	-
UGC 01385	$2.120^{+0.153}_{-0.169}$	$0.438^{+0.025}_{-0.025}$	$-0.185^{+0.028}_{-0.025}$	-	-	-	-
UGC 01845	$\mathbf{0.390^{+0.016}_{-0.014}}$	$\mathbf{0.271^{+0.012}_{-0.012}}$	$-1.630^{+0.017}_{-0.018}$	$\mathbf{3.501^{+0.341}_{-0.234}}$	$0.685^{+0.015}_{-0.016}$	✓	-
UGC 02238	$\mathbf{0.419^{+0.027}_{-0.029}}$	$0.280^{+0.014}_{-0.015}$	$-1.556^{+0.059}_{-0.062}$	$3.340^{+0.377}_{-0.311}$	$0.643^{+0.026}_{-0.031}$	-	-
UGC 02608	$0.507^{+0.039}_{-0.041}$	$0.409^{+0.032}_{-0.036}$	$-0.767^{+0.055}_{-0.062}$	-	-	-	-
UGC 02894	$0.856^{+0.051}_{-0.056}$	$0.445^{+0.023}_{-0.021}$	$-0.422^{+0.067}_{-0.064}$	-	-	-	-
UGC 02982	$0.589^{+0.01}_{-0.01}$	$0.373^{+0.01}_{-0.011}$	$-0.947^{+0.022}_{-0.022}$	-	-	-	-
UGC 03094	$0.509^{+0.02}_{-0.021}$	$0.349^{+0.013}_{-0.016}$	$-0.820^{+0.037}_{-0.042}$	$2.617^{+0.527}_{-0.39}$	$0.406^{+0.046}_{-0.041}$	-	-
UGC 03351	$\mathbf{0.376^{+0.016}_{-0.016}}$	$0.301^{+0.012}_{-0.012}$	$-1.567^{+0.046}_{-0.045}$	$\mathbf{3.636^{+0.239}_{-0.205}}$	$0.621^{+0.025}_{-0.025}$	-	-
UGC 03356 NOTES01	$0.847^{+0.032}_{-0.034}$	$0.379^{+0.014}_{-0.015}$	$-1.033^{+0.025}_{-0.026}$	-	-	-	-
UGC 03405	$\mathbf{0.473^{+0.033}_{-0.038}}$	$0.373^{+0.028}_{-0.028}$	$-0.785^{+0.057}_{-0.062}$	-	-	-	-
UGC 03410*	$0.745^{+0.09}_{-0.097}$	$0.446^{+0.046}_{-0.047}$	$-0.654^{+0.113}_{-0.116}$	-	-	-	-
UGC 03410	$0.530^{+0.023}_{-0.023}$	$0.356^{+0.017}_{-0.015}$	$-0.946^{+0.033}_{-0.035}$	$2.933^{+0.55}_{-0.392}$	$0.472^{+0.036}_{-0.033}$	-	-
UGC 03608	$1.293^{+0.069}_{-0.077}$	$0.384^{+0.02}_{-0.019}$	$-0.455^{+0.034}_{-0.034}$	-	-	-	-
UGC 04261	$1.902^{+0.173}_{-0.346}$	$0.413^{+0.022}_{-0.025}$	$-0.030^{+0.029}_{-0.017}$	-	-	-	-
UGC 04438	$0.890^{+0.079}_{-0.094}$	$0.479^{+0.037}_{-0.044}$	$-0.105^{+0.062}_{-0.041}$	-	-	-	-
UGC 04881	$0.549^{+0.034}_{-0.042}$	$0.389^{+0.021}_{-0.02}$	$-1.110^{+0.056}_{-0.064}$	-	-	-	-
UGC 05101	$0.269^{+0.023}_{-0.027}$	$0.480^{+0.041}_{-0.044}$	$-1.444^{+0.053}_{-0.053}$	-	-	-	-
UGC 05408	$1.572^{+0.157}_{-0.168}$	$0.390^{+0.026}_{-0.029}$	$-0.130^{+0.043}_{-0.03}$	-	-	-	-
UGC 06514 NED01	$0.568^{+0.082}_{-0.123}$	$0.539^{+0.047}_{-0.049}$	$-0.395^{+0.113}_{-0.101}$	-	-	-	-
UGC 08335 NED02	$1.276^{+0.073}_{-0.085}$	$0.403^{+0.027}_{-0.031}$	$-1.067^{+0.043}_{-0.048}$	-	-	-	-
UGC 08335	$1.053^{+0.25}_{-0.257}$	$0.371^{+0.032}_{-0.038}$	$-0.533^{+0.175}_{-0.118}$	-	-	-	-
UGC 08739	$\mathbf{0.281^{+0.021}_{-0.021}}$	$0.296^{+0.02}_{-0.021}$	$-1.735^{+0.069}_{-0.061}$	$\mathbf{4.326^{+0.492}_{-0.407}}$	$0.595^{+0.035}_{-0.036}$	-	-
UGC 08850	$\mathbf{0.099^{+0.026}_{-0.027}}$	$0.375^{+0.051}_{-0.053}$	$-0.388^{+0.009}_{-0.009}$	-	-	-	-
UGC 11041	$0.510^{+0.019}_{-0.019}$	$0.403^{+0.017}_{-0.018}$	$-0.659^{+0.037}_{-0.039}$	-	-	-	-
UGC 12150	$0.562^{+0.026}_{-0.027}$	$0.318^{+0.01}_{-0.011}$	$-1.172^{+0.032}_{-0.033}$	-	-	-	-
UGC 2982	$1.280^{+0.048}_{-0.054}$	$0.445^{+0.013}_{-0.014}$	$-0.205^{+0.022}_{-0.016}$	-	-	-	-
UGC 8387	$0.572^{+0.048}_{-0.049}$	$\mathbf{0.259^{+0.013}_{-0.014}}$	$-1.924^{+0.068}_{-0.063}$	$\mathbf{3.590^{+0.285}_{-0.237}}$	$0.705^{+0.027}_{-0.03}$	-	-
VII Zw 031	$1.544^{+0.102}_{-0.119}$	$0.500^{+0.016}_{-0.016}$	$-0.284^{+0.036}_{-0.031}$	-	-	-	-
VV 059a	$\mathbf{0.486^{+0.035}_{-0.041}}$	$0.303^{+0.014}_{-0.017}$	$-1.392^{+0.051}_{-0.057}$	$\mathbf{5.705^{+1.258}_{-0.954}}$	$0.533^{+0.025}_{-0.027}$	-	-
VV 283a	$\mathbf{0.476^{+0.04}_{-0.043}}$	$\mathbf{0.267^{+0.014}_{-0.016}}$	$-1.877^{+0.07}_{-0.068}$	$\mathbf{3.908^{+0.322}_{-0.287}}$	$0.700^{+0.024}_{-0.025}$	-	-
ZW049.057*	$\mathbf{0.459^{+0.058}_{-0.063}}$	$\mathbf{0.278^{+0.034}_{-0.036}}$	$-1.679^{+0.081}_{-0.085}$	$\mathbf{4.444^{+0.962}_{-0.697}}$	$0.519^{+0.05}_{-0.044}$	-	-

• Column (1): Object Name. Column (2): Ratio of the EW of the 6.2 μm PAH to the 11.3 μm PAH. Column (3): Ratio of the EW of the 12.7 μm PAH to the 11.3 μm PAH. Column (4): Silicate strength according to Eq. (2.6). Column (5): Nuclear optical depth. Column (6): Nuclear fraction. Column (7): Detection of HCN (14 μm) absorption above 5σ in low-res *Spitzer* spectra. Column (8): Detection of Crystalline silicate absorption from Spoon et al. (2022). Method I selects sources with $z < 0.068$, $s_{23} < 0$ and $s_{33} < 0$. Method II selects sources with $z < 0.257$, $s_{23} < -0.09$ and $s_{33} < -0.02$.

• Sources marked * use the innermost aperture from the spectral maps

• Values for τ_N and β are only shown for $\beta > 0.4$ and $\tau_N > 2.5$ where these values are reliable as discussed in Sect. 2.3.6.

• PAH EW ratios with values lower than the threshold for CON classification are shown in bold. For those from spectral maps marked as *, the threshold used is the one adjusted for the aperture correction. Optical depths of $\tau_N > 3.5$ are also shown in bold.

A.2 Chapter 3:

A.2.1 Extinction Curve

There are many extinction curves presented in the literature (e.g. Chiar and Tielens, 2006; Kemper et al., 2004) however I found that none of these produced good fits for highly obscured objects and in particular the obscured nucleus (A) from VV 114E. I therefore created an empirically based extinction curve using a heavily obscured galaxy that has no apparent PAH emission, namely IRAS 08572+3915.

I use the Spitzer IRS spectra of IRAS 08572+3915 from the IDEOS database (Spoon et al., 2022), where I find a local continuum using a cubic spline interpolation with anchor points 5.5, 7.8, 13.0, 14.5 and 26.5 μm. This underlying continuum is shown in Fig. A.4 with the blue dashed line. I find the optical depth as a function of wavelength by calculating the log of the ratio of the underlying continuum to the data. This results in the middle panel of Fig. A.4. I take the silicate absorption features as a smoothed version of the optical depth data. I then construct an extinction curve by adding a power law component with exponent 1.7 making up 10% of the optical depth at 9.8μm following the original PAHIFT (Smith et al., 2007b) i.e

$$\tau_\lambda = 0.1\,(9.8/\lambda)^{1.7} + 0.9\tau_{\rm Sil}(\lambda), \tag{A.1}$$

where $\tau_{\rm Sil}$ is the extracted silicate profile from IRAS 08572+3915. The extinction curve is shown in the right panel of Fig. A.4. Comparing the extinction curve to others from the literature it is clear that ours contains crystalline absorption features at 11 μm, 16 μm, 19 μm, 23 μm and 28 μm which are not present in the others. These absorption features are typically weak in less obscured systems however are common in the ISM of galaxies (Spoon et al., 2022). Our extinction curve also features a significantly lower 18 μm silicate absorption feature relative to the 9.8 μm silicate feature than the other curves. This may be due to the presence of emission from cold silicates that emit at 18 μm but not 10μm, filling up the 18 μm silicate absorption band relative to the 9.8 μm band (e.g. Jones and Merrill, 1976). The final model continuum is a combination of numerous blackbodies at

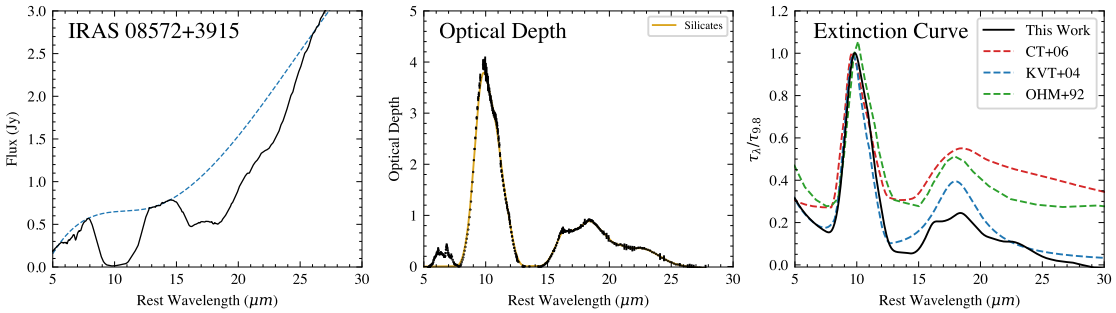

Figure A.4: *Left:* Spitzer IRS spectrum of IRAS 08572+3915 in black with the interpolated cubic spline continuum shown as the dashed blue line. *Middle:* Optical depth profile extracted from the log ratio of the interpolated continuum to the spectrum. The inferred silicate absorption is shown with the gold line. *Right:* Extinction curve constructed from a power law + silicate template. This is compared to three popular choices from the literature Chiar and Tielens (2006), Kemper et al. (2004), Ossenkopf et al. (1992).

different temperatures and the chosen extinction curve which will compensate for these differences. Therefore this is not an issue in this work as I are interested in the resulting full continuum rather than accurately diagnosing the dust constituency based on the shape of the extinction curve.

A.2.2 Uncorrected H_2 Maps

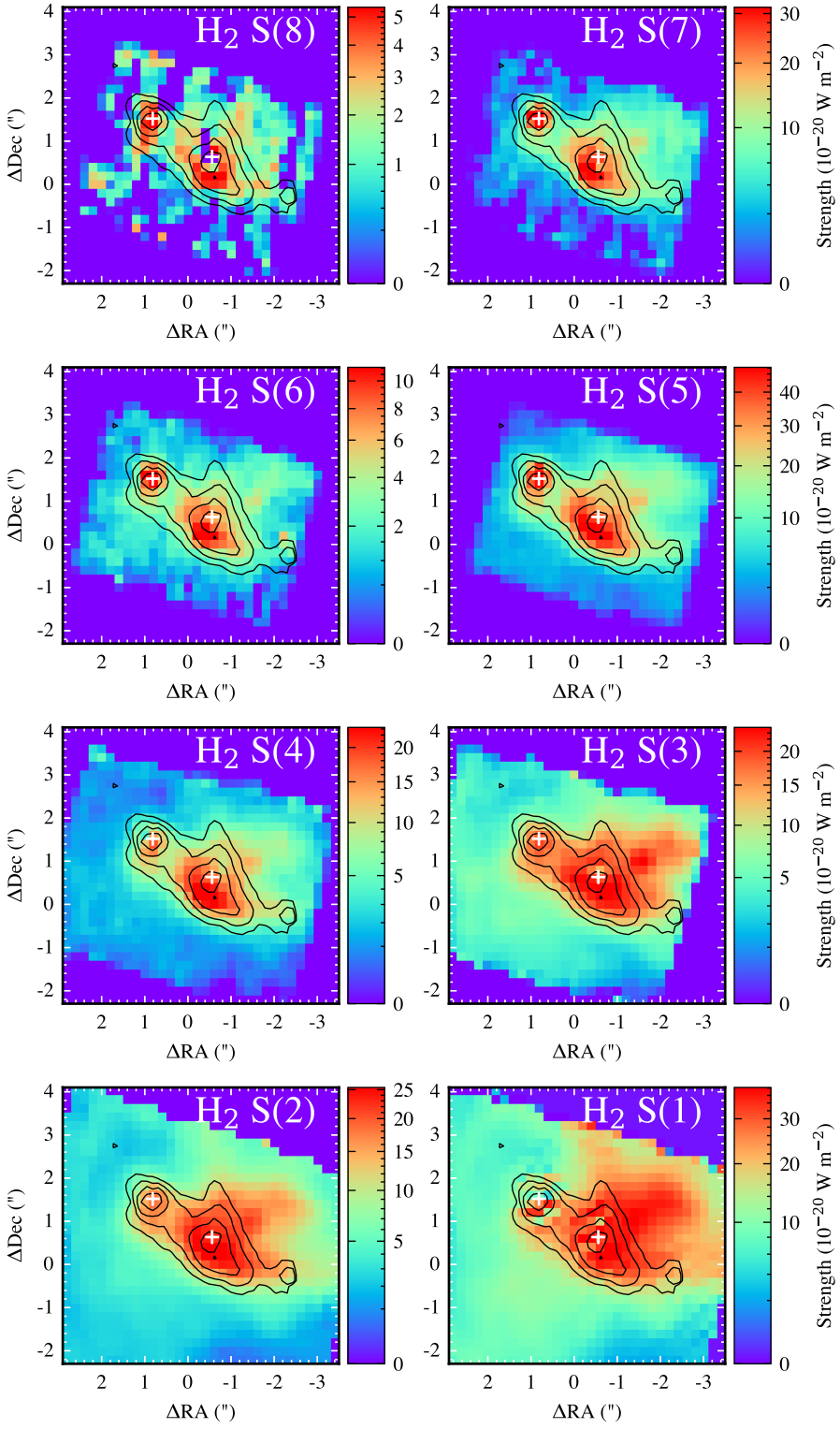

Figure A.5: Same as Fig. 3.12 but without any extinction correction applied.

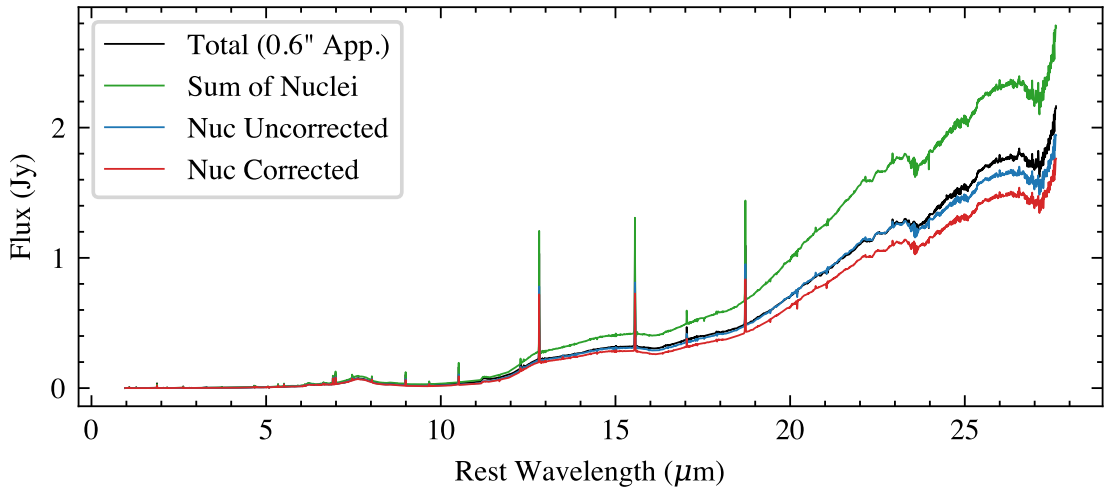

Figure A.6: Correction of IIZw96 SW spectrum for contamination from nearby nucleus. The black line shows the total spectrum of the two nuclei from a 0.6" aperture, while the green shows the sum of the individual nuclei which displays an excess flux due to contamination. The blue spectrum shows the individual nucleus of interest which once corrected for contamination, returns the spectrum shown in red.

A.3 Chapter 4:

A.3.1 PAH Features

I show in Table A.2, the parameters governing the Drude profiles used to model the PAH emission (equations (4.16) and (4.17)).

A.3.2 IIZw96 SW Contamination Correction

Fig. A.6 shows the correction of the extracted spectrum of IIZw96 SW for contamination, due to the nearby secondary nucleus. This process is described in detail in Section 4.2.2.

Table A.2: PAH Feature Parameters of equations (4.16,4.17)

λ_0 μm (1)	γ_0 μm (2)	a (3)
3.29	0.04	0.52
3.40	0.03	-10.0
3.47	0.10	-0.80
5.18	0.05	0.00
5.24	0.10	-3.00
5.45	0.15	0.00
5.53	0.10	0.00
5.64	0.10	0.00
5.70	0.10	0.00
5.76	0.10	0.00
5.87	0.15	0.00
6.00	0.20	0.00
6.20	0.15	-6.00
6.69	0.40	0.00
7.10	0.40	0.00
7.42	0.94	0.00
7.55	0.30	0.00
7.61	0.10	0.00
7.82	0.40	0.00
8.33	0.20	0.00
8.50	0.20	0.00
8.61	0.34	0.00
10.60	0.10	0.00
10.74	0.10	0.00
11.00	0.10	-1.10
11.20	0.10	0.00
11.26	0.30	-10.0
11.99	0.54	0.00
12.60	0.50	0.00
12.77	0.15	0.00
13.15	0.50	0.00
13.55	0.20	-5.00
14.04	0.20	0.00
14.19	0.20	-5.00
15.90	0.32	0.00
16.45	0.23	0.00
17.04	1.11	0.00
17.38	0.21	0.00

Column (1): Initial central wavelength for the fit with range $\pm 0.05\mu$m. Column (2): Initial FWHM allowed to vary within $+10\%$ and -60%. Column (3): Initial asymmetry parameter a, allowed to vary within $+50\%$ and -50%. Those with $a = 0.00$ are fixed to a symmetric profile.

References

Aalto, S. et al. (2015a). A&A 574, A85, A85.

Aalto, S. et al. (2015b). *A&A* 584, A42, A42.

Aalto, S. et al. (2019). *A&A* 627, A147, A147.

Akins, H. B. et al. (2024). *arXiv e-prints*, arXiv:2406.10341, arXiv:2406.10341.

Algera, H. S. B. et al. (2023). MNRAS 518.4, pp. 6142–6157.

Algera, H. S. B. et al. (2024). MNRAS 533.3, pp. 3098–3113.

Allen, M. G. et al. (2008). ApJS 178.1, pp. 20–55.

Alonso Herrero, A. et al. (2024). A&A 690, A95, A95.

Alonso-Herrero, A. et al. (2014). MNRAS 443.3, pp. 2766–2782.

Alonso-Herrero, A. et al. (2016). MNRAS 455.1, pp. 563–583.

Alonso-Herrero, A. et al. (2020). *A&A* 639, A43, A43.

Alonso-Herrero, A. et al. (2006). ApJ 650.2, pp. 835–849.

Alonso-Herrero, A. et al. (2009). ApJ 697.1, pp. 660–675.

Alonso-Herrero, A. et al. (2011). ApJ 736.2, 82, p. 82.

Alonso-Herrero, A. et al. (2012). ApJ 744.1, 2, p. 2.

Antonucci, R. R. J. and Miller, J. S. (1985). ApJ 297, pp. 621–632.

Antonucci, R. (1993). ARA&A 31, pp. 473–521.

Argyriou, I. et al. (2023). *A&A* 675, A111, A111.

Armus, L. et al. (2006). ApJ 640.1, pp. 204–210.

Armus, L. et al. (2009). *Publications of the Astronomical Society of the Pacific* 121.880, p. 559.

Armus, L. et al. (2023). ApJ 942.2, L37, p. L37.

Asano, R. S. et al. (2013). *Earth, Planets and Space* 65.3, pp. 213–222.

Assef, R. J. et al. (2016). ApJ 819.2, 111, p. 111.

Baggen, J. F. W. et al. (2024). ApJ 977.1, L13, p. L13.

Bakes, E. L. O. and Tielens, A. G. G. M. (1994). ApJ 427, p. 822.

Barnard, E. E. (1919). ApJ 49, pp. 1–24.

Berman, L. (1936). MNRAS 96, p. 890.

Bianchin, M. et al. (2023). *arXiv e-prints*, arXiv:2308.00209, arXiv:2308.00209.

Blain, A. W., Ivison, R. J., and Smail, I. (1998). MNRAS 296.3, pp. L29–L33.

Bohlin, R. C., Gordon, K. D., and Tremblay, P. .-. (2014). *Publications of the Astronomical Society of the Pacific* 126.942, p. 711.

Bohlin, R. C. and Lockwood, S. (2022). *Update of the STIS CTE Correction Formula for Stellar Spectra*. Instrument Science Report STIS 2022-7, 11 pages.

Böker, T. et al. (2023). *Publications of the Astronomical Society of the Pacific* 135.1045, 038001, p. 038001.

Boksenberg, A. et al. (1977). MNRAS 178, pp. 451–466.

Boorman, P. G. et al. (2025). ApJ 978.1, 118, p. 118.

Boquien, M. et al. (2019). A&A 622, A103, A103.

Bowler, R. A. A. et al. (2022). MNRAS 510.4, pp. 5088–5101.

Brandl, B. R. et al. (2006). ApJ 653.2, pp. 1129–1144.

Brown, M. J. I. et al. (2019). MNRAS 489.3, pp. 3351–3367.

Buiten, V. A. et al. (2023). *arXiv e-prints*, arXiv:2312.01945, arXiv:2312.01945.

Calzetti, D., Kinney, A. L., and Storchi-Bergmann, T. (1994). ApJ 429, p. 582.

Cameron, E. (2011). *Publications of the Astronomical Society of Australia* 28.2, pp. 128–139.

Candian, A. and Sarre, P. J. (2015). MNRAS 448.3, pp. 2960–2970.

Cappellari, M. (2017). MNRAS 466.1, pp. 798–811.

Cappellari, M. (2023). MNRAS 526.3, pp. 3273–3300.

Cappellari, M. and Emsellem, E. (2004). PASP 116.816, pp. 138–147.

Carnall, A. C. et al. (2018). MNRAS 480.4, pp. 4379–4401.

Chandrasekhar, S. (1960). *Radiative transfer*.

Charmandaris, V., Le Floc'h, E., and Mirabel, I. F. (2004). ApJ 600.1, pp. L15–L18.

Chiar, J. E. and Tielens, A. G. G. M. (2006). ApJ 637.2, pp. 774–785.

Chien, T. C. .-. et al. (2024). MNRAS 532.1, pp. 719–733.

Chown, R. et al. (2023). *arXiv e-prints*, arXiv:2308.16733, arXiv:2308.16733.

Cid Fernandes, R. et al. (2005). MNRAS 358.2, pp. 363–378.

Conroy, C. and Gunn, J. E. (2010). *FSPS: Flexible Stellar Population Synthesis*. Astrophysics Source Code Library, record ascl:1010.043.

Conroy, C., Gunn, J. E., and White, M. (2009). ApJ 699.1, pp. 486–506.

Dartois, E. et al. (2007). ApJ 463.2, pp. 635–640.

Delvecchio, I. et al. (2014). MNRAS 439.3, pp. 2736–2754.

Devriendt, J. E. G., Guiderdoni, B., and Sadat, R. (1999). A&A 350, pp. 381–398.

Díaz-Santos, T. et al. (2007). ApJ 661.1, pp. 149–164.

Díaz-Santos, T. et al. (2017). ApJ 846.1, 32, p. 32.

Dole, H. et al. (2006). A&A 451.2, pp. 417–429.

Donnan, F. R. et al. (2023a). *A&A* 669, A87, A87.

Donnan, F. R. et al. (2023b). MNRAS 519.3, pp. 3691–3705.

Donnan, F. R. et al. (2024). MNRAS 529.2, pp. 1386–1404.

Donnan, F. R. (2022). *PAHDecomp: Decomposing the mid-IR spectra of extremely obscured galaxies*. Astrophysics Source Code Library, record ascl:2211.004.

Donnan, F. R. et al. (2025). *arXiv e-prints*, arXiv:2503.11611, arXiv:2503.11611.

Donnellan, J. M. S. et al. (2024). MNRAS 532.2, pp. 1966–1979.

Draine, B. T. (1989). In: *Infrared Spectroscopy in Astronomy*. Ed. by E. Böhm-Vitense, p. 93.

Draine, B. T. (2003). *Annual Review of A&A* 41, pp. 241–289.

Draine, B. T. and Li, A. (2001). ApJ 551.2, pp. 807–824.

Draine, B. T. and Li, A. (2007). ApJ 657.2, pp. 810–837.

Draine, B. T. (2011). *Physics of the Interstellar and Intergalactic Medium*.

Eddington, A. S. (1926). *The Internal Constitution of the Stars*.

Efstathiou, A., Hough, J. H., and Young, S. (1995). MNRAS 277.3, pp. 1134–1144.

Efstathiou, A. et al. (2013). MNRAS 436.2, pp. 1873–1882.

Efstathiou, A. et al. (2022). MNRAS 512.4, pp. 5183–5213.

Efstathiou, A. (2006). MNRAS 371.1, pp. L70–L73.

Eisenhardt, P. R. M. et al. (2012). ApJ 755.2, 173, p. 173.

Emonts, B. H. C. et al. (2014). *A&A* 572, A40, A40.

Engelbracht, C. W. et al. (2008). ApJ 678.2, pp. 804–827.

Evans, A. S. et al. (2022). *arXiv e-prints*, arXiv:2208.14507, arXiv:2208.14507.

Fabian, A. C. (2012). ARA&A 50, pp. 455–489.

Fabian, A. C., Vasudevan, R. V., and Gandhi, P. (2008). MNRAS 385.1, pp. L43–L47.

Falstad, N. et al. (2018). *A&A* 609, A75, A75.

Falstad, N. et al. (2019). *A&A* 623, A29, A29.

Falstad, N. et al. (2021). *A&A* 649, A105, A105.

Farrah, D. et al. (2013). ApJ 776.1, 38, p. 38.

Fawcett, V. A. et al. (2022). MNRAS 513.1, pp. 1254–1274.

Ferrara, A., Viti, S., and Ceccarelli, C. (2016). MNRAS 463.1, pp. L112–L116.

Feruglio, C. et al. (2015). A&A 583, A99, A99.

Frayer, D. T. et al. (1999). ApJ 118.1, pp. 139–144.

Fritz, J., Franceschini, A., and Hatziminaoglou, E. (2006). MNRAS 366.3, pp. 767–786.

Fritz, T. K. et al. (2011). ApJ 737.2, 73, p. 73.

Gallimore, J. F. et al. (2010). ApJS 187.1, pp. 172–211.

García-Bernete, I. et al. (2017). MNRAS 469.1, pp. 110–126.

García-Bernete, I. et al. (2019). MNRAS 486.4, pp. 4917–4935.

García-Bernete, I. et al. (2022a). *A&A* 666, L5, p. L5.

García-Bernete, I. et al. (2022b). *A&A* 663, A46, A46.

García-Bernete, I. et al. (2022c). MNRAS 509.3, pp. 4256–4275.

García-Bernete, I. et al. (2022d). *A&A* 667, A140, A140.

García-Bernete, I. et al. (2024a). *A&A* 682, L5, p. L5.

García-Bernete, I. et al. (2024b). A&A 691, A162, A162.

García-Bernete, I. et al. (2024c). *A&A* 681, L7, p. L7.

García-Bernete, I. et al. (2025). *arXiv e-prints*, arXiv:2502.16301, arXiv:2502.16301.

Genzel, R. et al. (1998). ApJ 498.2, pp. 579–605.

Gillett, F. C. and Forrest, W. J. (1973). ApJ 179, p. 483.

Giovannoli, E. et al. (2011). A&A 525, A150, A150.

Glazebrook, K. et al. (1999). MNRAS 306.4, pp. 843–856.

Gonzále Delgado, R. M. et al. (2010). In: *Stellar Populations - Planning for the Next Decade*. Ed. by G. R. Bruzual and S. Charlot. Vol. 262. IAU Symposium, pp. 341–342.

González-Alfonso, E. and Sakamoto, K. (2019). ApJ 882.2, 153, p. 153.

González-Alfonso, E. et al. (2021). *A&A* 645, A49, A49.

González-Alfonso, E. et al. (2024). *A&A* 682, A182, A182.

González-Martín, O. et al. (2019a). ApJ 884.1, 10, p. 10.

González-Martín, O. et al. (2019b). ApJ 884.1, 11, p. 11.

Gordon, K. D. et al. (2021). ApJ 916.1, 33, p. 33.

Gorski, M. D. et al. (2023). *A&A* 670, A70, A70.

Gorski, M. D. et al. (2024). *A&A* 684, L11, p. L11.

Haidar, H. et al. (2024). MNRAS 532.4, pp. 4645–4660.

Harrison, C. M. and Ramos Almeida, C. (2024). *Galaxies* 12.2, 17, p. 17.

Hatziminaoglou, E. et al. (2015). ApJ 803.2, 110, p. 110.

Henyey, L. G. and Greenstein, J. L. (1941). ApJ 93, pp. 70–83.

Herbst, T. M. et al. (1996). ApJ 111, p. 2403.

Hernán-Caballero, A. et al. (2016). MNRAS 463.2, pp. 2064–2078.

Hernán-Caballero, A. et al. (2020). MNRAS 497.4, pp. 4614–4625.

Hernandez, S. et al. (2023). ApJ 948.2, 124, p. 124.

Herschel, W. (1785). *Philosophical Transactions of the Royal Society of London Series I* 75, pp. 213–266.

Hickox, R. C. and Alexander, D. M. (2018). ARA&A 56, pp. 625–671.

Holland, W. S. et al. (1999). MNRAS 303.4, pp. 659–672.

Hollenbach, D. (1997). In: ed. by B. Reipurth and C. Bertout. Vol. 182, pp. 181–198.

Hollenbach, D. and McKee, C. F. (1989). ApJ 342, p. 306.

Hönig, S. F. et al. (2010). *A&A* 515, A23, A23.

Hönig, S. F. et al. (2012). ApJ 755.2, 149, p. 149.

Hönig, S. F. et al. (2013). ApJ 771.2, 87, p. 87.

Hönig, S. F. and Kishimoto, M. (2017). ApJ 838.2, L20, p. L20.

Hopkins, P. F. et al. (2006). ApJS 163.1, pp. 1–49.

Hopkins, P. F. et al. (2008). ApJS 175.2, pp. 356–389.

Houck, J. R. et al. (1984). ApJ 278, pp. L63–L66.

Houck, J. R. et al. (2004). In: *Optical, Infrared, and Millimeter Space Telescopes*. Ed. by J. C. Mather. Vol. 5487. Society of Photo-Optical Instrumentation Engineers (SPIE) Conference Series, pp. 62–76.

Hughes, D. H. et al. (1998). Nature 394.6690, pp. 241–247.

Hummer, D. G. and Storey, P. J. (1987). MNRAS 224, pp. 801–820.

Hunt, L. K. et al. (2010). ApJ 712.1, pp. 164–187.

Imanishi, M. et al. (2010). ApJ 721.2, pp. 1233–1261.

Inami, H. et al. (2010). ApJ 140.1, pp. 63–74.

Inami, H. et al. (2013). ApJ 777.2, 156, p. 156.

Inami, H. et al. (2022a). ApJ 940.1, L6, p. L6.

Inami, H. et al. (2022b). MNRAS 515.3, pp. 3126–3143.

IRAS Working Group (1983). Nature 303.5917, p. 480.

Iyer, K. G. et al. (2019). ApJ 879.2, 116, p. 116.

Jakobsen, P. et al. (2022). *A&A* 661, A80, A80.

Jarrett, T. H. et al. (2000). ApJ 119.5, pp. 2498–2531.

Jensen, J. J. et al. (2017). MNRAS 470.3, pp. 3071–3094.

Joblin, C., Leger, A., and Martin, P. (1992). ApJ 393, p. L79.

Jones, A. P. et al. (2013). *A&A* 558, A62, A62.

Jones, G. T., Stanway, E. R., and Carnall, A. C. (2022). MNRAS 514.4, pp. 5706–5724.

Jones, T. W. and Merrill, K. M. (1976). ApJ 209, pp. 509–524.

Juodžbalis, I. et al. (2023). MNRAS 525.1, pp. 1353–1364.

Kankare, E. et al. (2018). *The Astronomer's Telegram* 11156, p. 1.

Karson, M. (1968). *Journal of the American Statistical Association* 63.323, pp. 1047–1049.

Kaufman, M. J., Hollenbach, D. J., and Tielens, A. G. G. M. (1998). ApJ 497.1, pp. 276–287.

Kaufman, M. J., Wolfire, M. G., and Hollenbach, D. J. (2006). ApJ 644.1, pp. 283–299.

Kemper, F., Vriend, W. J., and Tielens, A. G. G. M. (2004). ApJ 609.2, pp. 826–837.

Killi, M. et al. (2024). MNRAS 531.3, pp. 3222–3241.

Kim, D. and Im, M. (2018). A&A 610, A31, A31.

Kishimoto, M. et al. (2007). *A&A* 476.2, pp. 713–721.

Kormendy, J. and Ho, L. C. (2013). ARA&A 51.1, pp. 511–653.

Kozasa, T., Hasegawa, H., and Nomoto, K. (1989). ApJ 344, p. 325.

Labbé, I. et al. (2025). ApJ 978.1, 92, p. 92.

Labiano, A. et al. (2016). In: *Observatory Operations: Strategies, Processes, and Systems VI*. Ed. by A. B. Peck, R. L. Seaman, and C. R. Benn. Vol. 9910. Society of Photo-Optical Instrumentation Engineers (SPIE) Conference Series, 99102W, 99102W.

Labiano, A. et al. (2021). *A&A* 656, A57, A57.

Lahuis, F. et al. (2007). ApJ 659.1, pp. 296–304.

Lai, T. S. .-. et al. (2020). ApJ 905.1, 55, p. 55.

Lai, T. S. .-. et al. (2022). ApJ 941.2, L36, p. L36.

Lai, T. S. .-. et al. (2023). ApJ 957.2, L26, p. L26.

Lai, T. S. .-. et al. (2024). ApJ 967.2, 83, p. 83.

Lambrides, E. L. et al. (2019). MNRAS 487.2, pp. 1823–1843.

Leach, S. (1986). *Journal of Electron Spectroscopy and Related Phenomena* 41.2, pp. 427–438.

Leftley, J. H. et al. (2024). A&A 689, A314, A314.

Leftley, J. H. et al. (2018). ApJ 862.1, 17, p. 17.

Leja, J. et al. (2019). ApJ 876.1, 3, p. 3.

Li, A. (2020). *Nature Astronomy* 4, pp. 339–351.

Li, A. and Draine, B. T. (2001). ApJ 554.2, pp. 778–802.

Li, A. et al. (2015). "Dust in the Local Group: A Conference in honour of David Block and Bruce Elmegreen". In: *Lessons from the Local Group: A Conference in honor of David Block and Bruce Elmegreen*, pp. 85–103.

Liffman, K. and Clayton, D. D. (1989). ApJ 340, p. 853.

Lira, P. et al. (2008). MNRAS 384.1, pp. 316–322.

Lonsdale, C. J., Persson, S. E., and Matthews, K. (1984). ApJ 287, pp. 95–107.

López-Gonzaga, N. et al. (2014). A&A 565, A71, A71.

López-Gonzaga, N. et al. (2016). A&A 591, A47, A47.

Lutz, D. (1999). In: *The Universe as Seen by ISO*. Ed. by P. Cox and M. Kessler. Vol. 427. ESA Special Publication, p. 623.

Ma, Y. et al. (2024). *arXiv e-prints*, arXiv:2410.06257, arXiv:2410.06257.

Madau, P., Ghisellini, G., and Fabian, A. C. (1994). MNRAS 270, pp. L17–L21.

Madau, P. and Dickinson, M. (2014). *Annual Review of A&A* 52.1, pp. 415–486.

Magnelli, B. et al. (2011). *A&A* 528, A35, A35.

Mancini, M. et al. (2015). MNRAS 451, pp. L70–L74.

Marin, F. (2016). MNRAS 460.4, pp. 3679–3705.

Marshall, J. A. et al. (2007). ApJ 670.1, pp. 129–155.

Martínez-Paredes, M. et al. (2015). MNRAS 454.4, pp. 3577–3589.

Martínez-Paredes, M. et al. (2020). ApJ 890.2, 152, p. 152.

Martínez-Paredes, M. et al. (2021). ApJ 922.2, 157, p. 157.

Matthee, J. et al. (2024). ApJ 963.2, 129, p. 129.

Micelotta, E. R., Jones, A. P., and Tielens, A. G. G. M. (2010). *A&A* 510, A36, A36.

Michałowski, M. J. et al. (2012). A&A 541, A85, A85.

Morganti, R. (2017). *Frontiers in Astronomy and Space Sciences* 4, 42, p. 42.

Moullet, A. et al. (2023). *arXiv e-prints*, arXiv:2310.20572, arXiv:2310.20572.

Mushotzky, R. F., Done, C., and Pounds, K. A. (1993). ARA&A 31, pp. 717–717.

Nenkova, M. et al. (2008a). ApJ 685.1, pp. 147–159.

Nenkova, M. et al. (2008b). ApJ 685.1, pp. 160–180.

Netzer, H. et al. (2007). ApJ 666.2, pp. 806–816.

Neugebauer, G., Becklin, E., and Hyland, A. R. (1971). ARA&A 9, p. 67.

Öberg, K. I. et al. (2011). ApJ 740.2, 109, p. 109.

Ohyama, Y., Terashima, Y., and Sakamoto, K. (2015). ApJ 805.2, 162, p. 162.

Ossenkopf, V., Henning, T., and Mathis, J. S. (1992). *A&A* 261, pp. 567–578.

Osterbrock, D. E. and Martel, A. (1993). ApJ 414, p. 552.

Osterbrock, D. E., Shaw, R. A., and Veilleux, S. (1990). ApJ 352, p. 561.

Paradis, D., Bernard, J. .-., and Mény, C. (2009). A&A 506.2, pp. 745–756.

Peeters, E., Spoon, H. W. W., and Tielens, A. G. G. M. (2004). ApJ 613.2, pp. 986–1003.

Peeters, E. et al. (2002). A&A 390, pp. 1089–1113.

Pereira-Santaella, M. et al. (2021). *A&A* 651, A42, A42.

Pereira-Santaella, M. et al. (2022). *arXiv e-prints*, arXiv:2208.04835, arXiv:2208.04835.

Pereira-Santaella, M. et al. (2023). *arXiv e-prints*, arXiv:2309.06486, arXiv:2309.06486.

Pereira-Santaella, M. et al. (2010). ApJ 725.2, pp. 2270–2280.

Pereira-Santaella, M. et al. (2014). *A&A* 566, A49, A49.

Pereira-Santaella, M. et al. (2015). *A&A* 577, A78, A78.

Pérez-Beaupuits, J. P. et al. (2011). *A&A* 533, A56, A56.

Pérez-González, P. G. et al. (2024). ApJ 968.1, 4, p. 4.

Perger, K. et al. (2025). A&A 693, L2, p. L2.

Perna, M. et al. (2022). A&A 662, A94, A94.

Perna, M. et al. (2024). *arXiv e-prints*, arXiv:2403.13948, arXiv:2403.13948.

Peterson, B. M. (1997). "The Black-Hole Paradigm". In: *An Introduction to Active Galactic Nuclei*. Cambridge University Press, pp. 32–39.

Petric, A. O. et al. (2018). ApJ 156.6, 295, p. 295.

Phan, D., Pradhan, N., and Jankowiak, M. (2019). *arXiv e-prints*, arXiv:1912.11554, arXiv:1912.11554.

Pound, M. W. and Wolfire, M. G. (2008). In: *Astronomical Data Analysis Software and Systems XVII*. Ed. by R. W. Argyle, P. S. Bunclark, and J. R. Lewis. Vol. 394. Astronomical Society of the Pacific Conference Series, p. 654.

Pound, M. W. and Wolfire, M. G. (2011). *PDRT: Photo Dissociation Region Toolbox*.

Raban, D. et al. (2009). MNRAS 394.3, pp. 1325–1337.

Ramos Almeida, C. et al. (2009). ApJ 702.2, pp. 1127–1149.

Rapacioli, M. et al. (2006). A&A 460.2, pp. 519–531.

Reach, W. T. et al. (2019). ApJ 884.1, 81, p. 81.

Ricci, C. et al. (2021). MNRAS 506.4, pp. 5935–5950.

Rich, J. et al. (2023). ApJ 944.2, L50, p. L50.

Rich, J. A., Kewley, L. J., and Dopita, M. A. (2011). ApJ 734.2, 87, p. 87.

Richards, G. T. et al. (2003). AJ 126.3, pp. 1131–1147.

Rieke, G. H. and Lebofsky, M. J. (1979). ARA&A 17, pp. 477–511.

Rieke, G. H. et al. (2015). *Publications of the Astronomical Society of the Pacific* 127.953, p. 584.

Rigby, J. et al. (2022). *arXiv e-prints*, arXiv:2207.05632, arXiv:2207.05632.

Rigopoulou, D. et al. (1999). ApJ 118.6, pp. 2625–2645.

Rigopoulou, D. et al. (2002). *A&A* 389, pp. 374–386.

Rigopoulou, D. et al. (2021). MNRAS 504.4, pp. 5287–5300.

Rigopoulou, D. et al. (2024). MNRAS 532.2, pp. 1598–1611.

Riguccini, L. et al. (2011). A&A 534, A81, A81.

Roche, P. F. and Aitken, D. K. (1985). MNRAS 213, pp. 789–797.

Roche, P. F., Aitken, D. K., and Whitmore, B. (1983). MNRAS 205, 21P–26.

Roche, P. F., Alonso-Herrero, A., and Gonzalez-Martin, O. (2015). MNRAS 449.3, pp. 2598–2603.

Roche, P. F. et al. (1984). MNRAS 207, pp. 35–45.

Roche, P. F. et al. (1986). MNRAS 218, 19P–23.

Roche, P. F. et al. (1991). MNRAS 248, p. 606.

Rolffs, R. et al. (2011). A&A 527, A68, A68.

Rupke, D. S. N. and Veilleux, S. (2011). ApJ 729.2, L27, p. L27.

Saito, T. et al. (2015). ApJ 803.2, 60, p. 60.

Saito, T. et al. (2017). ApJ 834.1, 6, p. 6.

Sajina, A. et al. (2009). ApJ 703.1, pp. 270–284.

Sakamoto, K. et al. (2010). ApJ 725.2, pp. L228–L233.

Sakamoto, K. et al. (2014). ApJ 797.2, 90, p. 90.

Salim, S. and Narayanan, D. (2020). *Annual Review of A&A* 58, pp. 529–575.

Salpeter, E. E. (1955). ApJ 121, p. 161.

Sanders, D. B. et al. (1988). ApJ 328, p. L35.

Sanders, D. B. et al. (2003). ApJ 126.4, pp. 1607–1664.

Sarangi, A., Dwek, E., and Kazanas, D. (2019). ApJ 885.2, 126, p. 126.

Schmidt, M. (1963). Nature 197.4872, p. 1040.

Scholtz, J. et al. (2023). *arXiv e-prints*, arXiv:2311.18731, arXiv:2311.18731.

Schweitzer, M. et al. (2006). ApJ 649.1, pp. 79–90.

Setti, G. and Woltjer, L. (1989). A&A 224, pp. L21–L23.

Setton, D. J. et al. (2024). *arXiv e-prints*, arXiv:2411.03424, arXiv:2411.03424.

Seyfert, C. K. (1943). ApJ 97, p. 28.

Shakura, N. I. and Sunyaev, R. A. (1973). A&A 500, pp. 33–51.

Shannon, M. J. and Boersma, C. (2019). ApJ 871.1, 124, p. 124.

Shapley, H. and Curtis, H. D. (1921). *Bulletin of the National Research Council* 2.11, pp. 171–217.

Shen, Y. and Liu, X. (2012). ApJ 753.2, 125, p. 125.

Shipley, H. V. et al. (2016). ApJ 818.1, 60, p. 60.

Shivaei, I. et al. (2017). ApJ 837.2, 157, p. 157.

Siebenmorgen, R., Krügel, E., and Spoon, H. W. W. (2004). *A&A* 414, pp. 123–139.

Siebenmorgen, R., Heymann, F., and Efstathiou, A. (2015). A&A 583, A120, A120.

Silva, L. et al. (1998). ApJ 509.1, pp. 103–117.

Smith, J. D. T. et al. (2007a). *Publications of the Astronomical Society of the Pacific* 119.860, pp. 1133–1144.

Smith, J. D. T. et al. (2007b). ApJ 656.2, pp. 770–791.

Sommovigo, L. et al. (2022). MNRAS 517.4, pp. 5930–5941.

Spilker, J. S. et al. (2023). Nature 618.7966, pp. 708–711.

Spoon, H. W. W. et al. (2001). ApJ 365, pp. L353–L356.

Spoon, H. W. W. et al. (2002). A&A 385, pp. 1022–1041.

Spoon, H. W. W. et al. (2007). ApJ 654.1, pp. L49–L52.

Spoon, H. W. W. et al. (2022). *arXiv e-prints*, arXiv:2203.03071, arXiv:2203.03071.

Stalevski, M. et al. (2016). MNRAS 458.3, pp. 2288–2302.

Stancik, A. L. and Brauns, E. B. (2008). *Vibrational Spectroscopy* 47.1, pp. 66–69.

Stebbins, J., Huffer, C. M., and Whitford, A. E. (1939). ApJ 90, p. 209.

Stecher, T. P. and Donn, B. (1965). ApJ 142, p. 1681.

Stetson, P. B. (1987). *Publications of the Astronomical Society of the Pacific* 99, p. 191.

Stierwalt, S. et al. (2013). ApJS 206.1, 1, p. 1.

Strauss, M. A. et al. (1992). ApJS 83, p. 29.

Sturm, E. et al. (1996). A&A 315, pp. L133–L136.

Sturm, E. et al. (2002). A&A 393, pp. 821–841.

Tielens, A. G. G. M. (2005). *The Physics and Chemistry of the Interstellar Medium*.

Tielens, A. G. G. M. (2008). ARA&A 46, pp. 289–337.

Tielens, A. G. G. M. and Hagen, W. (1982). A&A 114.2, pp. 245–260.

Tinsley, B. M. (1968). ApJ 151, p. 547.

Togi, A. and Smith, J. D. T. (2016). ApJ 830.1, 18, p. 18.

Tojeiro, R. et al. (2007). MNRAS 381.3, pp. 1252–1266.

Tristram, K. R. W. et al. (2014). A&A 563, A82, A82.

Tsuchikawa, T. et al. (2021). *A&A* 651, A117, A117.

U, V. et al. (2022). ApJ 940.1, L5, p. L5.

Valentijn, E. A. et al. (1996). A&A 315, pp. L145–L148.

Valiante, R. et al. (2009). MNRAS 397.3, pp. 1661–1671.

Varnava, C. and Efstathiou, A. (2024). MNRAS 531.2, pp. 2304–2329.

Veilleux, S. et al. (2009). ApJS 182.2, pp. 628–666.

Verro, K. et al. (2022). A&A 660, A34, A34.

Verstraete, L. et al. (2001). *A&A* 372, pp. 981–997.

Villa-Vélez, J. A. et al. (2024). A&A 688, A96, A96.

Voit, G. M. (1992). MNRAS 258, p. 841.

Wada, K. (2012). ApJ 758.1, 66, p. 66.

Wanders, I. et al. (1997). ApJS 113.1, pp. 69–88.

Wang, F. et al. (2021). ApJ 907.1, L1, p. L1.

Welch, B. et al. (2022). Nature 603.7903, pp. 815–818.

Wells, M. et al. (2015). *Publications of the Astronomical Society of the Pacific* 127.953, p. 646.

Wright, G. S. et al. (2015). *Publications of the Astronomical Society of the Pacific* 127.953, p. 595.

Yang, G. et al. (2020). MNRAS 491.1, pp. 740–757.

Yang, G. et al. (2023). ApJ 950.1, L5, p. L5.

York, D. G. et al. (2000). ApJ 120.3, pp. 1579–1587.

Young, J. et al. (2023). ApJ 958.1, L5, p. L5.

Zavala, J. A. et al. (2021). ApJ 909.2, 165, p. 165.

Zhang, L. and Ho, L. C. (2023a). ApJ 943.1, 60, p. 60.

Zhang, L. and Ho, L. C. (2023b). ApJ 953.1, L9, p. L9.

Zhang, L. et al. (2024). ApJ 975.1, L2, p. L2.